Theoretical developments to model microstructural effects on the rheology of complex fluids

A Thesis
Presented to
The Academic Faculty

by

Salah Aldin Faroughi

In Partial Fulfillment
of the Requirements for the Degree
Doctor of Philosophy

School of Civil and Environmental Engineering
Georgia Institute of Technology
August 2016

Theoretical developments to model microstructural effects on the rheology of complex fluids

Approved by:

Dr. Christian Huber, Advisor
School of Civil and Environmental Engineering
Georgia Institute of Technology

Professor David Frost
School of Civil and Environmental Engineering
Georgia Institute of Technology

Dr. Chloé Arson
School of Civil and Environmental Engineering
Georgia Institute of Technology

Dr. Josef Dufek
School of Earth and Atmospheric Sciences
Georgia Institute of Technology

Professor Susan Burns
School of Civil and Environmental Engineering
Georgia Institute of Technology

Date Approved: June, 15, 2016

DEDICATED

To my parents, my siblings and my beloved wife

without whom none of my success in this work would have happened.

ACKNOWLEDGEMENTS

I had a wonderful journey at Georgia Tech in the past four years. I was gifted with a life that was full of adventure and great opportunities to grow personally and academically. Of course, without the support gaining from family, friends and many other people at Georgia Tech, this success would not have been possible. I am extremely grateful that I had the opportunity to do my PhD under the supervision of Dr. Christian Huber, the most supportive advisor ever I have seen, heard and felt. Dr. Huber not only taught me the requirements to be a good researcher and get the most out of a research, but also shared without any reservation to me how to come up with a better work-life balance. In addition, his countless energy and encouragement made me keep continuing on the work to always obtain better and better results. I would also like to greatly thank my committee members, Prof. David Frost, Prof. Susan Burns, Dr. Chloe Arson and Dr. Josef Dufek who provided me with instructive comments and suggestions to empower my work.

Moreover, I am exceptionally thankful to my wife and family who provided me with innumerable supports; more than I could even imagine. Their behavior and encouragement have always been inspiring me to dream and to bravely fight for my dreams. My gratefulness to them is beyond words.

TABLE OF CONTENTS

LIST OF TABLES

LIST OF FIGURES

SUMMARY

Many processes in engineering and science involve multiphase flow, and the rate at which they operate is controlled by multiphase rheology. A rheology model with predictive capability over a wide range of physical and flow conditions is, therefore, of interest to quantify and optimize these processes. Complex fluids, a family of multiphase fluids, are ubiquitous across a broad range of industrial setting, including Pharmaceutical products, Food & Dairy, Oil & Gas, Mining & Coating, Cement & Concrete, Cosmetics, Composite & Powder, and Polymers and Biological fluids. Complex fluids include one continuous phase and one or more external phases such as suspended solid particles, droplets of liquid, bubbles of gas that can be rigid or deformable, and can stick together or repel each other. The interactions between constituents cause the overall behavior of these fluids to be different from pure fluids and solids. The rheology of complex fluids can be highly non-linear. At very low volume fraction of the dispersed phase (volume fraction of $\psi < 0.1$), the relationship between the relative viscosity of the complex fluids and ψ is simple and linear, i.e. it does not depend on the particle size distributions and the deformation history. Under these conditions, experimental data agree well with each other and allow the development and application of simple rheology models. The situation becomes more challenging as the volume fraction of particles increases and hydrodynamic interactions between particles become more important. For instance, as particle volume fractions approach the maximum packing limit, the particle shape, deformation and size distributions, the formation of a microstructure or fabric (including the orientation of particles, their arrangement along shear planes) and the shear conditions under which the fluid is flowing play a more crucial role. This complexity is illustrated by the non-linear response of complex fluids to deformation and especially the lack of self-similarity observed experimentally. This loss of self-similarity, however, might be an artifact resulting from ignoring several important processes and key

variables describing the dependence of complex fluids rheology on the rate of deformation.

We present a theoretical framework to build a generalized rheological model for non-Brownian complex fluids subjected to a steady straining flow at low Reynolds number. We first consider the effect of a single deformable fluid particle on the ambient velocity and stress fields to constrain the rheological behavior of dilute mixtures. We then extend the solution to the rheology of concentrated complex fluids using an incremental differential effective medium theory operating in a fixed and finite volume. These analyses provide a framework to include non-linear microstructural processes in the description of the shear deformation of complex fluids, e.g., particle shape and size distribution, particle deformation and breakage, and particle alignment and rearrangement. The proposed framework is based on new state variables and is designed to restore self-similarity by providing a microscopic parameterization for the influence of the shearing condition on the rearrangement and evolution of microstructures. It forms the basis for the derivation of a predictive model for the effective viscosity of concentrated complex fluids.

CHAPTER I

INTRODUCTION

Complex Fluids are a family of multiphase fluids that include an ambient phase and one or more external phases such as suspended solid particles, droplets of liquid, bubbles of gas that can be rigid or deformable, and can stick together or repel each other. Complex fluids such as suspensions and emulsions are ubiquitous in everyday's life (e.g. detergents, shaving cream, and coffee), industrial applications (e.g. oil & gas, ceramic, pharmaceutical and cosmetic), and natural systems (e.g. magmas and sediment transport). The shear dynamic viscosity is one of the physical quantities that controls the rate at which these complex fluids flow. When these fluids are subjected to a shear flow, they can exhibit shear thinning, shear thickening, jamming, shear banding and yield stress. In general, a mixture of these processes controls the response of a complex fluid to deformation. From the complexity of the processes involved to describe the rheology of a complex fluid, one should consider the following potential factors:

1. the shear dynamic viscosity of the ambient fluid in the absence of particles,
2. the particle volume fraction,
3. the particle shape, sphericity, angularity and roughness,
4. elastic, viscoelastic and viscous deformation of particles as well as possible breakage causing changes in the particle shape and size distributions,
5. hydrodynamic interactions of particles with each other and with the ambient fluid for deformation regimes where hydrodynamic forces are dominant,
6. the state of particle-particle interactions under different shear conditions to assess the relevance of friction and lubrication forces,

7. particle clustering, ordering and in general the spatial distribution of particles to assess the effect of shear induced microstructural arrangement,

8. Jamming and transition from fluid-like to solid-like behavior,

9. transient effects to include time-dependent rheology.

Studies on rheology generally focus on the shear viscosity, and as such, attempt to constrain the relationship between shear stresses and shear strains of a material under the effect of imposed forces within different experimental setups, conditions and time-frames. When inertia can be neglected, the fluid flow is sheet-like, and the velocity of the fluid decreases towards the solid boundary. The rate by which the shear strain is changing along the sheet layers or simply, for the simple shear case, the gradient of velocity vector, $\boldsymbol{\nabla u}$, from the bulk fluid to the wall is called shear rate, $\boldsymbol{\Upsilon}$, with the unit of reciprocal seconds. As we will refer throughout this review to the rate of viscous energy dissipation, $\dot{E}$, under several circumstances, we define it here as the tensorial contraction between the shear stress, τ, and shear rate integrated over the control volume (volume of the fluid V),

$$\dot{E} = \int_V \tau_{ij} \Upsilon_{ij} \, \mathrm{dV}, \tag{1.1}$$

where the summation over repeated indices is used and $i \neq j$.

The response of fluids to shear stresses is generally classified into two categories, (i) Newtonian where the shear stresses correlate linearly with shear rates and the constant of proportionality is the shear viscosity $\mu = \tau/\Upsilon$ where $\Upsilon = |\boldsymbol{\Upsilon}|$ is the magnitude of the shear rate, and (ii) non-Newtonian fluids where the relationship is no longer linear. Commonly, the flow behavior of fluids under steady shear flow condition is characterized by a constitutive equation such as $\boldsymbol{\tau} = f(\boldsymbol{\Upsilon})$. These empirical constitutive equations are retrieved from the structural study of fluids under deformation. For example, the Herschel-Bulkley (HB) model

$$\boldsymbol{\tau} = \boldsymbol{\tau_0} + k\boldsymbol{\Upsilon}^n, \tag{1.2}$$

is a widely applied structural model that characterizes the rheology of viscoplastic materials with a yield stress $\boldsymbol{\tau_0}$ (Herschel & Bulkley, 1926). In Eq. (1.2), K and n are fitting constants representing the consistency and flow index, respectively.

For the case of a Newtonian fluid ($n = 1$), the consistency, K, reduces to the shear viscosity μ. In practice, fluids can be Newtonian only over a limited range of conditions, and the majority of materials show non-Newtonian behaviors. For non-Newtonian fluids ($n \neq 1$, $K \neq \mu$), the shear viscosity is a function of the imposed shear stress $\mu = f(\tau)$ or shear rate $\mu = f(\Upsilon)$. This non-linearity is generally caused by internal microstructural changes in fluids. Therefore, for non-Newtonian fluids, the effective shear viscosity can be only defined for a specified shear condition.

Two families of curves are generally plotted to illustrate the rheology of fluids; (1) flow curves, and (2) viscosity curves. Figure 1.1 provides a schematic example of typical trends expected for various fluids at steady state (i.e. a dynamic equilibrium condition). In some non-Newtonian fluids, the measured viscosity decreases with increasing shear rate, a behavior defined as shear thinning, while other fluids display the opposite behavior, known as shear thickening.

Shear thinning and shear thickening are very common behaviors among fluids within which structural changes (molecules ordering and disordering, respectively) occur in response to applied shear stresses. When the viscosity of a fluid is time-dependent, the flow and viscosity curves display a hysteresis loop caused by the history-dependent nature of the fluid response to ramping shear stresses or shear rates. These fluids are either thixotropic (Mewis & Wagner, 2009b) or rheopectic (see Fig. 1.1), and the size of the hysteresis loop depends on the shear history and the rate at which the deformation conditions (e.g. shear rate) are varying.

The viscosity of complex fluids, e.g. suspensions of solid particles, commonly shows shear rate dependence. This behavior is rooted into the suspension microstructure (spatial arrangement and orientation of particles) that deforms under different shear conditions (see Fig. 1.2). It is common practice to parameterize the apparent (or effective) viscosity of a suspension μ_ψ at dynamic equilibrium based on the volume fraction of particles ψ and the

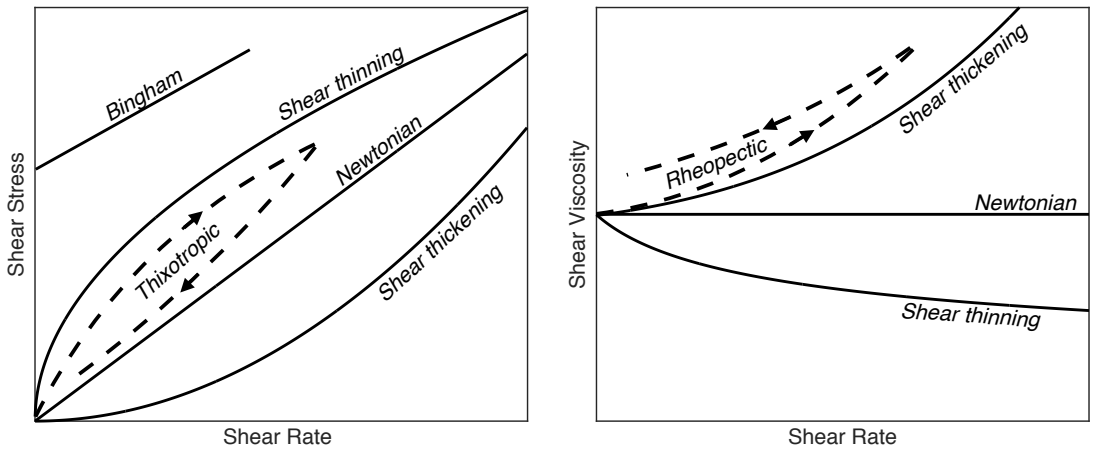

Figure 1.1: Typical rheological behavior of materials under dynamic equilibrium conditions on flow curve (left) and viscosity curve (right).

viscosity of the ambient fluid μ_m such that

$$\mu_\psi = \mu_m f(\psi). \tag{1.3}$$

With this approach, one calculated the ratio of shear stress to shear rate obtained from measurements of forces and velocity gradients without discriminating between Newtonian and non-Newtonian behaviors. However, it is more appropriate to refer to Eq. (1.3) as a non-Newtonian apparent viscosity when the viscosity depends also on shear rate (or stress).

Equation (1.3) is a rheological model and it is implemented into macroscopic models as a constitutive equation in order to predict the transport behavior of complex fluids. However, there is an important distinction between rheological models and constitutive equations (or material equations) that is often overlooked. Theoretical models, extending the seminal work of (Einstein, 1906, 1911) (i.e. $f(\psi) = 1 + 2.5\psi$), are rheological models and not constitutive equations. A rheological model provides information about the (shear) viscosity of a material under steady or quasi-steady conditions within a certain flow geometry. In contrast, one could simply define a constitutive equation (e.g., Eq. (1.2)) as the relationship between field variables, here shear stress and shear rate tensors, that is valid for any flow configuration and even under transient conditions. The applicability of rheological models is therefore more restrictive than constitutive equations which are the ultimate goal of rheological measurements.

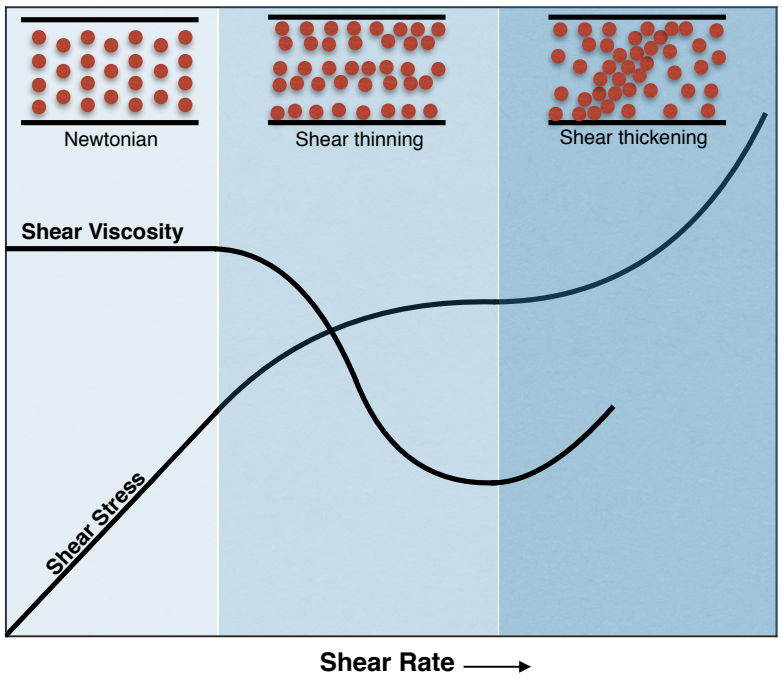

Figure 1.2: Typical rheological behavior of suspensions of solid spherical particles under dynamic equilibrium conditions.

Expressions for the effective shear viscosity of a suspension under a given flow geometry are generally derived under steady conditions (avoiding thixotropy when possible) and provide no constraint on the shear stress-shear rate relationships beyond the simple shear flow conditions tested in the laboratory or imposed in the theoretical model. For a rheological model to be used as a constitutive equation in flow calculations, one needs to show that

1. the rheological model for suspension provides suitable information for the shear stress-shear rate relationship under any possible flow configuration and also during flow transients,

2. the equation provided for the suspension viscosity preserves material objectivity,

3. once inserted into governing equations (e.g. Navier-Stokes or Stokes equations), the system of equation is Hadamard stable,

4. no flow solution using that rheological law violates the second law of thermodynamics,

5. and finally that the rheological law portrays material symmetry.

Material objectivity refers to a property that guarantees the rheological model is independent of the choice of reference frame, i.e. it is invariant under Galilean changes of reference frame. The definition of a Newtonian fluid preserves material objectivity because the shear stress-shear rate relationship is constructed from tensors that are individually material objective. The velocity gradient tensor is not material objective but the shear rate is (its symmetric counterpart), and so is the divergence of the velocity gradient. For the case of solid particles embedded in a Newtonian fluid, we expect, although it is not demonstrated, that a material objective representation of the rheology is preserved as long as the law is itself build on objective tensors such as shear rate or scalars variables like the particle volume fraction.

A constitutive equation is also required to lead to macroscopic flows that are consistent with positive entropy production. Any realistic macroscopic flow should satisfy the Clausius-Duhem inequality, i.e. that entropy can only increase with time with viscous flows. A famous example of violation of the second law of thermodynamics occurs when flows violate Hadamard stability for instance. In overly simplified terms, Hadamard instability arises with flow instabilities (e.g. Kelvin-Helmholtz) such that the growth of perturbations becomes infinitely fast for large wave numbers (power spectra diverges at small wavelength). In reality, viscous dissipation or capillary forces (in multiphase flows) prevent this issue.

The last item in the list above, material symmetry, is perhaps the most problematic for suspensions. Material equations should be constructed so as to display the same symmetry as the material they model. For instance a cubic lattice requires elastic constitutive equations that have a cubic symmetry. For homogeneous Newtonian fluids, the symmetry is basically unimodular (high symmetry), because molecules can be displaced randomly without changing the behavior of the fluid. This is the reason why material symmetry is not an issue for Newtonian single phase fluids. For complex fluids, microstructure plays an important role on rheology (Stickel & Powell, 2005). Deformation in complex fluids can affect the microstructure (distribution of particles and their orientation) which partially breaks this symmetry. A proper constitutive equation should reflect the development or destruction of symmetries in microstructure. We argue that a better understanding of microstructure

changes under different shear rate conditions, the development and lifetime of planar sheets of particles sliding over each other and their destruction at higher shear rates (dilation and possible shear thickening) for example, is the missing link to extend the various rheological models to real constitutive equations for complex fluids flows.

An analysis of Eq. (1.3) reveals that it does not contain any information about the shear history, the formation and deformation of microstructural arrangement of particles, particle shape and size distributions, particle orientation, and particle deformation. These various parameters have limited impact on dilute suspensions, but become critical when one considers concentrated suspensions where the particle volume fraction approaches the threshold packing limit. Therefore, further information about the flow (shear) conditions and the mechanics of microstructures are required to retrieve and analyze the complex response of complex fluids to deformation. As a first step, Eq. (1.3) can be modified to

$$\mu_r = \frac{\mu_\psi}{\mu_m} = f(\psi, St, Re, Pe). \tag{1.4}$$

where μ_r is the relative viscosity of the suspension, and St, Re and Pe represent the Stokes, Reynolds and Péclet numbers, respectively, which convey information about the relative density between the suspending fluid and solid particles, particle size, shear flow conditions and the importance of thermal energy on the motion of particles in the suspension. The Stokes number quantifies the coupling between the motion of particles and the fluid. When particles are small or the relative density is small, the coupling between the particles and fluid will be strong and the resulting Stokes number will be small (i.e. advection-dominated flow). At low Reynolds number, inertial stresses can be neglected and the stress balance is governed by viscous and applied stresses. Finally, suspensions characterized by a large Péclet number are such that they are not affected by Brownian motion (exchange of kinetic energy at the molecular level). Another dimensionless number, the Schmidt number, is sometimes considered for suspensions. It is defined as the ratio of the Péclet to Reynolds numbers and is used to categorize whether the suspension is within Newtonian or non-Newtonian phase regime (Stickel & Powell, 2005). For Schmidt number $\geq 10^6$ both inertia and Brownian forces can be neglected from the analyses, and, if particles are neutrally

buoyant ($St \to 0$), Eq. (1.4) reduces to Eq. (1.3).

Laboratory experiments on concentrated suspensions show a strong dependence of the effective viscosity on the applied shear rate; suspensions often display shear thinning at low to moderate shear rates and a transition to shear thickening at high shear rates (Mari *et al.* , 2014; Brown & Jaeger, 2014). It is shown that these complex transitions (illustrated in Fig. 1.2) occur because of microstructure ordering (leading to shear thinning) and dilation due to friction and inertial forces (leading to shear thickening) (Hoffman, 1972; Brown & Jaeger, 2014; Mari *et al.* , 2014; Cwalina & Wagner, 2014).

However, as reported by many observations, the viscosity curve for suspensions may show two plateaus at very low and high shear rates. In other terms, suspensions behave like Newtonian fluids at very low and high shear rates and like shear thinning fluids in between (a S-shaped viscosity curve). These observations motivate us to modify Eq. (1.4) and account for non-Newtonian behaviors (shear thinning) due to microstructural rearrangement. The effective viscosity of suspensions under different shear conditions can be then characterized using two extreme cases, at very low and high shear rates (or shear stresses), as well as a shear rate-dependent fitting parameter (like Cross-fluids (Cross, 1965) and Carreau-Yasuda-fluids (Owens & Phillips, 2002; Hayat *et al.* , 2014)) or shear stress-dependent fitting parameter (like Ellis-fluids (Steller, 2001) and Meter-fluids (Hackley & Ferraris, 2001)). One example of such models for shear thinning fluids is

$$\frac{\mu_\psi - \mu_{\psi_\infty}}{\mu_{\psi_0} - \mu_{\psi_\infty}} = (1 + (g\Upsilon)^a)^{(n-1)/a}, \tag{1.5}$$

where μ_{ψ_0} and μ_{ψ_∞} denote the effective viscosity of the suspensions at very low and high shear rates, respectively, that are calculated from a model like Eq. (1.3). In Eq. (1.5), parameters a, n and g are fitting constants that vary with fluids (Krieger, 1972; Hackley & Ferraris, 2001). As mentioned, suspensions may also show a dilatant behavior under very high shear rates, and the application of models like Eq. (1.5) becomes problematic, and needs further corrections and fitting parameters (Cross, 1965; Hackley & Ferraris, 2001).

As an alternative and more general approach, one can introduce two additional dimensionless number, $\psi_t(r_p, \Upsilon)$ and $[\eta(r_p, \Upsilon)]$, into Eq. (1.4) to account for the effect of

microstructural properties and rearrangement on the macro-scale suspension flow,

$$\mu_r = \frac{\mu_\psi}{\mu_m} = f(\psi, \psi_t, [\eta], St, Re, Pe). \tag{1.6}$$

$\psi_t(r_p, \Upsilon)$ and $[\eta(r_p, \Upsilon)]$, defined as state variables, convey important information about the particle shapes (characterized here with r_p, the particle aspect ratio), orientation, aggregation and shear induced microstructure rearrangement. ψ_t represents a threshold volume fraction at which jamming condition occurs (often called the maximum random close packing fraction) and $[\eta]$ is the intrinsic viscosity providing information about a characteristic hydrodynamic function for a single particle (or an assembly of particles, for instance, in aggregated systems). One of the goal of this study is to interpret published experimental datasets on the rheology of suspensions based on Eq. (1.6) to restore self-similar behaviors, if possible. Before we can do so, it is important to provide a physical and theoretical context for the rheology of suspensions across a wide range of particle volume fractions. This is used as the basis to constrain the microstructural effects on the viscosity of suspensions through the state variables $\psi_t(r_p, \Upsilon)$ and $[\eta(r_p, \Upsilon)]$.

The approach in this thesis is to incorporate some of the microstructural effects and shear history in a rheological model, e.g. Eq. (1.6), and provide a predictive constitutive-like rheology model. We advocate that applying rheological models (Eqs. (1.3)-(1.6)) directly into governing equations requires some care. The main conditions under which effective viscosity laws can be inserted into flow models are listed below,

1. The particles are well-mixed such that at the macroscopic level the complex fluid can be treated as homogeneous.

2. The flow geometry is simple and shear flow conditions prevail everywhere.

3. Steady state conditions apply. Viscosity needs to be defined when the change in microstructure is dynamically under equilibrium, i.e. microstructure formation and destruction occur at the same rate.

1.1 Scope of work

The thesis focuses on hydrodynamic interactions within complex fluids. This investigation covers different regimes, from dilute to concentrated complex fluids. This thesis is undertaken to fulfill the following goals:

1. To present a derivation of the macroscopic rheology for both dilute and concentrated monomodal suspensions/emulsions under simple steady shearing flow conditions. The resulting model for the macroscopic rheology of emulsions is applicable for a wide range of viscosity ratio, capillary number and bubble (or droplet) volume fraction. In the context of an emulsion of droplets or bubbles, the theoretical model allows us to construct a regime diagram which constrain the rheological behavior of emulsions sheared under different regimes of viscous/capillary stresses. These regimes are delimited by two critical dimensionless numbers; a critical viscosity ratio and a critical capillary number.

2. To extend the rheology model to suspensions including bimodal (or polymodal) size distribution of particles. As a result, a crowding-based model for the effective viscosity of suspensions of rigid bimodal-sized particles is introduced. In this model, the mutual crowding factor is defined to account for the change in the amount of fluid trapped in the interstices formed by particles when two class of particles with different sizes are mixed with each other. In addition, a new semi-theoretical model for random close packing of bimodal mixture of particles is provided.

3. To find a self-similar behavior and characterize the effect of microstructures on the rheological behavior of suspensions. We first extend our model to suspension of rigid, randomly oriented and bi-axially symmetric ellipsoids, and build a framework that forms the basis for a predictive model that includes microstructural evolution and rearrangement into the description of the effective viscosity of suspensions.

4. To investigates the rheology of crystal-bearing magmatic suspensions. Here, the striking resemblance and differences between magma and synthetic industrial suspensions

are discussed, and some of the most important microstructural-level phenomena causing crystal-bearing magmas to display shear thinning are explored. Based on the proposed self-similar behavior, a new approach to interpret experimental data on magmatic suspensions is outlined.

5. To propose a new model for particle settling or bubble rising in a confined medium where the new rheology model plays a key role in on phase separation. In this part, we also extend the work to propose a general hindrance model and compute the rate of settling of poly-disperse spheroids solid particles through a suspension. The hindrance model is then used to correct soil size distribution data obtained with the hydrometer test.

CHAPTER II

LITERATURE REVIEW

2.1 Rheology of dilute suspensions

Sutherland (1905) and Einstein (1906, 1911) were the first to introduce the theoretical framework to describe the effective shear viscosity of suspensions. In dilute infinite suspensions, particles are distributed homogeneously at distances large enough to neglect particle-particle and hydrodynamics interactions. In these idealized suspensions, the rate of energy dissipation per unit volume increases linearly with volume of dispersed solid particles. In real and finite dilute suspensions, the rate of energy dissipation increases even more due to particle interferences. In the last century, since the calculation conducted independently by Sutherland (1905) and Einstein (1906) to obtain the viscosity of a very dilute suspension of non-deformable solid spheres, the macroscopic rheological behavior of complex fluids has received a remarkable attention. Solutions are mainly based on conceptual models that account for the change in hydrodynamic interactions based on the particle concentration and deformation. For theses multi-particle systems, the macroscopic quantities are defined based on volume averages (Batchelor, 1967; Landau & Lifshitz, 1987). To this end, a dilute complex fluid, e.g. suspension, can be treated as a homogeneous equivalent fluid with the same average density (Einstein, 1906, 1911; Taylor, 1932; Batchelor, 1967; Goddard & Miller, 1967; Frankel & Acrivos, 1970; Landau & Lifshitz, 1987). The equivalence assumption between the stress tensor in the suspension and the stress tensor for the homogeneous equivalent fluid implies the equality of the total rate of work performed on the boundary of the suspension. The equivalence of the volume averaged stress fields leads to the virial equation for the effective viscosity of dilute suspensions derived by Einstein (1906)

$$\mu_r(\psi) = \frac{\mu_\psi}{\mu_m} = 1 + [\eta]\psi. \tag{2.1}$$

where $[\eta]$ is the intrinsic viscosity. The value of $[\eta]$ depends on many factors such as the

shape and orientation of particles, the boundary condition applied on the interface between phases and particle deformation (e.g., fluid particles with finite shear viscosity, Hookian elastic or viscoplastic behavior). The distance between particles is also important for the intrinsic viscosity, because particle aggregation and clustering can affect $[\eta]$ greatly. For a rigid spherical particle in a dilute suspension with negligible particle interactions, Einstein (1906, 1911) calculated $[\eta] = 2.5$ (his first calculation did not lead to the exact value of 2.5, and it was corrected after experiments). It is noteworthy that $[\eta] > 2.5$ for dilute suspensions of non-spherical solid particles. Moreover, due to the particles' orientation and alignment with the principal flow direction, $[\eta]$ shows a shear rate (or stress) dependence. In these cases, $[\eta]$ should be defined as a tensor instead of a scalar quantity especially where the shear rate is small (Wildemuth & Williams, 1984).

Einstein-Sutherland theory was first extended to very dilute emulsions by Taylor (1932) where he assumed that fluid particles remain spherical, i.e. the dimensionless capillary number, Ca, (the ratio of viscous force to the force associated with the interface tension) is assumed $Ca \ll 1$. These models predict an increase in the macroscopic effective viscosity of the system that is linearly proportional to the particle concentration, with a greater effect for solid spheres. Other investigations by Mackenzie (1950), Ducamp & Raj (1989) and Bagdassarov & Dingwell (1992) have constrained expressions for the rheology of dilute emulsions including highly deformed bubbles ($Ca \gg 1$). More generalized constitutive equations for the rheology of dilute systems were derived by Oldroyd (1959) for emulsions of two immiscible Newtonian fluids, by Goddard & Miller (1967) for suspensions including deformable Hookian solid sphere, and by Frankel & Acrivos (1970) for emulsions consisting of deformable droplets up to the first order of the particle deformation. These constitutive equations predict the effective viscosity of relatively dilute systems over a wide range of deformation rates (capillary number) and viscosity ratios.

Because particle hydrodynamic interactions are neglected, Eq. (2.1) for dilute suspensions of solid particles (and other dilute models for emulsions) predicts the effective viscosity only as $\psi \to 0$ (Mewis & Wagner, 2012; Stickel & Powell, 2005; Chang & Powell, 1994), and violates the lower bound for the effective viscosity at any particle volume fraction as

described by Kachanov & Abedian (2015). The bounds for the effective shear modulus of a heterogenous material including two isotropic phases possessing $k_0,\ \mu_0$ and $k_1,\ \mu_1$ as the bulk and shear moduli, repectively, are (Abedian & Kachanov, 2010; Sevostianov & Kachanov, 2012)

$$\mu_0 + \frac{\psi}{\frac{1}{\mu_1-\mu_0} + \frac{6(1-\psi)(k_0+2\mu_0)}{5\mu_0(3k_0+4\mu_0)}} \leq \mu_\psi \leq \mu_1 + \frac{1-\psi}{\frac{1}{\mu_0-\mu_1} + \frac{6\psi(k_1+2\mu_1)}{5\mu_1(3k_1+4\mu_1)}}. \tag{2.2}$$

For the case of non-deformable (rigid) solid particles ($k_1 \to \infty, \mu_1 \to \infty$) suspended into an incompressible fluid ($k_0 \to \infty$), Eq. (2.2) can be simplified to

$$1 + 2.5\frac{\psi}{1-\psi} \leq \mu_r < \infty. \tag{2.3}$$

The upper bound is trivial and will be discussed in more detail later. The lower bound is identical to the effective viscosity model

$$\mu_r(\psi) = \frac{\mu_\psi}{\mu_m} = 1 + [\eta(r_p, \Upsilon)]\psi_c, \qquad \psi_c = \frac{\psi}{1-\psi}, \tag{2.4}$$

derived by Saitô (1950) by taking into account the hydrodynamic interactions between uncorrelated solid spheres. The viscosity model expressed in Eq. (2.4) accounts for the excluded volume of ambient fluid replaced by particles that is overlooked in Eq. (2.1), i.e. ψ is replaced by ψ_c. In other words, in Eq. (2.1) the suspending fluid is considered unbounded which results in particles being represented as mass points (Mendoza, 2011). The effective viscosity of Eq. (2.4) applies to finite volume suspensions, and does not violates the lower bound of Eq. (2.3).

When the particle volume fraction increases beyond a few percents, Eqs. (2.1) and (2.4) are no longer valid, but extensive experimental data on sphere suspensions and emulsions show their accuracy up to particle volume fraction approaching even 10%. Thus practically, the dilute regime for complex fluids hosting spherical particles is assumed to range from $0 \leq \psi \leq 0.1$.

2.2 Rheology of semi-dilute suspensions

As more particles are fed to a complex fluids, e.g. suspension, the effective distances between particles decreases. The assumption of limited or negligible particle hydrodynamic

interactions can no longer be applied to obtain the effective shear viscosity. The reduction in the mean distance between particles leads to a higher rate of energy dissipation due to viscous forces between particles. The seminal work of Einstein (1906, 1911) for solid sphere suspensions has been extended to a quadratic form of

$$\mu_r(\psi) = 1 + 2.5\psi + A\psi^2, \tag{2.5}$$

in order to include particle hydrodynamic interactions to the first order of approximation, and provide a better prediction of experimental and numerical data obtained for semi-dilute (or intermediate) suspensions where $0 \leq \psi \leq 0.2$. The first extension was performed by Thomas (1965) who empirically proposed $A = 10.06$ for suspensions of solid spheres. Batchelor & Green (1972) using a statistical study to account for the hydrodynamic interactions in a shear flow found that $A = 5.2 \pm 0.3$ provides a good approximation (Pasquino *et al.* , 2008; Hwang & Hulsen, 2006). Choi & Schowalter (1975) used a cell model approach, and proposed $A = 15.62$. Using different approaches, Cichocki & Felderhof (1991); Thomas & Muthukumar (1991); Wagner & Woutersen (1994); Verberg *et al.* (1997) and Pasquino *et al.* (2008) proposed $A = 5.0$, 4.83, 5.0, 6.03, and 7 ± 0.18, respectively. More recently, Housiadas & Tanner (2014) and Housiadas (2015) developed an analytical model for the effective shear and elongational viscosity by solving the fluid flow around a single spherical particle, and characterized a relationship between a resistance parameter and the volume fraction of particles. Their model suggests $A = 4.05$ and $A = 4.50$ for the effective shear and elongational viscosity of semi-dilute suspensions of spherical particles, respectively.

It should be noted that the intrinsic viscosity, the coefficient of the linear term in Eq. (2.5), remains constant in all discussed models even when considering different applied flow conditions (shear and elongational). The reason is that the intrinsic viscosity is determined under the assumption that particle do not interact. Whereas, the coefficient of the quadratic term accounts for hydrodynamic interactions, and varies under different imposed flow conditions. The disagreement between the coefficient of the quadratic term in these models for a semi-dilute regime illustrates the degree of complexity of the physics that govern the deformation of complex fluids.

2.3 Rheology of concentrated suspensions

To retrieve a correct effective viscosity for concentrated complex fluids where $\psi > 0.2$, one needs to account for hydrodynamic and physical interactions, like interparticle forces and friction at contacts, lubrication and viscous forces in the film between particles, deformation, break up and coalescence when considering emulsions, and microstructure effects due to different flow conditions. Different upscaling methods have been proposed to approximate particle interactions in concentrated systems. These studies initiated a large body of work devoted to find a model for the rheology of concentrated suspensions (see Table 2.1 and emulsions (see Table 2.2). The strategy behind these models differs even though they are designed to describe the same phenomena, highlighting the complexity of processes. A common feature, for a complex fluid with non-deformable particles, is that the effective viscosity should satisfy the following asymptotic behavior,

$$\lim_{\psi \to \psi_t} \frac{\mu_\psi}{\mu_m} \simeq \infty, \tag{2.6}$$

which is equivalent to the trivial upper bound of the effective viscosity, see Eq. (2.3). In Eq. (2.6), ψ_t is a threshold volume fraction at which a transition between fluid and solid states occurs.

2.3.1 Threshold packing, ψ_t

The threshold packing volume fraction depends strongly on the protocol followed to produce the packing. This explains the range of values reported in the literature, even for monomodal spherical particles. The mechanical stability condition for monomodal sphere packing starts from the very loose random packing ($\psi_{RL} = 0.56$ that represents the least dense packing that can support an external load) to the face-centered-cubic or hexagonal structure ($\psi_{FC} = 0.7405$) which is the most efficient way to pack equal-sized spheres. For random packing, in practice, a value between these two extremes has been reported, $\psi_{RL} \leq \psi_t \leq \psi_{FC}$.

For random close packing (or amorphous maximally random jammed packing (Donev *et al.* , 2004)) of monomodal spheres, known as a threshold transition between fluid and solid states, Scott & Kilgour (1969) found a maximum of $\psi_t = 0.637$ and a minimum of

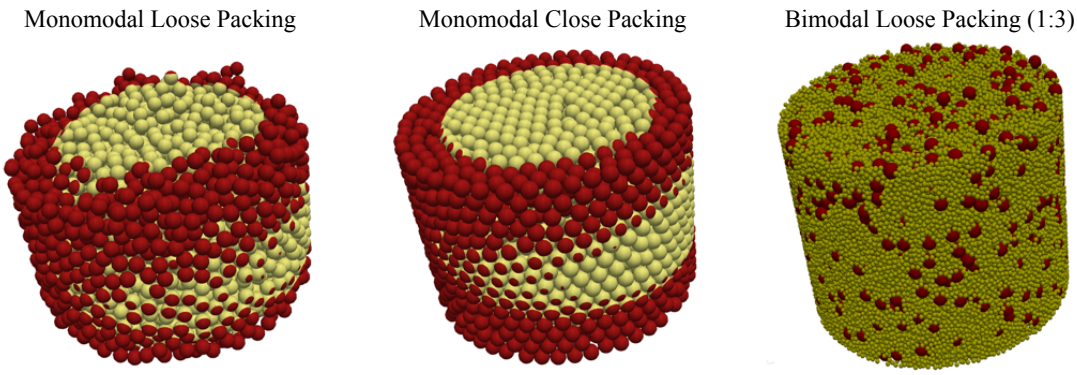

Figure 2.1: Monomodal and bimodal random packing of spherical particles. Left: random loose packing constructed by gravitational settling leading to $\psi_t \approx 0.58$. Middle: random close packing constructed by gravitational settling and continued by overlap minimization and vibrations that leads to $\psi_t \approx 0.62$. Right: bimodal random loose packing of spherical particles with size ratio $\zeta = 3$ and 60% of small particles leading $\psi_{t_b} \approx 0.605$. Colors here do not point to specific information, and are used only for better visualization. The detailed information about gravitational settling, overlap minimization and vibration methods to produce random loose and close packing of spheres can be found in Roozbahani *et al.* (2013) and He *et al.* (1999), respectively.

$\psi_t = 0.605$ experimentally. The minimum is consistent with the result provided by Chong *et al.* (1971) where the viscosity of dense suspensions diverges. Song *et al.* (2008) argued that random packing of hard spheres in three dimensions cannot exceed a density limit of $\psi_t = 0.634$. More recently, Boyer *et al.* (2011) constrained the threshold packing (maximum random close packing) at $\psi_t = 0.585 \pm 0.002$.

The threshold packing is affected by the particle size distribution (polydispersity) as small particles can fill the void space between large particles (see Fig. 2.1). In addition, as asphericity is introduced, locally jammed particles can rotate and the threshold packing varies significantly. Donev *et al.* (2004) showed that for monomodal assemblages of oblate and prolate spheroids (with small aspect ratios) the threshold packing fraction increases from $\psi_t \approx 0.71$ up to 0.735. On the other hand, by introducing the particles slenderness and angularity, the threshold packing fraction decreases because of interlocking. Furthermore, in sheared suspensions, orientation and deformation of particle clusters and changes in microstructures affect the threshold packing limit (Krieger & Dougherty, 1959; Wildemuth & Williams, 1984). See, for example, the change in the state of particle packing in Figs.

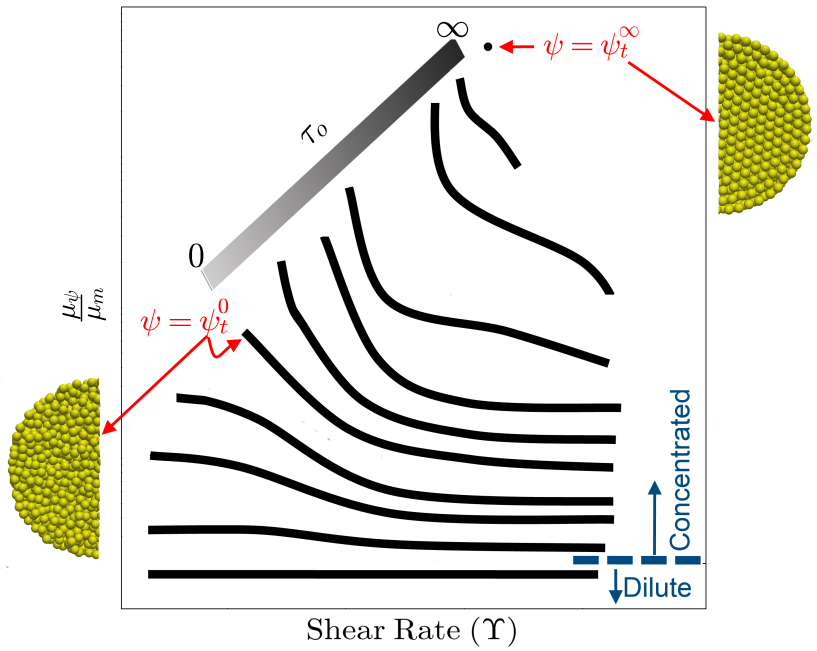

Figure 2.2: Conceptual representation of shear thinning in concentrated suspensions of spherical solid particles. The shaded area highlights the region where the yield stress appears. It starts from the threshold packing fraction for very loose random packing, ψ_t^0, and diverges at the threshold packing fraction for face-centered packing, ψ_t^∞. Sensitivity of the effective viscosity to the shear rate increases with the volume fraction of dispersed particles. At dilute to semi-dilute concentrations ($\psi < \psi_t^0$) Newtonian plateaus exist at both high and low shear rates. For higher concentrations ($\psi \geq \psi_t^0$) the viscosity diverges in the low shear rate limit which corresponds to the presence of the apparent yield stress.

(2.1) and (2.2) for typical low and high applied shear rates. These phenomena also impact the intrinsic viscosity $[\eta]$, as will be discussed later. Thus, the threshold packing depends on the particle shape and size distribution, particle deformation as well as the imposed shear rate (or shear stress).

2.3.2 Effective viscosity models

It is well documented that both dilute and concentrated suspensions of monomodal solid spheres under very low shear rates behave like Newtonian fluids (Snabre & Mills, 1999). Concentrated suspensions subjected to higher shear rates or shear stresses exhibit a non-Newtonian (shear thinning and thickening) as well as hysteretical behavior (Chong *et al.* , 1971). These observations are depicted schematically in Fig. 2.2, where one can see, for example, the effect of shear rate on the relative viscosity of shear thinning suspensions

(or emulsions). Particles adopt a denser packing configuration as they are sheared more vigorously. The shaded area in Fig. 2.2 highlights the region where a yield stress τ_0 appears. The yield stress develops when the concentration of particles ranges between the density of a very loose random packing, $\psi = \psi_t^0$, and the face-centered-cubic volume fraction, $\psi = \psi_t^\infty$.

As an illustration of the variability in effective viscosity, different experimental data for relative viscosity of dilute and dense suspensions of rigid spherical particles are compared in Fig. 2.3. These data are measured under different conditions, such as different apparatus, shear stress or shear rate, and different particle sizes (Maron & Levy-Pascal, 1955; Maron & Shiu Ming, 1955; Rodriguez *et al.* , 1992; Mueller *et al.* , 2010; Boyer *et al.* , 2011). One observes that, at low concentration $\psi < 0.2$, all datasets collapse on each other. However, in intermediate and concentrated regimes, a scatter is observed, which indicates that these different experiments cannot be captured by a single effective viscosity-volume fraction curve.

The differential effective medium (DEM) theory (Norris *et al.* , 1985) approach is widely used to approximate the effective viscosity of concentrated complex fluids. The DEM theory does not explicitly solve for the interaction between particles, but offers a good parameterization for the steady state effective viscosity of suspensions and emulsions (Mooney, 1951; Brinkman, 1952; Roscoe, 1952; Krieger & Dougherty, 1959; Mendoza, 2011). For concentrated systems, Pal (2003b, 2004) employed the Differential Effective Medium (DEM) theory to determine phenomenologically the relative viscosity for elastic solid particle suspension ($\lambda \to \infty$) and bubbly emulsion ($\lambda \to 0$). Pal (2003c) developed a more general model for concentrated emulsions with different viscosity ratio and deformable particle using the analogy between shear modulus and shear viscosity. In all these studies, different interpretations are used to define the change in the volume available for adding particles (termed "free volume" by Robinson (1949)), which leads to different models.

The model proposed by Eilers (1943) (see Table 2.1) performs well to evaluate the relative viscosity of suspensions with spherical particles at high shear rates. In essence, this equation accounts for the effective volume of particles through the maximum packing fraction ψ_t, but does not consider that suspensions occupy a finite volume. As a consequence,

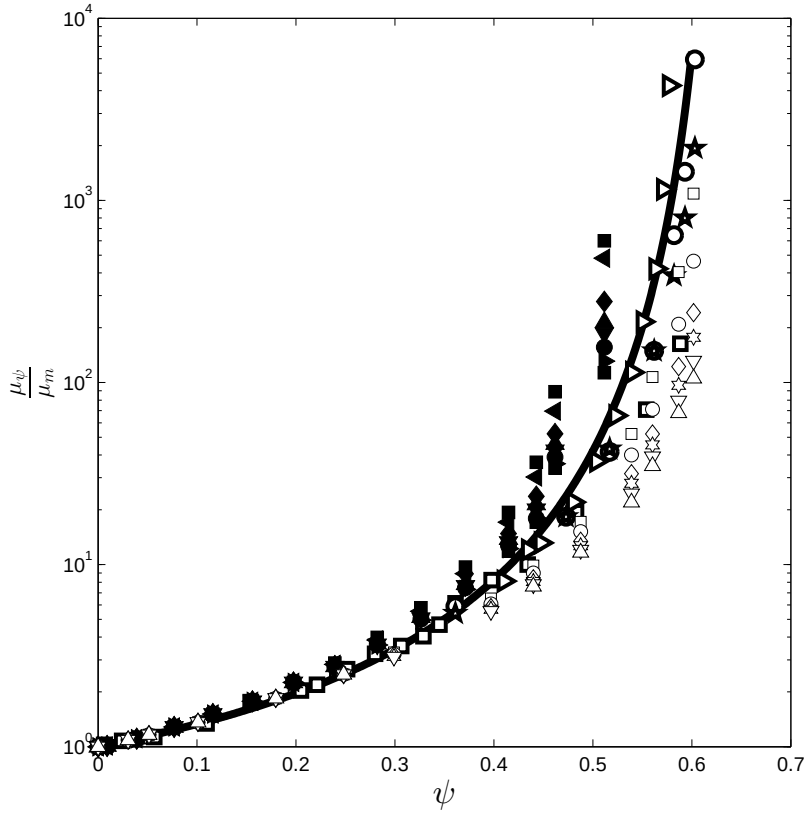

Figure 2.3: Relative viscosity of suspension of rigid solid particles as a function of particle volume fraction. Filled markers from Maron & Levy-Pascal (1955), open markers from Maron & Shiu Ming (1955), bold squares from Mueller *et al.* (2010), bold circles and stars from Rodriguez *et al.* (1992), and bold triangles from Boyer *et al.* (2011). The bold line show the prediction of a sample rheology model (Eq. (3.49) using $\psi_t = 0.633$), see next chapter.

it slightly underestimates the relative viscosity of concentrated suspensions over a wide range of shear rates. Mooney (1951) noticed that in concentrated suspensions some of the fluid phase is trapped between particles and is immobile. From this observation, he defined the concept of crowding which describes the interaction among particles and the trapped dead fluid. He derived his well-known rheological expression, using a bimodal suspension of spherical particles, arguing that the sequence of particle addition with which particles of different sizes should not affect the final viscosity of the suspension.

The equation of Roscoe (1952) (see Table 2.1), commonly referred to as the Einstein-Roscoe equation is also derived for an unbounded suspension where adding particles does

not require removing a commensurable amount of host fluid. Maron & Pierce (1956) introduced the concept of varying particle threshold packing limit as a function of shear rates. In addition, the model of Maron & Pierce (1956) does not retrieve Einstein's coefficient (intrinsic viscosity) in the limit $\psi \to 0$, but yields a value of 3 for the intrinsic viscosity. Krieger & Dougherty (1959) addressed this issue when they represented the exponent by the product of the intrinsic viscosity $[\eta]$ and the maximum packing fraction ψ_t,

$$\frac{\mu_\psi}{\mu_m} = (1 - \frac{\psi}{\psi_t})^{-[\eta]\psi_t} \tag{2.7}$$

In practice, the majority of authors use the model of Krieger & Dougherty (1959) assuming $[\eta]$ and ψ_t are fitting parameters, and neglecting the underlying physics that governs the exponent.

Brouwers (2010) arrived to his rheology model using a different upscaling approach. Brouwers (2010) studied the viscosity of bimodal suspensions of spherical particles with size ratio close to unity to yield an exact analytical closed-form solution for the effective viscosity of monomodal suspensions.

We schematically summarize the contribution and applicability of several studies (non-exhaustive) for the rheology of suspensions and emulsions as function of the particle volume fraction, ψ, viscosity ratio, λ, and capillary number, Ca in Fig. 2.4. For example, the model proposed by Lim *et al.* (2004) is suitable for emulsions with $\psi < 0.2$, $\lambda \to 0$ and $Ca \ll 1$, while models of Pal (2003a, 2004) cover the entire range of ψ and capillary number within the limit of $\lambda \to 0$. This diagram serves to clearly identify regions of the volume fraction, viscosity ratio, capillary number parameter space that need to be further explored. It also points to the lack of unified model valid over the entire space. A more complete list of published equations developed for solid particle suspensions and emulsions along with the range over which they are deemed applicable is reported in Tables 2.1 and 2.2, respectively.

Theoretical models have been tested and complemented with several numerical and experimental studies. For instance, experimental studies have provided a great insight into the role of particles on the suspension rheology (e.g. Rutgers (1962); Rodriguez *et al.* (1992); Boyer *et al.* (2011)) and bubbly emulsion rheology (e.g. Stein & Spera (2002); Manga &

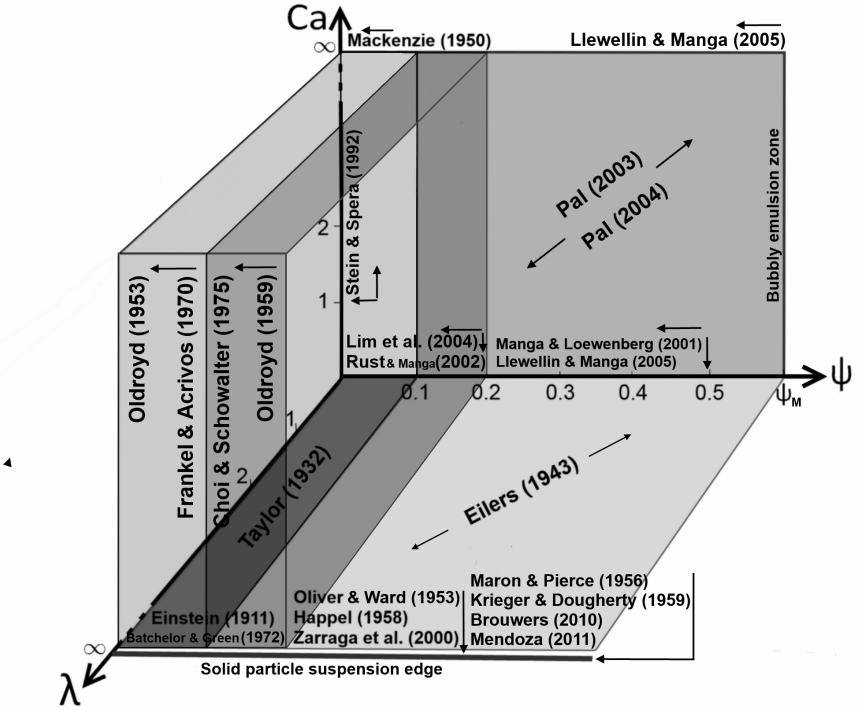

Figure 2.4: Summary of some of published rheological models and their range of applicability with respect to particle volume fraction, ψ, viscosity ratio, λ, and capillary number, Ca. See tables 2.1 and 2.2 for more details about published models.

Loewenberg (2001); Rust & Manga (2002)). Additionally, the role of the viscosity ratio and capillary number on the viscoelastic properties and rheology of dilute and concentrated emulsions has been studied extensively by Pal & Rhodes (1989); Pal (1992, 1996, 2001, 2003c). These studies provided many experimental data on the relative viscosity of emulsions which will be used in this thesis to validate the accuracy of our new theoretical model for predicting the shear viscosity in multiparticle systems.

Numerical simulations have also been widely used in the course of the past two decades to gain more insight into and better constrain the rheological behavior of concentrated complex fluids. For this reason, several particle-based simulation techniques in two and three dimensional have been developed. Stokesian Dynamics where the linearized fluid flow equations (Stokes flow) for all particles in a meshless environment are solved at once has been intensively applied to study both Brownian and non-Brownian suspensions of solid particles (Bossis & Brady, 1984; Brady & Bossis, 1988; Sierou & Brady, 2002; Singh & Nott, 2000). Other numerical particle-based techniques that operate well in the creeping flow conditions are Dissipative Particle Dynamics (Hoogerbrugge & Koelman, 1992; Boek *et al.* , 1997; van der Kooij *et al.* , 2001; Martys, 2005; Pivkin & Karniadakis, 2005), Lagrange Multiplier Fictitious Domain (Glowinski *et al.* , 1999), Double Layer Boundary Element (Nasseri *et al.* , 2000), and Representative Elementary Volume methods (Bertevas *et al.* , 2010). These methods, in addition to Molecular Dynamics (Doi, 1980; Jabbarzadeh & Tanner, 2006), were successful to study the effect of microstructures on the rheology of particle-laden fluid flow at low Reynolds numbers.

Several numerical studies have explored the rheological behavior of complex fluids, when inertial forces matter ($Re > 1$) (Patankar & Hu, 2002; Shakib-Manesh *et al.* , 2002; Mikulencak & Morris, 2004; Li & Sarkar, 2005; Srivastava, 2013) where the general conclusion is that suspensions are shear thickening, and this tendency increases with Reynolds number. The development of Lattice Boltzmann methods for suspension rheology were first conducted by Ladd (1994); Ladd & Verberg (2001). The Lattice Boltzmann method has then been combined with several other methods, e.g., Immersed Boundary (Niu *et al.* , 2006; Yuan *et al.* , 2014; Favier *et al.* , 2014), Smoothed Profile (Nakayama & Yamamoto, 2005;

Javaran *et al.* , 2014) and Discrete Element methods Feng *et al.* (2010); Leonardi *et al.* (2014); Zhang *et al.* (2014); Brumby *et al.* (2015) to include a better representation for lubrication forces and hard-sphere collisions and increase the overall method's robustness for suspensions modeling.

One of the essential problems in developing an accurate numerical simulation for modeling a variety of concentrated complex fluids, is related to solid-solid and solid-fluid interactions near to and at particle surfaces. The aforementioned numerical approaches are promising and provide results in agreement with experiments up to 40-50% particle volume fractions (for sphere suspensions, and the range is smaller for non-spherical particles). At higher volume fractions because of the difficulty to model the near contact hydrodynamics, particle-particle interactions and other geometrical effects, these methods are less successful (Mewis & Wagner, 2009a; Dai *et al.* , 2013) and need further corrections (see for example Seta *et al.* (2014); Lee *et al.* (2015); Zhang *et al.* (2015b).

Despite the large amount of studies devoted to the rheology of complex fluids and the effect of microstructures, e.g. see Fig. 2.4, a complete microscopic/macroscopic description including all potential processes to model the flow of complex fluids under different shear conditions has not been provided yet. One of the main reasons for this shortcoming is that the generalization of processes that take place at different scales (micro to macro-scale) is difficult.

Table 2.1: Selected published models to predict the relative viscosity of suspensions of rigid solid particles and the range of volume fraction over which they intend to be applied.

Reference	Equation	Specific Parameter	Concentration
Einstein (1906) and Sutherland (1905)	$\frac{\mu_\psi}{\mu_m} = 1 + K\psi$	$K = 2.5$	$\lim_{\psi\to 0}$
Hatschek (1913)	$\frac{\mu_\psi}{\mu_m} = 1 + K\psi$	$K = 4.5$	Up to 40%
Eilers (1943)	$\frac{\mu_\psi}{\mu_m} = (1 + \frac{K\psi}{2(1-\frac{\psi}{\psi_t})})^2$	$K = 2.5$	All range
Vand (1948)	$\frac{\mu_\psi}{\mu_m} = exp(\frac{2.5\psi+2.7\psi^2}{1-K\psi})$	$K = 0.609$	Up to 60%
Mooney (1951)	$\frac{\mu_\psi}{\mu_m} = exp(\frac{2.5\psi}{1-K\psi})$	$1.35 < K < 1.91$	Up to 50%
Simha (1952)	$\frac{\mu_\psi}{\mu_m} = 1 + 2.5\psi(1 + \frac{25\psi}{4f^3})$	$1 < f < 2$	Up to 10%
	$= 1 + \frac{54}{5f^3}\frac{\psi^2}{(1-\frac{\psi}{\psi_t})^3}$	$1 < f < 2$	$\lim_{\psi\to\psi_t}$
Oliver & Ward (1953)	$\frac{\mu_\psi}{\mu_m} = \frac{1}{1-K\psi}$	$2.34 \leq K \leq 2.77$	Up to 35%
Maron & Pierce (1956)	$\frac{\mu_\psi}{\mu_m} = (1 - \frac{\psi}{\psi_t})^{-2}$	—	All range
Happel (1958)	$\frac{\mu_\psi}{\mu_m} = exp(4.58\psi)$	—	Up to 30%
Krieger & Dougherty (1959)	$\frac{\mu_\psi}{\mu_m} = (1 - \frac{\psi}{\psi_t})^{-K\psi_t}$	$K = 2.5$	All range
Thomas (1965)	$\frac{\mu_\psi}{\mu_m} = 1 + 2.5\psi + 10.06\psi^2$	$A = 0.0027$	Up to 60%
	$+ Aexp(B\psi)$	$B = 16.6$	
Frankel & Acrivos (1967)	$\frac{\mu_\psi}{\mu_m} = C'(\frac{C^{1/3}}{1-C^{1/3}}),\quad C = \frac{\psi}{\psi_t}$	$C' = \frac{9}{8}$	$\lim_{\psi\to\psi_t}$
Roscoe (1952)	$\frac{\mu_\psi}{\mu_m} = (1 - K\psi)^{-2.5}$	$K = 1.35$	Up to 50%
Batchelor & Green (1972)	$\frac{\mu_\psi}{\mu_m} = 1 + 2.5\psi + 5.2\psi^2$	—	Up to 15%
Chong *et al.* (1971)	$\frac{\mu_\psi}{\mu_m} = (1 + K\frac{\frac{\psi}{\psi_t}}{(1-\frac{\psi}{\psi_t})})^2$	$K = 0.75$	All range
Barnea & Mizrahi (1973)	$\frac{\mu_\psi}{\mu_m} = exp(\frac{K_1\psi}{1-K_2\psi})$	$K_1 = \frac{5}{3}, K_2 = 1$	Up to 10%
Quemada (1977)	$\frac{\mu_\psi}{\mu_m} = (1 - \frac{1}{2}K_0\psi)^{-2}$	$2.54 \leq K \leq 3.71$	Up to 50%
Leighton & Acrivos (1986)	$\frac{\mu_\psi}{\mu_m} = (1 + \frac{K\psi}{1-\frac{\psi}{\psi_t}})^2$	$K = 1.5$	All range
Cichocki & Felderhof (1991)	$\frac{\mu_\psi}{\mu_m} = 1 + 2.5\psi + K\psi^2$	$K = 5.00$	Up to 15%
Verberg *et al.* (1997)	$\frac{\mu_\psi}{\mu_m} = 1 + 2.5\psi + K\psi^2$	$K = 6.03$	Up to 20%
Morris & Boulay (1999)	$\frac{\mu_\psi}{\mu_m} = 1 + 2.5\psi(1 - \frac{\psi}{\psi_t})^{-1}$	—	Up to 20%
	$+ 0.1(\frac{\psi}{\psi_t})^2(1 - \frac{\psi}{\psi_t})^{-2}$		
Zarraga *et al.* (2000)	$\frac{\mu_\psi}{\mu_m} = exp(K\psi)(1 - \frac{\psi}{\psi_t})^{-3}$	$K = -2.34$	Up to 30%
Cheng *et al.* (2002)	$\frac{\mu_\psi}{\mu_m} = \frac{1+1.5(1+K)\psi}{1-(1+K)\psi}$	$K = \psi + \psi^2 - 2.3\psi^3$	Up to 56%
Brouwers (2010)	$\frac{\mu_\psi}{\mu_m} = (\frac{1-\psi}{1-\frac{\psi}{\psi_t}})^{\frac{K\psi_t}{1-\psi_t}}$	$K = \frac{5}{2}$	All range
Mendoza (2011)	$\frac{\mu_\psi}{\mu_m} = (1 - \frac{\psi}{1-K\psi})^{-2.5}$	$K = \frac{1-\psi_t}{\psi_t}$	All range
This study	**Equation (3.49)**	—	**All range**

Table 2.2: Selected published models to predict the relative viscosity of emulsions of deformable fluid particles and the range of volume fraction, viscosity ratio, λ, and capillary number, Ca, over which they intend to be applied.

Reference	Equation	Specific Parameter	Concentration	Deformation	Viscosity ratio
Taylor (1932)	$\frac{\mu_\psi}{\mu_m} = 1 + K\psi$	$K = \frac{1+2.5\lambda}{1+\lambda}$	$\lim_{\psi\to 0}$	$Ca \ll 1$	All range
Eilers (1943)	$\frac{\mu_\psi}{\mu_m} = (1 + \frac{K\psi}{2(1-\frac{\psi}{\psi_t})})^2$	$K = \frac{1+2.5\lambda}{1+\lambda}$	All range	$Ca \ll 1$	All range
Mackenzie (1950)	$\frac{\mu_\psi}{\mu_m} = 1 - K\psi$	$K = \frac{5}{3}$	$\lim_{\psi\to 0}$	$Ca > 1$	$\lim_{\lambda\to 0}$
Oldroyd (1959)	$\frac{\mu_\psi}{\mu_m} = \frac{1+\frac{3}{5}\psi}{1-\frac{2}{5}\psi}\left[\frac{1+K_1K_2(\frac{6Ca}{5})^2}{1+K_1^2(\frac{6Ca}{5})^2}\right]$	$\begin{cases} K_1 = \frac{1+\frac{2}{3}\psi}{1-\frac{2}{5}\psi} \\ K_2 = \frac{1-\psi}{1+\frac{3}{5}\psi} \end{cases}$	Up to 20%	All range	$\lim_{\lambda\to 0}$
Frankel & Acrivos (1970)	$\frac{\mu_\psi}{\mu_m} = 1 + \psi\left[\frac{1-\frac{12}{5}Ca^2}{1+(\frac{6}{5}Ca)^2}\right]$	—	Up to 10%	All range	$\lim_{\lambda\to 0}$
Choi & Schowalter (1975)	$\frac{\mu_\psi}{\mu_m} = 1 + \psi(1+2.5\psi)\left[\frac{1-\frac{12}{5}Ca^2}{1+(\frac{6}{5}Ca)^2}\right]$	—	Up to 20%	All range	$\lim_{\lambda\to 0}$
Scherer (1979)	$\frac{\mu_\psi}{\mu_m} = \frac{3(1-\psi)}{2(1+2\psi)+(1+\psi-2\psi^2)^{0.5}}$	—	Up to 5%	$Ca > 1$	$\lim_{\lambda\to 0}$
Ducamp & Raj (1989)	$\frac{\mu_\psi}{\mu_m} = exp(-k\frac{\psi}{1-\psi})$	$2.5 \le K \le 4$	Up to 45%	$Ca > 1$	$\lim_{\lambda\to 0}$
Pal & Rhodes (1989)	$\frac{\mu_\psi}{\mu_m} = (1 + \frac{K\psi}{1-K\psi})^{2.5}$	$K = \frac{0.8415}{\psi_{\frac{\mu_\psi}{\mu_m}=100}}$	—	$Ca \ll 1$	$\lim_{\lambda\to 0}$
Bagdassarov & Dingwell (1992)	$\frac{\mu_\psi}{\mu_m} = (1 + K\psi)^{-1}$	$K = 22.4$	Up to 70%	$Ca > 1$	$\lim_{\lambda\to 0}$
Stein & Spera (1992)	$\frac{\mu_\psi}{\mu_m} = 1 + K\psi$	$K = 13.1$	Up to 5%	$1 < Ca < 100$	$\lim_{\lambda\to 0}$
Manga & Loewenberg (2001)	$\frac{\mu_\psi}{\mu_m} = \begin{cases} 1+\psi \\ 1-\frac{5\psi}{3+2\psi} \end{cases}$	—	Up to 40%	$\begin{matrix} Ca < 1 \\ Ca \ge 1 \end{matrix}$	$\lim_{\lambda\to 0}$
Rust & Manga (2002)	$\frac{\mu_\psi}{\mu_m} = A - (\frac{A-(1-\frac{\psi}{\psi_t})^{-K\psi_t}}{1+(0.72Ca)^{1.43}})$	$\begin{cases} A = 1 - 1.14\psi - 9.8\psi^2 \\ K = \frac{1+2.5\lambda}{1+\lambda} \end{cases}$	Up to 17%	$Ca \ll 1$	All range
Lim *et al.* (2004)	$\frac{\mu_\psi}{\mu_m} = \frac{1.22+\psi+(22.1+369\psi-202\psi^2)K}{1+(23.9+412\psi)K}$	$K = (\frac{16}{9}Ca)^2$	Up to 15%	$Ca < 0.25$	$\lim_{\lambda\to 0}$
Pal (2004)	$\frac{\mu_\psi}{\mu_m} = (1-\frac{\psi}{\psi_t})^{-\psi_t}(\frac{1+K_1K_2(\frac{6Ca}{5})^2}{1+K_1^2(\frac{6Ca}{5})^2})$	$\begin{cases} K_1 = (1-\frac{\psi}{\psi_t})^{\frac{-16}{15}\psi_t} \\ K_2 = (1-\frac{\psi}{\psi_t})^{\frac{8}{5}\psi_t} \end{cases}$	All range	All range	$\lim_{\lambda\to 0}$
Llewellin & Manga (2005)	$\frac{\mu_\psi}{\mu_m} = \begin{cases} (1-\psi)^{-1} \\ (1-\psi)^{5/3} \end{cases}$	Minimum model	Up to 7%	$\begin{matrix} Ca \le 1 \\ Ca > 1 \end{matrix}$	$\lim_{\lambda\to 0}$
	$\frac{\mu_\psi}{\mu_m} = \begin{cases} 1+9\psi \\ (1+22.4\psi)^{-1} \end{cases}$	Maximum model	$\begin{matrix} \text{Up to } 50\% \\ \text{Up to } 70\% \end{matrix}$	$\begin{matrix} Ca \le 1 \\ Ca > 1 \end{matrix}$	$\lim_{\lambda\to 0}$
This study	**Equation (3.54)**	—	**All range**	**All range**	**All range**

CHAPTER III

A NEW MODEL FOR THE RHEOLOGY OF SUSPENSIONS AND EMULSIONS

3.1 Introduction

This chapter presents a generalized rheological model for suspensions and emulsions of non-Brownian particles. When the Brownian motion due thermal energy is neglected, the dynamics of complex fluids is mainly governed by external body forces, interparticle forces and hydrodynamic interactions due to the presence of other particles. The first goal, here, is to present a complete derivation of the macroscopic rheology for both dilute and concentrated monomodal suspensions/emulsions under simple steady shearing flow conditions. The effective viscosity is determined from the knowledge of the influence of individual particles on the fluid flow and the pressure field by taking two volume corrections into consideration. The first volume correction serves to build a general rheological model for dilute complex fluids. With this correction, each particle inside the finite volume can interact with all particles added simultaneously to the system through a decrease in the volume of the ambient fluid (finite medium). We then introduce the second volume correction to extend the model phenomenologically to highly concentrated systems (up to the random close packing). This correction accounts for the interaction of particles added during the Differential Effective Medium procedure with particles already present in the system. Therefore, the second volume correction includes a term that carries the effect of the particle shape and size distribution as a geometrical constraint on the amount of volume that can be eventually filled by particles (i.e. the second volume correction accounts for the volume of matrix trapped in interstices formed by particles through a crowding factor). The second objective is to generalize the equation for the macroscopic rheology of emulsions applicable for a wide range of viscosity ratio, capillary number and particle concentration which is missing in the

literature (see figure 2.4). This general equation shall reduce to the well-known effective viscosity law developed by Sutherland-Einstein (1906) and Taylor (1932) in the limiting cases when $\psi \ll 1$ along with either $\lambda \to \infty$ or $\lambda \to 0$, respectively. The third objective is to provide a regime diagram which illustrates how the effective viscosity for emulsions depends on the viscosity ratio and capillary number. These regimes constrain the influence of different parameters on the deformation of particles, and provide insights into transitions from Newtonian to shear thinning due to the particle deformation.

Note: the content of this chapter is published as:

Faroughi, S. A., & Huber, C. (2015). A generalized equation for rheology of emulsions and suspensions of deformable particles subjected to simple shear at low Reynolds number. Rheologica Acta, 54(2), 85-108.

3.2 Physical description

We shall consider two incompressible and immiscible Newtonian fluids forming a matrix (the continuous phase) and the dispersed phase (a single fluid particle at this stage). The fluid flow at large distances from the fluid particle satisfies the conditions of a simple steady straining flow:

$$\boldsymbol{u}_{\odot}(\boldsymbol{x}) = \boldsymbol{\Upsilon} \cdot \boldsymbol{x}. \tag{3.1}$$

Here, $\boldsymbol{x}$ denotes the position vector with respect to the origin located at the center of the fluid particle, and $\boldsymbol{\Upsilon}$ is a given velocity gradient tensor for which the incompressibility of the matrix imposes $tr\boldsymbol{\Upsilon} = 0$. We shall assume that inertial forces can be neglected (small Reynolds number, $Re \ll 1$), and the density of dispersed particles is the same as that of the matrix. The force balance which governs the equation of motion is characterized by Stokes creeping equations

$$\boldsymbol{\nabla} \cdot \boldsymbol{\sigma}^m = 0, \boldsymbol{\sigma}^m = -p^m \boldsymbol{I} + \mu_m \left[\boldsymbol{\nabla} \boldsymbol{u}^m + (\boldsymbol{\nabla} \boldsymbol{u}^m)^T \right], \tag{3.2}$$

where sub/superscript m refers to properties associated with the matrix, $\boldsymbol{\sigma}^m$ is the total stress tensor, p^m is the dynamic pressure, $\boldsymbol{I}$ is the unit tensor, and μ_m denotes the shear dynamic viscosity of the matrix. $\boldsymbol{u}^m$ is the velocity vector that satisfies the continuity

equation, $\boldsymbol{\nabla} \cdot \boldsymbol{u}^m = 0$. Similar expressions can be formulated for the fluid flow inside the particle just by changing the superscript m to d which refers to the dispersed phase. We assume that the particle deforms due to the shearing. To the first order, the stress that acts to elongate the particle is proportional to $\mu_m \Upsilon$ where $\Upsilon = |\boldsymbol{\Upsilon}|$ is the magnitude of the velocity gradient (or the shear rate magnitude) with unit $[t^{-1}]$. The resisting stress on the surface of the particle opposing the induced shear stress is of order γ/R_d where γ is the surface tension, and R_d is the radius of the particle. For the case of a deformable elastic solid particle, the resisting stress will be proportional to the shear modulus G. The equilibrium state between these two counteracting surface stresses on the surface of particle controls the final shape of the particle, and leads to the definition of the dimensionless deformation number; the capillary number,

$$Ca = \frac{\Upsilon \mu_m R_d}{\gamma}, \tag{3.3}$$

for the case of fluid particles and the Weissenberg number,

$$Wi = \frac{\Upsilon \mu_m}{G}, \tag{3.4}$$

for the case of solid particles. The required sets of boundary conditions directly depends on the order of particle deformation considered. Here, we shall consider a homogeneous straining flow at a large distance from the center of the fluid particle, along with the continuity of tangential velocity and tangential components of the stress tensor at the surface of the particle in order to find the zeroth order of deformation solution (assuming the particle remains spherical). We can also obtain the first order of deformation solution by using the discontinuity in normal components of the stress tensor across the particle surface based on Laplace's equation. Overall, the velocity, pressure and stress fields outside the particle are decomposed up to the second order of the particle deformation $O(D^2)$ as follows

$$\begin{aligned} \boldsymbol{u}^t &= \boldsymbol{u}_\odot + \boldsymbol{u}^{0,d} + D\boldsymbol{u}^{1,d} + O(D^2), \\ p^t &= p_\odot + p^{0,d} + Dp^{1,d} + O(D^2), \\ \boldsymbol{\sigma}^t &= \boldsymbol{\sigma}_\odot + \boldsymbol{\sigma}^{0,d} + D\boldsymbol{\sigma}^{1,d} + O(D^2). \end{aligned} \tag{3.5}$$

Here, D is a dimensionless parameter which specifies the amount of deformation (departure from the spherical shape), and it is proportional to either Ca or Wi number respectively for fluid particle and solid particle. $p_{\odot}$ is an arbitrary constant pressure at a large distance from the particle which is normally assumed to be zero. At large distances from the particle, the zeroth and first order correction terms (parameterized by superscript $0, d$ and $1, d$) vanish.

3.2.1 Zeroth order deformation

Using the general solution for Stokes equations formulated by Lamb, and considering appropriate solid spherical harmonics of degree j (p_j & ϕ_j) for the exterior fluid, one can express both velocity and pressure fields. The zeroth order deformation solution was first provided by Taylor (1932) who used the following solid spherical harmonic functions of degree -3:

$$\begin{aligned} p_{-3}^{0,d} &= \mu^m A_{-3}^{0,d} \left(\frac{R_d}{r^2}\right)^3 (\boldsymbol{\Upsilon}^{\boldsymbol{\mathcal{S}}} : \boldsymbol{xx}), \\ \phi_{-3}^{0,d} &= B_{-3}^{0,d} \left(\frac{R_d}{r}\right)^5 (\boldsymbol{\Upsilon}^{\boldsymbol{\mathcal{S}}} : \boldsymbol{xx}), \end{aligned} \tag{3.6}$$

where $\boldsymbol{\Upsilon}^{\boldsymbol{\mathcal{S}}}$ is the normalized pure shear rate tensor (the rate of deformation tensor as the symmetric part of the velocity gradient normalized by the magnitude of the shear flow). By applying the aforementioned boundary conditions for the zeroth order, Taylor (1932) arrived at the following expression for the constants in Eq. (3.6):

$$A_{-3}^{0,d} = -5\Upsilon \left(\frac{\lambda + \frac{2}{5}}{\lambda + 1}\right), \quad B_{-3}^{0,d} = -\frac{\Upsilon}{2} \left(\frac{\lambda}{\lambda + 1}\right), \tag{3.7}$$

in which λ is the viscosity ratio defined as,

$$\lambda = \frac{\mu_d}{\mu_m}. \tag{3.8}$$

3.2.2 First order deformation

The solution for a first order deformation can be obtained with the same method, and by using Laplace's equation as a proper boundary condition to define the stress jump at the boundary of the particle (see Frankel & Acrivos (1967, 1970) for more details). The solid spherical harmonics p_{-3} are the only functions needed for the integration of the stress

components over a large volume, owing to the fact that other solid spherical harmonics vanish. The final result for the solid spherical harmonic reduces to the following expression Schowalter *et al.* (1968):

$$\begin{aligned} p_{-3}^{1,d} &= \frac{20}{7}\mu_m \Upsilon \frac{25\lambda^2+41\lambda+4}{25(\lambda+1)^2}\left(\frac{R_d}{r}\right)^3 \\ &\cdot \left[(\boldsymbol{\Upsilon^S} : \boldsymbol{\Upsilon^S}) - \frac{3}{r^2}(\boldsymbol{\Upsilon^S}\cdot\boldsymbol{x})^2\right] + 12\mu_m\Upsilon\frac{19\lambda+16}{15(\lambda+1)} \\ &\cdot \left(\frac{R_d}{r^2}\right)^3\left[(\frac{\boldsymbol{u}_\odot}{\Upsilon} - \boldsymbol{\Upsilon^S}\cdot\boldsymbol{x})\cdot(\boldsymbol{\Upsilon^S}\cdot\boldsymbol{x})\right]. \end{aligned} \tag{3.9}$$

Furthermore, the shape of the particle up to the second order of the deformation ($O(D^2)$) is calculated as:

$$r - R_d\left[1 + \frac{2}{r^2}\underbrace{\frac{Ca}{16}\frac{19\lambda+16}{\lambda+1}}_{D}(\boldsymbol{\Upsilon^S} : \boldsymbol{xx})\right] = 0. \tag{3.10}$$

3.2.3 Second order deformation

To proceed to higher orders deformation, for instance to Ca^2, one needs to derive the complete second-order solutions of the spherical harmonics for the pressure and velocity fields and an expression for the particle shape. Deriving these solutions following the same methodology is complex and tedious (Chaffey & Brenner, 1967; Greco, 2002). Alternatively, Greco (2002) presented an analysis that calls for rotational invariance to find all unknown fields (velocity and pressure) and the particle shape. According to Greco (2002), one arrives to the following function for the fluid particle shape up to the third order of the deformation ($O(D^3)$),

$$\begin{aligned} r - R_d\Bigg[1 + \frac{2}{r^2}\frac{Ca}{16}\frac{19\lambda+16}{\lambda+1}(\boldsymbol{\Upsilon^S} : \boldsymbol{xx}) + Ca^2 \\ \cdot\left(\frac{S_1(\lambda)}{r^3}(\boldsymbol{\Upsilon^S\Upsilon^S} :: \boldsymbol{xxx}) + \frac{S_2(\lambda)}{r^2}(\boldsymbol{\Upsilon^S\Upsilon^S} : \boldsymbol{xx})\right. \\ \left. + S_3(\lambda)(\boldsymbol{\Upsilon^S} : \boldsymbol{\Upsilon^S}) + \frac{S_4(\lambda)}{r^2}(\boldsymbol{\Pi} : \boldsymbol{xx})\right)\Bigg] = 0, \end{aligned} \tag{3.11}$$

where coefficients S_1 through S_4 depend only on the viscosity ratio and are listed in the *Appendix F* of Greco (2002). In Eq. (3.11), $\boldsymbol{\Pi}$ is the second Rivlin-Ericksen tensor that,

under simple shear flow conditions, reduces to

$$\boldsymbol{\Pi} = 2(\boldsymbol{\Upsilon}^{\mathcal{S}} \cdot \boldsymbol{\Upsilon}^{\mathcal{A}} - \boldsymbol{\Upsilon}^{\mathcal{A}} \cdot \boldsymbol{\Upsilon}^{\mathcal{S}}) + 4\boldsymbol{\Upsilon}^{\mathcal{S}} \cdot \boldsymbol{\Upsilon}^{\mathcal{S}}, \tag{3.12}$$

where $\boldsymbol{\Upsilon}^{\mathcal{A}}$ is the normalized spin tensor (skew-symmetric part of the velocity gradient normalized by the magnitude of the shear flow).

While Greco (2002) provides a starting point to further develop our model to higher orders of particle deformation, we restrict our derivation to the first order of the deformation (up to $O(D^2)$, therefore the model is theoretically applicable only for small particle deformations). Interestingly, we show below that our model predictions for emulsions sheared at high Ca are in good agreement with experiments which suggest that the second order truncation with respect to particle deformation does not introduce significant errors when extrapolated to high Ca.

The harmonic functions for the case of a matrix including a Hookean elastic solid particle are obtained with the same methodology to the zeroth order of deformation. For first order deformations, we replace Laplace's equation with another stress boundary condition at the fluid-elastic solid interface (Goddard & Miller, 1967). This is the case even for a fluid particle which has a infinite viscosity where the spherical shape of the particle is not maintained by surface tension forces, but rather by its shear modulus G.

3.3 Relative viscosity of a dilute complex fluid

According to Batchelor (1967), the rate of energy dissipation per unit volume inside a suspension (or emulsion) increases when more solid particles (or fluid particles possessing high surface tension or shear viscosity) are fed to the system. Therefore, a complex fluids can be treated as a homogeneous Newtonian fluid of the same average density in a fixed volume of $V_\psi = V_m^r + V_p^t$ (in which V_p^t is the total volume occupied by particles, and V_m^r is the remaining volume of the matrix) and with viscosity μ_ψ. The stress tensor at any point of the system (outside particles), $\boldsymbol{\sigma}^t$, is given by

$$\boldsymbol{\sigma}^t = -p^m \boldsymbol{I} + 2\mu_m \Upsilon \boldsymbol{\Upsilon}^{\mathcal{S}} \underbrace{-p' \boldsymbol{I} + \mu_m \left[\boldsymbol{\nabla u'} + (\boldsymbol{\nabla u'})^T\right]}_{\boldsymbol{\sigma'}}, \tag{3.13}$$

where the primed terms are associated with the disturbance in stress tensor, velocity and pressure fields due to the presence of particles, and consequently they include both perturbation arising from zeroth and first order of deformation. Namely,

$$\boldsymbol{\sigma'} = \boldsymbol{\sigma}^{0,d} + D\boldsymbol{\sigma}^{1,d}. \tag{3.14}$$

Besides, the stress tensor for the homogeneous equivalent fluid at any point can be calculated as

$$\boldsymbol{\sigma}^{\psi} = -p^{\psi}\boldsymbol{I} + 2\mu_{\psi}\Upsilon\boldsymbol{\Upsilon}^{\boldsymbol{\mathcal{S}}}. \tag{3.15}$$

The equivalence assumption implies the equality of the total rate of work done on the boundary of the emulsion/suspension, A_{ψ}, in both structures characterized with the stress tensors defined in Eqs. (3.13) and (3.15).

In previous models (Einstein, 1906; Taylor, 1932; Batchelor & Green, 1972; Goddard & Miller, 1967; Frankel & Acrivos, 1970; Schowalter *et al.* , 1968), the matrix is considered unbounded (infinite volume). Therefore, the excluded volume taken by particles has been overlooked which results in particles being represented as mass points. These models provide valuable results only in cases where the particle concentration is low (less than 5%). In this study, a finite volume for the matrix is considered, however it is assumed large enough to satisfy the fact that the perturbation of single particles on the flow fields are independent of each other (no hydrodynamic interactions in the dilute limit). The model, thus, takes into account the excluded volume of the matrix replaced by particles using a first volume correction. Using this correction, particles added simultaneously interact by decreasing the volume available in the ambient fluid. We note that the consideration of a finite volume is physically more consistent when the model is tested against experiments.

Owing to the fact that the rate of work associated with the isotropic component of the stress tensors stated in Eqs. (3.13) and (3.15) are the same on the boundary of the physical domain (far from particles), the equality of the rate of work exerted by the deviatoric components, represented by $\boldsymbol{\tau}$, yields

$$\int_{A_{\psi}} \boldsymbol{u}_{\odot}^{\psi}\boldsymbol{\tau}^{\psi}\cdot\boldsymbol{n}\,dA = \int_{A_{\psi}} \boldsymbol{u}_{\odot}(\boldsymbol{\tau}_{\odot} + \boldsymbol{\sigma'})\cdot\boldsymbol{n}\,dA, \tag{3.16}$$

$$\int_{A_\psi} \Upsilon_{ik}(2\mu_\psi \Upsilon_{ij}) x_k n_j dA = \int_{A_\psi} \Upsilon_{ik}(2\mu_m \Upsilon_{ij}) x_k n_j dA + \int_{A_\psi} \Upsilon_{ik} \sigma'_{ij} x_k n_j dA, \tag{3.17}$$

where $\boldsymbol{n}$ is a outward unit vector normal to the surface. We proceed by transforming the first two surface integrals into integrals over the boundary of the remaining ambient fluid, A_m, (a surface enclosing the matrix). Thus, by applying the divergence theorem, Eq. (3.17) can be recast as

$$\begin{aligned} \int_{V_\psi - V_m^r} 2\mu_\psi \Upsilon_{ij} \frac{\partial u_i}{\partial x_j} dV + \int_{A_m} 2\mu_\psi \Upsilon_{ij} \Upsilon_{ik} x_k n_j dA = \\ \int_{V_\psi - V_m^r} 2\mu_m \Upsilon_{ij} \frac{\partial u_i}{\partial x_j} dV + \int_{A_m} 2\mu_m \Upsilon_{ij} \Upsilon_{ik} x_k n_j dA + \\ \int_{A_\psi} \Upsilon_{ik} \sigma'_{ij} x_k n_j dA. \end{aligned} \tag{3.18}$$

Assuming that equations governing the perturbation in the fluid flow caused by particles are in Stokes regime, we obtain

$$\frac{\partial(\sigma'_{ij} x_k)}{\partial x_j} = \sigma'_{ik}. \tag{3.19}$$

Using Eq. (3.19), the third integral in the right hand side of Eq. (3.18) can be expressed as

$$\begin{aligned} \int_{A_\psi} \Upsilon_{ik} \sigma'_{ij} x_k n_j dA = \\ \underbrace{\int_{V_\psi - N V_p} \Upsilon_{ik} \sigma'_{ik} dV}_{-N \int_{A_p} 2\Upsilon_{ik} \mu_m u'_i n_k dA} + N \int_{A_p} \Upsilon_{ik} \sigma'_{ij} x_k n_j dA. \end{aligned} \tag{3.20}$$

N is the number of particles fed to the system, and A_p is the surface of a particle. Integrals in Eq. (3.20) are treated in such a way that it is assumed particles are far apart and the disturbance they generate does not affect the flow field around other particles. Therefore, the averaged rate of energy dissipation per unit of volume is calculated only for one particle and then generalized (linearly summed) to account for the effect of other particles on the rate of dissipation. This assumption is true only for very dilute suspensions/emulsions where $V_\psi \to V_m^r$. As a result, the following equation can be retrieved from Eq. (3.18) by a

simple integration,

$$\begin{aligned} 2\Upsilon_{ij}\Upsilon_{ij}(\mu_\psi - \mu_m)V_m^r &= \\ N\int_{A_p}(\Upsilon_{ik}\sigma'_{ij}x_k n_j &- 2\Upsilon_{ik}\mu_m u'_i n_k)dA. \end{aligned} \tag{3.21}$$

The integral in the right hand side of Eq. (3.21) indicates the average additional rate of energy dissipation caused by a single particle (Batchelor, 1967). To calculate this integral, we can use the reciprocal theorem developed by Happel & Brenner (2012) or simply replace A_p by an arbitrary large surface, A_a, enclosing a single particle at its center. For the latter method, the ambient stress and velocity fields of the fluid disturbed by the presence of this particle should be considered as well, namely

$$\begin{aligned} \boldsymbol{u}'' &= \boldsymbol{u}_\odot + \boldsymbol{u}' \\ \boldsymbol{\sigma}'' &= \boldsymbol{\sigma}_\odot + \boldsymbol{\sigma}'. \end{aligned} \tag{3.22}$$

Therefore, we shall restate Eq. (3.21) as follows

$$\begin{aligned} \tau_{ik} &= 2\mu_m\Upsilon\Upsilon^S_{ik} + \frac{V_p^t}{V_\psi - V_p^t} \\ &\cdot \left(\frac{1}{V_p}\int_{A_a}\sigma''_{ij}x_k n_j dA - \frac{2}{V_p}\int_{A_a}\mu_m u''_i n_k\ dA\right), \end{aligned} \tag{3.23}$$

where $V_p^t = NV_p$, Using Lamb's general solution we have

$$\boldsymbol{u}'' = \boldsymbol{u}_\odot + \frac{1}{2\mu_m}\boldsymbol{x}p_{-3}, \tag{3.24}$$

and

$$\begin{aligned} \boldsymbol{\sigma}'' &= \mu_m\left[\boldsymbol{\nabla}\boldsymbol{u}_\odot + (\boldsymbol{\nabla}\boldsymbol{u}_\odot)^T\right] \\ &+ \frac{1}{2}\left[\boldsymbol{\nabla}(\boldsymbol{x}p_{-3}) + (\boldsymbol{\nabla}(\boldsymbol{x}p_{-3})^T\right] - \boldsymbol{I}p_{-3}, \end{aligned} \tag{3.25}$$

with

$$p_{-3} = p_{-3}^{0,d} + \left(\frac{\Upsilon\mu_m R_d}{16\gamma}\right)\left(\frac{19\lambda + 16}{\lambda + 1}\right)p_{-3}^{1,d}. \tag{3.26}$$

In Eq. (3.23), the first correction that accounts for the volume taken by particles appears in the homogenization process. Models which overlook this correction underpredict the shear dynamic viscosity of the equivalent fluid in a finite system. Therefore, if a set of particles are added to the matrix (forming a dilute complex fluid), the position of each particles is restricted by the presence of other particles.

The detailed solution to integrals in Eq. (3.23) can be found in Landau & Lifshitz (1987); Batchelor (1967) for complex fluid of non-deformable particles and in Goddard & Miller (1967); Frankel & Acrivos (1967); Schowalter *et al.* (1968) for complex fluids composed of deformable particles. Finally,

$$\begin{aligned} \boldsymbol{\tau} &= 2\mu_m \Upsilon \left[1 + \frac{\psi}{1-\psi}\left(\frac{1+2.5\lambda}{1+\lambda}\right)\right] \boldsymbol{\Upsilon^S} \\ &+ \frac{\mu_m^2 \Upsilon^2 R_d}{\gamma}\left(\frac{\psi}{1-\psi}\right)(\mathfrak{A} - \mathfrak{B}), \end{aligned} \tag{3.27}$$

where $\psi \equiv \frac{NV_p}{V_\psi}$ is the particle volume fraction and

$$\begin{aligned} \mathfrak{A} &= \frac{3(19\lambda+16)(25\lambda^2+41\lambda+4)}{140(\lambda+1)^3} \\ &\cdot \left[\boldsymbol{\Upsilon^S \cdot \Upsilon^S} - \frac{1}{3}\boldsymbol{I}\left(\boldsymbol{\Upsilon^S : \Upsilon^S}\right)\right], \end{aligned} \tag{3.28}$$

and

$$\mathfrak{B} = \frac{1}{40}\left(\frac{19\lambda+16}{\lambda+1}\right)^2 \left(\boldsymbol{\Upsilon^A \cdot \Upsilon^S} - \boldsymbol{\Upsilon^S \cdot \Upsilon^A}\right). \tag{3.29}$$

Equation (3.27) is a special case of *simple fluids* family of constitutive equations (Schowalter *et al.* , 1968). We note that the deformation introduces a non-linear relationship between the stress and the rate of strain. Thus, emulsions/suspensions behave as non-Newtonian fluids. Following Frankel & Acrivos (1970), we can apply the operator

$$1 + \Lambda \frac{\mathfrak{D}}{\mathfrak{D}t}, \tag{3.30}$$

on both sides of Eq. (3.27). In Eq. (3.30), $\frac{\mathfrak{D}}{\mathfrak{D}t}$ denotes the Jaumann derivative (Goddard & Miller, 1967), which is defined as follows for an arbitrary tensor $\boldsymbol{\alpha}$,

$$\frac{\mathfrak{D}}{\mathfrak{D}t}\boldsymbol{\alpha} = \frac{d}{dt}\boldsymbol{\alpha} + \boldsymbol{u}\cdot\boldsymbol{\nabla\alpha} + \Upsilon\left(\boldsymbol{\Upsilon^A \cdot \alpha} - \boldsymbol{\alpha \cdot \Upsilon^A}\right). \tag{3.31}$$

In Eq. (3.30), Λ is determined as

$$\Lambda = \frac{(2\lambda+3)(19\lambda+16)}{40(\lambda+1)}\left(\frac{\mu_m R_d}{\gamma}\right), \tag{3.32}$$

has unit of time and is defined as the relaxation time that characterizes the time-dependency of the flow response to deformation (the time required for a slightly deformed particle to relaxes exponentially to its spherical equilibrium shape). The value of the relaxation time diverges as the viscosity ratio approaches to infinity or as surface tension approaches zero.

In a steady and laminar simple straining flow, when $\boldsymbol{\alpha} = \boldsymbol{\Upsilon}^{\boldsymbol{\mathcal{S}}}$, the material derivative part of the Jaumann derivative, first two terms of the RHS of Eq. (3.31), vanishes. This simplification is valid even when the Jaumann derivative is applied to the stress tensor associated with dilute complex fluids subjected to a steady simple shear. For these complex fluids, fluctuations caused by variation in particle arrangement and deformation far away from the considered particle remain relatively small, therefore, we expect this simplification does not affect our model under steady conditions.

By applying the operator defined in Eq. (3.30) to Eq. (3.27), we obtain Eq. (3.33),

$$\begin{aligned}\boldsymbol{\tau} + \Lambda\Upsilon\left(\boldsymbol{\Upsilon}^{\boldsymbol{\mathcal{A}}}\cdot\boldsymbol{\tau} - \boldsymbol{\tau}\cdot\boldsymbol{\Upsilon}^{\boldsymbol{\mathcal{A}}}\right) = 2\mu_m\Upsilon\left[1+\frac{\psi}{1-\psi}\left(\frac{1+2.5\lambda}{1+\lambda}\right)\right]\times \\ \left[\boldsymbol{\Upsilon}^{\boldsymbol{\mathcal{S}}} + \Lambda\Upsilon\left(\boldsymbol{\Upsilon}^{\boldsymbol{\mathcal{A}}}\cdot\boldsymbol{\Upsilon}^{\boldsymbol{\mathcal{S}}} - \boldsymbol{\Upsilon}^{\boldsymbol{\mathcal{S}}}\cdot\boldsymbol{\Upsilon}^{\boldsymbol{\mathcal{A}}}\right)\right] + \frac{\mu_m^2\Upsilon^2 R_d}{\gamma}\left(\frac{\psi}{1-\psi}\right)(\mathfrak{A}-\mathfrak{B}) + \\ \frac{\mu_m^2\Upsilon^3 R_d}{\gamma}\left(\frac{\psi}{1-\psi}\right)\Lambda\left(\boldsymbol{\Upsilon}^{\boldsymbol{\mathcal{A}}}\cdot(\mathfrak{A}-\mathfrak{B}) - (\mathfrak{A}-\mathfrak{B})\cdot\boldsymbol{\Upsilon}^{\boldsymbol{\mathcal{A}}}\right),\end{aligned} \tag{3.33}$$

in which $\mathfrak{A}$ and $\mathfrak{B}$ are defined in Eqs. (3.28) and (3.29), respectively. We drop the last term in Eq. (3.33) to maintain the order of deformation in Eq. (3.33) similar to that of Eq. (3.27) (second order with respect to Υ).

For a simple steady straining flow with the following dimensionless symmetric and skew-symmetric part of the velocity gradient

$$\boldsymbol{\Upsilon}^{\boldsymbol{\mathcal{S}}} = \frac{1}{2}\begin{bmatrix}0 & 1 & 0\\ 1 & 0 & 0\\ 0 & 0 & 0\end{bmatrix}, \qquad \boldsymbol{\Upsilon}^{\boldsymbol{\mathcal{A}}} = \frac{1}{2}\begin{bmatrix}0 & -1 & 0\\ 1 & 0 & 0\\ 0 & 0 & 0\end{bmatrix},$$

we can restate Eq. (3.33) in a matrix form, see Eq. (3.34).

$$\begin{bmatrix} \tau_{11}-\Lambda\Upsilon\tau_{12} & \tau_{12}+\frac{\Lambda\Upsilon}{2}(\tau_{11}-\tau_{22}) & 0 \\ \tau_{12}+\frac{\Lambda\Upsilon}{2}(\tau_{11}-\tau_{22}) & \tau_{22}+\Lambda\Upsilon\tau_{12} & 0 \\ 0 & 0 & \tau_{33} \end{bmatrix} =$$

$$\mu_m\Upsilon\left[1+\frac{\psi}{1-\psi}(\frac{1+2.5\lambda}{1+\lambda})\right]\begin{bmatrix} -\Lambda\Upsilon & 1 & 0 \\ 1 & \Lambda\Upsilon & 0 \\ 0 & 0 & 0 \end{bmatrix} +$$

$$\left(\frac{\mu_m\Upsilon^2\Lambda}{14(2\lambda+3)(\lambda+1)^2}(\frac{\psi}{1-\psi})\right)\times$$

$$\begin{bmatrix} (158\lambda^2+286\lambda+116) & 0 & 0 \\ 0 & -(108\lambda^2+204\lambda+108) & 0 \\ 0 & 0 & -(50\lambda^2+82\lambda+8) \end{bmatrix}, \qquad (3.34)$$

The deviatoric stress components in the direction of the first and second principal axes are obtained in Eq. (3.35).

$$\begin{aligned} \tau_{11} &= \Lambda\Upsilon\tau_{12}-\mu_m\Lambda\Upsilon^2\left(1+\frac{70\lambda^3+45\lambda^2-111\lambda-74}{14(2\lambda+3)(\lambda+1)^2}(\frac{\psi}{1-\psi})\right), \\ \tau_{22} &= -\Lambda\Upsilon\tau_{12}+\mu_m\Lambda\Upsilon^2\left(1+\frac{70\lambda^3+95\lambda^2-29\lambda-66}{14(2\lambda+3)(\lambda+1)^2}(\frac{\psi}{1-\psi})\right), \\ \tau_{12} &= -\frac{1}{2}\Lambda\Upsilon(\tau_{11}-\tau_{22})+\mu_m\Upsilon\left(1+\frac{1+2.5\lambda}{1+\lambda}(\frac{\psi}{1-\psi})\right). \end{aligned} \qquad (3.35)$$

A simple manipulation of Eq. (3.35) yields an expression for τ_{12} which can be used to find the macroscopic viscosity of the emulsion, $\mu_\psi = \tau_{12}/\Upsilon$. Finally, we obtain

$$\begin{aligned} \frac{\mu_\psi}{\mu_m} &= 1+\frac{1}{1+\Lambda^2\Upsilon^2}(\frac{\psi}{1-\psi}) \\ &\cdot \left[\frac{1+2.5\lambda}{1+\lambda}+\frac{140(\lambda^3+\lambda^2-\lambda-1)}{28(2\lambda+3)(\lambda+1)^2}\Lambda^2\Upsilon^2\right]. \end{aligned} \qquad (3.36)$$

Now by substituting Λ from Eq. (3.32) into Eq. (3.36), and using the definition of the capillary number in Eq. (3.3), we can recast Eq. (3.36) into the following general equation for any capillary number and finite viscosity ratio

$$\begin{aligned} \frac{\mu_\psi}{\mu_m} &= 1+\frac{1}{1+\kappa Ca^2}(\frac{\psi}{1-\psi}) \\ &\cdot \left[\frac{1+2.5\lambda}{1+\lambda}+\frac{140(\lambda^3+\lambda^2-\lambda-1)}{28(2\lambda+3)(\lambda+1)^2}\kappa Ca^2\right], \end{aligned} \qquad (3.37)$$

where

$$\kappa = \left(\frac{(2\lambda + 3)(19\lambda + 16)}{40(\lambda + 1)} \right)^2 . \tag{3.38}$$

It should be noted again that the model stated in Eq. (3.37) is only valid for a dilute complex fluid up to the second order of particle deformation for any finite viscosity ratios and capillary number. Note for the case of infinite viscosity ratio, the fluid particle acts like a Hookian solid particle and remains spherical because of the large shear dynamic viscosity, not surface tension. Therefore, another proper set of boundary conditions for the normal components of the stresses on the surface of the deformed particle should be used (Goddard & Miller, 1967). Applying the boundary condition of Goddard & Miller (1967) and introducing the first volume correction in the homogenization process, we find

$$\frac{\mu_\psi}{\mu_m} = 1 + \frac{2.5}{1 + \frac{9}{4}Wi^2} \left(\frac{\psi}{1 - \psi} \right) \left[1 - \frac{3}{2}Wi^2 \right], \tag{3.39}$$

for suspensions of elastically deformable solid particles.

We note that at low particle volume fraction, where $\frac{\psi}{1-\psi} = \psi + O(\psi^2)$, Eq. (3.37) recovers the equation of Taylor (1932) using $\lambda \to 0$ and $Ca \ll 1$, the equation of Mackenzie (1950) using $\lambda \to 0$ and $Ca \gg 1$ and that of Oldroyd (1959) using $\lambda \to 0$ (see table 2.1). Similarly, at low solid particle volume fraction, Eq. (3.39) reduces to the well-known Einstein-Sutherland law when $Wi \ll 1$ (see table 2.2).

An extension of rheological model to concentrated systems requires a self consistent approach to account for particle hydrodynamic interactions. Additionally, for a complex fluid of rigid solid or non-deformable fluid particles, the relative viscosity should satisfy

$$\lim_{\psi \to \psi_t} \frac{\mu_\psi}{\mu_m} \simeq \infty, \tag{3.40}$$

where ψ_t is the threshold packing fraction for spherical particles, see section 2.3.1. We note that in the case of emulsions including deformable fluid particles, the relative viscosity at $\psi = \psi_t$ exhibits considerable increase but does not diverge (Pal, 2000), however to the first order deformation for emulsions of slightly deformable fluid particles, we will assume that Eq. (3.40) still holds.

3.4 Extension to concentrated complex fluids

We use a phenomenological approach based on the Differential Effective Medium (DEM) method (Norris *et al.* , 1985) operating in a fixed volume to extend our model to high concentration systems. The DEM approach is an incremental method in which, at each conceptual step, a few particles are introduced into the suspension/emulsion and interact with particles present in the medium. The homogenized macroscopic property (effective viscosity) is then computed for the whole system. It should be noted that the Differential Effective Medium theory is physically appropriate only in the case where the incremental addition is sufficiently sparse that it does not form a preferential connected network throughout the system. Due to the first volume correction, particles added simultaneously can interact with each other. Therefore, we only need to account for interactions between a new generation of particles and previous generations. We should account for the fact that this procedure cannot be followed until the entire volume of the matrix is replaced by particles ($\psi \nrightarrow 1$). This restriction arises because of the geometrical constraint dictated by the shape and size distribution of particles. Firstly, we will extend the model for the relative viscosity of a dense complex fluid in the case of zeroth order of particle deformation. Then, we can find an expression for the geometrical constraint by utilizing the packing limit condition of Eq. (3.40).

3.4.1 Relative viscosity for a dense complex fluid with non-deformable particles

To start the procedure, we can rewrite Eq. (3.37) in the following form (assuming $Ca \ll 1$)

$$\frac{\mu_\psi}{\mu_m} = 1 + \psi_c \left(\frac{1 + 2.5\lambda}{1 + \lambda} \right), \qquad \psi_c = \frac{\psi}{1 - \psi}. \tag{3.41}$$

Here ψ_c is called the corrected volume fraction of particles for the dilute system (first volume correction). In other words, this volume correction considers the finite space taken by other particles of the same generation. Based on the fixed volume DEM theory, the homogenization process is characterized by taking a portion of the ambient fluid out and replacing it with particles at each step. We define the particle fraction added to the system

during each step as $d\psi^i$, and the corresponding corrected particle fraction (effective concentration) added to be $\Delta\psi_c^i$. Therefore, the viscosity change of the homogenized equivalent fluid during step $i+1$ is

$$\mu_{i+1} - \mu_i = \mu_i \Delta\psi_c^{i+1} \left(\frac{1+2.5\lambda}{1+\lambda} \right), \tag{3.42}$$

where the current value μ_i represents the matrix viscosity μ_m and the next value μ_{i+1} denotes the effective suspension viscosity μ_ψ. The effective concentration in Eq. (3.42) is defined as,

$$\Delta\psi_c^{i+1} = \frac{d\psi^{i+1}}{1-\Omega\psi^i}, \tag{3.43}$$

where ψ^i is the total volume fraction of particles inside the medium at step i. In Eq. (3.43), the effective concentration at step $i+1$, $\Delta\psi_c^{i+1}$, introduces the second volume correction combining the first volume correction ψ_c and a self-crowding factor parameter denoted by Ω. This parameter, Ω, is a positive constant that accounts for the fact that particles cannot fill all the volume of the suspension/emulsion (a geometrical constraint). Theoretically, this parameter takes the effective volume of particles into consideration knowing that some fluid located in interstices formed by particles is no longer available to suspend particles. Ω is called the self-crowding factor because we assume that all particles have the same size (volume). In general, we argue that Ω is related to the size distribution (assuming small deformation) through the maximum random close packing concentration, ψ_t. Substituting Eq. (3.43) into Eq. (3.42) yields

$$\frac{\mu_{i+1} - \mu_i}{\mu_i} = \frac{d\psi^{i+1}}{1-\Omega\psi^i} \left(\frac{1+2.5\lambda}{1+\lambda} \right). \tag{3.44}$$

Upon integrating Eq. (3.44) from a system with zero particle and shear dynamic viscosity μ_m to a desired particle volume fraction ψ_c and shear dynamic viscosity μ_ψ,

$$\int_{\mu_m}^{\mu_\psi} \frac{1}{\mu} d\mu = \int_0^{\psi_c} \frac{1}{1-\Omega\psi} \left(\frac{1+2.5\lambda}{1+\lambda} \right) d\psi, \tag{3.45}$$

Eq. (3.41) becomes

$$\frac{\mu_\psi}{\mu_m} = \left(1 - \Omega \frac{\psi}{1-\psi} \right)^{-\frac{1+2.5\lambda}{\Omega(1+\lambda)}}. \tag{3.46}$$

The model described by Eq. (3.46) predicts the relative viscosity for a dense complex fluid at any finite viscosity ratio to the zeroth order of particle deformation. The self-crowding factor Ω is determined by applying the constraint stated in Eq. (3.40)

$$\lim_{\psi \to \psi_t} \frac{\Omega \psi}{1-\psi} = 1 \qquad \longrightarrow \qquad \Omega = \frac{1-\psi_t}{\psi_t}. \tag{3.47}$$

Based on Eq. (3.47), we find that $\Omega < 1$ if $\psi_t > 0.5$. This implies that the added particle volume fraction, say $\psi = a$, practically occupies an effective volume of a/Ω. This is also equivalent to argue that the volume $a(1/\Omega - 1)$ of the matrix is trapped in interstitial spaces between particles.

Substituting Eq. (3.47) into Eq. (3.46) yields the following equation for the relative viscosity of emulsions of non-deformable fluid particles

$$\frac{\mu_\psi}{\mu_m} = \left(\frac{\psi_t - \psi}{\psi_t (1-\psi)} \right)^{-\frac{\psi_t (1+2.5\lambda)}{(1-\psi_t)(1+\lambda)}}. \tag{3.48}$$

For the particular case of a suspension of rigid solid particles ($\lambda \to \infty$ and $G \to \infty$), Eq. (3.48) reduces to

$$\frac{\mu_\psi}{\mu_m} = \left(\frac{\psi_t - \psi}{\psi_t (1-\psi)} \right)^{-\frac{2.5\psi_t}{1-\psi_t}}. \tag{3.49}$$

Some of the well-known models in Table 2.1 can be re-derived using the DEM theory by applying different approaches to characterize particle interactions, i.e. (i) considering infinite suspensions, and (ii) choosing different infinitesimal volumes of new particles added over each incremental step of the DEM. The definition of the infinitesimal volume fraction of particles added at each incremental step in the DEM theory to retrieve these effective viscosity models are reported in Table 3.1.

Equation (3.49) is plotted for intermediate and high volume fractions of particles respectively in Figs. 3.1 and 3.2 where it is compared to published experimental data and well-known equations listed in Table 2.1. Figure 3.1 shows a monotonically increasing relative viscosity with particle concentration. The shaded area in Fig. 3.1 highlights the region that regroups most of the experimental data. Our model agrees very well with published

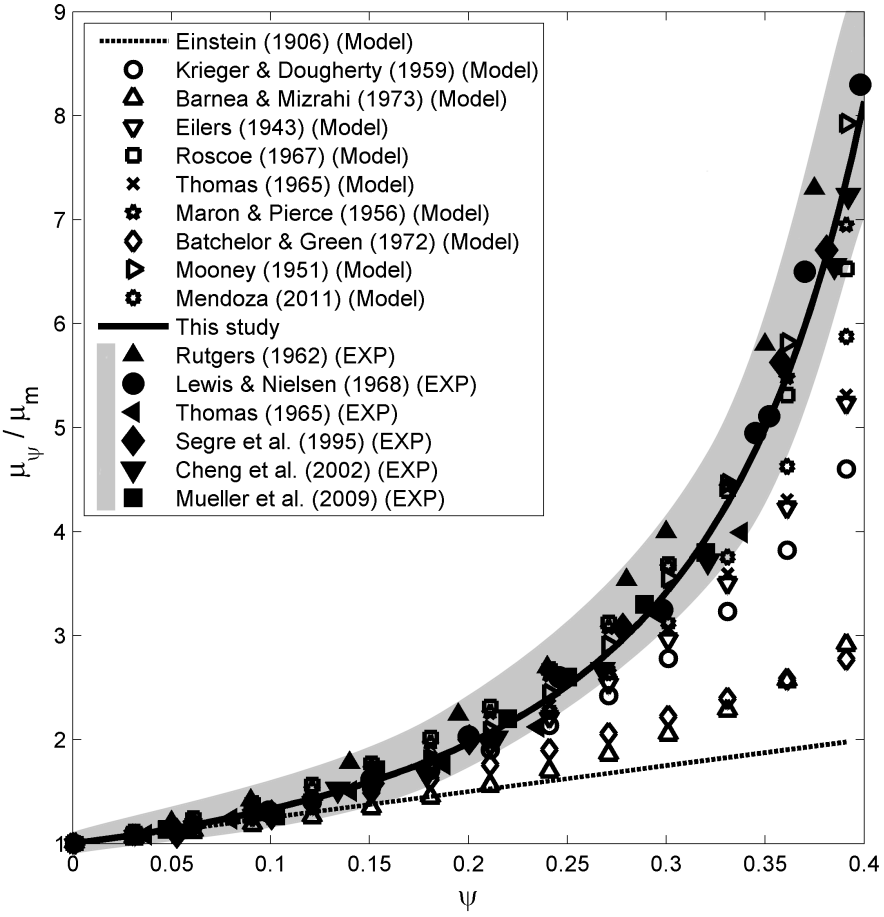

Figure 3.1: Rheology of suspension of rigid solid particles ($\lambda \to \infty$ and $G \to \infty$). Comparison of the model in Eq. (3.49) with previous published models (see Table 2.1) and experimental data from dilute up to the intermediate particle concentration. The shaded area highlights the region that regroups most of the experimental data.

Table 3.1: The definition of the infinitesimal volume fraction of particles added at each incremental step in the DEM theory to retrieve some of the well-known viscosity models.

Model	infinitesimal volume fraction
Mooney (1951)	$d\left(\psi/(1-\frac{\psi}{\psi_t})\right)$
Brinkman (1952)	$d\psi/(1-\psi)$
Krieger & Dougherty (1959)	$d\psi/(1-\frac{\psi}{\psi_t})$
Mendoza (2011)	$d\psi_e/(1-\psi_e)$, where $\psi_e = \psi/(1-\Omega\psi)$

experiments for suspensions. One can observe that commonly used models for concentrated suspensions, like (Krieger & Dougherty, 1959), (Barnea & Mizrahi, 1973) and (Eilers, 1943), deviate from the experimental data as the particle concentration increases. As mentioned earlier, ignoring the first volume correction (e.g. (Einstein, 1906)) results in underpredicting the shear viscosity of even dilute suspensions. It is also interesting to stress that our model closely follows the empirical model proposed by Mooney (1951) when the free parameter in his model is set to 1.35 (see Table 2.1). In Fig. 3.2, the relative viscosity predicted with our model Eq. (3.49) is plotted for dense systems up to the packing limit $\psi \to \psi_t$, and shows an excellent agreement with experimental data. Here again the shaded area indicates the range observed in experiments. Over this range of particle concentration ($0.35 < \psi < 0.6$), we observe that models that do not include the volume corrections discussed above underpredict the relative viscosity by up to two orders of magnitude. As a note, we emphasize here that the model does not include free parameters to fit the data and that we used $\psi_t = 0.637$ which corresponds to the volume fraction for the random close packing of spherical particles under static conditions.

We compare the model in Eq. (3.48) with published data for dense emulsions in the limit of $Ca \to 0$. The predicted value of the relative viscosity as function of particle volume fraction is depicted in Fig. 3.3 for an emulsion of non-deformable fluid particles where $\lambda \to 0$ (bubbly emulsion). Similarly to the results for solid suspensions in Fig. 3.1, we observe that the relative viscosity increases monotonically with volume fraction, but with a smaller rate than for solid particles. Based on Fig. 3.3, one can see that our model performs very well to reproduce experimental data in the limit of $\lambda \to 0$. Predicted results from other well-known models reported in Table 2.2 that are applicable to this range of ψ, $Ca \ll 1$ and $\lambda \to 0$ are also depicted in Fig. 3.3 for comparison. Figures 3.1-3.3 clearly show the importance of considering a finite volume (the influences of the first volume correction in the range of dilute emulsions $\psi < 0.15$) and defining an appropriate self-crowding factor (second volume correction) to improve the model's ability to describe interparticle hydrodynamic interactions at high volume fraction.

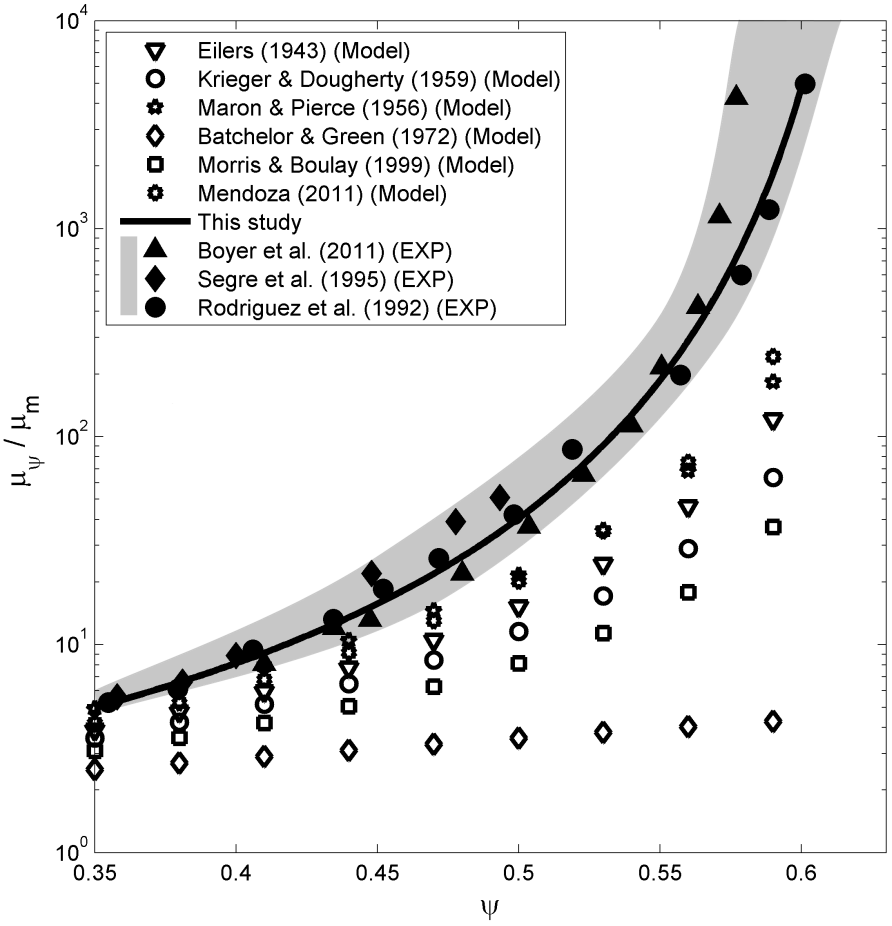

Figure 3.2: Rheology of suspension of rigid solid particles ($\lambda \to \infty$ and $G \to \infty$). Comparison of the model in equation (3.49) with previous published models (see table 2.1) and experimental data at intermediate to high particle volume fraction.

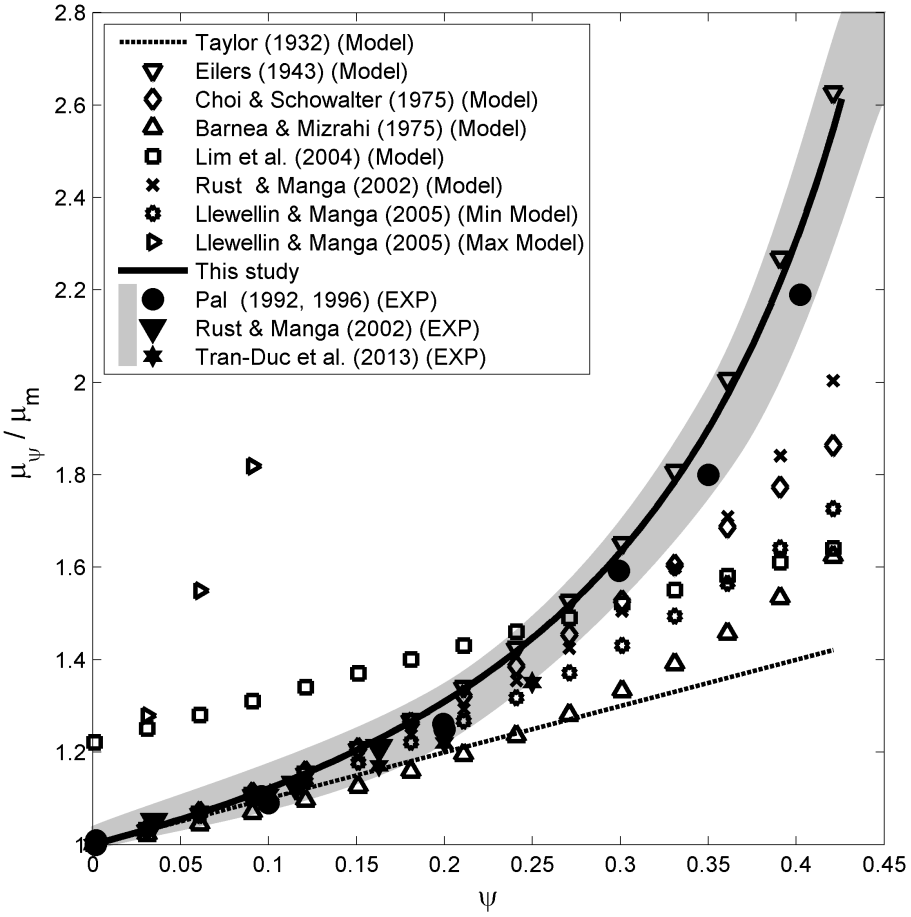

Figure 3.3: Rheology of emulsion of non deformable inviscid fluid particles (bubbly emulsion where $\lambda \to 0$ and $Ca \ll 1$). Comparison of the model in equation (3.48) with existing models (see table 2.2) and published experimental data.

3.4.2 Relative viscosity for a dense complex fluid with deformable particles

To extend our model to concentrated complex fluids with deformable particles, we shall first rewrite Eq. (3.37) as

$$\frac{\mu_\psi}{\mu_m} = 1 + \frac{1}{1+\kappa\mathcal{L}^2\mu_m^2}\left(\frac{\psi}{1-\psi}\right)\left[\mathcal{N} + \mathcal{M}\kappa\mathcal{L}^2\mu_m^2\right], \tag{3.50}$$

in which $\mathcal{L} = \Upsilon R_d/\sigma$ and

$$\mathcal{N} = \frac{1+2.5\lambda}{1+\lambda}, \quad \mathcal{M} = \frac{140(\lambda^3+\lambda^2-\lambda-1)}{28(2\lambda+3)(\lambda+1)^2}. \tag{3.51}$$

Applying the same procedure (fixed volume DEM theory) to Eq. (3.50) leads to the following ordinary differential equation

$$\left(\frac{1}{\mu} - \frac{\mathcal{M}\kappa\mathcal{L}^2\mu}{\mathcal{N}+\mathcal{M}\kappa\mathcal{L}^2\mu^2} + \kappa\mathcal{L}^2\mu - \frac{\mathcal{M}\kappa^2\mathcal{L}^4\mu^3}{\mathcal{N}+\mathcal{M}\kappa\mathcal{L}^2\mu^2}\right)d\mu = \mathcal{N}\frac{d\psi}{1-\Omega\psi}. \tag{3.52}$$

Upon integrating this equation with respect to the volume fraction from zero to ψ_c, with corresponding viscosity of μ_m and μ_ψ, we can find the following non-linear relation for the relative viscosity

$$\frac{\mu_\psi}{\mu_m}\left(\frac{\mathcal{N}+\mathcal{M}\kappa\mathcal{L}^2\mu_\psi^2}{\mathcal{N}+\mathcal{M}\kappa\mathcal{L}^2\mu_m^2}\right)^{\frac{1}{2}(\frac{\mathcal{N}}{\mathcal{M}}-1)} = \left(\frac{\psi_t-\psi}{\psi_t(1-\psi)}\right)^{-\frac{\mathcal{N}\psi_t}{1-\psi_t}}. \tag{3.53}$$

Alternatively, defining $f^\mu(\psi,\lambda,Ca) = \mu_\psi/\mu_m$ and $Ca = \mathcal{L}\mu_m$, Eq. (3.53) can be restated in the following general form

$$f^\mu\left(\frac{\mathcal{N}+\mathcal{M}\kappa Ca^2(f^\mu)^2}{\mathcal{N}+\mathcal{M}\kappa Ca^2}\right)^{\frac{1}{2}(\frac{\mathcal{N}}{\mathcal{M}}-1)} = \left(\frac{\psi_t-\psi}{\psi_t(1-\psi)}\right)^{-\frac{\mathcal{N}\psi_t}{1-\psi_t}}. \tag{3.54}$$

We note that for bubbly emulsions (where $\lambda \to 0,\ \mathcal{N}=1,\ \mathcal{M}=-5/3$ and $\kappa=(6/5)^2$), the left hand side of Eq. (3.54) reduces to the phenomenological equation of Pal (2003a). Further, for non-deformable particles, Eq. (3.54) reduces to Eq. (3.48) or (3.49) that have been successfully compared with experiments in Figs. 3.1 to 3.3.

To validate the effective viscosity model for emulsions of deformable particles defined in Eq. (3.54), we compare it with experiments conducted by Rust & Manga (2002) for

bubbly emulsion ($\lambda \to 0$) over intermediate capillary number ranges (small deformation) and relatively dilute systems with $\psi = 0.115$ and $\psi = 0.163$, respectively (see Fig. 3.4(a-b)). Based on these comparisons, one can see that using $\psi_t = 0.637$, our model provides a satisfying fit to experimental data. In addition, in panels (c) and (d) of Fig. 3.4, we show that Eq. (3.54) is in excellent agreement with experiments conducted by Stein & Spera (2002) at high shear rate (high capillary number) for relatively concentrated bubbly emulsions of $\psi = 0.29$ and $\psi = 0.45$. These results suggest that the errors associated with neglecting higher orders of particle deformation have a limited impact on the rheology of emulsions at ($Ca \gg 1$).

For complex fluids containing deformable particles, the physics of interactions between particles becomes more complicated when the particle volume fraction approaches or exceeds the maximum random close packing. Dense complex fluids have displayed elastic and plastic behavior at small and large strains, respectively. Even at very low shear rates, high particle concentration leads to deformation, possibly coarsening and drainage phenomena (Bénito *et al.* , 2008). It should be emphasized that our rheological model defined in Eq. (3.54) does not account for these processes such as plastic flow resulting from particle rearrangements and compaction, aging and yield stress. Our model is therefore limited to volume fractions below the random close packing, ψ_t. Nevertheless, Eq. (3.54) provides a valid rheological model for $0 \leq \psi < \psi_t$) over any of finite viscosity ratio and capillary number.

The relative viscosity as function of the capillary number predicted by Eq. (3.54) for two viscosity ratios $\lambda = 0$ and $\lambda = 1.1$ and different particle volume fractions is plotted in panels a-b of Fig. 3.5. We distinguish three regions: i) the relative viscosity is constant at low values of capillary numbers ($Ca \leq 10^{-3}$), ii) the relative viscosity decreases over intermediate values of capillary numbers ($10^{-3} < Ca < 10$), and finally, iii) the relative viscosity is constant again at high values of capillary numbers ($Ca \geq 10$). Furthermore, the viscosity ratio exerts a significant control on the viscosity of emulsions. For instance, based on the relation between the relative viscosity and capillary number in the limit of $\lambda \to 0$, (Fig. 3.5(a)), we observe that at capillary number values smaller than a critical capillary number (where curves intersect each other), the relative viscosity is greater than unity

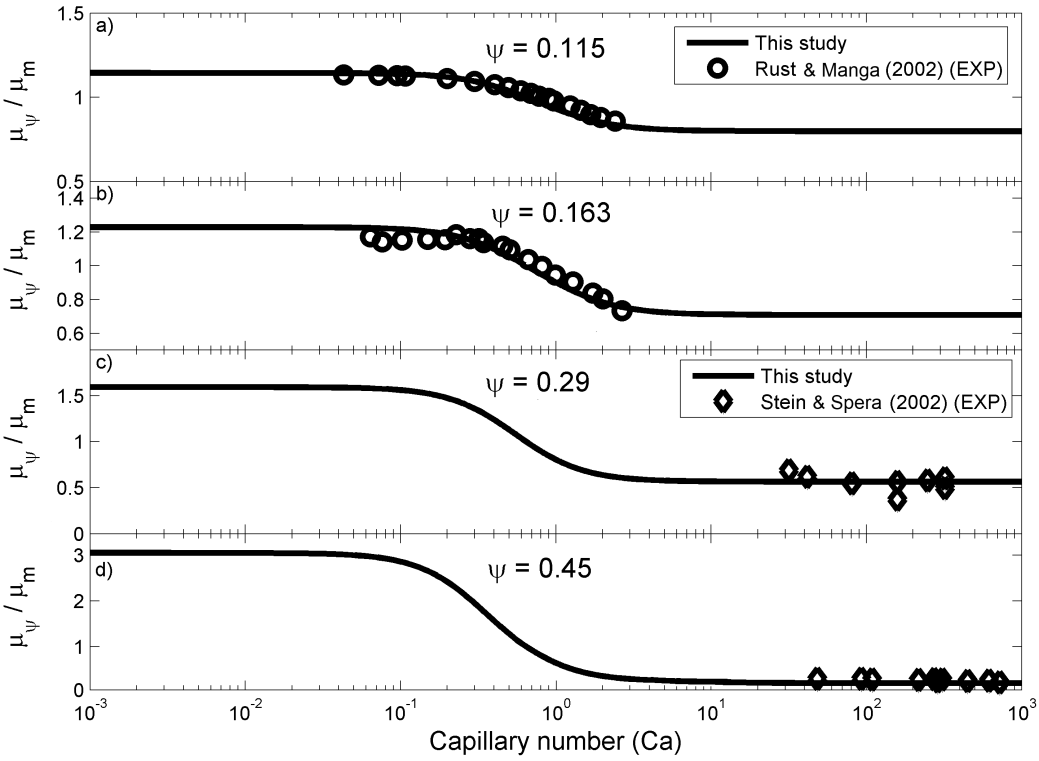

Figure 3.4: Rheology of emulsion of deformable inviscid fluid particles ($\lambda \to 0$) versus capillary number. Comparison between our model (solid line), containing no fitting parameter, and experimental data for four different measured particle concentrations.

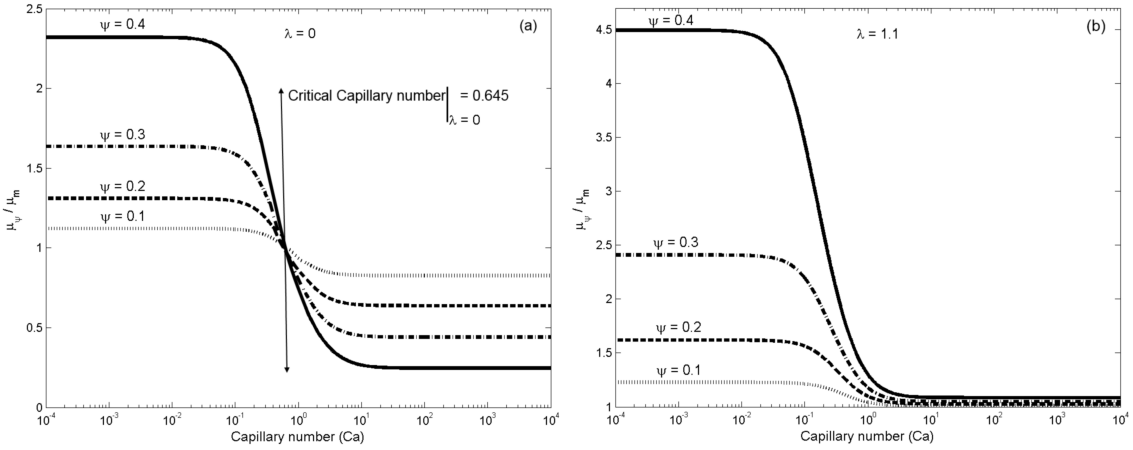

Figure 3.5: Relative viscosity, $f^{\mu} = \mu_{\psi}/\mu_m$, as a function of capillary number for different particle concentrations calculated with (3.54) for a system where (a) the viscosity ratio is zero (bubbly emulsion) and, (b) the viscosity ratio is $\lambda = 1.1$. Our model predicts that a critical capillary number exists only when the viscosity ratio $\lambda < 1$, while for emulsions with $\lambda > 1$, the effective viscosity is greater than that of the ambient fluid for all Ca.

($f^{\mu} > 1$), and its value increases with particle concentration. At higher capillary numbers an opposite trend is captured where the relative viscosity is smaller than one ($f^{\mu} < 1$), and higher particle concentration leads to lower relative viscosity. All curves intersect at a critical capillary number where the viscosity of the system is independent of particle concentration, and is equal to the viscosity of the matrix ($f^{\mu} = 1$). This behavior does not exist for the system shown in Fig. 3.5(b), where the viscosity of the matrix is slightly smaller than that of the dispersed phase ($\lambda = 1.1$). In this case, the relative velocity is greater than one ($f^{\mu} > 1$) over the entire range of capillary number. At small capillary number, the force associated with capillary stresses controls the resistance against deformation, and a higher particle concentration (greater surface area) results in a greater macroscopic shear viscosity for the emulsion. At high capillary number, the resisting force against deformation is mostly controlled by shear stresses (Fig. 3.5(b)). As a consequence, introducing more particle does not significantly affect the overall viscosity of the emulsion.

Interestingly, the relative viscosity is more sensitive to the capillary number in the intermediate regime (Fig. 3.5(b)), and this sensitivity is enhanced at higher particle concentration. It suggests that shear thinning occurs dominantly when $0.1 < Ca < 1$, and that the reduction in viscosity is greater at higher particle concentration. Zinchenko *et al.* (2003) observed a similar behavior for $\lambda = 1$ using a hybrid approach between a boundary integral method and a multi-pole approach.

The relative viscosity of emulsions behaves differently for different combinations of the viscosity ratio and capillary number at a given particle concentration. This interesting behavior captured by Eq. (3.54) is demonstrated in Fig. 3.6(a-b). These results suggest that the capillary number does not have a comparable effect on the dynamics of the problem over the entire range of viscosity ratio. At low viscosity ratio ($\lambda < 10^{-1}$), the effect of the capillary number remains constant and then increases gradually until it reaches unity viscosity ratio ($\lambda = 1$) at which the capillary number exerts the greatest influence on the viscosity of the emulsion (maximum possible shear thinning). For viscosity ratios $\lambda > 1$, the effect of the capillary number decreases. At high viscosity ratio ($\lambda > 10^{3}$), the capillary number plays a negligible role on the rheology of emulsions (Fig. 3.6(a-b)). In addition,

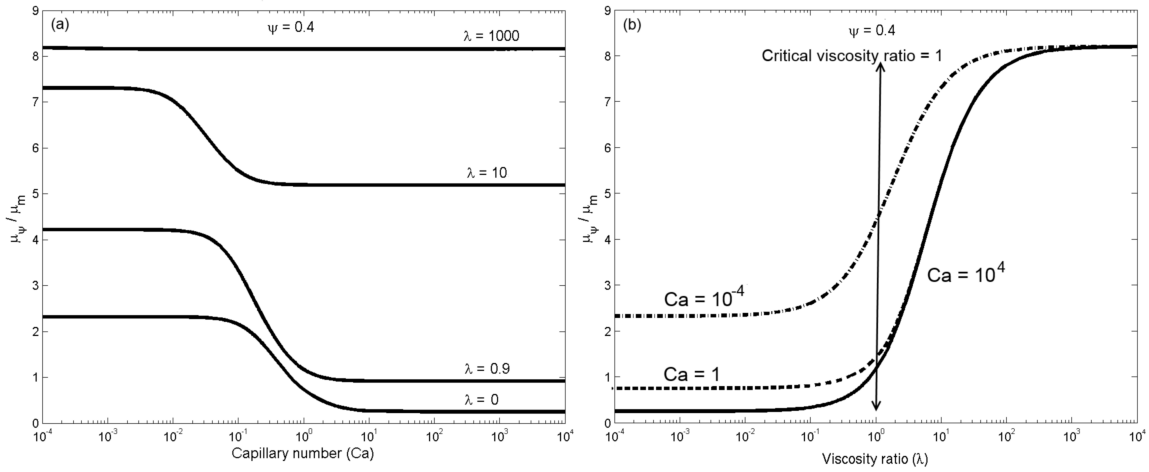

Figure 3.6: The effect of the capillary number and viscosity ratio on the relative viscosity at a constant particle volume fraction $\psi = 0.4$; (a) shows that increasing the viscosity ratio results in an increase in relative viscosity up to a point ($\lambda > 10^3$) beyond which increasing viscosity ratio does not affect the relative viscosity. Also the sensitivity of the shear thinning behavior to viscosity ratio first increases from zero to unity, and then as viscosity ratio increases the shear thinning behavior decreases. The shear thinning behavior vanishes for systems where $\lambda > 10^3$. (b) shows the effect of the capillary number in different viscosity ratios. We observe that the effect of the capillary number on the relative viscosity is maximum around the critical viscosity ratio, and decreases as the viscosity ratio increases.

at $\lambda > 10^3$, the relative viscosity of emulsions for a given particle volume fraction does no longer depend on the viscosity ratio. This effect is clearly depicted in Fig. 3.6(b). It suggests that when the shear viscosity of the dispersed phase is much greater than that of the matrix, the deformation of the particle is no longer controlled by surface tension (and consequently the capillary number). Under these conditions, the physical property that acts to keep the particle's shape spherical is the shear viscosity of the dispersed phase.

For solid suspensions, $\lambda \to \infty$, of elastic particles (Hookian particles), the deformation is controlled by the Weissenberg number. The rheological behavior of these concentrated suspensions is also obtained by applying the fixed volume DEM theory along with the second volume correction to account for the geometrical constraint described by Eq. (3.39). This leads to

$$f^{\mu}\left(\frac{1-\frac{3}{2}Wi^2(f^{\mu})^2}{1-\frac{3}{2}Wi^2}\right)^{-\frac{5}{4}} = \left(\frac{\psi_t-\psi}{\psi_t(1-\psi)}\right)^{-\frac{2.5\psi_t}{1-\psi_t}}, \tag{3.55}$$

which is a non-linear equation in terms of the relative viscosity, f^{μ}. As expected, the relative viscosity of a suspension including Hookian solid particles increases as more particles are fed to the system. At a fixed particle volume fraction, when the Weissenberg number increases (i.e. particles deform), shear thinning behavior occurs. The shear thinning behavior decreases as the particle shear modulus increases, and at $G \to \infty$ the suspension behaves like a Newtonian fluid. It is also worth mentioning that $Wi = 0.816$ calculated based on Eq. (3.55) is a critical Weissenberg number at which the shear viscosity of the deformable solid suspensions is independent of the particle volume fraction, and it is equivalent to the shear viscosity of the matrix.

3.5 Regime diagram

The macroscopic responses of emulsions to shear, and more specifically the role of λ and Ca observed in Figs. 3.5 and 3.6, suggest that there should be a set of critical numbers that controls transitions in the behavior of the relative viscosity. Based on Eq. (3.54), we can deduce that a critical capillary number, Ca_{cr}, at which the viscosity of the emulsion is identical to that of the matrix and hence is independent of the particle volume fraction satisfies

$$\mathcal{N} + \mathcal{M}\kappa Ca_{cr}^2 = 0. \tag{3.56}$$

Equation (3.56) has a real and physical root only in cases where $\mathcal{M} < 0$, owing to the fact that $\mathcal{N}$ and κ are always positive. For a bubbly emulsion, $\lambda \to 0$, the critical capillary number is found to be 0.645 (Fig. 3.5(a)), while for a complex fluid where $\lambda \geq 1$, the relative viscosity is always a function of the particle concentration. In other words, there is no critical capillary number for such system (because $\mathcal{M} > 0$) as depicted in Fig. 3.5(b). Thus, the presence of the critical capillary number strongly depends on the viscosity ratio between the two phases which controls the sign of the parameter $\mathcal{M}$. Following this assertion, we define the critical viscosity ratio λ_{cr} such that $\mathcal{M}(\lambda_{cr}) = 0$. Therefore, the critical viscosity ratio satisfies

$$\lambda_{cr}^3 + \lambda_{cr}^2 - \lambda_{cr} - 1 = 0, \tag{3.57}$$

which has only one real physical root, $\lambda_{cr} = 1$. For $\lambda < \lambda_{cr}$ a critical capillary number exists and consequently a behavior similar to that shown in Fig. 3.5(a) will be expected. For a viscosity ratio greater than λ_{cr}, the behavior of the complex fluid (the relation between the relative viscosity, capillary number and the particle concentration) will be similar to that displayed in Fig. 3.5(b). Note that the critical viscosity ratio and capillary numbers are independent of the particle volume fraction.

We summarize the prediction of our rheological model for the relative viscosity of emulsions as function of the viscosity ratio λ and capillary number Ca in a regime diagram in Fig. 3.7. This regime diagram includes three regions A, B & C, which are delimited by the critical numbers discussed above. In the region where the viscosity of the dispersed phase is greater than the viscosity of the matrix (region A in Fig. 3.7 where $\lambda > \lambda_{cr}$), the viscosity of the emulsion is always greater than the viscosity of the matrix for any given particle concentration. In this region of the diagram, the high viscosity of the dispersed phase generates a resisting stress that balances the shear applied on the surface of the particles. We note that increasing the volume fraction of particles results in an increase in the effective viscosity of the emulsion.

As the viscosity ratio of the emulsion decreases below the critical viscosity ratio $\lambda_{cr} = 1$, two opposite scenarios emerge for the relative viscosity depending on the capillary number. When the capillary number is smaller than its critical value Ca_{cr} (region C in Fig. 3.7 where $\lambda < \lambda_{cr}$ and $Ca < Ca_{cr}$), the viscosity of the emulsion is greater than the viscosity of the matrix. The large capillary stresses between the two phases strongly oppose particle deformation. On the other hand, when the capillary number increases beyond its critical value (region B in Fig. 3.7 where $\lambda < \lambda_{cr}$ and $Ca > Ca_{cr}$), the viscosity of the emulsion is lower than the viscosity of the matrix. This reduction is more pronounced as more particle are fed to the system (see Figs. 3.5(a) and 3.7). This shear thinning behavior results from the accommodation of most of the induced shear stress by low viscosity and deformable particles. Finally, considering a viscosity ratio smaller than λ_{cr} and a capillary number equals to that of determined by Eq. (3.56) for that specific viscosity ratio ($Ca = Ca_{cr}\,|_{\lambda}$), the viscosity of the emulsion is identical to the viscosity of the matrix regardless of particle

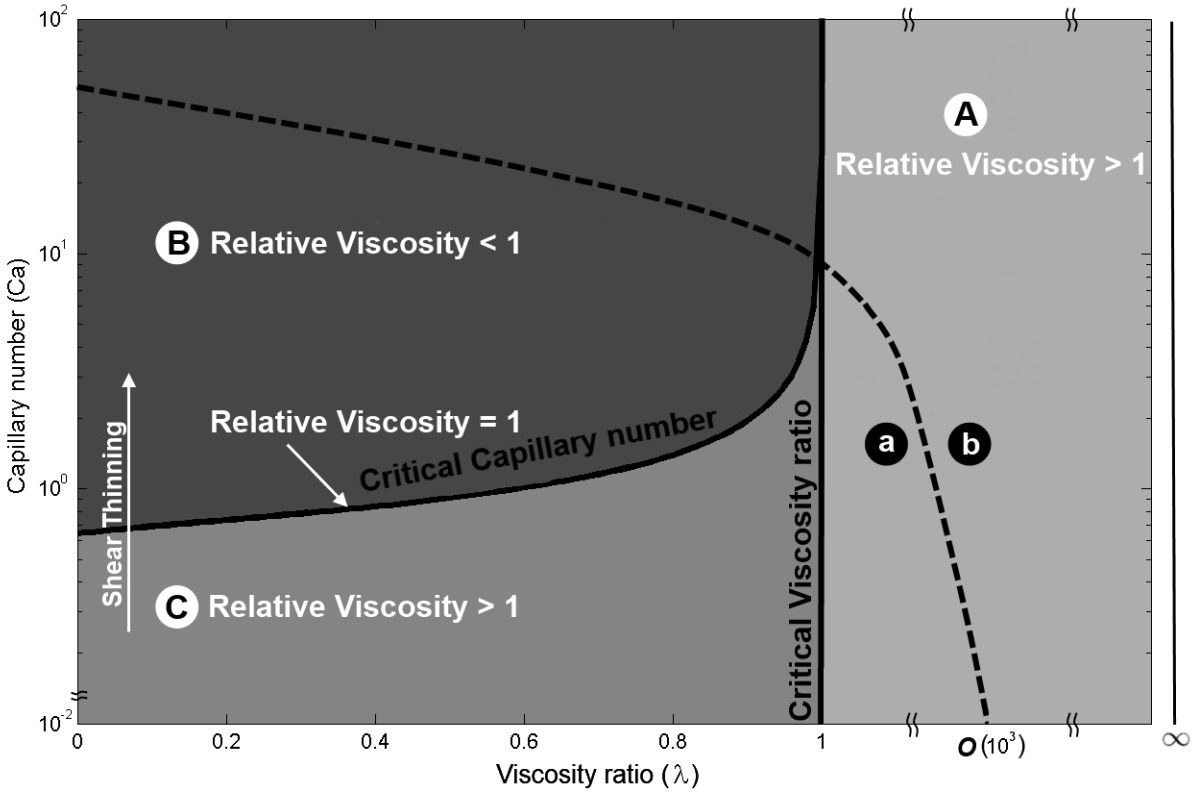

Figure 3.7: A regime diagram constrained by the critical viscosity ratio (λ_{cr}) and critical capillary number (Ca_{cr}) shown by solid lines. In region A, where the viscosity ratio is bigger than λ_{cr}, the relative viscosity is always greater than unity. While at smaller viscosity ratio ($\lambda < \lambda_{cr}$), regions B & C, there is a critical capillary number determined by Eq. (3.56) at which a transition in the macroscopic rheological behavior occurs. Right at Ca_{cr}, the relative viscosity is always unity and is independent of the particle volume fraction. In region C, where $Ca < Ca_{cr}$ the relative viscosity is greater than unity, whereas at $Ca > Ca_{cr}$ the shear viscosity of the emulsion becomes lower than that of matrix (region B). The dashed line separates regions where different parameters control the stress partitioning between the matrix and particles, and the shape of the fluid particles (deformation), surface tension in region ⓐ and shear viscosity of the dispersed phase in region ⓑ.

concentration. From Fig. 3.7, we can also observe the limiting behavior of the relative viscosity at $\lambda = \lambda_{cr}$ and $\gamma \to 0$ where the two phase fluid flow actually reduces to a single phase flow. In this scenario, the shear viscosity of the emulsion is independent of the particle concentration and morphology, and hence the critical capillary number approaches infinity.

This regime diagram can be interpreted differently by highlighting four regions as shown in Fig. 3.8. The solid lines that delimit these regions represent transitions in the general rheological behavior (Newtonian or non-Newtonian) of emulsions. In region ①, the resistance to deformation of fluid particles is controlled by surface tension, γ. According to Fig. 3.5, at $Ca \ll 1$ where the capillary stresses are important, an increase in the viscosity of the emulsion is expected. Therefore, at low capillary numbers (region ①), emulsions behave like a Newtonian fluid, i.e. the shear dynamic viscosity of the emulsion is independent of the strain rate for a given particle volume fraction. When the capillary number increases beyond Ca_{cr}, the emulsion displays a non-Newtonian behavior indicated by region ② in Fig. 3.8. This implies that an increase in the strain rate leads to a decrease in the viscosity of the emulsion). We observe that the range of capillary number over which shear thinning occurs is the broadest at $\lambda = 0$, and decreases as the viscosity ratio increases. However, it is worth mentioning that for a given particle volume fraction the amount of viscosity reduction due the shear thinning is the greatest at $\lambda = \lambda_{cr}$. This range shrinks gradually when the viscosity ratio decreases, and it also decreases significantly as the viscosity ratio increases beyond λ_{cr} as illustrated in Fig. 3.6.

In regions ③ and ④ of Fig. 3.8, the resisting force against deformation is dominated by the shear viscosity of the dispersed phase which tends to keep the particle spherical regardless of surface tension. Therefore, the viscosity of emulsions in these region strongly depends on the viscosity ratio and particle concentration. Region ③ is characterized by a Newtonian behavior for emulsions, however it has lower shear viscosity than that obtained in region ①. In the portion of region ③ where the viscosity ratio is smaller than λ_{cr} (which belongs to the region B in Fig. 3.7) the resisting forces imposed by both surface tension and the viscosity of the dispersed phase are small compared to the external shear force exerted by the ambient fluid. As a results, particles deform and align with the flow direction. Owing

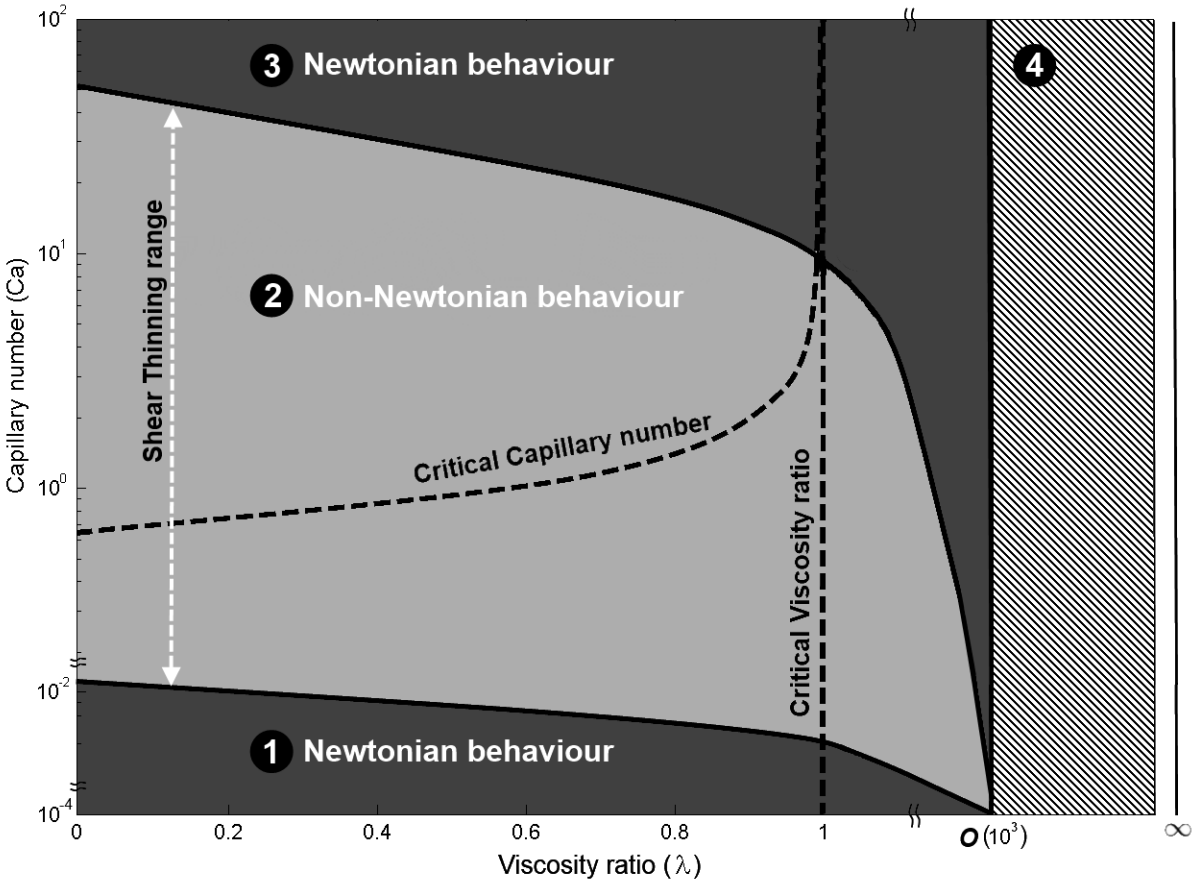

Figure 3.8: Same regime diagram highlighting four regions that distinguish different rheological responses for emulsions. In region ①, where the capillary stresses between two phases are important, an increase in the viscosity of the emulsion is expected, and emulsions behave like Newtonian fluid. Region ② illustrates the shear thinning behavior that occurs when the capillary number at a given viscosity ratio is increased. The largest shear thinning occurs at $\lambda = 1$. Region ③, where the resistance force against deformation is dominated by the shear dynamic viscosity of the dispersed phase, is characterized by a Newtonian behavior for emulsions. However, it has lower shear viscosity than that obtained for the region ①. The hatched area (region ④) represents a region where the value of the relative viscosity is independent of both capillary number and viscosity ratio and behaves like a Newtonian fluid.

to the smaller viscosity of the dispersed phase, as the particle volume fraction increases, the shear viscosity of emulsions decreases (see Fig. 3.5(a)). Thus in this portion of the regime diagram, the relative (Newtonian) viscosity is smaller than unity. However, for parts of the region ③ that belong to region A in Fig. 3.7 ($\lambda > \lambda_{cr}$), the relative (Newtonian) viscosity is greater than unity.

The hatched area (region ④ in Fig. 3.8) represents a region where the value of the relative viscosity is independent of both capillary number and viscosity ratio (Fig. 3.6(b)), and emulsions behave macroscopically like Newtonian fluids. Beyond a viscosity ratio of $O(10^3)$, the viscosity of emulsions is only controlled by the volume fraction of particles (e.g. it will be roughly 8.2 and 3.4 times greater than the viscosity of the matrix for fluid particle concentrations of $\psi = 0.4$ and $\psi = 0.3$, respectively). Mathematically, for the hatched region we have

$$\lim_{\lambda \to \lambda \geq O(10^3)} \mathcal{M} \simeq \lim_{\lambda \to \lambda \geq O(10^3)} \mathcal{N} \to 2.5, \tag{3.58}$$

consequently, the non-linear part of Eq. (3.54) vanishes, and the expression to estimate the relative viscosity of emulsions becomes

$$f^{\mu} \approx \left(\frac{\psi_t - \psi}{\psi_t (1 - \psi)} \right)^{-\frac{2.5\psi_t}{1-\psi_t}} \tag{3.59}$$

which is similar to the relative viscosity of a suspension of rigid spherical particles in (3.49).

It is important to stress that for an emulsion possessing a viscosity ratio exactly equal to λ_{cr}, the model presented here diverges because $\mathcal{M}(\lambda_{cr}) = 0$. Thus, we consider two emulsions of viscosity ratios $\lambda = \lambda_{cr} + \varepsilon$ and $\lambda = \lambda_{cr} - \varepsilon$, where ε is an arbitrary small number. We then determine the relative viscosity of the emulsion by matching solutions in the limit where $\varepsilon \to 0$.

Our model for the rheology of emulsions ($\lambda < \infty$) or suspension ($\lambda = \infty$) relies on our choice for the maximum random close packing ψ_t. For slightly deformable particles (up to the first order of deformation) we expect ψ_t to deviate slightly from its value for the random close packing of spherical particles. In the majority of published models for monomodal complex fluids, ψ_t has been used as a fitting parameter. ψ_t must be a function of particle

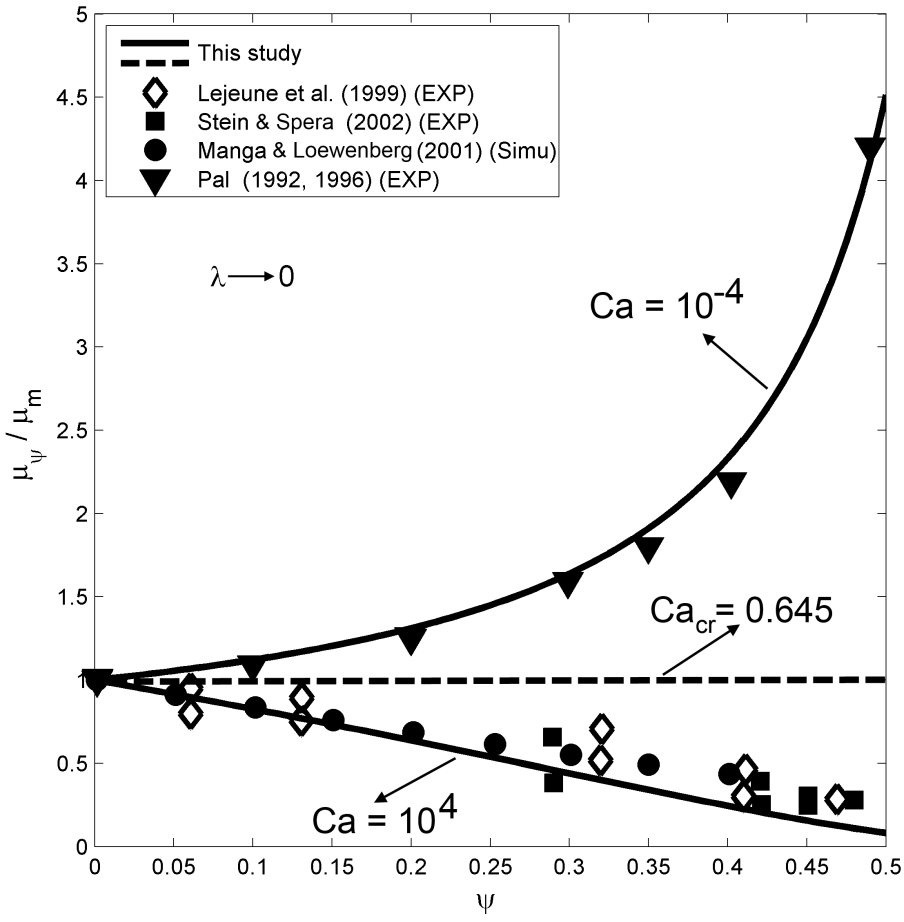

Figure 3.9: Comparison between our model and published experimental and numerical data for the rheology of bubbly emulsion ($\lambda \to 0$) over a range of volume fraction. The comparison is performed for two bounding values of the capillary number representing emulsions including non-deformable fluid particles (small capillary number) and deformable fluid particles (large capillary number) using Eq. (3.54). The dashed line represents the relative viscosity versus particle volume fraction for a bubbly emulsion at $Ca = Ca_{cr}$.

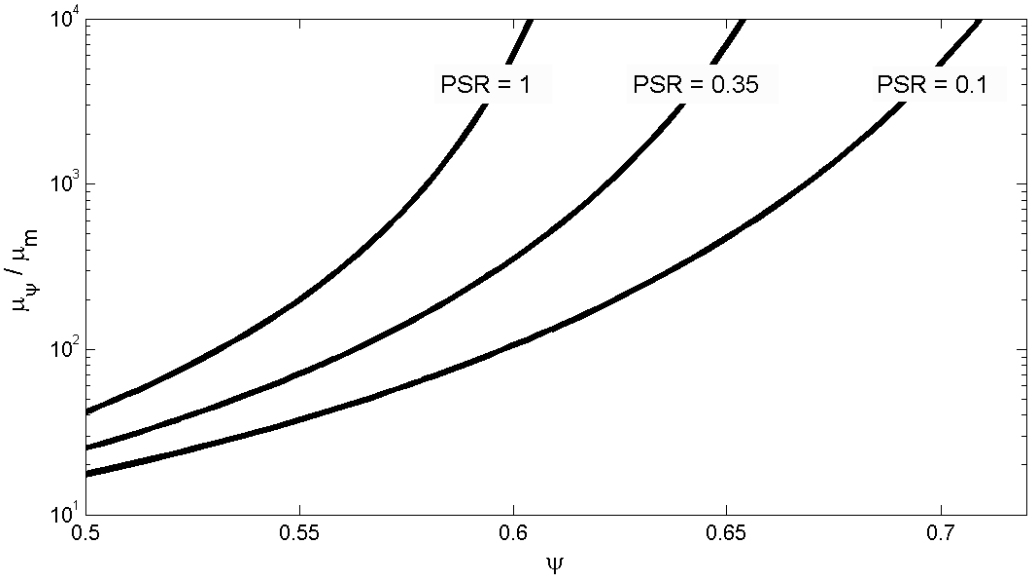

Figure 3.10: Relative viscosity versus solid phase concentrations and particle size ratio (PSR) for bimodal systems obtained from Eq. (3.49). The maximum packing is computed from Eq. (3.60) where it is assumed that the fraction of the small size particles is 25%.

shape, size distribution and dynamical conditions (order of deformation). However, for monomodal spherical particles undergoing no or small deformation, which is assumed to be the case here, it should remain mostly constant. We test this hypothesis by comparing the predictions from our model, Eq. (3.54) with the experimental and numerical data published in Lejeune & Richet (1995); Stein & Spera (2002); Pal (2004) and Manga & Loewenberg (2001) in Fig. 3.9 . These datasets for bubbly emulsions ($\lambda \to 0$) provide useful test for our model in the limit of non-deformable ($Ca = 10^{-4}$) and highly deformable bubbles ($Ca = 10^4$). As shown in Fig. 3.9, both limits are successfully modelled by our model Eq. (3.54) using a fixed maximum packing $\psi_t = 0.637$, corresponding to the random close packing of uniform spherical particles. The model developed by Pal (2003a) (model 4) fits these datasets with a varying maximum random packing limit that increases significantly with Ca (ψ_t is changed from 0.54 to 0.7). In Fig. 3.9, we also show the relative viscosity of bubbly emulsion predicted by our model at Ca_{cr} to highlight the transition in the rheological behavior across $Ca = Ca_{cr}$, and the fact that at $Ca = Ca_{cr}$ the relative viscosity is independent of particle concentration.

3.6 Poly-disperse complex fluids

Providing a theoretical value for ψ_t in poly-disperse emulsions/suspensions is more challenging because the void space between large particles can be filled by smaller particles. This causes ψ_t to reach a higher limit in poly-disperse complex fluids. Therefore, we expect to observe lower effective viscosities in poly-disperse suspensions/ emulsions compared to monomodal systems for a given volume fraction (below ψ_t). For a poly-disperse system (with a wide range of particle sizes), the particle size distribution and the particle size ratio have significant impact on the rheological behavior of the system. The greatest effect of polydispersity occurs when the modality is changed from monomodal to bimodal, subsequent modality changes have lesser influences on rheology (Farris, 1968).

Experiments on bimodal suspensions reported by Chong *et al.* (1971) at constant fraction of smaller size particles revealed that the effective viscosity decreases as the size ratio of spheres (small to large) decreases. They also showed a negligible reduction in the shear viscosity when the particle size ratio decreases below 0.1 (Chong *et al.* , 1971; Stickel & Powell, 2005). For bimodal suspensions of any size ratio, the largest fraction for the random close packing (and hence the minimum relative shear viscosity) in a fixed volume of total particles occurs when suspensions consist of 65% to 80% large particles, or in other words, 20% to 35% of the total particle volume fraction is made of small particles (Stickel & Powell, 2005). Quemada (1977) discussed that for a highly poly-disperse complex fluids ψ_t approaches unity, because the broad distribution of particle sizes decreases the void ratio to a negligible value. It is important to stress that, using poly-disperse size distribution, we can produce an emulsion/suspension possessing a fixed shear viscosity but with various amount of particles. For example, in a bimodal suspension, the particle concentration can be increased while maintaining the shear viscosity fixed by varying the size ratio. This is illustrated in Fig. 3.10 where we compare the relative viscosity for two bimodal suspensions possessing particle size ratio of $PSR = 0.35$ and $PSR = 0.1$ and containing 25% of small particles with a monomodal suspension ($PSR = 1$). The maximum packing for these

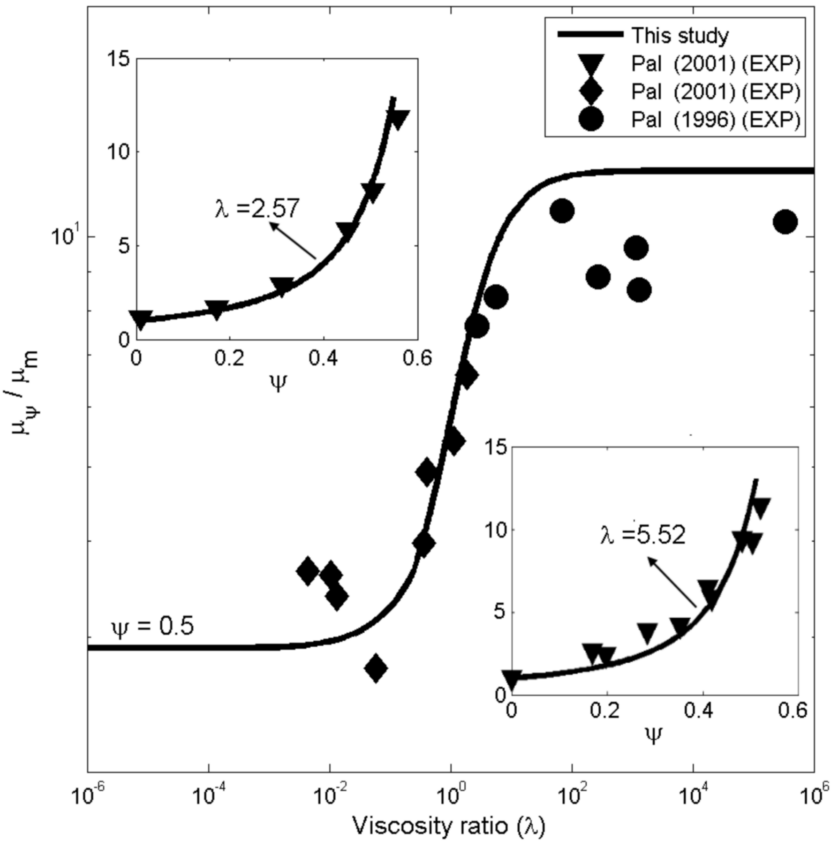

Figure 3.11: Comparison between experimental data and our model in (3.54) at $\psi = 0.5$, $Ca \to 0$ and assuming $\psi_t = 0.9$ for the maximum packing of poly-disperse emulsions. The two insets also show how the relative viscosity of poly-disperse emulsions varies as function of volume fraction for two different viscosity ratios at $Ca \to 0$.

bimodal systems are estimated with the experimental correlation (Chong *et al.* , 1971)

$$\psi_t^b = \psi_t \left(\frac{R_p^s}{R_p^l} \right)^{-0.104}, \tag{3.60}$$

where ψ_t^b denotes the estimated critical fraction for a bimodal system, and R_p^s and R_p^l are the radius of the smaller and larger particles respectively. Other models for the maximum close packing of bimodal systems with different size ratios and fraction of sizes have been published recently and can be used alternatively (Qi & Tanner, 2012; Brouwers, 2013). The maximum attainable packing for bimodal systems is around 0.869, which occurs when the size ratio (small to large) approaches zero. Therefore, we expect that the maximum random close packing can be even higher than 0.869 for poly-disperse systems involving

a broad range of particle sizes where the smaller particles fill void spaces between larger particles. In Fig. 3.11, we use our rheological model for monomodal particles Eq. (3.54) and test it against experimental data provided for poly-disperse emulsions at $Ca \ll 1$. For this comparison, we use $\psi_t = 0.9$ in Eq. (3.54) and plot the results from the model against experimental data over a wide range of viscosity ratio and particle volume fraction. For example, the experiments associated with $\lambda = 5.52$ (inset of Fig. 3.11), was conducted with particle sizes ranging from 1 μm to 24 μm (Pal, 2001).

While our model, in the limit of $Ca \ll 1$, provides satisfying approximation of the rheology of poly-disperse emulsions by considering a corrected maximum packing limit, a more rigorous account of poly-disperse dynamics is required to find more accurate results, and extend the model to predict the relative viscosity of poly-disperse emulsions at ($Ca \gg 1$). Chapter 5 explores the effect of polydispersity in more details, and provide a theoretical mean to compute the effective viscosity of poly-disperse and more specifically bimodal suspensions of spherical particles.

CHAPTER IV

THE COMPLEXITY OF CONCENTRATED SUSPENSIONS

4.1 Introduction

As discussed in the previous chapters and in more details in the reviews by Stickel & Powell (2005); Morris (2009); Denn & Morris (2014); Kalyon & Aktas (2014), microstructures and their evolution and rearrangement during flow are the main causes for the non-Newtonian behavior of suspensions. Ness & Sun (2015) also showed that the transitions between rheological regimes originate from microscopic phenomena, such as the contribution of lubrication forces and interparticle forces. For example, Mari *et al.* (2014) explored the effect of frictional contact forces, and demonstrated that considering friction at particle contacts reduces the threshold packing limit and leads to shear thickening. The reason for this phenomenon is that in concentrated suspensions, under high shear rates, more contacts are formed which leads to a transition from a mostly friction-less to a mostly frictional rheology (Mari *et al.* , 2014; Pan *et al.* , 2014). However, shear thickening behavior is observed less frequently for suspensions because of two main reasons: (i) the relative importance of different stress scales that might be higher for particle interactions than that of confining stress scale, and thus shear thinning is dominant, and (ii) the range of parameter space and volume fraction of particles over which shear thickening occurs is small, and rarely covered by experiments (Brown *et al.* , 2010). Brown & Jaeger (2014) recently reviewed the common physical properties of suspensions exhibiting shear thickening, and discussed different approaches that have been proposed to describe these phenomena.

In this chapter, the most apparent processes that are known to cause shear thinning behavior in suspensions of solid particles are discussed.

4.2 Particle size distributions

The rheological models listed in Table 2.1 are originally derived for dense suspensions of mono-disperse rigid spherical particles. Industrial suspensions, e.g., ceramic and cement and natural suspensions, e.g., crystal-bearing magmas are polydisperse and include generally a broad distribution of particle sizes. Therefore, one needs to correct for the threshold packing limit in order to account for the effect of particles size ratio and size distribution (Kansal *et al.* , 2002; Spangenberg *et al.* , 2014; Shewan & Stokes, 2014; Zhang *et al.* , 2015a). As discussed in section 3.6, the most significant effect of polydispersity on suspension viscosity appears when the modality is changed from monomodal to bimodal, and the subsequent modality alterations have lesser influence (Farris, 1968). As a consequence, one may assume, as a first order approximation, that the effect of polydispersity with a narrow size distribution on the effective viscosity can be described with bimodal models.

In general, there are two distinct methods to introduce the effect of polydispersity into rheological models. In the first approach, the threshold packing corresponding to the bimodal (or poly-disperse) suspension, namely ψ_t^b, is substituted into the monomodal rheological stiffening function, e.g., the model proposed in chapter 3, which leads to,

$$\mu_r(\psi) = \left(1 - \frac{1-\psi_t^b}{\psi_t^b}\frac{\psi}{1-\psi}\right)^{-[\eta]\left(\frac{\psi_t^b}{1-\psi_t^b}\right)} . \tag{4.1}$$

This approach is straightforward and works properly in many cases (Chang & Powell, 2002; Marti *et al.* , 2005). However, it is not general and does not account for the underlying physics governing the rheological behavior of bimodal (or polydisperse) suspensions. For instance, the effect of mutual crowding due to the interference between different particle size classes is overlooked (Mooney, 1951; Farr, 2014).

The second method aims at incorporating some of the physics associated with the mutual crowding that takes place between the two size classes specifically at high volume fraction of particles. This approach is broken up into two categories of models. The first one relies on the assumption that the particle sizes do not interfere ($\zeta \to \infty$ where ζ denotes the particle size ratio), which in other words means that smaller particles are fully crowded in the interstices formed by large particles. The viscosity of these bimodal suspensions is then

calculated as the product of the viscosity of two monodisperse suspensions (Mooney, 1951; Farris, 1968). Therefore, the relative viscosity of bimodal suspensions of non-interfering sizes ($\zeta \to \infty$), namely μ_r^b reads as,

$$\mu_r^b(\psi_l, \psi_s) = \mu_r(\Psi_1)\, \mu_r(\Psi_2), \tag{4.2}$$

where μ_r represents the monomodal stiffening function (models reported in Table 2.1), and

$$\Psi_1 = \psi_l, \quad \Psi_2 = \frac{\psi_s}{1 - \psi_l}, \tag{4.3}$$

in which $\psi_l = V_l/V_t$ and $\psi_s = V_s/V_t$ refer to the actual volume fraction of the large and small particles, respectively. V_s and V_l also refer to the volume of small and large particles, respectively, and V_t is the total volume of the suspension.

The second category of models, developed in this thesis and discussed in chapter 5, accounts for the behavior of suspensions with particles having interfering size ratios (particles of comparable sizes possessing $1 \leq \zeta \leq 7$) through a mutual crowding factor, defined as a measure of dead and excess fluid, to constrain the rheological response of bimodal systems.

4.3 Particle shape

One of the most complex challenge to construct a predictive rheology model is related to the textures of suspended particles. In many industrial applications and natural suspentions particles are rarely spherical and display a broad range of aspect ratios. For non-spherical particles, the study of interparticle forces and hydrodynamic interactions becomes more complicated (Brenner, 1974; Kerr & Lister, 1991). At a given volume fraction, non-sphericity increases the effective viscosity of suspensions when compared to spherical particle suspensions (Goldsmith & Mason, 1962; Ganani & Powell, 1985). In addition, the imposed flow field significantly affects the rheology of suspensions of anisometric and irregular particles because they can orient with the imposed flow Coussot (2014); Rosén *et al.* (2015); Philippe *et al.* (2013). The viscosity of suspensions of non-spherical particles is also more shear dependent due to an increase in the range between the very loose random packing at low shear rate, ψ_t^0, and the highest attainable packing fraction at high shear rate, ψ_t^∞. Interlocking between particles occurs at smaller volume fractions when the aspect ratio

of crystals departs from unity, and a finite yield stress exists over a wider range of particle volume fraction (see Fig. 2.2).

Several investigations have been devoted to suspensions of spheroids to simulate and approximate the effective viscosity of suspensions of non-spherical particles (Claeys & Brady, 1993c; Boek *et al.* , 1997; Bicerano *et al.* , 1999; Phan-Thien & Pham, 2000). In these studies, spheroids have been chosen to study non-spherical particles, because of the existence of analytical solutions in the dilute regime (Jeffery, 1922; Cox, 1970; Mackaplow & Shaqfeh, 1996; Kachanov & Abedian, 2015) and the fact that a wide range of shapes can be parameterized with a single factor, the aspect ratio $r_p = b/a$, where a and b are the equatorial and polar radii, respectively. The shape of particles affects the value of the intrinsic viscosity and the threshold packing limit (Wildemuth & Williams, 1984; Wouterse *et al.* , 2007).

It is shown that these two parameters are interrelated, and one needs to study them separately to quantify their dependence on the particle aspect ratio. The effect of particle shape is thoroughly discussed in Chapter 6, where a new model is presented to characterize how particle shape influences the rheology of suspensions.

4.4 Particle deformation and breakage

Another plausible explanation for shear thinning is the deformation of particles in the suspension. When elastic or viscoelastic particles, that are spherical in a stress-free state, are in a suspension, deformation and orientation of particles introduce additional stresses in the suspension. These additional stresses cause a non-linear behavior even in dilute suspensions. Goddard & Miller (1967) and Roscoe (1967) have proposed rheological models for the rheology of dilute suspensions of elastic and viscoelastic particles to a first order approximation for the particle deformation. For a dilute suspension of solid-like elastic particles (obeying Hooke's law) under simple shear flow conditions, the equation of Goddard & Miller (1967), modified to account for the volume correction defined in chapter 3 and to not violate the lower effective viscosity bound, reduces to,

$$\mu_r = 1 + \underbrace{\frac{2.5}{1+\frac{9}{4}Wi^2}\left[1-\frac{3}{2}Wi^2\right]}_{[\eta(Wi)]^D}\left(\frac{\psi}{1-\psi}\right), \tag{4.4}$$

where

$$Wi = \frac{\Upsilon \mu_m}{G} \tag{4.5}$$

is the Weissenberg number and G denotes the shear modulus of the elastically deformable solid particles.

Roscoe (1967) developed a model for dilute suspensions of viscoelastic particles possessing a finite viscosity μ_p that is valid only for small deformation. Modifying it to account for the preempted ambient fluid, this model under simple shear flow condition reduces to

$$\mu_r = 1 + \underbrace{\frac{2.5}{1 - \frac{9}{4}Wi^2 + Vi^2 + 3Wi \cdot Vi} \left[1 - \frac{3}{2}Wi^2 + Vi^2 + \frac{1}{2}Wi \cdot Vi\right]}_{[\eta(Wi,Vi)]^D} \left(\frac{\psi}{1-\psi}\right), \tag{4.6}$$

where,

$$Vi = \frac{\Upsilon \mu_p}{G}, \tag{4.7}$$

is a dimensionless number characterizing the viscous behavior of particles (Deborah number that measures the ability of a material to deform by viscous creep). According to Eqs. (4.4) and (4.6) developed for dilute suspensions, one can conclude that the intrinsic viscosity for purely elastic and viscoelastic particles is shear rate-dependent, and, consequently, that elastic and viscoelastic deformation of particles introduces a non-Newtonian behavior (Gao *et al.* , 2011; Avazmohammadi & Ponte Castañeda, 2015).

Particle damage and breakage may also contribute as a factor to induce shear thinning. The transient behavior of the particle size distribution changing in response to shearing, and its impact on the suspension viscosity is mostly studied in colloidal particle aggregates (Barthelmes *et al.* , 2003; Tolpekin *et al.* , 2004; Song *et al.* , 2015). Very few investigation have been conducted for non-Brownian natural suspensions where particles and their asperities might be capable of breaking at a critical imposed shear stress or shear rate. As reflected in many monomodal stiffening function (models reported in Table 2.1), the viscosity of a suspension increases with the particle volume fraction monotonically, and diverges at the jamming transition where $\psi = \psi_t$. This is a true statement if particles are rigid and the Weissenberg number is not large enough so that particles break. However,

at high Weissenberg number, the assumption of small viscoelastic or elastic deformation for particles is no longer satisfied, and particles' breakage would occur and results in shear induced modality alteration. This reduction in particle size results in widening the particle size distribution, and a treatment is required to follow and parametrize the effect of shear induced modality alteration on the shear thinning behavior of suspensions of solid particles.

4.5 Microstructural rearrangement

The development of microstructures is a complex process, and despite many investigations (Stickel & Powell, 2005; Mewis & Wagner, 2009b; Denn & Morris, 2014; Van Loon *et al.* , 2014; Zia & Brady, 2015), it remains only partially understood to this date. At low shear rates, the formation of random clustering structures are observed in dense suspensions of spherical and non-spherical particles (Lin *et al.* , 2015). Under higher shear stresses particles adopt a more efficient configuration as they start to align with the flow direction and form planar structures perpendicular to the velocity gradient. At very high shear stress, suspensions undergo disordering and dilation because of friction at particle-particle contacts, which ultimately leads to shear thickening (Brown *et al.* , 2010; Brown & Jaeger, 2014; Mari *et al.* , 2014). The influence of particle orientation is obviously more pronounced for suspensions with elongated particles (Boek *et al.* , 1997). This effect will be discussed in details in Chapter 6.

4.6 Shear induced heterogeneities

In synthetic an natural non-Brownian suspensions with complex evolving structures, shear localization, shear banding and wall-slip or, in general, spatially inhomogeneous flow regions are frequently observed under deformation (Lejeune & Richet, 1995; Forien *et al.* , 2011). Shear banding generally refers to a stress state in the system where two adjoining regions with almost identical shear stress acquire two different shear rates. This phenomenon is physically identical to the concept of failure (due to the shear localization in thin regions of around one order of magnitude larger than grain diameters) in saturated soil mechanics under simple shear or triaxial compression. For suspensions, shear banding can occur

by continuum and complex particle level mechanisms. One of the important continuum mechanisms leading to trivial shear banding is related to the geometrical setup, i.e., the stress field is inhomogeneous when the suspension is subjected to a pressure-driven flow within a pipe or two parallel plates and cylindrical couette flow. In uniform shear stress distributions, for example in planar couette flow, nontrivial shear banding occurs due to particle level mechanisms such as particle shape, orientation and distribution as well as the anisotropic network of contact forces especially at concentrated regimes. The presence of these bands cause a discrepancy between local and global rheology, especially when the suspension is subjected to shearing flow in geometries with narrow gaps. The trivial and nontrivial inhomogeneous flow regions must not be, however, confused with the concept of plug flow, e.g., the flow of Bingham fluids, where one region is flowing and the other part is stationery due to the yielding behavior. See review by Schall & van Hecke (2009), and more recently by Divoux *et al.* (2015) for a detailed description of shear banding in complex fluids.

It is also often observed that the size of particles close to the shear bands are smaller than those in the particle-rich regions which shows the role of particle breakage as one possible cause for shear banding in suspensions. Shear localization is accelerated if the systems contain a phase which is less resistant to shearing (e.g., the existence of gas bubbles in the sample under deformation). For example, consider a suspension under shearing with particle volume fraction close to the threshold packing limit, where neither particle deformation nor comminution take place. If suspensions undergo shear localization, the relationship between the shear stress and the shear rate displays a S sigmoidal shape which results from the development of shear bands where every parts slide past each other as rigid bodies. The relationship between relative viscosity and particle volume fraction, however, can not capture this behavior explicitly. The coexistance of multiple local shear rates thus disqualifies the application of homogeneous flow model to estimate a macroscopic effective viscosity for suspensions.

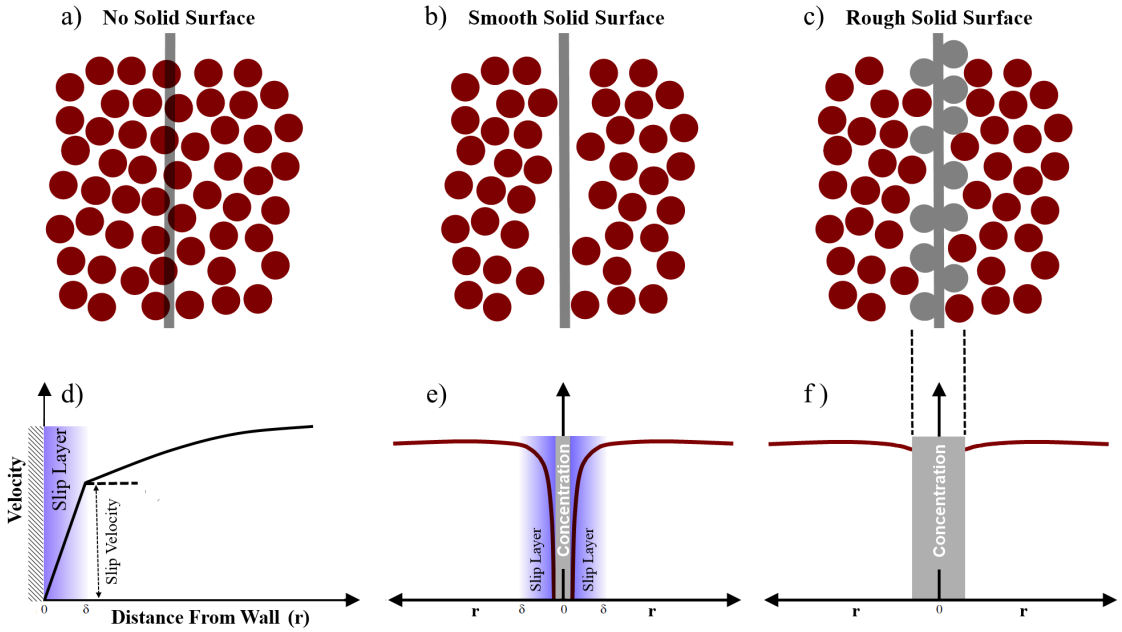

Figure 4.1: Schematic representation of the wall-slip effect. a) Packing of particles in an unbounded medium. b) Packing of particles near a smooth solid surface that causes a depletion layer with thickness, δ, close to wall. c) Packing of particles near a rough solid surface (schematically the roughness is on the order of one particle) that dramatically decreases the thickness of the depletion layer. d) A magnified look at the velocity profile versus distance from a smooth solid surface to see the sharp gradient of the velocity in the thin sheared layer depleted from particles. e) Volume fraction of suspended particles as a function of the distance from a smooth solid surface where the depletion layer is obvious. f) Volume fraction as a function of the distance from a rough solid surface that suppresses the thin sheared layer and produces a more homogeneous suspension.

4.7 Wall slippage and particle migration

Rheology models do not explicitly account for the effect of solid, confining walls in their development. At best, it is assumed that the wall acts as a stress or kinematic boundary condition (imposed strain-rate). In fact, most theoretical models assume either an infinite suspension or, in limited cases, a finite domain with fixed boundary conditions. Under natural or laboratory conditions, the viscous suspension is generally bounded either by solid confining boundaries or in some particular cases (e.g., lava flows) a free surface. Over the last three decades, the effect of solid boundaries on the flow of viscous suspensions has received more attention. More specifically, the report of unexpectedly low suspension viscosity and thixotropy in dense suspensions supports, in many cases, the occurrence of wall-slip, where a thin lubricating layer depleted in solid particles develops near the solid boundaries of the apparatus, see Fig. 4.1.

Wall-slip, categorized as a nontrivial shear localization, is actually a misnomer and refers to particle depletion at the wall, which can seriously impact stress partitioning and the effective viscosity measured during experiments. For high viscosity suspending fluids where particle-wall contacts are unlikely under most conditions, slip refers only to an apparent jump in shear rate at the wall. The layer adjacent to the wall where the shear rate can be significantly greater than that of the bulk is the slip-layer and its thickness is generally much smaller than the gap width of the apparatus. Two effects cause particle depletion at the wall. The first effect is purely geometrical (static). The presence of a straight wall breaks the homogeneity in the distribution of the dispersed phase, because particles cannot intersect the boundary (see Fig. 4.1). It creates a depleted layer over a distance comparable to the size of particles. Because the effective viscosity of the suspension increases with particle concentration, the effective viscosity of the suspension close to the wall can be significantly lower than that of the bulk, especially for dense suspensions. For this reason, any rheometer can experience slip during measurements, but the most vulnerable are those with smooth surfaces (roughness $\ll$ particle size). One way to overcome this issue is to use rheometers with roughened or milled surfaces or with vane geometries (Barnes, 1995; Buscall, 2010; Carotenuto *et al.* , 2015).

The second effect that can lead to wall-slip is dynamic and relates to the propensity of particles (even non-brownian) to migrate from high to low shear rates when shear rate gradients are present, i.e., the highly sheared regions contain less particles which in turns leads to a particle density gradient and inhomogeneity in the flow (de Cagny *et al.* , 2015). For non-deformable particles, the stresses that influence particle migration away from walls remains poorly understood because it violates the flow reversibility at low Re. Migration of spherical rigid particles has been observed experimentally by Karnis *et al.* (1966); Arp & Mason (1977); Gadala-Maria & Acrivos (1980); Hookham (1986); Leighton & Acrivos (1987) and Graham *et al.* (1991) and numerically by Spangenberg *et al.* (2012) and Yadav *et al.* (2015). These studies commonly show that there is a difference between global and local effective viscosity measurements for concentrated suspensions. Huang & Bonn (2007) explored this effect, and showed that if one accounts for the migration of particles inside the gap, local and global measurements can be reconciled.

Wall-slip can also be enhanced by gravitational settling (creaming) in suspensions (Barnes, 1995). Leighton & Acrivos (1987) proposed a model where shear-induced diffusion, normal to the plane of shear, controls particle migration. Another approach is to introduce an additional stress term in the constitutive equation for the particle pressure, and describe the migration as a response to the build-up of osmotic pressure gradient next to the solid wall (Phillips *et al.* , 1992).

Wall-slip introduces a large error into rheological measurements. The lubricating layer that forms next to the apparatus wall can be as thick as about 5 particle radii and can accommodate most of the shear in the suspension. In the most extreme case the velocity profile through the gap of the apparatus can reach that of plug flows. Buscall *et al.* (1993) and others (Barnes, 1995; Buscall, 2010) developed a simple scaling argument to estimate the error ϵ caused by wall-slip on rheological measurements that assume a homogeneous suspension,

$$\epsilon = \frac{x}{1+x} \qquad x = \frac{\mu_\Psi \delta}{\mu_m l}, \tag{4.8}$$

where δ/l is the ratio of the size of the lubrication layer to the distance that separates the plates in the rheometer.

This shows that even for high density suspension, where the slip thickness is generally at most the size of a single particle, the error can easily reach 99 % because of the contrast in effective viscosity between the bulk suspension and the suspending fluid. For example, Barnes & Carnali (1990) measured the viscosity of molten chocolate at 40 degrees C and found that wall-slip reduces the relative viscosity by up to 7 orders of magnitude at low shear stresses. In general, wall-slip can lead to a significant underestimation of the viscosity of suspensions, a parasitic effective shear thinning behavior at intermediate stresses (stresses lower than that needed to affect microstructure in dense suspensions) and finally an underestimate of yield stress in dense suspensions. Over the last few decades, the rheology community has been able to establish the conditions that are prone to lead to significant wall-slip. Those that are relevant for non-Brownian suspensions are (Barnes, 1995; Buscall, 2010)

- the suspension consists of large particles (e.g. non-brownian particles),
- a large dependence of viscosity on the concentration of the dispersed phase,
- smooth walls and small flow dimensions, and
- usually low speeds/flow rates (although centripetal artifactual effects can be seen at high speeds of rotation).

A good practice to assess the occurrence of wall-slip effects during laboratory measurements of suspension rheology is to report the character of the surface in the apparatus (rough, smooth), resort to milled surfaces when possible and repeat measurements over different gap sizes if possible, because the effect of wall-slip decreases as the ratio of the slip thickness and gap width decreases. For a detailed discussion of the processes that govern wall-slip and their effect on the measurement of suspensions rheology, readers are referred to the through review paper of Barnes (1995); Kalyon & Aktas (2014) and the book of Coussot (2005). One must consider that the presence of such shear induced heterogeneities (e.g. wall-slip and shear banding) disable the theroretical model to correctly predict the effective viscosity of complex fluids.

CHAPTER V

THE EFFECT OF BIMODALITY

5.1 Introduction

The majority of rheology studies on suspensions are conducted to quantify the relative viscosity of monomodal size distributions. However, in nature and in many industrial application, suspensions generally involve poly-disperse distributions. The relative viscosity of poly-disperse suspensions depends not only on the volume fraction of the solid phase, particle deformation and induced shear rate, but also on the particle size ratio and particle size distribution. The previous poly-disperse models (Mooney, 1951; Farris, 1968; Chong *et al.* , 1971; Shapiro & Probstein, 1992; Storms *et al.* , 1990; Poslinski *et al.* , 1988; Probstein *et al.* , 1994; Pishvaei *et al.* , 2006; Qi & Tanner, 2012; Dörr *et al.* , 2013) mostly approximate the relative viscosity based on the two approaches explained in section 4.2, which neglect the interaction between particles of different size classes. The first approach is to define a crowding factor that accounts for the interaction between different particle size classes. This idea, first introduced by Mooney (1951), remains poorly constrained. According to Farris (1968), for non-interfering particle sizes R_1 and R_2 ($R_1 \gg R_2$), the viscosity of the suspension can be written as the product of two stiffening functions, see Eq. (4.2) in section 4.2. Farris (1968) argued that by introducing a crowding factor, one could extend his model to account for the behavior of all interfering size ratios. However, to date, a theoretical model for the crowding factor and its effect on the rheology of bimodal suspensions is still missing. In this chapter, a crowding based rheological model including self-crowding and mutual crowding for bimodal particle size suspensions is developed. The crowding factor is introduced through a measure of the change in dead fluid volume in the suspension and is therefore related to the threshold packing limit. The model is valid for all bimodal suspensions with interfering size ratios ($1 \leq \zeta \leq 7$).

Note: the content of this chapter is published as:

Faroughi, S. A., & Huber, C. (2014). Crowding-based rheological model for suspensions of rigid bimodal-sized particles with interfering size ratios. Physical Review E, 90(5), 052303.

5.2 Theory for crowding based rheological model

We follow the model of Farris (1968) and the idea of Mooney (1951) to define generally the bimodal viscosity of the suspension as

$$\mu_r(\psi_l, \psi_s) = \mu_r(\psi_l)\,\mu_r(\psi_s) + \underbrace{\mu_{r_{12}}(\psi_l, \psi_s)}_{\text{crowding effect}}, \tag{5.1}$$

for interfering size ratios. We draw here a parallel between this definition of bimodal rheology and the field of probability. The crowding factor plays here a role similar to that of a conditional probability to relate the joint (probability) effect of each individual size classes to the rheology of a bimodal suspension. The crowding term is therefore a measure of the interaction between particles of different sizes and its effect decreases as the size ratio, denoted by ζ, increases. The objective here is to derive a relationship that includes the effect of crowding to predict the relative viscosity of bimodal suspensions. To this end, we first suggest a practical model to estimate the threshold or maximum volume fraction for bimodal system.

5.2.1 Bimodal maximum random close packing

Providing a theoretical value for the random close packing of bimodal systems is one of the major challenges to quantify the rheological properties of bimodal suspensions. The mechanical stability condition for monomodal sphere packing starts from the random loose packing (with the volume fraction around $\psi = 0.56$) to the face-centered cubic structure ($\psi = 0.74$). In bimodal systems, the maximum packing limit depends on the particle size ratio and individual size fractions, and, therefore, the macroscopic rheological behavior of these systems is very sensitive to these two parameters.

To quantify the effect of bidispersity on the maximum packing limit, we set up a semi-theoretical argument that will form the basis of the definition of the mutual crowding factor later on. The key aspect of the model starts with finding suitable bounds for the maximum

packing limits for a bimodal suspension where the particle size ratio approaches infinity Santiso & Müller (2002),

$$\psi^b_{M_\infty} = \min\left[\frac{\psi_t}{1-k_s}, \frac{\psi_t}{\psi_t + (1-k_l)(1-\psi_t)}\right], \tag{5.2}$$

where $k_s = \psi_s/\psi$ and $k_l = \psi_l/\psi$ represent the fraction of small and large particles, respectively (note that $\psi = \psi_s + \psi_l$ is the total solid phase volume fraction, and thus $k_s + k_l = 1$). The limits in Eq. (5.2) respectively correspond to situations where i) large particles are dominant and they reach the jamming density (small particles are crowded only in interstices), and ii) small particles dominate the suspension and jam. The two expressions in Eq. (5.2) match when the fraction of the small spheres is $k_s^M = (1-\psi_t)/(2-\psi_t)$ where both sizes produce jamming conditions. We can predict this singular point and its associated threshold packing for any finite size ratio by replacing k_s and k_l respectively by $k_s f_s$ and $k_l f_l$ in Eq. (5.2). We refer to f_s and f_l as *contracting factors*, and assume they depend only on the particle size ratio. These contracting factors account for the bed (solid plus interstices) volume contraction that occurs upon mixing different particle sizes with a fixed overall volume of solid particles. Contracting factors approach zero when the size ratio approaches unity, and approach unity when the size ratio approaches infinity. Therefore, we may assume empirically, that $f_s(\zeta) = (1-\zeta^{-1})^\alpha$ and $f_l(\zeta) = (1-\zeta^{-1})^\beta$, where ζ denotes the particle size ratio (large to small). The exponents α and β are constants that are estimated by fitting

$$k_s^M(\zeta) = 1 - \frac{f_s}{f_s + f_l(1-\psi_t)}, \quad 1 < \zeta \leq \infty \tag{5.3}$$

and its corresponding threshold packing fraction to published experimental and simulation data (Brouwers, 2013; Biazzo *et al.* , 2009; Santiso & Müller, 2002; Clusel *et al.* , 2009; Kyrylyuk *et al.* , 2010). Using this mapping procedures, we obtain $\alpha = 2.1 \pm 0.1$ and $\beta = 1.9 \pm 0.1$. In Eq. (5.3), $k_s^M(\zeta)$ expresses the fraction of the small particles at which the threshold random close packing (where the two limits converge to each other and form a cusp) occurs for a mixture of hard spheres of size ratio ζ. These points are depicted in Fig. 5.1 with black circles for different size ratios.

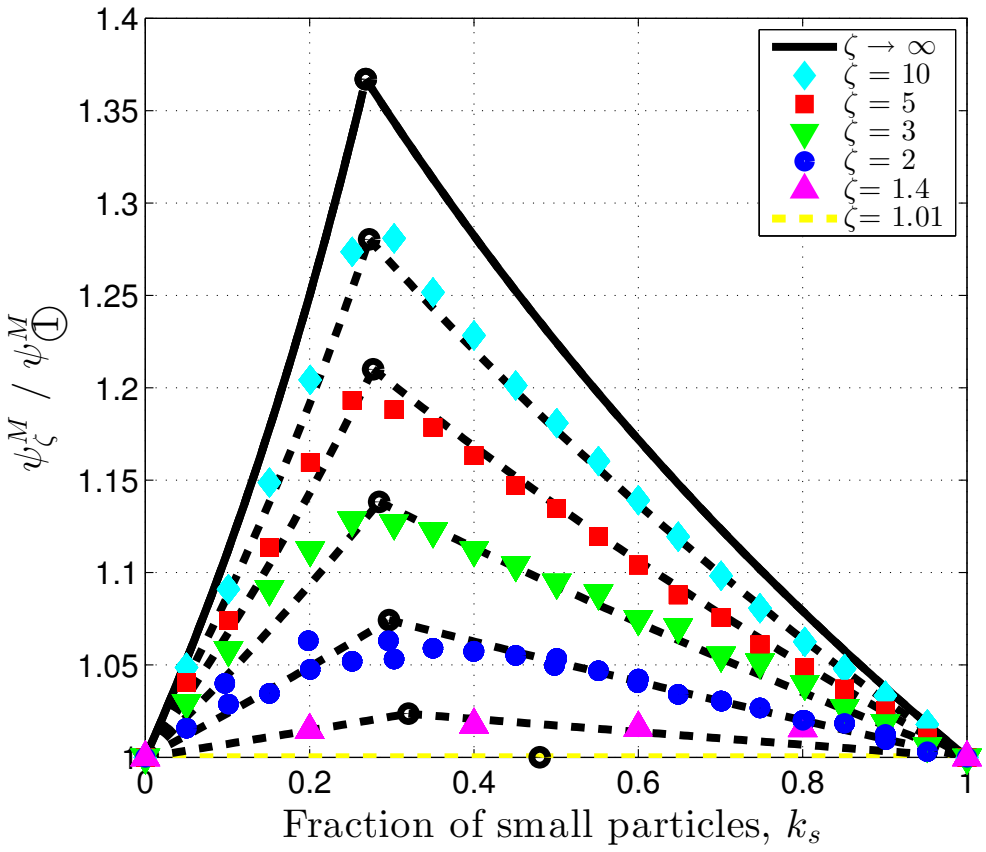

Figure 5.1: Comparison between our theory stated in Eq. (5.4) and published experimental and numerical data (Brouwers, 2013; Clarke & Wiley, 1987; Kyrylyuk *et al.* , 2010) for different values of size ratio (ζ) as indicated. Solid line shows the theoretical value of packing fraction for infinite size ratio given by Eq. (5.2); and dashed lines represent the value predicted by our model (Eq. (5.4)) using $\psi_t = 0.633$. The block circles show the required fraction of the small particles for each size ratio in order to have both sizes separately in a jammed condition.

It is interesting to note that Eq. (5.3) reduces to $(1 - \psi_t)/(2 - \psi_t)$ as the size ratio approaches infinity, while it approaches unity as $\zeta \to 1$. Bournonville *et al.* (2004); Vu *et al.* (2010) developed a model where $k_s^M(\zeta)$ approaches zero as the bidispersity vanishes, $\zeta \to 1$. More recently, Brouwers (2013) showed that for small size ratios, $\zeta \downarrow 1$, the value of $k_s^M(\zeta)$ approaches the limit of 0.5, because of the parabolic nature of random close packing in bimodal systems. The choice of this limit has a small impact on the fitting parameters α and β, but it is important to note that the relationship between the maximum packing and k_s becomes flat when $\zeta \to 1$. As a side note, we report that we tested our rheology model for bimodal suspensions (discussed later) using our packing model (Eqs. (5.3) and (5.4)) and

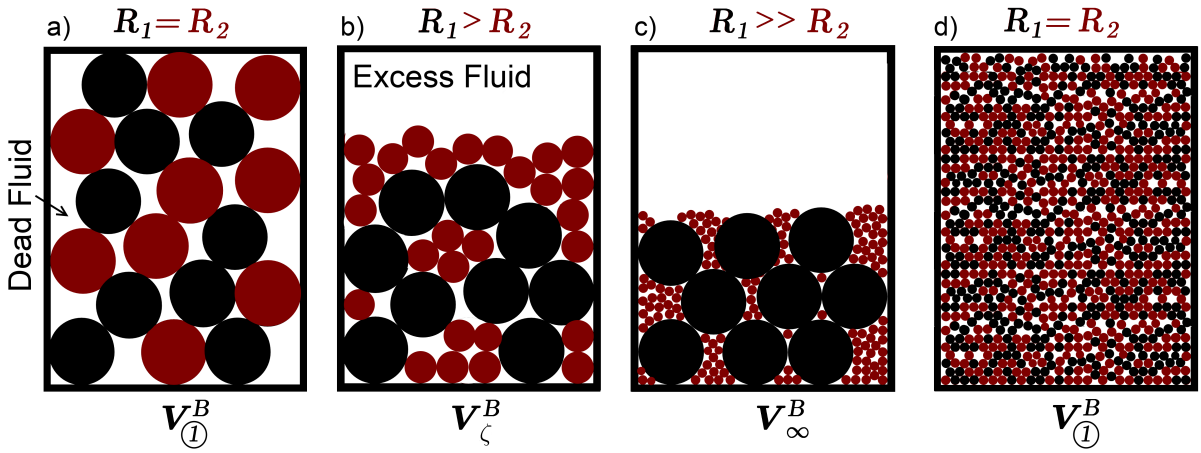

Figure 5.2: Schematic representation of the excess and dead fluid volume in different binary systems. a) A packed monomodal system of large particles with the bed volume of $V^B_{①}$, b) a binary system with a size ratio in the range of $1 < \zeta < 7$ and bed volume of V^B_{ζ}, c) a binary packed system of non-interacting particles ($\zeta \to \infty$) with the smallest possible bed volume of V^B_{∞}, d) a packed monomodal system of small particles with the bed volume of $V^B_{①}$.

compared it to the results obtained similarly but with the packing model of Brouwers (2013) at small size ratios $\zeta \downarrow 1$. We found that the discrepancy in the predicted relative viscosity remains less than a percent at small size ratios even at high volume fraction. The model of Brouwers (2013) is more accurate to predict the optimal packing of bimodal suspensions with size ratio close to unity. However, because of the limited sensitivity of the viscosity prediction to the location of the cusps at small size ratios, $\zeta \downarrow 1$, and the better performance of Eq. (5.3) over larger size ratios, we decided to proceed with Eq. (5.3) to estimate the power-law exponents α and β and establish a maximum close packing model for bimodal systems.

Consequently, one can approximate the maximum packing limit for binary systems of different ζ and k_s using

$$\psi^b_{M_\zeta} = \min[\frac{\psi_t}{1 - f_s k_s}, \frac{\psi_t}{\psi_t + (1 - f_l k_l)(1 - \psi_t)}], \tag{5.4}$$

which is plotted against some simulation and experimental data reproduced from (Kyrylyuk *et al.* , 2010; Clarke & Wiley, 1987; Brouwers, 2013) in Fig. 5.1. For normalization purpose, we used the reported value of monomodal packing of $\psi_t = 0.633$ and $\psi_t = 0.641 \pm 0.4\%$

that are reported in (Kyrylyuk *et al.* , 2010; Brouwers, 2013) and (Clarke & Wiley, 1987), respectively.

5.2.2 Crowding-based model for effective viscosity of bimodal suspensions

To proceed on the rheological properties of bimodal systems, we need to define a proper stiffening function which accurately accounts for the self-crowding and microscopical interactions among the embedded equal-sized particles in concentrated suspensions. For this purpose, one may use any of those models listed in Table 2.1 especially the one proposed by Mendoza (2011) or the model developed in chapter 3 of this thesis (see Eq. (3.49)) within which the self-crowding factor is defined as

$$\Omega = (1 - \psi_t)/\psi_t. \tag{5.5}$$

As size ratio increases, the amount of trapped matrix, so-called *dead fluid* (see Fig. 5.2) decreases, and hence more fluid is available to suspend the total particles. Consider a step-wise construction for a system with total particle volume fraction $\psi = \psi_s + \psi_l$. By introducing the large particles, we note that the viscosity of the suspension increases by a factor $\mu_r(\psi_l)$. The viscosity is further increased if we add the small particles. This increment is smaller than if the small particles were large, because of the reduction in the dead fluid volume. The added small particles are homogeneously placed in the available space not occupied by the effective volume of the large particles, and may frustrate the jamming network of the large particles. Therefore, particles with interfering sizes feel the effective volume (particle + associated dead fluid) of each other, and they are crowded mutually (the addition of small particles also decreases the available free space for the large particles). When the size ratio between particles increases, the amount of dead fluid trapped between particles decreases and the effective volume approaches the volume of particles. Following the model in Eq. (4.2), we aim to find the corrected volume fractions, Ψ_1 and Ψ_2, such that Eq. (5.1) reduces to Eq. (4.2) in a way that $\mu_{r_{12}}$ is merged into $\mu_r(\Psi_1)$ and $\mu_r(\Psi_2)$. These corrected volume fraction therefore should depend on the mutual crowding factor, C_f, volume fractions of small particles ψ_s and large particles ψ_l. In the dilute limit, there is no dead fluid, therefore, the bimodal system can be interpreted as a monomodal system

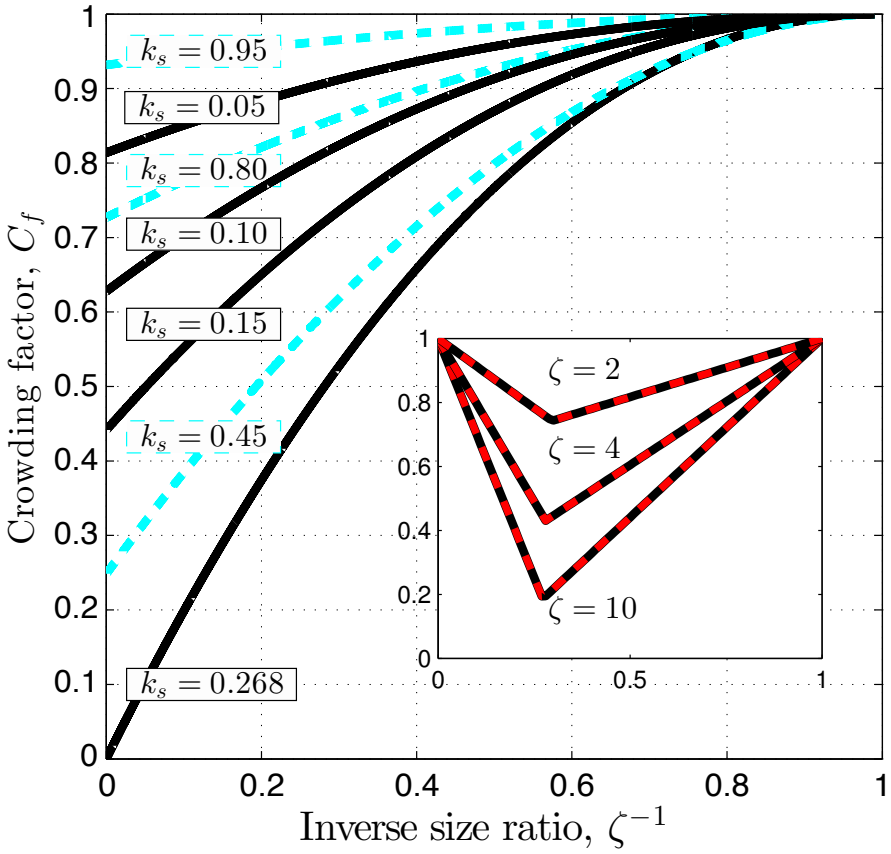

Figure 5.3: Crowding factor variation with respect to the size ratio and small particles fraction in a binary system computed using Eq. (5.7) where calculations are performed for $\psi_t = 0.633$.

of total solid phase ψ. This highlights that the crowding effect is crucial at high particle concentrations, where crowding among particles becomes important.

Although Mooney (1951) outlined two different physical trends as function of size ratio for the crowding factor, we argue that there is a direct relationship between the crowding factor and the dead fluid volume as shown in Fig 5.2. The crowding factor should depend on both size ratio and size distribution. For monomodal suspensions of jammed small or large particles, the amount of the dead fluid is the same, i.e. the same bed volume, as shown in Figs. 5.2(a) and 5.2(d). At a fixed total volume of particles, as ζ departs from unity, an excess in the available matrix (excess fluid) is observed as shown in Figs. 5.2(b) and 5.2(c), i.e. both bed volume and dead fluid decreases. The lowest volume of dead fluid for any packed binary systems is reached when $\zeta \to \infty$ and the small size fraction is $k_s^M(\zeta \to \infty)$

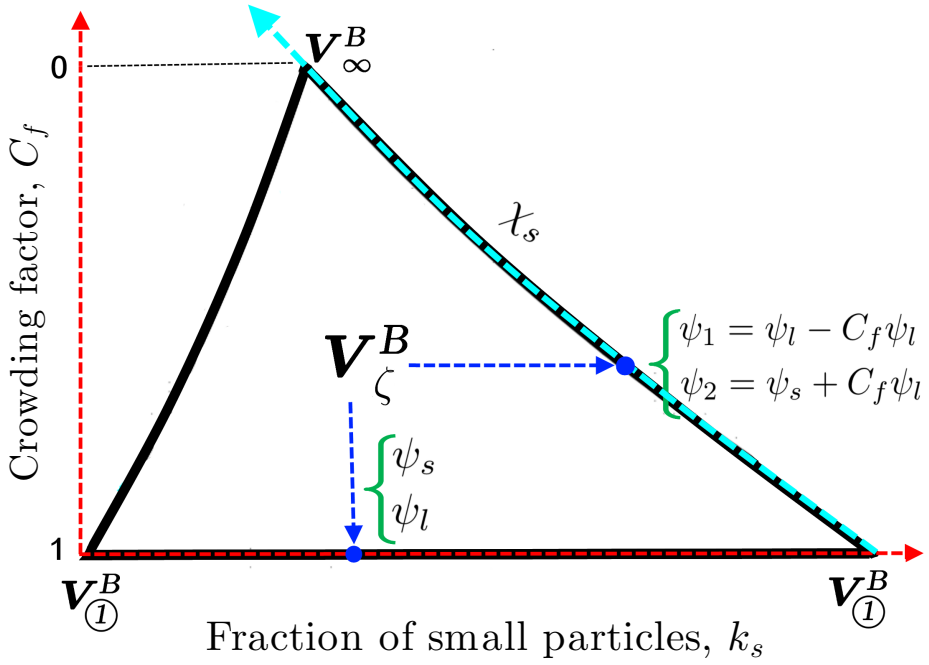

Figure 5.4: The linear projection of an arbitrary bimodal system of volume particle fractions ψ_s and ψ_l to a new configuration where sizes are not interfering and small particles are in a jamming state. This transformation conserves the crowding factor (same amount of dead fluid) and yields a new set of particle volume fractions ψ_1 and ψ_2 projected on a new coordinate χ_s.

as schematically depicted in Fig. 5.2(c). Therefore, we establish crowding as the reduction in the dead fluid upon mixing two interfering particle sizes. We define the crowding factor as,

$$C_f(\zeta, k_s) = \frac{V^B_\zeta - V^B_\infty}{V^B_{①} - V^B_\infty}, \tag{5.6}$$

where V^B represents the bed volume, and subscripts refer to different size ratios (see Fig. 5.2). Equation 5.6 reduces to

$$C_f(\zeta, k_s) = \frac{\psi_t}{\psi^b_{M_\zeta}} \left(\frac{\psi^b_{M_\zeta} - \psi'^b_{M_\infty}}{\psi_t - \psi'^b_{M_\infty}} \right), \tag{5.7}$$

when the total solid phase fraction remains constant. In Eq. (5.7), $\psi'^b_{M_\infty}$ represents the maximum packing fraction for a suspension of non-interfering size ratio, $\zeta \to \infty$, at which the cusp is formed (where the fraction of the small particles is such that both sizes produce jamming conditions, $k_s = k_s^M(\infty)$). This function is plotted in Fig. 5.3 for an arbitrary

system where $\psi_t = 0.633$. We observe that, for each size ratio, the minimum crowding factor occurs at $k_s = 0.268$ which corresponds to the minimum possible dead fluid. The crowding factor approaches unity when either $k_s \to 0$ or $k_s \to 1$. A zero crowding factor represents a specific situation where each particle size jams without disturbing the monomodal packing structure of the other size. It also points to the minimum possible dead fluid (maximum excess fluid) as schematically shown in Fig. 5.2(c). According to Fig. 5.3, as the size ratio increases, the effect of k_s on the crowding factor and hence the dead fluid increases.

To remove the crowding effect, $\mu_{r_{12}}$, from Eq. (5.1), we need to decorrelate the two particle size classes while conserving the volume of dead fluid. First, we map an arbitrary binary system of size ratio ζ with particle volume fractions ψ_s and ψ_l to a binary system of non-interfering size ratio, where the small particles jam. We construct a linear transformation $\Pi_1 : [0,1] \times [0,1] \to [0,1] \times [0,1]$ such that the new set of volume fractions $(\psi_1, \psi_2) = \Pi_1(\psi_l, \psi_s)$ conserve the amount of dead fluid in the suspension (same crowding factor),

$$\Pi_1 : (\psi_1, \psi_2) = (\psi_l - C_f \psi_l, \psi_s + C_f \psi_l). \tag{5.8}$$

This transformation is illustrated in Fig. 5.4. Through this mapping, the size classes ($\zeta \to \infty$) and volume fractions change, but it conserves the amount of dead fluid (constant crowding factor) and hence the rheological behavior of the suspension is not modified. One can understand the mapping of ψ_l and ψ_s into ψ_1 and ψ_2 as a linear transformation that decorrelates the two distributions, and removes the effect of the crowding factor arising from the size ratio. The resultant bimodal suspension is located on a new coordinate system χ_s, (along the curve on the right in Fig. 5.4) between the two extreme illustrated in Fig. 5.2(c) and (d). Along this coordinate, the excess fluid volume of the real suspension (ψ_l, ψ_s, ζ) can be retrieved by performing a second linear transformation $(\Psi_1, \Psi_2) = \Pi_2(\psi_1, \psi_2)$ that conserves the amount of excess and dead fluid in the suspension, but does not necessarily conserve the total volume fraction. In summary, the transformation Π_1 allows us to decouple the two size classes ($\zeta \to \infty$) while Π_2 corrects the bed volume for each new distribution by adjusting the amount of dead fluid that each new particle size fraction traps. Finally,

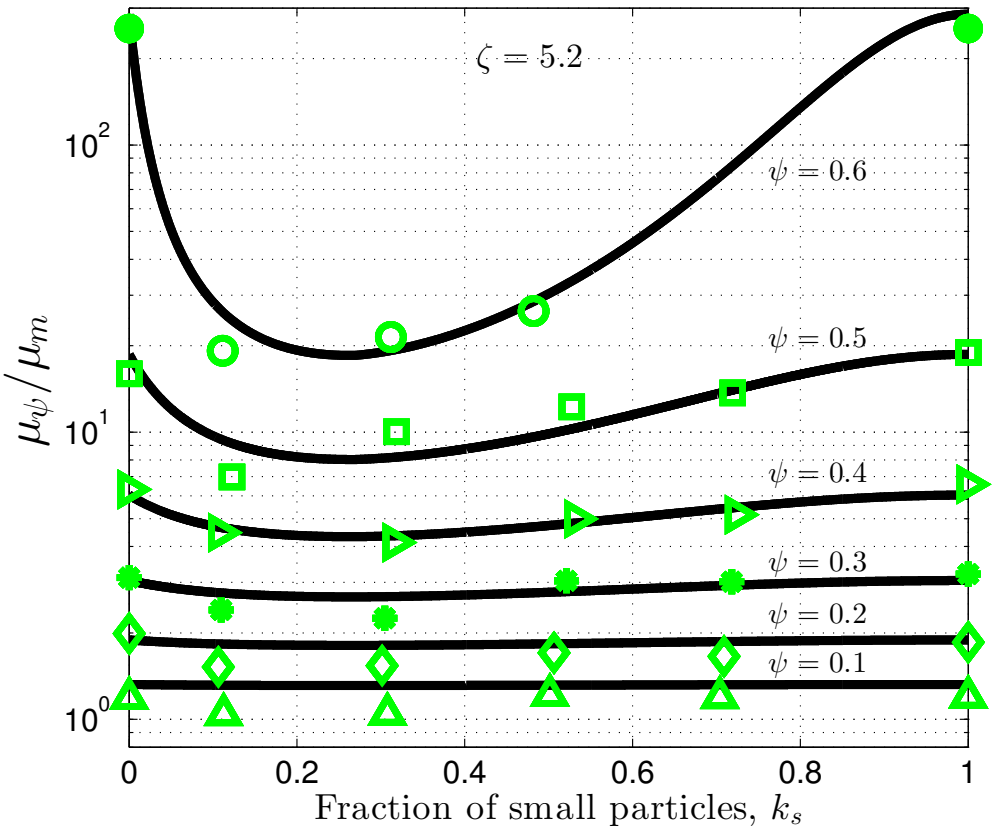

Figure 5.5: Relative viscosity in bimodal suspensions. Comparison of our crowding factor based model results (solid lines) with experimental datasets provided by Poslinski *et al.* (1988) for a binary system with $\zeta = 5.2$ and different total solid phase fractions. Solid circles are extracted from Chong *et al.* (1971) for relative viscosity of monomodal suspensions at total solid phase fraction of $\psi = 0.6$.

we define the transformation $(\Psi_1, \Psi_2) = \Pi_2(\psi_1, \psi_2)$ as

$$\Psi_1 = \frac{\psi_1}{1 - C_f \psi_2}, \quad \Psi_2 = \frac{\psi_2}{1 - (1 - C_f)\psi_1}. \tag{5.9}$$

These totally decorrelated volume fractions for $\zeta \to \infty$ can be directly used to compute the relative viscosity of suspension of interfering sizes using Eq. (4.2).

When $\zeta = 1$, we obtain $C_f = 1$, $\Psi_1 = 0$ and $\Psi_2 = \psi_2 = \psi_s + \psi_l$, and the relative viscosity of the bimodal system computed by this model reduces to that of a monomodal system. On the other hand, when $\zeta \to \infty$ and $k_s = k_s^M(\infty)$, we obtain $\Psi_1 = \psi_l$ and $\Psi_2 = \psi_s/(1 - \psi_l)$, which exactly reduces to the formulation proposed by Mooney (1951) and Farris (1968).

5.3 Results

The ability of our model to capture the effect of bidispersity and crowding on the viscosity of bimodal suspensions is tested against experimental data conducted by Poslinski *et al.* (1988) for a system with $\zeta = 5.2$ over a wide range of total solid phase volume fraction ($0.1 \leq \psi \leq 0.6$). This comparison is depicted in Fig. 5.5 in which we set $\psi_t = 0.64 \pm 0.5\%$ following (Probstein *et al.* , 1994; Poslinski *et al.* , 1988; Clarke & Wiley, 1987). Figure 5.5 shows the excellent agreement between the proposed theory and the rheology of bimodal sized suspensions. One can see that the effect of bidispersity is much higher in denser suspensions where the crowding among particles is important, and the excess fluid plays a significant role on the relative viscosity of such systems. Previous models like those recently proposed by Dörr *et al.* (2013); Qi & Tanner (2012) fit these datasets only at the lowest volume fractions (low effect of bidispersity), and their model does not provide a good approximation when the solid phase concentration increases.

In Fig. 5.6, we compare the bimodal viscosity model against the experimental data of Storms *et al.* (1990); Shapiro & Probstein (1992) and Poslinski *et al.* (1988) for bimodal suspensions with different size ratios. In Fig. 5.7, the contribution of bidispersity as one of the possible condition that causes an apparent shear thinning behavior is illustrated. In this figure, the relative viscosity against the total volume fraction of particles is illustrated for different states of suspensions. We conclude that an increase in modality results in a reduction of shear viscosity. In summary, particle breakage or any process that affects and increases the modality of suspensions during the course of an experiment is translated into an apparent shear thinning.

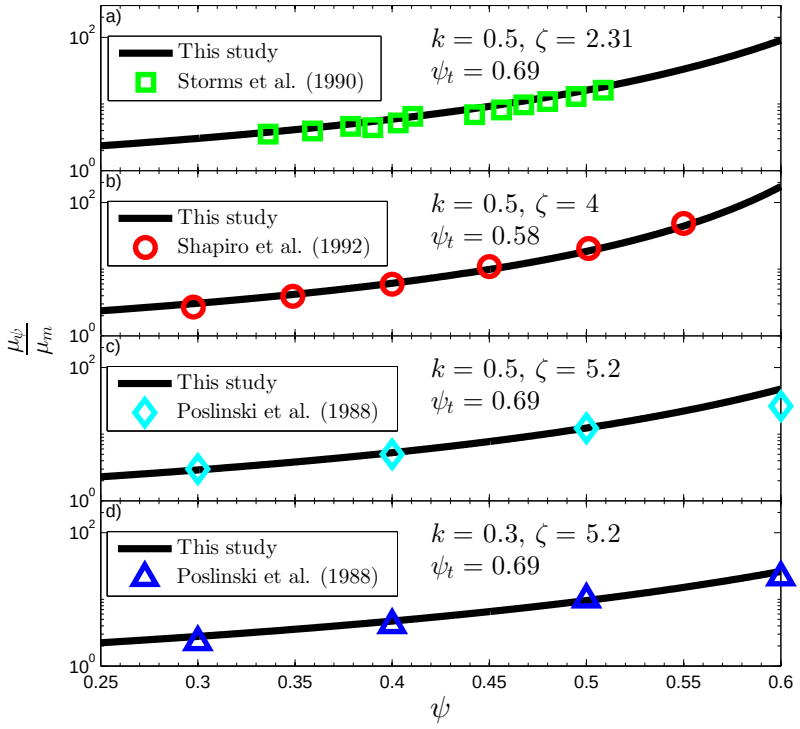

Figure 5.6: Relative viscosity in bimodal suspensions. Comparison of our crowding-based model results (solid lines) with published experimental datasets for different binary systems. ψ_t^b for these systems is calculated using Eq. (5.4) with given ψ_t.

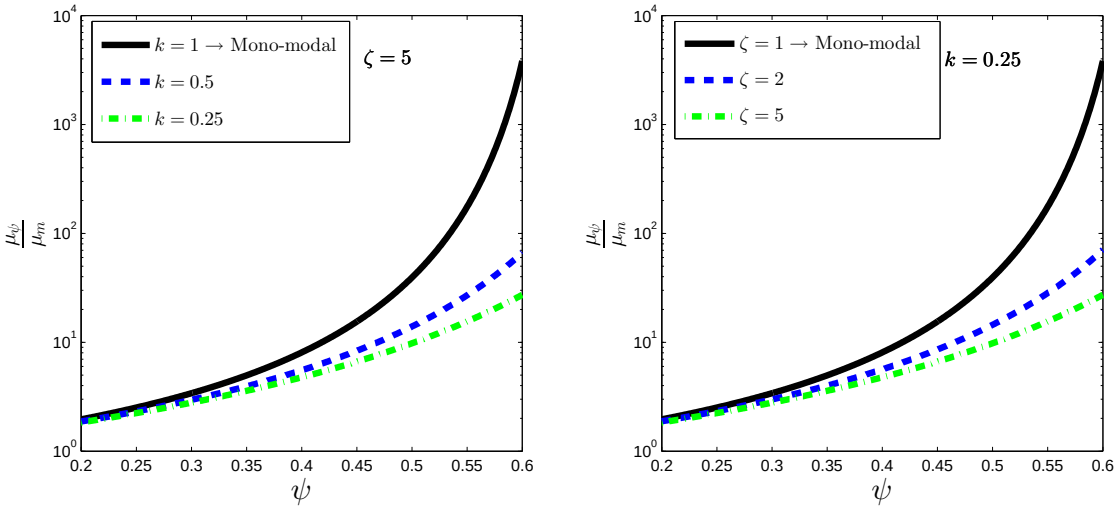

Figure 5.7: Modality changes, e.g., from monomodal to bimodal, as a possible shear induced particle level phenomenon causing apparent shear thinning behavior. Left: relative viscosity as a function of particle volume fraction for a constant size ratio, ζ, and varying percentages of fine particles, k. Right: relative viscosity as a function of particle volume fraction for a constant percentage of fine particles, k, and varying size ratios, ζ.

CHAPTER VI

PREDICTIVE RHEOLOGY MODEL

6.1 Introduction

The rheological behavior of suspensions of non-spherical particle such as spheroids has attracted less attention, because their properties are more intricate even under dilute conditions (Claeys & Brady, 1993a,b). For a given particle volume fraction, the presence of non-spherical particles increases the rate of viscous dissipation and leads to a higher shear dynamic viscosity when compared to a suspension of spherical particles (see for example Claeys & Brady (1993b); Boek *et al.* (1997)). The viscosity of suspensions of spheroids is more shear stress (or shear rate) dependent, because particles can orient with the imposed background flow. Consequently, these particular suspensions exhibit a strong non-Newtonian behavior at high particle concentration. We provide some references for studies considering spheroid particles in Fig. 6.1(b) and emphasize that they mostly consider dilute to intermediate particle concentrations (Jeffery, 1922; Goldsmith, 1967; Cox, 1971; Brenner, 1974; Haber & Brenner, 1984; Ganani & Powell, 1985; Kerr & Lister, 1991; Luciani *et al.* , 1999; Mueller *et al.* , 2011). To the best knowledge of the authors, a general model for the rheology of suspensions of spheroids valid over a wide range of particle volume fractions and under different imposed shear conditions is yet to be proposed.

Different choices of flow conditions considerably affect the shear viscosity of suspension. The microstructural rearrangement and evolution that occurs during deformation remains the most difficult challenge to the development of a predictive model for the rheology of solid particle suspensions. The present chapter investigates a self-similar behavior in suspensions of rigid particles, and provides a framework toward the development of a predictive viscosity model for suspensions of bi-axially symmetric ellipsoids.

Note: the content of this chapter has been submitted for publication as:

S. A. Faroughi and C. Huber. A predictive viscosity model for concentrated suspensions

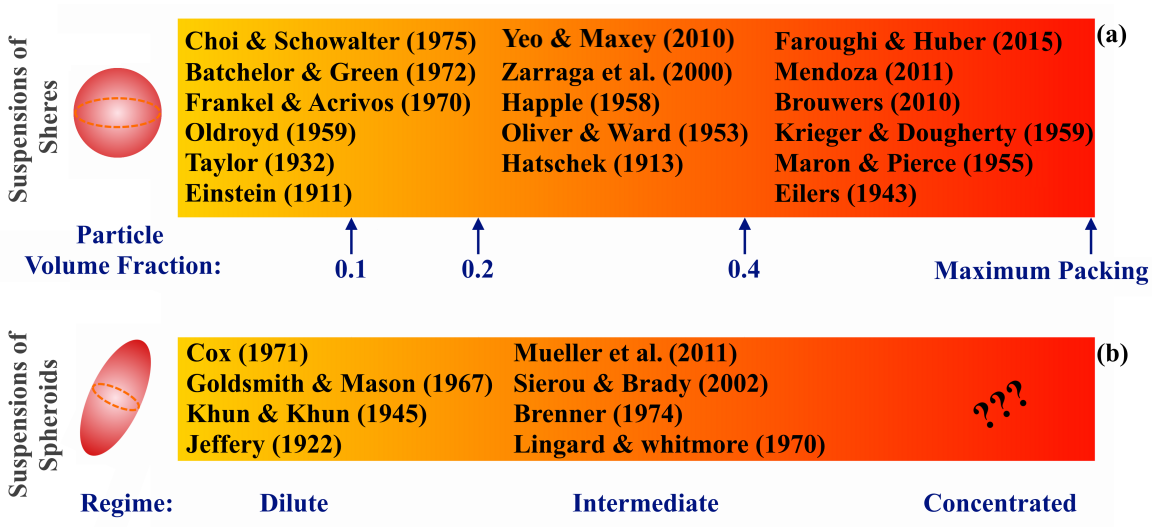

Figure 6.1: A non-exhaustive summary of previous studies on the rheology of suspensions of rigid (a) spherical and (b) spheroid particles and their applicability with respect to the particle volume fraction, ψ.

of rigid, randomly oriented and bi-axially symmetric ellipsoids, Journal of Rheology.

6.2 Rheology of suspensions with spheroid particles

Starting with a rheology model for dilute regime, we define

$$\mu_r(\psi) = 1 + [\eta]^D \psi_c, \qquad \psi_c = \frac{\psi}{1-\psi}, \tag{6.1}$$

where $[\eta]^D$ takes on a value of 2.5 (Einstein, 1906; Batchelor & Green, 1972) for rigid spherical particles with negligible hydrodynamic and inter-particle interactions. $[\eta]^D$ is the intrinsic viscosity for suspensions of rigid particles in the dilute limit, and increases as the particle shape departs from a sphere (Jeffery, 1922; Brenner, 1974; Haber & Brenner, 1984; Bicerano *et al.* , 1999; Douglas & Garboczi, 1995). We note that Eq. (6.1) complies with the lower bound for the relative viscosity (Abedian & Kachanov, 2010).

Non-spherical particles are often approximated to a first order as spheroids (Jeffery, 1922; Brenner, 1974; Bicerano *et al.* , 1999) with defined aspect ratio $r_p = b/a$ where b is the polar radius and a is the equatorial radius (see Fig 6.2). To quantify the effect of the particle shape on the intrinsic viscosity for dilute suspensions, one can use the similarity of effective transport properties in heterogeneous media. To this end, the general equation developed for the intrinsic electrical conductivity of suspensions of spheroids, $[\sigma]_\infty$, derived

from the solution of Laplace's equation can be used to estimate the intrinsic viscosity. Douglas & Garboczi (1995) determined the constant of proportionality between $[\eta]^D$ and $[\sigma]_\infty$ in three dimensions as,

$$[\eta]^D = \frac{5}{6}[\sigma]_\infty, \tag{6.2}$$

which provides an estimate of the intrinsic viscosity within an accuracy of 95% (Douglas & Garboczi, 1995). Using this argument and the exact values determined for $[\sigma]_\infty$ in suspensions of randomly oriented bi-axially symmetric ellipsoids (Douglas & Garboczi, 1995), and following Bicerano *et al.* (1999), we suggest an approximation that provides an excellent fit for $[\eta]^D$ over the range $10^{-3} \leq r_p \leq 10^3$,

$$\begin{aligned} [\eta(r_p)]^D &= 2.5 r_p \\ &+ \frac{1012 + 2904 r_p - 1855 r_p^{1.5} - 2138.5 r_p^2 + 77.94 r_p^3}{1497 r_p + r_p^2}. \end{aligned} \tag{6.3}$$

Note that all curve fitting procedures in this study are performed using the solution of nonlinear least-squares problems based on the iterative Levenberg-Marquardt algorithm (Lourakis, 2005). We must mention here that the exact values for $[\sigma]_\infty$, and thus for $[\eta]^D$ following Eq. (6.2), are obtained for dilute suspensions of arbitrary oriented spheroids (i.e. it is averaged isotropically over the entire range of orientations for both prolate a oblate particles). Therefore, the value of $[\eta]^D$ can be considered invariant under particle rotation in the limit of an infinitely dilute suspensions of arbitrary oriented spheroids (Douglas & Garboczi, 1995). Equation (6.3) is plotted in Fig. 6.2(a,b) to show the effect of particle shape on the intrinsic viscosity of dilute suspensions.

To extend the rheology model of Eq. (6.1) and (6.3) to concentrated regime of spheroid particles, we rewrite our concentrated model developed in chapter 3 in the form of

$$\mu_r(\psi) = \left(1 - \Omega(\tau, r_p)\psi_c\right)^{-[\eta(\tau,r_p)]^C \Omega^{-1}(\tau,r_p)}, \tag{6.4}$$

where τ is the imposed shear stress, $[\eta(\tau, r_p)]^C$ is the intrinsic viscosity equivalent for concentrated regimes, and $\Omega(\tau, r_p)$ denotes the self-crowding factor that accounts for the volume of dead fluid (i.e. immobile fluid in voids between particles) at jamming conditions. $\Omega(\tau, r_p)$

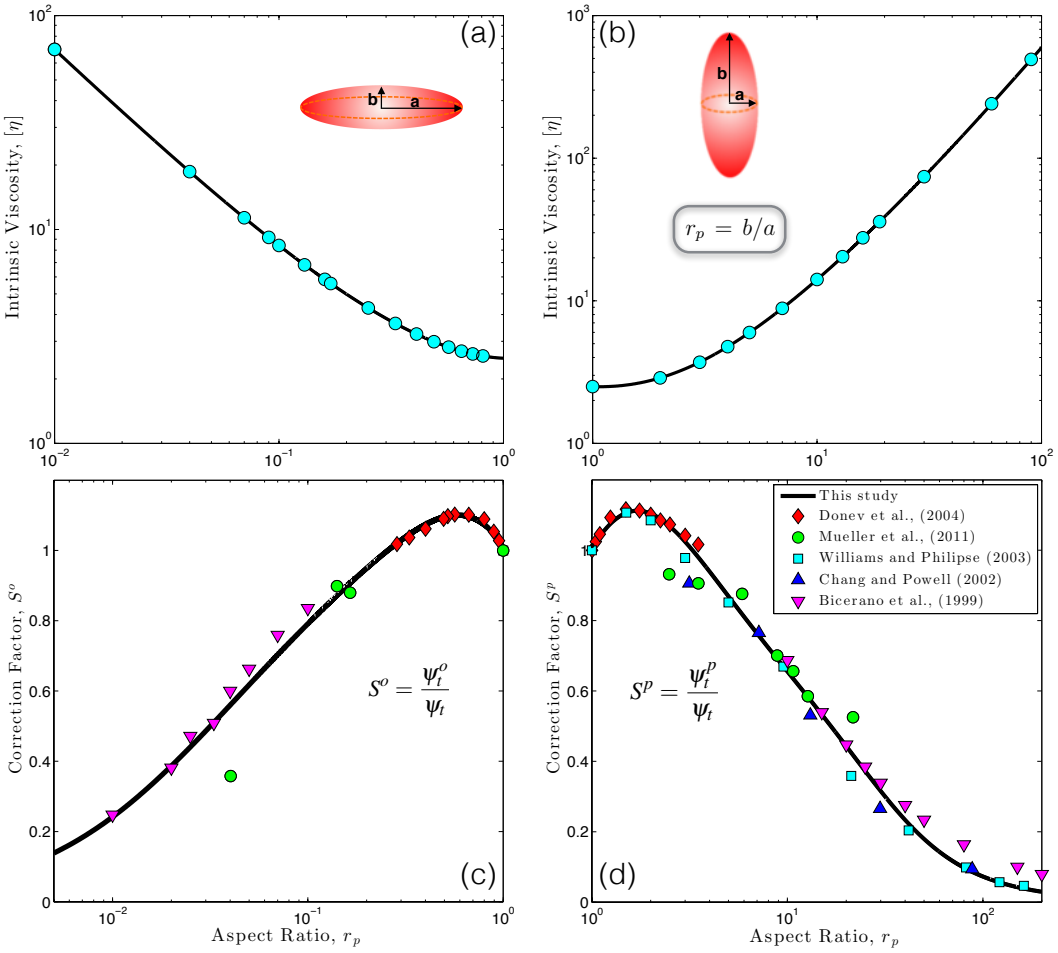

Figure 6.2: Panels (a) and (b) represent the intrinsic viscosity versus aspect ratio for dilute suspensions of rigid randomly oriented oblate and prolate spheroids, respectively (symbols indicate the results of Douglas & Garboczi (1995) with 95% accuracy, and the solid lines show the fitting model expressed in Eq. (6.3)). Panels (c) and (d) represent the threshold packing limit for suspensions of rigid oblate and prolate spheroids, respectively. Symbols show data at very low applied shearing conditions (Bicerano *et al.* , 1999; Mueller *et al.* , 2010, 2011) as well as the stress-free states (Williams & Philipse, 2003; Donev *et al.* , 2004) (as a first order approximation originated from the random close packing of spherical particles). Solid lines show the fitting models (Eqs. (6.6) and (6.7)) obtained from experimental and numerical data. Error-bars are only reported in the study of Mueller *et al.* (2011), where they considered a finite (small) deviation from the mean aspect ratio of the particles. These extent of these error-bars do not affect the best-fit solution shown as a solid-line.

is then determined by

$$\Omega(\tau, r_p) = \frac{1 - \psi_t(\tau, r_p)}{\psi_t(\tau, r_p)}, \tag{6.5}$$

where $\psi_t(\tau, r_p)$ is the threshold volume fraction.

We note that the the intrinsic viscosity $[\eta(\tau, r_p)]^C$, in Eq. (6.4), is a characteristic property of concentrated suspensions. Its value and dependence on the applied shear stress and particle shape may differ from $[\eta(\tau, r_p)]^D$, although they have often been used interchangeably for one another in many studies. A physical understanding of $[\eta(\tau, r_p)]^C$ and its relation to microstructural rearrangement and evolution is not clearly established. One may seek a quantitative description for $[\eta(\tau, r_p)]^C$ only in specific conditions, e.g. assuming $[\eta(\tau, r_p)]^C$ entirely controls the microstructural rearrangement. However, interestingly, $[\eta(\tau, r_p)]^C$ appears in the exponent, and we argue that the exponent characterizes the microstructural arrangement that particles with a given aspect ratio take under a given applied shear rate. As such, we seek a closure model for the product $\Omega^{-1} \times [\eta]^C$ for suspended particles with a range of shapes (here aspect ratio) and under various shear conditions.

In concentrated suspensions of anisometric particles, particle interlocking occurs at smaller volume fractions because particles possess a larger orbit of rotation. Therefore, the threshold packing volume fraction depends not only on the applied shearing condition, but also strongly on the aspect ratio, r_p. This has been verified experimentally (Bicerano *et al.* , 1999; Mueller *et al.* , 2010, 2011) and numerically (Williams & Philipse, 2003; Donev *et al.* , 2004). Different empirical correlations have been proposed (e.g. see Fig. 3 of Mueller *et al.* (2011)), and generally shown that the threshold packing decreases with increasing aspect ratio, r_p. However, when there is only a small departure from a spherical shape, larger values for ψ_t have been reported (Donev *et al.* , 2004). We use the available published data for the threshold packing limit either in the stress-free state (Williams & Philipse, 2003; Donev *et al.* , 2004) (as a first order approximation motivated by spheres packing), and slowly sheared suspensions (Bicerano *et al.* , 1999; Mueller *et al.* , 2010, 2011) to propose approximants to estimate the threshold packing of suspensions of prolate and oblate spheroids with aspect ratio varying from $10^{-3} \leq r_p \leq 10^3$ under low (near zero)

shear rates or shear stresses. The threshold packing limit for prolate particles, $r_p \geq 1$, is

$$S^p = \frac{\psi_t^p}{\psi_t} = \left[\frac{45.146 - 37.946 r_p + 59.993 r_p^{1.5} - 7.417 r_p^2 + 0.237 r_p^3}{59.374 r_p + r_p^2}\right]^{-1}, \tag{6.6}$$

and for oblate particles, $r_p < 1$, is

$$S^o = \frac{\psi_t^o}{\psi_t} = \left[\frac{5.085 + 193.385 r_p - 124.945 r_p^{1.5} + 57.774 r_p^2 + 34.205 r_p^3}{166.748 r_p + r_p^2}\right]^{-1}. \tag{6.7}$$

These fitting curves are plotted against experimental data in Fig. 6.2. Except for the study of Mueller *et al.* (2011), the errorbars for the experimental data used in the fit in Fig. 6.2 were not provided in the original references (see the caption for more details).

The threshold packing of spheroids estimated by Eqs. (6.6) or (6.7) is not invariant with respect to shear conditions. Therefore, as the shear conditions change (applied shear rate or shear stress changes), the actual packing limits deviate from that of the equilibrium particle configuration because of possible particle rearrangement and alignment. The threshold packing limit increases under higher shear rates as particles align with the direction of shear. We note that, when different shear conditions are applied to concentrated suspensions, particle alignment not only affects the threshold packing configuration, but also the intrinsic viscosity, $[\eta]^C$.

According to Eq. (6.4), one finds that the microstructural rearrangement and evolution can be practically captured by the product of $\Omega^{-1} \times [\eta]^C$. In the reminder of this study, we define the state of particle dispersion (or simply state of dispersion) as the set of state variables, in addition to the particle volume fraction, that fully characterize the relative viscosity of a suspension. Thus, the two state variables that enter the definition of the state of dispersion are $[\eta]^C$ and the self-crowding factor, Ω, which can alternatively be expressed with the threshold packing limit ψ_t (Eq. (6.5)). We note that each state variables depends individually on the particle shape, size distribution and the shear rate (or stress) imposed on the suspension.

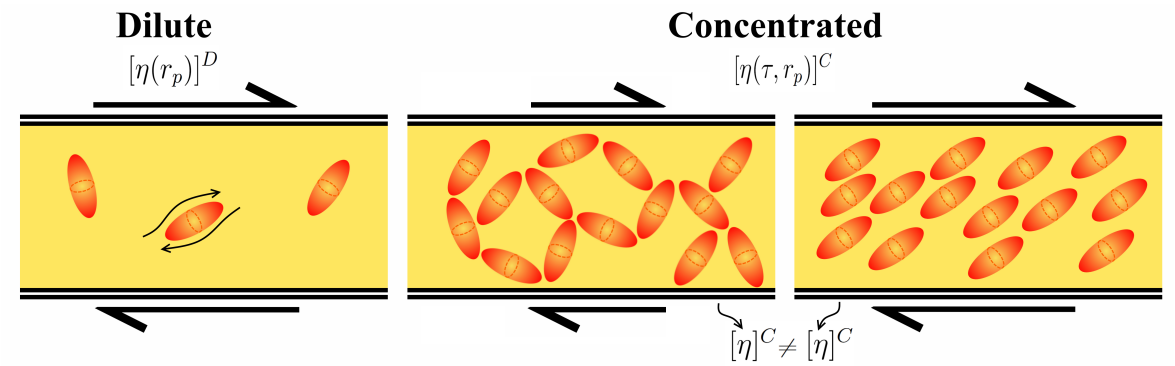

Figure 6.3: A schematic representation of the state of dispersion under different regimes and shear conditions. In the dilute regime, particles are far apart and do not interact hydrodynamically, and one can readily calculate the intrinsic viscosity for randomly oriented spheroids using Eq. (6.3). However, for concentrated suspensions, the value of $[\eta(\tau, r_p)]^C$ depends on the state of dispersion, and thus, both $[\eta(\tau, r_p)]^C$ and the threshold packing limit significantly change as particles orient with the imposed flow field.

The alignment of elongated particles under moderate to high shear rates forms particle layering and leads to an apparent shear thinning, because it increases the maximum packing threshold, ψ_t, and, possibly, decreases $[\eta]^C$. However, as discussed by Mari *et al.* (2014), concentrated suspensions subjected to very high shear rates display shear thickening. The reason for this phenomenon is that at high shear rates contacts between particles increase, and lead to a transition from a mostly friction-less to a mostly frictional rheology. The smooth (continuous) shear thickening, where the relative viscosity of suspensions remains proportional to the shear rate, occurs mostly in suspensions with particle volume fraction below the jamming threshold and under the condition of high particle inertia. While, discontinuous shear thickening, where the shear stress suddenly increases over a narrow range of shear rates, has been mostly observed in suspensions with negligible particle inertia. Recently, Ness & Sun (2015) showed numerically that particle friction and particle inertia are the leading mechanisms causing shear thickening. They found that the frictional shear thickening occurs mostly in colloidal suspensions, while the inertial shear thickening occurs in granular suspensions as results of both friction and inertial effects. As such, non-Brownian suspensions of rigid particles deformed under creeping regimes and below the jamming condition display more frequently a shear thinning behavior (Stickel & Powell, 2005). Shear

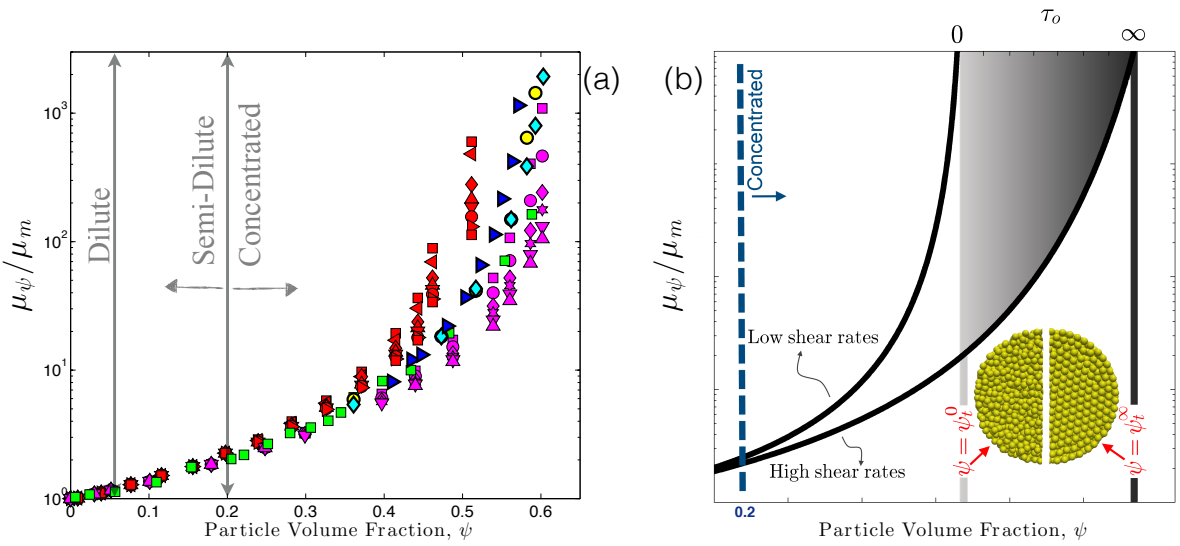

Figure 6.4: The relative viscosity of suspension of rigid sphere particles as function of particle volume fraction. Panel (a) shows the experimental data reported by Maron & Shiu Ming (1955); Maron & Levy-Pascal (1955) (thin filled symbols), Rodriguez *et al.* (1992) (bold filled circles and diamonds) and Boyer *et al.* (2011) (bold filled triangles) under different shear conditions (see the original papers for discussions on the data accuracy). Under the dilute limit, all data collapse on each other, while a large scatter is observed in the concentrated regime where suspensions show non-Newtonian behaviors, e.g. shear thinning. Panel (b) provides a schematic illustration for the shear thinning behavior of concentrated suspensions caused by particle rearrangement (particle layering and packing ordering) under higher shear rates. The shaded area highlights a region where a finite yield stress, τ_0, exists.

thinning, also, has been seen often in colloidal suspensions of rigid particles sheared at small to moderate shear rates (Boek *et al.* , 1997). As a consequence, here, we limit the discussion on the inter-dependency of the state variables and the behavior of $\Omega^{-1} \times [\eta]^C$ only for shear thinning suspensions.

6.3 Behavior of state variables

Based on Eq. (6.4), the intrinsic viscosity of concentrated suspensions, $[\eta]^C$, and self-crowding factor, Ω, are individually function of the imposed shear stress and particle shape. The processes that govern these dependencies are illustrated schematically in Fig. 6.3. Under dilute conditions, the value of the averaged intrinsic viscosity in the dilute regime, $[\eta]^D$, is invariant with respect to the applied shear stress (see Fig. 6.3(a)), and changes only as function of the aspect ratio Bicerano *et al.* (1999). For concentrated suspensions,

the value of the intrinsic viscosity and the self-crowding factor can both vary significantly because of particle alignment and rearrangement along the direction of shear. As shown in Fig. 6.3 (b) and (c), when the imposed shear rate (or stress) is increased, particle clusters can break and cause shear thinning. Therefore, when the shear stress (or shear rate) imposed on suspensions varies, the state of dispersion is changed and so are the values of the state variables. Consequently, we propose that the product of $\Omega^{-1} \times [\eta]^C$, and ψ_t may provide an adequate macroscopic description of the state of dispersion.

Figure 6.4(a) shows different sets of experimental data (Maron & Levy-Pascal, 1955; Maron & Shiu Ming, 1955; Rodriguez *et al.* , 1992; Boyer *et al.* , 2011) conducted on synthetic sphere suspensions under varying shear condition. The data displays a significant scatter, especially at high particle concentration. Shear thinning caused by particle rearrangement under different imposed shear conditions is often reported as the main reason for this scattering (Maron & Pierce, 1956; Maron & Levy-Pascal, 1955; Wildemuth & Williams, 1984). Other effects such as wall-slip (Barnes, 1995), particle migration and slight departure from a monomodal particle size distribution can also affect the scatter observed at high particle content.

We provide a schematic representation of shear thinning in rigid sphere suspensions at high volume fraction in Fig. 6.4(b). In suspensions subjected to low shear rates (or shear stress), particle aggregation or clustering is likely the main cause for the lower threshold packing volume fraction (relative viscosity diverges at lower particle volume fraction). Experiments show that the lowest fraction of solid phase at which the viscosity may diverge is the very loose random packing volume fraction, here termed ψ_t^0. At volume fractions higher than ψ_t^0, a finite yield stress appears and the suspension can support a finite external load. The shaded area in Fig. 6.4(b) highlights the region where yield stress occurs. When the particle volume fraction due to particle layering reaches the face-centered packing fraction, indicated by ψ_t^∞, the yield stress and viscosity of the suspension diverge. At this point, particles reach a configuration with the highest level of order, and shear shinning no longer occurs in response to particle ordering or microstructural rearrangement. Increasing the imposed shear stress may results in dilation (Ness & Sun, 2015) or modality alteration due

to possible particle comminution (Picard *et al.* , 2011) which in turn leads to shear banding (Divoux *et al.* , 2015; Pistone *et al.* , 2012).

The shear-dependence of the intrinsic viscosity and threshold packing limit (and by extension the self-crowding factor) are not new concepts. The effect of the shear rate on the threshold packing fraction in suspensions has been studied by Maron & Levy-Pascal (1955); Maron & Shiu Ming (1955), Krieger & Dougherty (1959) and Wildemuth & Williams (1984). The studies of Maron & Levy-Pascal (1955) and Wildemuth & Williams (1984) have provided different correlations for the shear dependence of the threshold packing limit. Bicerano *et al.* (1999) also formulated the effect of shear rate on both the intrinsic viscosity and the threshold packing limit. In these classical studies the interrelation between state parameters is not discussed, in fact, $[\eta]^D$ which is a characteristic property for the dilute limit is assumed to apply to concentrated suspensions (Lewis *et al.* , 1949).

To demonstrate the dependence of $[\eta]^C$ and ψ_t with respect to the applied shear stress, we use Eq. (6.4) with the experimental data provided by Maron & Levy-Pascal (1955) for suspensions of latex spheres (Neoprene Type 60 latex). First, we assume that the state of dispersion is entirely controlled by the threshold packing limit and not by the intrinsic viscosity, and set $[\eta]^C = [\eta]^D = 2.5$. We fit our model to find a trend for $\psi_t(\tau)$, and by extension for $\Omega(\tau)$. To do the fitting procedure, we plot $(\mu_r)^\Omega$ as function $\Omega\psi_c$ instead of the relative viscosity as function of solid particles content, which provides a unique rheological curve under the assumptions of $[\eta]^C = [\eta]^D$ and $\psi_t(\tau)$. The relative viscosity of any suspension must follow this unique, monotonic curve, which provides us with values of ψ_t for each set of experiments. In Fig. 6.5, we show the results of this analysis, and observe that ψ_t increases monotonically with the imposed shear stress as expected.

In order to study the dependence of $[\eta]^C$ on the imposed shear stress, we now assume that the state of dispersion of particles is entirely controlled by the intrinsic viscosity $[\eta(\tau)]^C$, while ψ_t is fixed to $\psi_t = 0.585$ following Boyer *et al.* (2011). Using Eq. (6.4), we plot $(\mu_r)^{(1/[\eta])}$ as a function of ψ and retrieve again a unique rheological curve. This fitting procedure provides us with the modified values of the intrinsic viscosity in the concentrated limit, $[\eta]^C(\tau)$, at different applied shear stresses. These results, reported in Fig. 6.5(b),

illustrate that the intrinsic viscosity decreases monotonically with increasing shear stress. The results we obtain in Figs. 6.5(a) and (b) are consistent with the analyses of Wildemuth & Williams (1984).

In practice, state variables change simultaneously with the shear stress, i.e. the state of dispersion is controlled by a mixed contribution of $[\eta]^C$ and ψ_t. Due to the strong inter-dependency between these two variables, it is difficult to constrain their individual contribution to the state of dispersion and consequently the relative viscosity of suspensions subjected to different shearing conditions. Several investigators have made the observation that the product of the intrinsic viscosity and the threshold packing limit is nearly invariant with respect to the shear conditions for suspensions of spherical particles (Maron & Pierce, 1956; Krieger & Dougherty, 1959; Wildemuth & Williams, 1984; Bicerano *et al.* , 1999). Therefore, one may consider

$$[\eta(\tau)]^C \times \psi_t(\tau) \approx Cst. \tag{6.8}$$

For suspensions of rigid spheres that are highly sheared, one expects from theory and Eq. (6.8) that $[\eta]^C \times \psi_t^\infty = 2.5 \times 0.74 = 1.85$, if $[\eta]^C = [\eta]^D$, which is not a valid assumption. Wildemuth & Williams (1984) suggested that the invariant in Eq. (6.8) takes a value of about 1.7 by fitting the viscosity model of Krieger & Dougherty (1959) to published experimental data for suspensions of non-aggregating rigid spherical particles. As discussed in Chapter 3, the model of Krieger & Dougherty (1959) does not account for the finite volume of suspensions (underestimates the relative viscosity of suspensions), and does not satisfy the lower bound for the relative viscosity of suspension (Sevostianov & Kachanov, 2012; Abedian & Kachanov, 2010). The existence of an invariant exponent for the relative viscosity of suspensions of spherical particles was also suggested implicitly by **?** assuming $\psi_t \times [\eta]^C \approx 2$. The discrepency between the aforementioned inferred values for the constant of Eq. (6.8) may originate from the basis of the viscosity models that assume an infinite suspension.

We followed the same strategy, but we set the invariant to be the product $\Omega^{-1} \times [\eta]^C$ as suggested by Eq. (6.4). To constrain the product $\Omega^{-1} \times [\eta]^C$ for suspensions of rigid

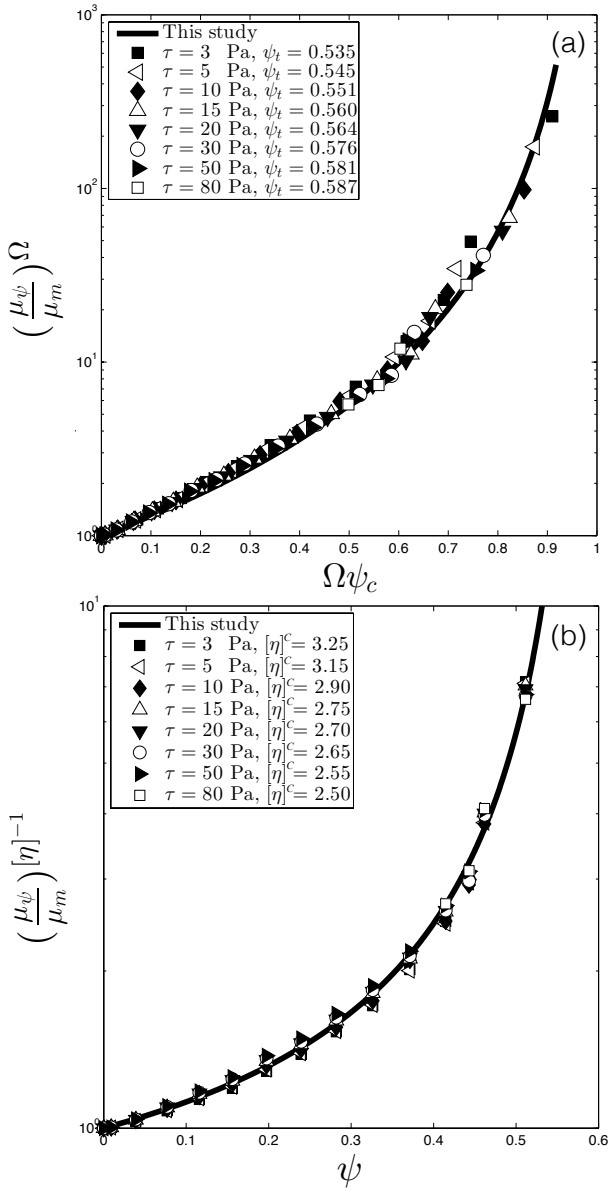

Figure 6.5: The interrelation between $[\eta]^C$ and ψ_t with respect to different applied shear stresses. In panel (a), using Eq. (6.4), we plot the scaled relative viscosity as $(\mu_r)^\Omega$ versus $\Omega\psi_c$, under the assumption of $[\eta]^C = [\eta]^D = 2.5$ to retrieve the behavior of threhold packing with varying the applied shear stress, $\psi_t(\tau)$. The plot shows the dataset of Maron & Levy-Pascal (1955) for different induced shear stresses that are fitted to the rheological curve (Eq. (6.4)) rerranged under aforementioned assumptions. We find that higher shear stresses imply a higher threshold packing limit. In panel (b), using Eq. (6.4), we plot the scaled relative viscosity as $(\mu_r)^{[\eta]^{-1}}$ versus the particle volume fraction, ψ, under the assumption of $\psi_t = 0.585$ to retrieve the behavior of the intrinsic viscosity for concentrated suspensions, $[\eta(\tau)]^C$, with varying the applied shear stress. We use the same dataset of Maron & Levy-Pascal (1955), and observe that $[\eta(\tau)]^C$ decreases monotonically as the applied shear stress increases.

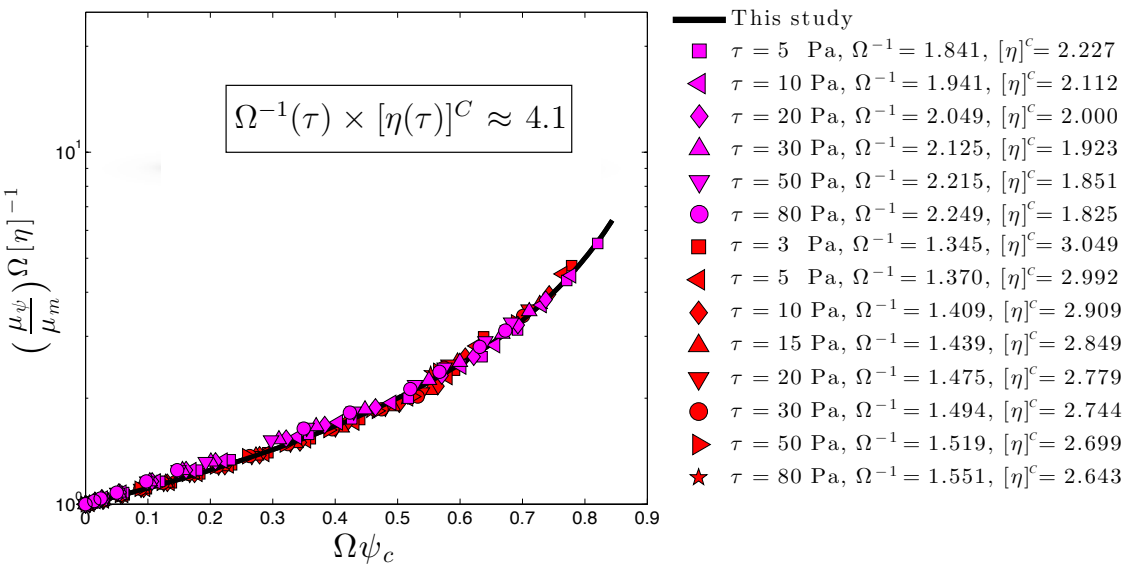

Figure 6.6: A self-similar behavior in the relative viscosity of suspensions of rigid spherical particles as function of the particle volume fraction under different shear stresses. Experimental data of Maron & Levy-Pascal (1955) and Maron & Shiu Ming (1955) are fitted to the relative viscosity model described in Eq. (6.9). The state variables vary individually with the imposed shear stress, however the product $\Omega^{-1} \times [\eta]^C$ remains invariant over the entire range of applied shear stresses.

spheres under different flow conditions, it becomes useful to rewrite Eq. (6.4) as

$$\Pi = (1 - \Psi)^{-1}, \tag{6.9}$$

where $\Pi = \mu_r^{(\Omega/[\eta]^C)}$ is the scaled relative viscosity and $\Psi = \Omega\psi_c$ denotes the effective corrected volume fraction; note that $0 \leq \Omega\psi_c \leq 1$. According to Eq. (6.9), we expect that experimental data (e.g. here we use those reported by Maron & Levy-Pascal (1955) and Maron & Shiu Ming (1955)) collapse on a unique curve irrespective of the imposed shearing condition with a constant value of $\Omega^{-1} \times [\eta]^C$.

Figure 6.6 confirms the hypothesis, and show that while the state variables vary individually with the imposed shear stress, the product $\Omega^{-1} \times [\eta]^C$ remains constants over the entire range of applied shear stresses. From these analyses for suspensions of rigid spherical particles, $r_p = 1$, we retrieve

$$\Omega^{-1}(\tau) \times [\eta(\tau)]^C = 4.1 \pm 0.05, \tag{6.10}$$

for the exponent of Eq. (6.4) (see Figure 6.6).

It is noteworthy that the value of state variables should be unique at a fixed shear rate and for a given set of material properties. According to Fig. 6.6, the state variables vary individually with the imposed shear stress, however the dependence of state variables on the shear stress are not unique, e.g. at $\tau = 80\ Pa$, $[\eta]^C$ admits two different values, 1.825 and 2.643, and the same is true for the crowding factor which is $\Omega = 0.445$ and $\Omega = 0.645$, respectively. However, the product $\Omega^{-1} \times [\eta]^C$ is identical for both sets of experiments. The disagreement in the values of state variables is expected as the experiments have been conducted with latex having different thermo-mechanical properties (Neoprene Type 60 latex (Maron & Levy-Pascal, 1955) versus GR-S X-667 latex (Maron & Shiu Ming, 1955)). This suggests that the state variables may also carry information about the behavior of individual constituent, which can be potentially used to differentiate thermo-mechanical properties of microstructures in different systems.

The question that follows these results is whether an invariant $\Omega^{-1} \times [\eta]^C$ also exists for non-spherical particles (here spheroids). To the best of our knowledge, no studies have tested the existence of an invariant with respect to shear stress for a given particle aspect ratio. A series of experiments covering a wide range of particle shape (aspect ratio) and shear stress would provide the necessary constraint to test the invariant nature of $\Omega^{-1}(\tau, r_p) \times [\eta(\tau, r_p)]^C$ for non-spherical particles.

As discussed earlier, the interlocking between non-spherical particles occurs at smaller particle concentrations, and they can orient along the shear direction as the imposed shear rate increases. This ultimately leads to a higher threshold packing limit, and a broader range of particle volume fraction over which the suspensions' microstructure can carry a load (yielding behavior), see Fig 6.4(b). As a result, the rheological behavior of suspensions of anisometric particles is more shear-dependent, and exhibits a more pronounced non-Newtonian behavior due to particles layering and aligning with the background flow. According to the dynamic response of spheroids in shearing flow (Jeffery, 1922), we know that both state variables as well as the product, $\Omega^{-1} \times [\eta]^C$ are necessarily a function of the particle aspect ratio r_p. We, thus, hypothesize that, for a fixed spheroid particle aspect ratio, the product $\Omega^{-1} \times [\eta]^C$ remains invariant with respect to the shear stress conditions.

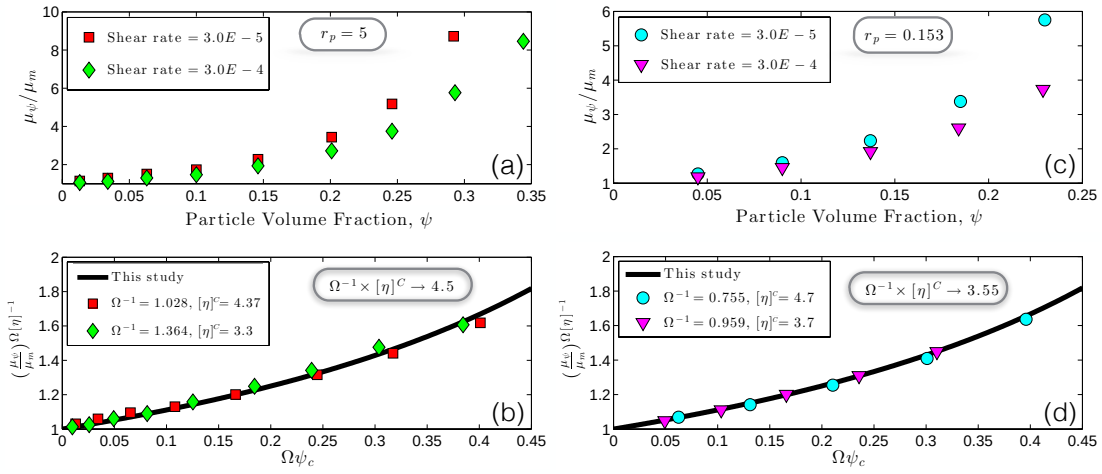

Figure 6.7: The self-similar behavior in the relative viscosity of suspensions of rigid oblate and prolate particles under different shear rates. Panel (a) shows the results of numerical simulation performed by Boek *et al.* (1997) on (colloidal) rigid prolate suspensions using dissipative particle dynamics, and panel (b) shows the fitting results according to Eq. (6.9) to obtain Ω^{-1} and $[\eta]^C$. The outcomes indicate that the product $\Omega^{-1} \times [\eta]^C$ is invariant with respect to the imposed shear rates. Panels (c) and (d) provide similar trends for the results of numerical simulation by van der Kooij *et al.* (2001) conducted on suspensions with (colloidal) rigid cylindrical disks as a proxy for platelet particles. Note that we use the exact data points inferred from simulations in the fitting procedure; readers may refer to the original papers for detailed discussions on the errors caused by numerical limitations and instabilities.

Our aim here is to test this hypothesis, and constrain $\Omega^{-1}(\tau, r_p) \times [\eta(\tau, r_p)]^C$ using available published experimental and numerical datasets for suspensions of rigid spheroids.

Figure 6.7(a) shows the results of numerical simulations for the relative viscosity of a (colloidal) suspension of rigid rod-like (prolate) particles with $r_p = 5$ subjected to shear rates of 3×10^{-5} $[s^{-1}]$ and 3×10^{-4} $[s^{-1}]$ up to 35% of particle volume fraction. These calculations were performed by Boek *et al.* (1997) using dissipative particle dynamics for randomly positioned and oriented particles. As expected, by increasing the applied shear rates, particle are forced to orient along the principal direction of shear, which causes shear thinning. In Fig. 6.7(b), we use Eq. (6.9) to explore the invariant nature of $\Omega^{-1} \times [\eta]^C$ with respect to the applied shear rates. The results of fitting procedures yields, as expected, different values for each state variables, but Interestingly, the product of $\Omega^{-1} \times [\eta]^C$ is constant. For these particular suspensions, the datasets associated with each of the two applied shear rates are captured satisfactorily by Eq. (6.9) using $\Omega^{-1} \times [\eta]^C = 4.5$.

We proceed to further test our hypothesis for suspensions of disk-like (oblate) particles. To this end, we use the results from the numerical calculations of van der Kooij *et al.* (2001) for the relative viscosity of suspensions of rigid plate-like colloids with $r_p = 0.153$. van der Kooij *et al.* (2001) also used the dissipative particle dynamics method to constrain the relative viscosity under two different shear rates of 3×10^{-5} $[s^{-1}]$ and 3×10^{-4} $[s^{-1}]$ and up to a particle volume fraction of 25%. As shown in Fig. 6.7(c), the value of the relative viscosity of these suspensions exhibits a significant shear rate dependence because of particle orientation at $\psi > 10\%$. Again, we retrieve both datasets accurately using Eq. (6.9) and a constant value for the product, $\Omega^{-1} \times [\eta]^C = 3.55$ (see Fig. 6.7(d)).

Consequently, the two independent results presented in Fig 6.7 confirm our hypothesis for the invariance of the exponent in Eq. (6.4) with respect to the imposed shearing condition for suspensions of rigid, bi-axially symmetric ellipsoids, and suggest that

$$\Omega^{-1}(\tau, r_p) \times [\eta(\tau, r_p)]^C = \mathfrak{f}(r_p). \tag{6.11}$$

In other words, these datasets suggest that $\Omega^{-1} \times [\eta]^C$ preserves its invariant nature with respect to the imposed shear conditions for suspensions of solid particles that can be approximated by spheroids, and changes only as function of the particles' aspect ratio, $\mathfrak{f}(r_p)$.

In order to constrain $\mathfrak{f}(r_p)$, we need a comprehensive set of experiments (or numerical investigations) on suspensions of spheroids with a wide range of particle aspect ratio, which is unfortunately not available at the present. As a result, we attempt to constrain $\mathfrak{f}(r_p)$ based on available published datasets. We use the experimental data published by Mueller *et al.* (2011, 2010) on intermediate (to concentrated) synthetic suspensions of non-Brownian, non-spherical particles with aspect ratio $0.04 \leq r_p \leq 22$, and the theoretical results of Jeffery (1922) for dilute suspensions of spheroids with $r_p \to 1$. Mueller *et al.* (2011), in their experiments, characterized the rheological behavior of suspensions with the structural Herschel-Bulkley model, where the suspension consistency, K and flow index n were measured as function of the particle aspect ratio and volume fraction. From these parameters and the imposed shear rates, one can retrieve the value of relative viscosity of these suspensions as function of the particle volume fraction and particle aspect ratio. Mueller

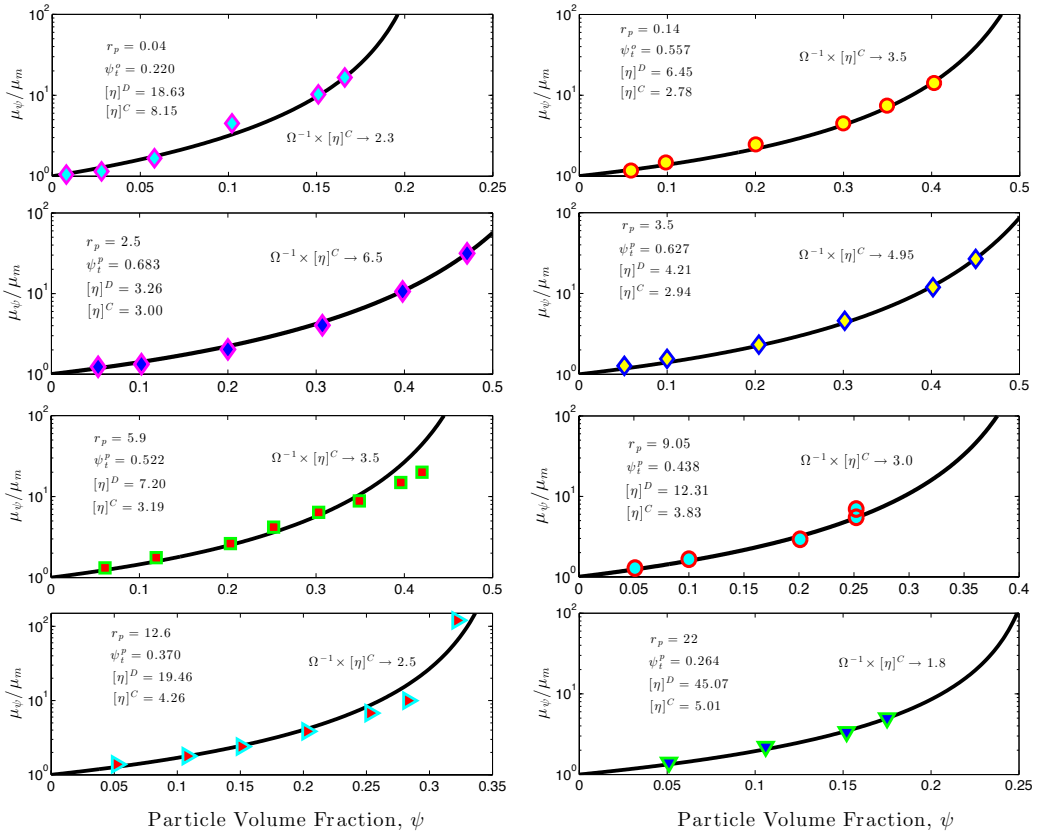

Figure 6.8: Relative viscosity of suspensions of oblate and prolate particles. Each panel shows the results of fitting our model, Eq. (6.4), to experimental data provided by Mueller *et al.* (2011, 2010) to constrain the value of $\Omega^{-1} \times [\eta]^C$ as function of the particle aspect ratio. Reported error bars in these experiments are smaller than the size of the symbols.

et al. (2011) argued that, in their experiments, K can be used as a proxy for the viscosity of suspensions, especially at dilute to intermediate particle concentration $\psi/\psi_t < 0.7$ where $n \to 1$, because the suspension were sheared at low to intermediate shear rates. Our analysis of these experimental dataset is shown in Fig. 6.8. For each dataset, assuming the suspension is sheared at low strain rate, the associated value of $[\eta]^D$, ψ_t^p or ψ_t^o are calculated using Eq. (6.3), (6.6) and (6.7). Next, the intrinsic viscosity for concentrated suspensions, $[\eta]^C$, is approximated using a fitting procedure with Eq. (6.9), which allows us to determine a unique value $\Omega^{-1}(r_p) \times [\eta(r_p)]^C$ for each suspension. The same procedure is performed on the theoretical data of Jeffery (1922) to calculate the best value for $\Omega^{-1}(r_p) \times [\eta(r_p)]^C$ where $r_p \to 1$. We note here that, to constrain the relative viscosity from Jeffery's work, one needs to calculate the time-averaged value of the relative viscosity over a complete spheroid rotational period for identical particles with a given distribution of orientations. This method, as described in detail by Mueller *et al.* (2010), almost retrieves the values of the intrinsic viscosity provided by Brenner (1974) and also by Eq. (6.3) but only in the limit of $r_p \to 1$.

An illustration of the relationship between $\Omega^{-1} \times [\eta]^C$ and the aspect ratio of particles r_p inferred from available datasets (Mueller *et al.* , 2011, 2010; Boek *et al.* , 1997; van der Kooij *et al.* , 2001; Jeffery, 1922) is shown in Fig. 6.9. We observe that the dependence of $\Omega^{-1}(r_p) \times [\eta(r_p)]^C$ on the aspect ratio mimics closely that of the threshold packing limit, see Fig. 6.2(c,d). Accordingly, we introduce the following approximants for suspensions of prolate $r_p \geq 1$

$$\mathfrak{f}(r_p) = \left[\frac{0.736 - 0.839 r_p + 0.348 r_p^{1.5} + 0.161 r_p^2 + 0.017 r_p^3}{0.743 r_p + r_p^2}\right]^{-1}, \tag{6.12}$$

and oblate $r_p \leq 1$

$$\mathfrak{f}(r_p) = \left[\frac{-0.018 + 41.957 r_p - 82.938 r_p^{1.5} + 48.390 r_p^2 + 7.898 r_p^3}{61.857 r_p + r_p^2}\right]^{-1}, \tag{6.13}$$

particles that provide a good fit for $0.03 < r_p < 30$ (i.e. from plate-like to rod-like particles).

The shaded areas in Fig. 6.9 show a region where the theoretical data of Jeffery (1922) is used. The work of Jeffery (1922) on dilute suspensions is not optimal in this case, because we are considering concentrated suspensions. More experiments to cover this range is necessary in the future to test and improve the accuracy of our correlation for $\mathfrak{f}(r_p)$ when $r_p \to 1$.

It is worth emphasizing that our model which consists of Eqs. (6.5), (6.12) and (6.13) is predictive in the limit of low (near zero) shear rates, because the threshold packing limit ψ_t (from Eqs. (6.6) and (6.7)) and the invariant product $\Omega^{-1} \times [\eta]^C$ are both constrained. Under these conditions, we test our closed-form model for sphere suspensions against the experimental data published by Rodriguez *et al.* (1992) and Zarraga *et al.* (2000). We find an excellent agreement between our closed-form model and these experimental datasets (Fig. 6.10 (a)-(b)) which are independent (to avoid circularity) of those used to parameterize our model.

As discussed earlier, each of the state variables vary significantly with the imposed shear stress. For suspensions subjected to high shear rates (or stresses), the closure of our model is contingent on constraining the effect of the applied shear stress on at least one of the state variables. At high shear stresses, Eqs. (6.6) and (6.7) do not provide a valid estimate of the threshold packing limit and by extension, the self-crowding factor Ω. However, $\Omega^{-1}(r_p) \times [\eta(r_p)]^C$ is invariant with respect to the shear stress and can be predicted using Eqs. (6.12) and (6.13).

Alternatively, at any shearing condition, the invariant nature of $\Omega^{-1}(r_p) \times [\eta(r_p)]^C$ with respect to the imposed shear conditions can be used to estimate the state variables under different experimental conditions. It is therefore possible to establish a link between the state variables and microstructure rearrangement and evolution. For example, we apply our model to the numerical results of Boek *et al.* (1997) conducted on suspensions of rigid, randomly oriented oblate particles with $r_p = 0.2$ sheared at a shear rate of 0.0003 $[s^{-1}]$ (Fig. 6.10 (c)) to estimate the unique values state variables and the threshold packing limit, ψ_t^o. Fitting our model, Eqs. (6.4) and (6.13), to this dataset yields the unique values $\psi_t^o = 0.57$ and $[\eta]^C = 3.17$ with $\Omega^{-1} \times [\eta]^C = 4.20$. One finds that the inferred value for the threshold packing limit is close to that estimated by Eq. (6.7). The value inferred for the

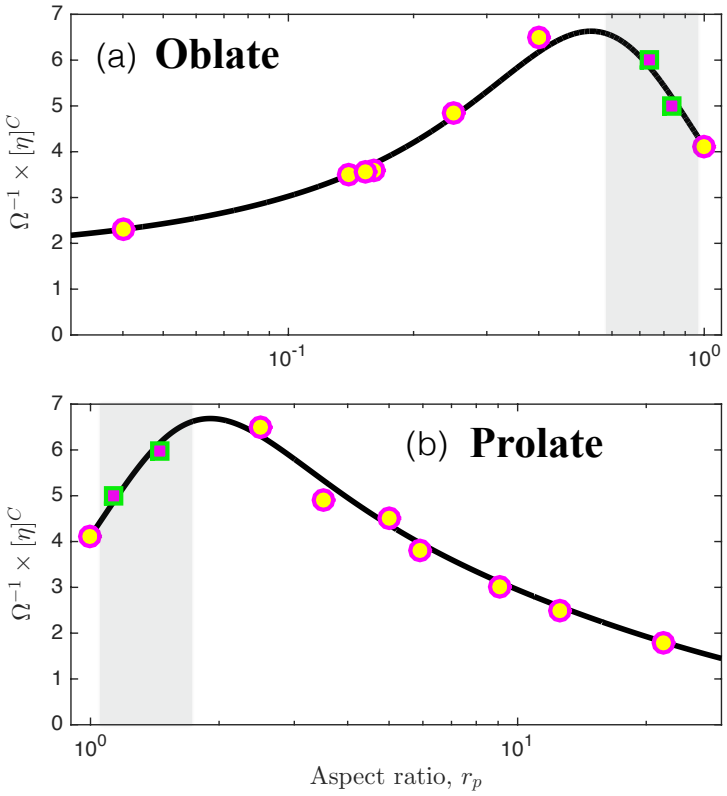

Figure 6.9: The behavior of $\Omega^{-1} \times [\eta]^C$ as function of the particle aspect ratio. The solid lines show the approximants expressed in Eqs. (6.12) and (6.13). The circle symbols show the data extrapolated from experiments(Mueller *et al.* , 2011, 2010) and numerical simulations(Boek *et al.* , 1997; van der Kooij *et al.* , 2001), and squares show sample results taken from the theoretical calculation of Jeffery (1922) for very dilute suspensions. The shaded areas highlight regions where further experimental data is required to better constrain $\Omega^{-1} \times [\eta]^C$ in concentrated suspensions containing particles with $r_p \to 1$.

threshold packing limit, thus, suggests that the random orientation of these oblate particles was preserved during the deformation in these particular simulations.

In summary, the proposed model and the self-similar behavior for the relative viscosity of suspensions of rigid spheroids as function of particle volume fraction can be applied

- to monomodal suspensions of randomly oriented spheroids sheared at low (near zero) shear rates even at particle volume fraction approaching the threshold packing limit, where both self-crowding factor and $\Omega^{-1} \times [\eta]^C$ are constrained and thus the model is fully determined.

- when one of the state variables controlling the state of dispersion can be constrained

independently for a specific setup and flow conditions. The relative viscosity of the suspension can be then predicted owing to the fact that $\Omega^{-1} \times [\eta]^C$ is known and depends only on the particle aspect ratio.

- when experiments or numerical simulations are conducted under a specific shear condition, where the use of our model provides information to constrain the state of dispersion of particles, i.e. the relation of $\psi_t(\tau)$ and $[\eta(\tau)]^C$ to microstructure evolution and rearrangement.

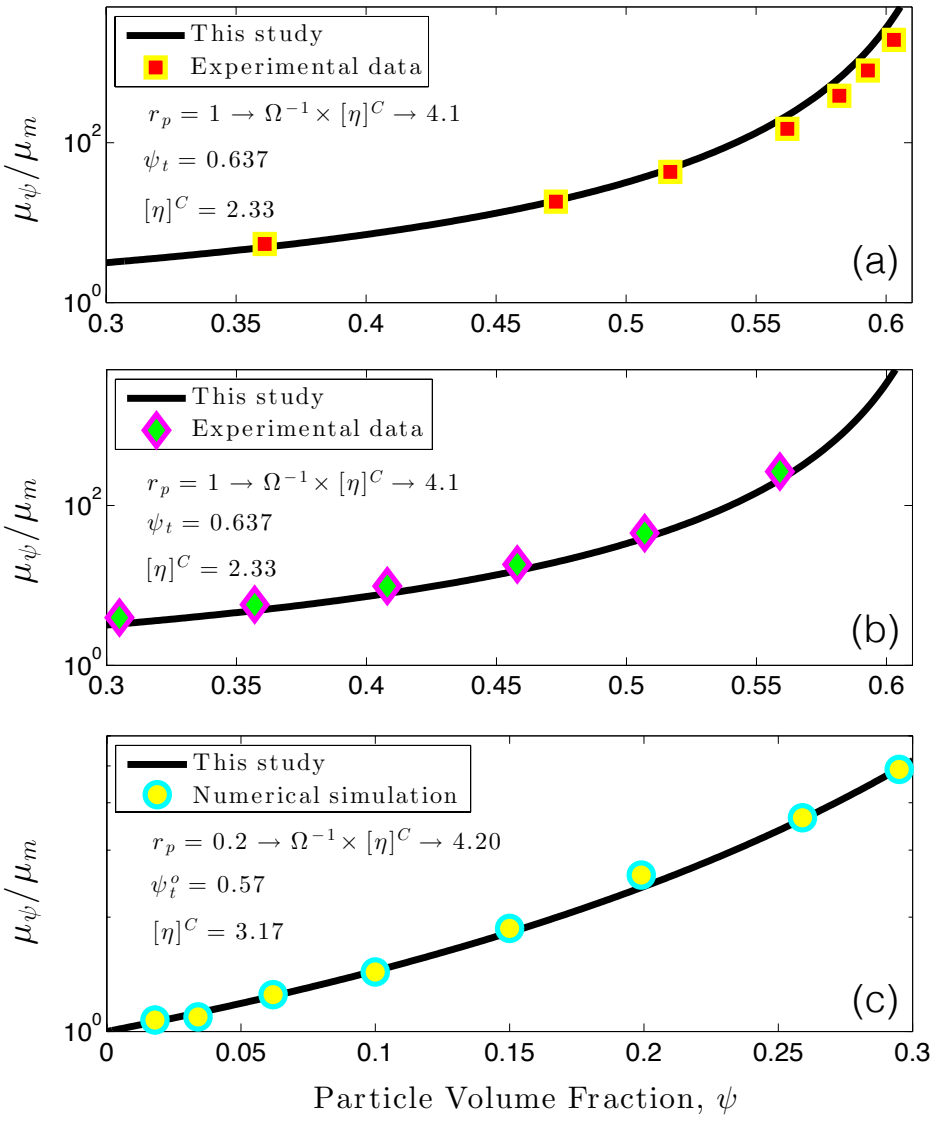

Figure 6.10: Comparisons between our model (Eq. (6.4) complemented by Eqs. (6.6), (6.7), (6.12) and (6.13)) and the experimental data of (a) Rodriguez *et al.* (1992), (b) Zarraga *et al.* (2000) conducted on rigid sphere suspensions (no error bars are reported for these two studies), and (c) the numerical simulation of Boek *et al.* (1997) on oblate suspensions with error bars smaller than the size of the symbols.

CHAPTER VII

APPLICATION I: RHEOLOGY OF CRYSTAL-BEARING MAGMAS

7.1 Introduction

Magmas, a type of complex fluid, consist of up to three different phases, a viscous silicate melt, solid crystals and exsolved gas bubbles. The shear viscosity of magmas controls the rate of many processes in physical volcanology such as magma emplacement in the crust (Petford, 2003), convection in magma reservoirs (Dufek *et al.* , 2013), mobilization of crystal mushes (Pistone *et al.* , 2013), the rate of crystal and bubble separation from melts (Martin & Nokes, 1988), magma ascent up to the surface (Gonnermann & Manga, 2007, 2013), lava flows (Harris, 2013), and cyclic dome dynamics (Wylie *et al.* , 1999). To quantify magma transport, and more carefully study volcanic processes, an accurate predictive model for the rheology of multiphase magmas is required.

This chapter focuses on developing a description for the rheology of melts with crystals only. The presence of an additional exsolved volatile phase and phase separation is neglected. In fact, we use the knowledge build in previous chapters on synthetic suspensions to address the following question,

- Is it possible to reduce experimental data for crystal-rich magmas into a coherent self-consistent framework, i.e. find a hidden self-similar behavior within the scatter?

We apply the framework developed in the previous chapters to hypothesize that the two state variables described earlier, namely the crowding factor Ω (or equivalently the threshold packing ψ_t) and the intrinsic viscosity $[\eta]^C$, provide a sufficient basis to parameterize the effect of the applied shear stress and the crystal shape and size distribution on the development of microstructure and ultimately on the rheology of crystal-rich magmas.

Note: the content of this chapter has been submitted for publication as:

S. A. Faroughi, W. Degruyter and C. Huber. The rheology of concentrated suspensions of solid particles with analyses on crystal-rich magmas, Reviews of Geophysics.

7.2 Important characteristics of crystal-bearing suspensions

Crystal-bearing magmas include large particles for which Brownian motion can be neglected, (Péclet number $Pe \gg 10^3$). The Reynolds number for these systems is well below $\ll 10^{-3}$, and thus the magma flow can be modeled using the creeping flow equations. For crystal-bearing magmas, the rate of phase separation is also negligible for short timescale due to the small relative density between phases and the high viscosity of the melt (Stokes number $St \ll 1$). For this reason, the theories developed in previous chapters and experiments with analogue materials are applicable to describe the rheology of crystal-bearing magmas (Mueller *et al.* , 2010; Cimarelli *et al.* , 2011; Del Gaudio, 2014; Moitra & Gonnermann, 2015).

A number of rheology experiments have been conducted using synthetic melts (Lejeune & Richet, 1995; Caricchi *et al.* , 2007; Champallier *et al.* , 2008), as well as natural magmas (Caricchi *et al.* , 2007; Ishibashi, 2009; Vona *et al.* , 2011) to cite a few. These experimental results provide a mean to test the validity of the model developed from analogue experiments, see Chapter 6. Mader *et al.* (2013) demonstrated that the similarity with analogue materials works well for dilute ($\psi \leq 0.1$) and intermediate ($0.1 \leq \psi \leq 0.2$) concentrations of crystals. However, the scatter observed in concentrated suspensions has led to various explanations. The following processes have been suggested: (i) non-Newtonian melt rheology, (ii) shear induced heterogeneities and localization (see chapter 4), (iii) crystal breakage, and (iv) microstructural rearrangement (Caricchi *et al.* , 2007; Lavallée *et al.* , 2008; Deubelbeiss *et al.* , 2011; Pistone *et al.* , 2012; Mader *et al.* , 2013). Some of these concepts are reviewed in this section, and the conditions when these processes are potentially important are discussed.

7.2.1 Melt rheology

The interstitial liquid in magmas is a silicate melt with a complex temperature and composition-dependent rheology (Hess & Dingwell, 1996; Giordano *et al.* , 2006; Neuville, 2006; Vetere

et al. , 2006; Giordano *et al.* , 2008; Whittington *et al.* , 2009). For instance, silicate melt are characterized by a strong increase in viscosity as the temperature and water content decrease or as the SiO_2 content increases. When the rate of deformation is much slower than the Maxwell relaxation timescale, defined as the ratio of the melt viscosity and the shear modulus of the melt μ_m/G_m, the melt behaves as a Newtonian fluid.

However, when the timescale of deformation approaches the Maxwell relaxation timescale to within three orders of magnitude, a non-Newtonian behavior is observed (Webb & Dingwell, 1990). At that point silicate melts display a shear thinning behavior. Recently, this behavior has been attributed to viscous heating where mechanical work is dissipated into heat and decreases the temperature-dependent viscosity of the melt (Hess *et al.* , 2008; Cordonnier *et al.* , 2012b). When the deformation rate increases further to within two orders of magnitude of the relaxation time, the melt transitions to a brittle-like behavior and fracturing occurs (Webb & Dingwell, 1990; Dingwell, 1996).

The addition of crystals to the melt will affect both the onset of the viscous heating, as well as the brittle behavior. When the distance between particles decreases and the particle volume fraction approaches the maximum packing fraction, the fluid has to squeeze in between particles causing viscous (shear) heating, which lubricates the flow, decreases the temperature-dependent melt viscosity, and reduces the apparent viscosity of the suspension at higher strain rates (Lavallée *et al.* , 2007; Mueller *et al.* , 2010). The same effect can also bring the rate of deformation locally above the critical rate for brittle behavior leading to fractures. Cordonnier *et al.* (2012a) have demonstrated that this critical rate decreases linearly with increasing crystal volume fraction. The numerical study of Deubelbeiss *et al.* (2011) suggest that viscous heating could only account for a small part of the observed shear thinning found in laboratory experiments and that brittle (plastic) failure of the particles, which we discuss below, is the dominant contributor. Note that in the previous chapters, we implicitly assumed that the deformation rate at all times is significantly lower than the Maxwell relaxation timescale.

7.2.2 Crystal comminution and breakage

Crystal breakage has been reported in lava flows and domes and along margins of conduit walls. This phenomenon has a critical impact on the rheology of magmas. A number of magma deformation experiments have been able to reproduce crystal breakage in the lab (van der Molen & Paterson, 1979; Lavallée *et al.* , 2007; Cordonnier *et al.* , 2009; Forien *et al.* , 2011; Picard *et al.* , 2013). Various authors have suggested different processes to explain crystal comminution:

1. Hertzian fractures that result from the contact across an elastic network of particles (Forien *et al.* , 2011).

2. Abrasion by repeated crystal-crystal interaction due to their rotation and relative motion (**?**). When the crystal volume fraction increases, contacts between crystals increases and frictional forces come to play a more fundamental role. Increasing shear rate (or shear stress) on the other hand push particles closer to each other, and interlocking becomes more important, i.e crystal breakage is highly favored at high crystal volume fractions (Passchier & Trouw, 2005; Pistone *et al.* , 2012).

3. Abrasion by melt stress transfer as the melt reaches the ductile-brittle transition and develops fractures (Forien *et al.* , 2011; Cordonnier *et al.* , 2012a).

In magmatic suspensions, the prevailing confining pressure and temperature may also contribute in enhancing or hindering crystal breakage. High confining pressure suppresses the dilation that appears when frictional contact forces control rheology and leads to intense stress localization and consequently large strain at contacts, especially when asperities are present. Forien *et al.* (2011) showed that lowering the operating temperature leads to higher possibility of crystal breakage for a suspension including haplogranitic melt with 54 vol % alumina crystals. All comminution mechanisms result in a loosening of the interlocking of crystals, and a contraction following by a reduction in the threshold packing limit. As noted, the crystal breakage is often reported in experiments with dense suspensions and highly viscous (silicic) interstitial melts (Lejeune & Richet, 1995; Caricchi *et al.* , 2007; Cordonnier

et al. , 2009; Forien *et al.* , 2011; Picard *et al.* , 2013), where the relative viscosity-crystal fraction curve admits a shape schematically represented in Fig. (7.1). Fig. (7.1) also provides an illustration of the role of possible crystal comminution on the relative viscosity of concentrated magmatic suspensions. Starting from an ideal monomodal crystal size distribution, as the crystal content approaches the threshold packing ψ_t, contact stresses between adjacent crystals become important. Forien *et al.* (2011) demonstrated that crystals were breaking during the sample preparation due to Hertzian fracturing. Additional breakage can then come from abrasion during deformation. These processes significantly alter the crystal size distribution from mono to polymodal. As a result, the threshold packing limit shifts to a higher value, which is accompanied by a sudden drop in relative viscosity. If the polymodal size distribution can be approximated by a bimodal distribution (two dominant modes), then the crowding model in chapter 5 will provide the theoretical framework to derive the post-comminution rheology trend (red curve in Fig. (7.1)). The prediction of the shift in the relative viscosity resulting from a disruption of crystal size distribution is possible if one can constrain the size ratio of the dominant modes and their relative proportions (respective fractions of the overall crystallinity). Because the polymodal suspension admits a higher value for the packing threshold ($\psi_t^b > \psi_t$), the suspension is no longer locked and can deform even if one considers a higher crystal fraction ($\psi_t < \psi < \psi_t^b$). Additional breakage events can take place when the suspension crystalinity approaches ψ_t^b which results in another alteration of the crystal-size distribution and a lower effective viscosity for the suspension. Considering curves like those shown in Fig. 7.1 in gray and pink, the slope-break often reported during experiments conducted with silicic crystal-rich magmas can potentially be attributed to an effective change in state variables related to successive breakage events (see section 7.5 for detailed discussion on the slope-break), or to shear localization.

The experimental studies conducted by Pistone *et al.* (2012, 2013); Picard *et al.* (2013) clearly show the occurrence of heterogeneous shear localization through the formation of melt-rich shear bands in crystal-rich magmas. It is also shown that the size of crystals close to the shear bands are smaller than those in the crystal-rich regions which suggests crystal breakage as a possible cause for shear banding in magmatic suspensions. Shear localization

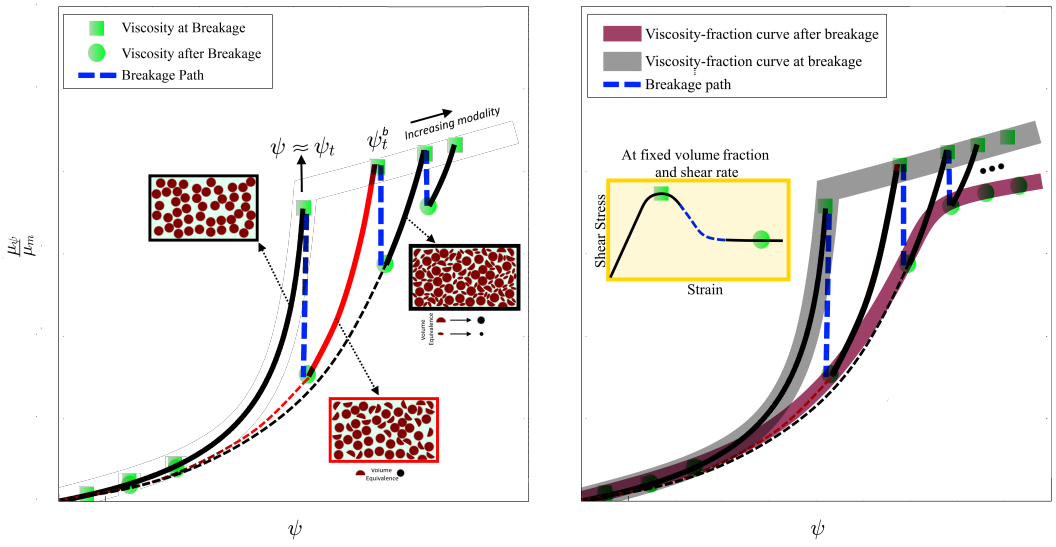

Figure 7.1: Conceptual representation of the slope-break in the relative viscosity-volume fraction curve based on crystal breakage. Left: if particles break, a change in modality occurs and, as a result, the measurement of the relative viscosity for the equivalent suspension follows a different (lower) curve. Right: the inset shows the shear stress as a function of strain as commonly observed in experiments on magmas with high crystal concentrations (van der Molen & Paterson, 1979; Picard *et al.* , 2013). Measurements of the maximum stress (green squares) will result in the gray trend, while measurements of the stress at steady state conditions (green circles) follows the red trend.

is accelerated if the systems contain a phase which is less resistant to shearing (e.g., the existence of gas bubbles in the sample under deformation) (Pistone *et al.* , 2012).

7.3 Laboratory results for crystal-bearing magmas rheology

The data for dense magmatic suspensions cannot be captured by the effective medium theory in a straightforward way (see Fig. 7.2). As the crystal concentration increases, the datasets lose coherence, especially when the slope of the relative viscosity-crystal content steepens. The rapid increase in slope is consistent with the presence of an inferred threshold packing limit as found in experiments conducted with analogue materials (e.g. Mueller *et al.* , 2010). However, experiments with high viscosity melt often show a break in slope observed as the data roll-over to high crystal fractions beyond the inferred threshold packing limit (Costa, 2005; Costa *et al.* , 2009).

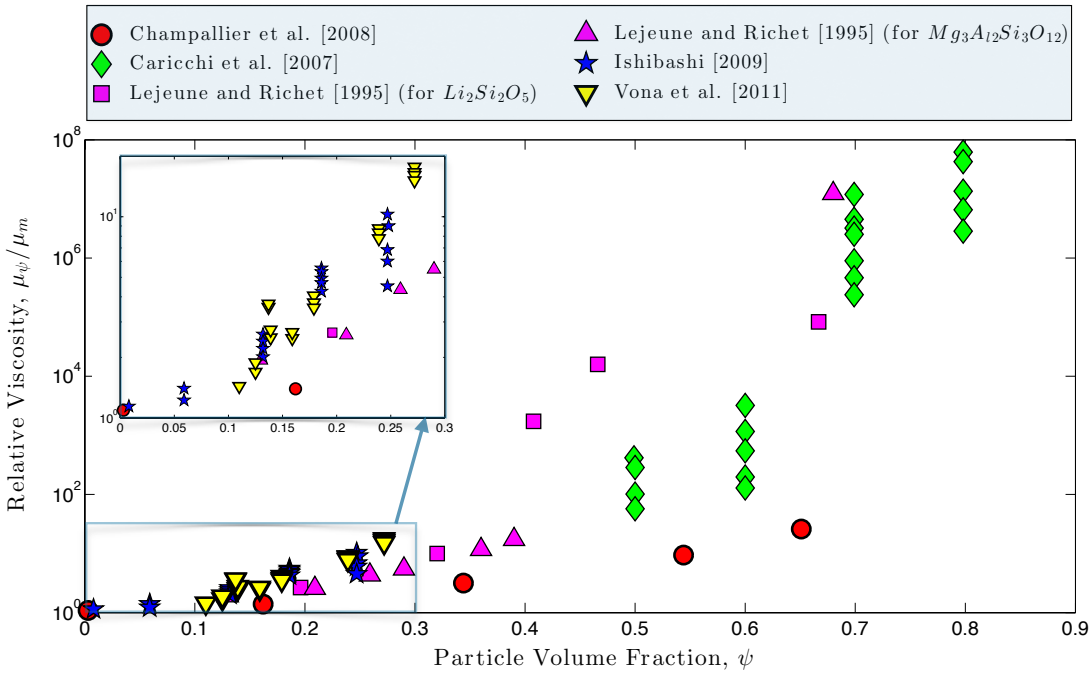

Figure 7.2: Experimental data compiled from several studis on crystal-bearing magmatic suspensions showing the relative viscosity as a function of the crystal volume fraction.

Dense magmatic suspensions have historically been investigated using two methodologies: (i) partial melting of solidified rock (Arzi, 1978; van der Molen & Paterson, 1979; Rushmer, 1995; Rutter & Neumann, 1995; Bagdassarov & Dorfman, 1998; Scott & Kohlstedt, 2006) and (ii) crystallization of liquid melt (Lejeune & Richet, 1995; Caricchi *et al.* , 2007; Champallier *et al.* , 2008; Picard *et al.* , 2013). We are mostly concerned with the latter in this study, but it is worth noting some concepts of the partial melting studies. In these studies, one important goal is to find the rheologically critical melt percentage (RCMP) at which the rheology transitions from solid-like behavior such as solid-state creep (Scott & Kohlstedt, 2006), brittle deformation (fault formation; Rushmer (1995); Rutter & Neumann (1995)), or cataclastic flow, i.e. pervasive crystal fracturing (van der Molen & Paterson, 1979; Rushmer, 1995; Rutter & Neumann, 1995) to viscous deformation such as that found for suspensions. This is essentially similar to the threshold packing limit in rheological models. It is found that this transition does not occur at the same crystal volume fraction during melting and crystallization (Vigneresse *et al.* , 1996). It is important to note that these studies show that it is possible to have flow above the threshold

packing limit and thus that in reality the relative viscosity does not diverge, but increases in a roughly linear way with increasing crystal content. A predictive rheology model thus needs to accommodate this effect (Costa, 2005; Costa *et al.* , 2009). To demonstrate the usefulness of the state variables framework to gain insight into the underlying physics of the deformation experiments, we apply it to the data sets of Lejeune & Richet (1995), Caricchi *et al.* (2007), and Champallier *et al.* (2008). We chose these studies because they cover the widest range of crystal fractions and shear rates, and observed the occurrence of shear banding and/or crystal breakage. We first discuss their findings in more detail.

The study of Lejeune & Richet (1995) investigated the rheology of crystal-bearing silicate melts using $Mg_3Al_2Si_3O_{12}$ and $Li_2Si_2O_5$ subjected to a constant stress by uniaxial compression. The material used is partially crystallized with crystals having spherical and ellipsoidal shapes for the $Mg_3Al_2Si_3O_{12}$ and $Li_2Si_2O_5$, respectively. The crystal volume fractions investigated range from 0 to 0.68. The experiments are conducted at constant shear stresses ranging from $\sim$ 1 and 700 bars leading to strain rates ranging from 10^{-6} s^{-1} and 10^{-3} s^{-1}. For the $Mg_3Al_2Si_3O_{12}$ it was found that at crystal fractions < 0.4 the suspension behaves as predicted by the Einstein-Roscoe relationship (Table 2.1). Near and above a crystal fraction of 0.4 deformation is irregular and no effective viscosity could be determined. Fractures develop and particles form clusters along a localized shear zone. The effective viscosity at crystal volume fraction of 0.68 was reported for a single imposed stress condition (670 bars), leaving a possible stress-dependence unexplored. Crystal growth was observed during these experiment because, at such viscosity, the time scale for crystal growth becomes comparable with the duration of the experiments. Experiments with $Li_2Si_2O_5$ were designed to study deformation with concurrent crystallization, as such, it is questionable if one could interpret it with a steady-state or even quasi-static rheology model. At low crystal content, the authors found a similar behavior to the experiments with $Mg_3Al_2Si_3O_{12}$. At higher crystal fractions the viscosity becomes stress dependent and shear thinning is observed.

Caricchi *et al.* (2007) performed torsion and compression experiments at constant strain rates (between 5×10^{-6} s^{-1} and 8×10^{-4} s^{-1}) at a confining pressure of 250 MPa and

temperatures between 737 and 1137 K using a Paterson-type deformation apparatus. These sets of experiments are conducted on haplogranitic melts with isometric quartz crystals as the suspended phase. The crystal fraction was varied between 0.5 and 0.8 (and was used in combination with data at low volume fraction from Thomas (1965)). Shear thinning behavior is very clearly observed in these experiments. The shear thinning observed at intermediate crystal content (before the break in slope) is most likely related to particle rearrangement. At higher volume fraction, the textures indicate the formation of shear bands and the average size of the grains in these shear bands is noted to be smaller than outside (suggesting breakage). Above the threshold packing fraction, Caricchi *et al.* (2007) suggest that dilation is required for the magma to flow. This would create pressure gradients and generate crystal-melt segregation.

The experiments of Arbaret *et al.* (2007) and Champallier *et al.* (2008) and the more recent studies of Picard *et al.* (2011, 2013) display a similar behavior as those of Caricchi *et al.* (2007). These experiments are performed at confining pressure of 300 MPa and temperatures between 748 and 1273 K. They also use a haplogranitic melt with isometric corundum crystals in suspension. They investigate the effect of the crystal fraction (up to a fraction of 0.76) on the shear viscosity of magmatic suspensions subjected to shear rates ranging from 10^{-4} s^{-1} to 2×10^{-3} s^{-1}. Shear thinning is observed and correlated with microstructural changes (Arbaret *et al.* , 2007). Interestingly, no compaction or crystal breakage are reported and the trends do not display a break in slope for the relative viscosity as the crystallinity approaches the inferred threshold packing limit. Picard *et al.* (2011, 2013) used anisotropic crystals (plagioclase) and qualitatively confirmed that the threshold packing fraction decreases with increasing aspect ratio. They report crystal breakage coinciding with the rupture in slope of the relative viscosity-crystal fraction curve.

7.4 Magma rheology model

Dynamicists have applied both (constitutive) structural and rheological models to constrain the effective viscosity of magmatic suspensions in plutonic and volcanic environments. At low and intermediate particle content, where the effect of microstructural rearrangement

and shear-induced localization are less pronounced, rheological models like those proposed by Roscoe (1952); Maron & Shiu Ming (1955) and Krieger & Dougherty (1959) (see Table 2.1) are extensively used to parametrize the rheology of crystal-bearing magmas (Moitra & Gonnermann, 2015).

Several other researchers, e.g., Mueller *et al.* (2010); Mader *et al.* (2013), referenced their data with the structural Herschel-Bulkley model (Eq. (1.2)). The normalized consistency can be described by a stiffening relationship like those listed in Table 2.1. Mader *et al.* (2013) found the model of Maron & Pierce (1956) to best describe the normalized consistency, whereby they parameterize the maximum packing limit as a function of the shape of the particles, and excursions from Newtonian behavior were captured by the flow index and the yield stress. For crystal contents significantly below the maximum packing limit, the flow index remains close to unity and yield stress is absent. Significant changes in flow index and yield stress are observed only when the crystallinity approaches the maximum packing limit (i.e., concentrated suspensions). Several empirical relationships have been introduced to describe the flow index, consistency and the yield stress as a function of the crystal shape and maximum packing fraction based on curve fitting (e.g. Gay *et al.* , 1969; Mader *et al.* , 2013).

Costa (2005) and Costa *et al.* (2009) proposed an empirical rheological model to characterize the rheology of concentrated crystal-bearing magmas and the common break in relative viscosity-crystal content slope observed experimentally at high crystal content (see Fig 7.2). In this model, the apparent viscosity does not diverge when the particle volume fraction reaches and exceeds the maximum packing fraction. Instead, the rapid increase of the apparent viscosity transitions into a shallow slope. This transition is introduced through an expression based on the error function,

$$\mu_r = \frac{1 + \left(\frac{\psi}{\psi_t}\right)^{\delta}}{\left(1 - (1-\xi)\mathrm{erf}\left(\frac{\sqrt{\pi}}{2(1-\xi)}\frac{\psi}{\psi_t}\left(1 + \left(\frac{\psi}{\psi_t}\right)^{\gamma}\right)\right)\right)^{[\eta]\psi_t}}. \tag{7.1}$$

In Eq. (7.1), δ, ξ and γ are additional fitting parameters. The increased number of tuning parameters in Eq. (7.1) allows for a better fit to experimental datasets as well as the scatter observed at high crystal content (see Fig. 7.2). However, it is not clear how

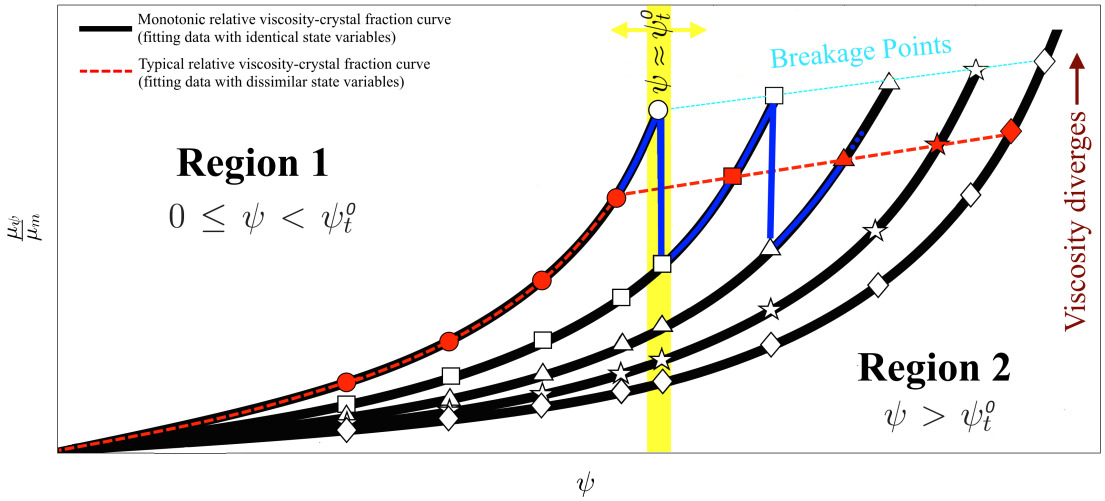

Figure 7.3: Schematic representation of the relative viscosity of crystal-bearing magmas as a function of the crystal volume fraction. Different symbols represent experimental data obtained at different shear rates. The solid black lines show the monotonic behavior of the relative viscosity as function of volume fraction for a suspension at different shear rates that possess different sets of state variables. The filled red symbols depict a typical experimental datasets for crystal-bearing magmas. For $\psi < \psi_t^0$, which we refer to as Region 1, the data follows a single monotonic curve for a given shear stress. One can see a sharp change in slope for the viscosity when the particle volume fraction exceeds ψ_t^0, which we call Region 2. The red dashed line schematically represents a typical interpretation of experimental data, e.g., using the model of Costa *et al.* (2009).

one could predict the value of these parameters to retrieve a predictive rheology model that can be extrapolated beyond the existing experimental datasets. Additionally, the coupling between the five tuning parameters makes it quite difficult to draw physical insights into the processes that govern the deformation of magmatic suspensions.

The simple use of either structural or rheological models to fit experimental data provides no guarantee to understand the underlying physics and therefore to build a predictive approach for the effective viscosity of magmas. In the next sections, we first attempt to interpret the origin of the slope-break occurring in concentrated crystal-bearing magmas under deformation. We then attempt to analyze experimental data using the state variables framework that was discussed in Chapter 6.

7.5 State variables framework for magmatic suspensions

The state variables framework proposed in Chapter 6 can provide a solid ground to explore the underlying mechanisms causing the break in slope in the relative viscosity-crystal content relationship of crystal-bearing magmas. A schematic representation of a typical rheological response of crystal-bearing magmas with a highly viscous melt is illustrated in Fig. 7.3, where each type of symbols report a set of viscosity measurements for suspensions that possess identical states variables (Ω and $[\eta]^C$). The solid black lines are best fits to each set of data showing the monotonic behavior of the relative viscosity as function of crystal volume fraction. The filled (red) symbols show a typical experimental dataset commonly reported for crystal-bearing magmatic suspensions, and the dashed red line shows the best fitting function (for example using the model of Costa *et al.* (2009)) for this sample data. Figure 7.3 shows that any experimental results (filled symbols) can be divided into two separate regions. In the first region, called Region 1 ($0 \leq \psi \leq \psi_t^0$), the datapoints are located on a single trend (black curve) and thus posess a unique set of state variables (Ω and $[\eta]^C$), i.e., they share the same state of dispersion. In the second region, Region 2 ($\psi > \psi_t^0$), the data (shown with different types of red symbols) lie outside of the trends formed in Region 1. As depicted, these data each belong to different trends (black curves), which implies that their state of dispersion and consequently the values of the state variables are dissimilar to the other data from this set. With a typical fitting (e.g., using Eq. (7.1)) of the entire set with a single curve, one observes a break in slope at the boundary across these regions (see the dashed red line in Fig. 7.3). The change in the slope of the relative viscosity-crystal volume fraction curve shown in Fig. 7.3 has been described as an intrinsic behavior of magmas in many studies (Lejeune & Richet, 1995; Caricchi *et al.* , 2007; Vona *et al.* , 2011; Pistone *et al.* , 2012). It is also demonstrated that the packing limit at which the rupture in slope occurs within experiments depend on the applied shear rate, as well as the crystal shape and size distributions (Caricchi *et al.* , 2007).

The clear change in the state variables below and above the transition suggests that these dataset should not be fitted with a single curve as they involve different states of dispersion. One can argue that the relative viscosity of a suspension at the maximum packing should

diverge, unless a drastic reconfiguration of the particle size distribution or shear-induced heterogeneities take place. These two processes both result in a sudden change in the state variables, which provides an microstructural explanation for the break in slope in $\mu_r(\psi)$ near or at the threshold packing.

Practically, the effective viscosity of a suspension with a fixed modality increases along a monotonic trend for volume fractions $0 \leq \psi \leq \psi_t^0$ until the particle volume fraction approaches the threshold packing limit, and suspensions becomes rheological locked (e.g., see the circles in Fig. 7.3). Over this region, each experimental dataset is characterized by a single state of dispersion, i.e. the state variables Ω, or alternatively ψ_t, and $[\eta]^C$ are uniquely defined by the shape and size distribution of particles as well as the imposed shear rate (or stress).

At the threshold packing, ψ_t^0, if the imposed shear rate remains constant, there are only two mechanisms that allow the suspension to flow; by modulating the state of dispersion due to (i) the breakage of clusters of particles and particle itself, and (ii) heterogeneities. Under the second mechanism, heterogeneities in particle distribution leads to the formation of shear bands, and the deformation is mostly accommodated by shear localization. The first mechanism is due to rearrangement and particle breakage **(see Section 7.2.2)**, which, in turn, affects the value of ψ_t (or Ω) and $[\eta]^C$. In response to either of these mechanisms, the measured relative viscosity drops to the next monotonic trend (e.g. from circles to square symbols in Fig. 7.3). The data now lies on a new curve defined by a different state of dispersion possessing $\psi_t > \psi_t^0$. This process can repeat several times. Consequently, we suggest that each measurement at high crystal content ($\psi > \psi_t^0$, within Region 2) is characterized by a different state of dispersion with respect to the rest of data. We must note that across the transition from Region 1 to Region 2, the state variables vary individually, but the product $\Omega^{-1} \times [\eta]^C$ varies only if the shape of the particles changes because of breakage for example.

Experimental studies only provide discrete data points for $\mu_r(\psi)$, and most likely miss the Z-shaped curve (shown with solid blue lines in Fig. 7.3) at the boundary across Region 1 and Region 2. Note that this boundary moves to the right after each alteration of the

state variables. It is important to note that we did not consider solid-state creep (Scott & Kohlstedt, 2006) in our model, which for the time-scale and physical conditions under which experiments for crystal-bearing magmas are conducted (upper crustal pressures) is negligible.

In the light of our interpretation, we can now test whether the scatter can be accounted for by the state variables framework we propose. As a proof of concept, we fit the experimental data of Lejeune & Richet (1995); Caricchi *et al.* (2007) and Vona *et al.* (2011) on the unique rheological curve derived from Eq. (3.49) under the assumption of identical state variables within both regions ($0 \leq \psi \leq \psi_t^0$ and $\psi > \psi_t^0$), see Fig. 7.4. We observe that only the data measured at Region 1 ($\psi < \psi_t^0$) collapses to the unique rheology curve, which supports that the state variables, Ω and $[\eta]^C$, are different in the two regions. The assumption of identical state variables over the whole range of crystal fraction for each of these experiments leads to $\Omega\psi_c > 1$ when $\psi > \psi_t$, i.e. the effective volume fraction of particles is greater than that of the total suspension. This is not physically possible and reflects that we underestimate the packing threshold in Region 2. This is another clue for the fact that crystal comminution or shear banding alter the value for ψ_t and $[\eta]^C$ for all measurements data beyond Region 1 ($\psi > \psi_t^0$).

To constrain the state of dispersion for experimental data on magmas under any specific flow conditions, an approach based on the state variables framework (Eq. (3.49) along with Eqs. (6.12) and (6.13)) can be established. For example,

- **Case 1:** If the suspension modality and crystal aspect ratio are constrained and increasing shear rates (or shear stress) results only in microstructure rearrangement (no breakage and localization), the product of $\Omega^{-1}(\tau, r_p) \times [\eta(\tau, r_p)]^C$ will be only a function of the particles' shape (Eqs. (6.12) and (6.13)).

- **Case 2:** If particle deformation occurs (e.g., shear induced elongation of a viscoelastic particle) during a specific flow and shear condition, the product of $\Omega^{-1}(\tau, r_p) \times [\eta(\tau, r_p)]^C$ changes as particle shape is changing. The best fit then gives the state of dispersion as well as a good estimation of particle deformation, i.e., comparing the

inferred value for $\Omega^{-1}(\tau, r_p) \times [\eta(\tau, r_p)]^C$ to Fig. **??** provides an estimate for r_p.

- **Case 3:** If the best fit at any specific shear condition provides inexplicable values for state variables, e.g., $\psi_t > 0.74$ for monomodal suspensions of rigid spheres, disruption like, shear localization, shear banding are expected to have accrued during deformation.

In Fig. 7.5, we establish the respective state variables for the datasets of (Lejeune & Richet, 1995; Caricchi *et al.* , 2007; Champallier *et al.* , 2008; Ishibashi, 2009; Vona *et al.* , 2011) based on the assumption that state variables are different and that $\Omega^{-1} \times [\eta]^C$ depends only on the crystal aspect ratio. To this end, we fit each individual experimental data beyond Region 1 separately to the unique rheological curve, as we posit that a self-similar behavior should be restored once Ω and $[\eta]^C$ are set correctly to account for changes in microstructures rearrangement and evolution. This fitting procedure provides values for the state parameters for each datasets (in both regions) as reported in Fig. 7.5. We find that the state variables framework provides a solution to restore a self-similarity for the relative viscosity of concentrated magmatic suspensions using Eq. (3.49) with values for $\Omega^{-1} \times [\eta]^C$ that agree with the shapes of crystals used in the different experiments, and that the onset of rupture in slope in $\mu_r(\psi)$ results from a sudden change in state variables.

The data provided by Champallier *et al.* (2008) where no crystal breakage is reported is an interesting example where one could predict the occurrence of shear localization zones from the state variables analyses. The experiments of Champallier *et al.* (2008) do not follow an exemplar rheology of crystal-bearing magmas. By fitting these data to the unique rhelogical curve, as shown in Fig. 7.5, we obtain that the threshold packing for the suspensions in Region 1 and 2 is $\psi_t = 0.72$ and $\psi_t = 0.77$, respectively. In Region 1, a high inferred value of ψ_t (i.e., 0.72 which is higher than the random close packing $\psi_t = 0.63$ for monomodal spherical particles) to fit the data can be linked to possible shear localization that result in better lubrication between crystals or crystal frameworks during deformation. Additionally, the value of $\psi_t = 0.77$ reported for Region 2 cannot be achieved, because it is beyond the

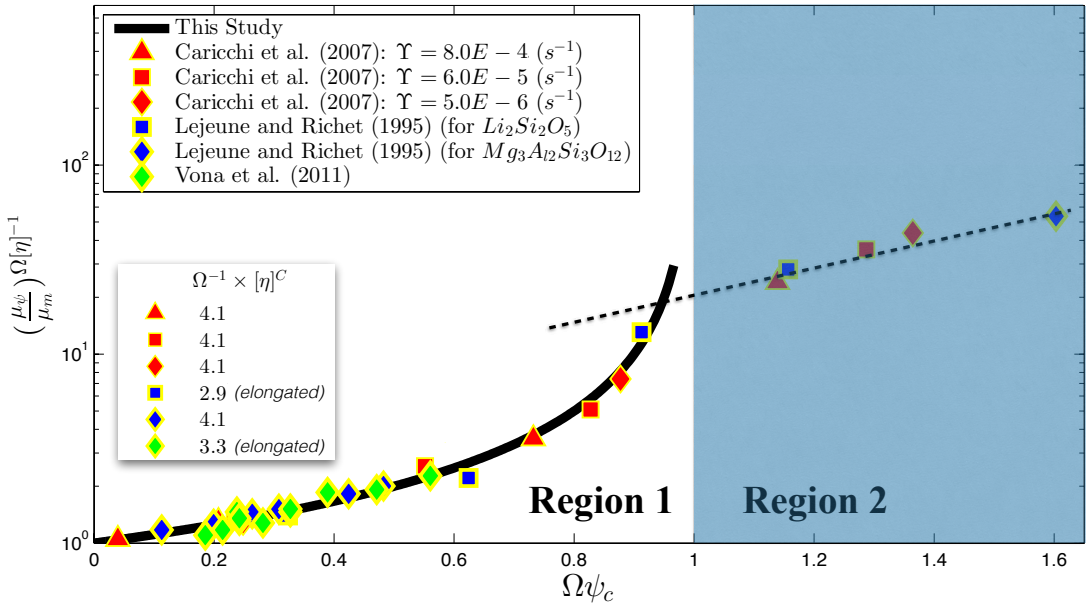

Figure 7.4: Comparison of Eq. (3.49) (bold black curve) with experimental data of crystal-bearing magmas (symbols) assuming identcal state variables over the entire range of particle volume fraction (i.e., same state varaibles in Region 1 and 2). Using this assumption, each dataset at $\psi < \psi_t^0$ coincides with the unique rheological curve leading to the respective product of the state variables. For particle volume fractions higher than ψ_t^0 (Region 2), the relative volume fraction, $\Omega\psi_c$ becomes greater than unity, which suggests either crystal breakage or shear localization. Therefore, when $\psi > \psi_t^0$, the state of dispersion controlled by $[\eta]^C$ and Ω changes from that of Region 1 and also from a data to another in Region 2.

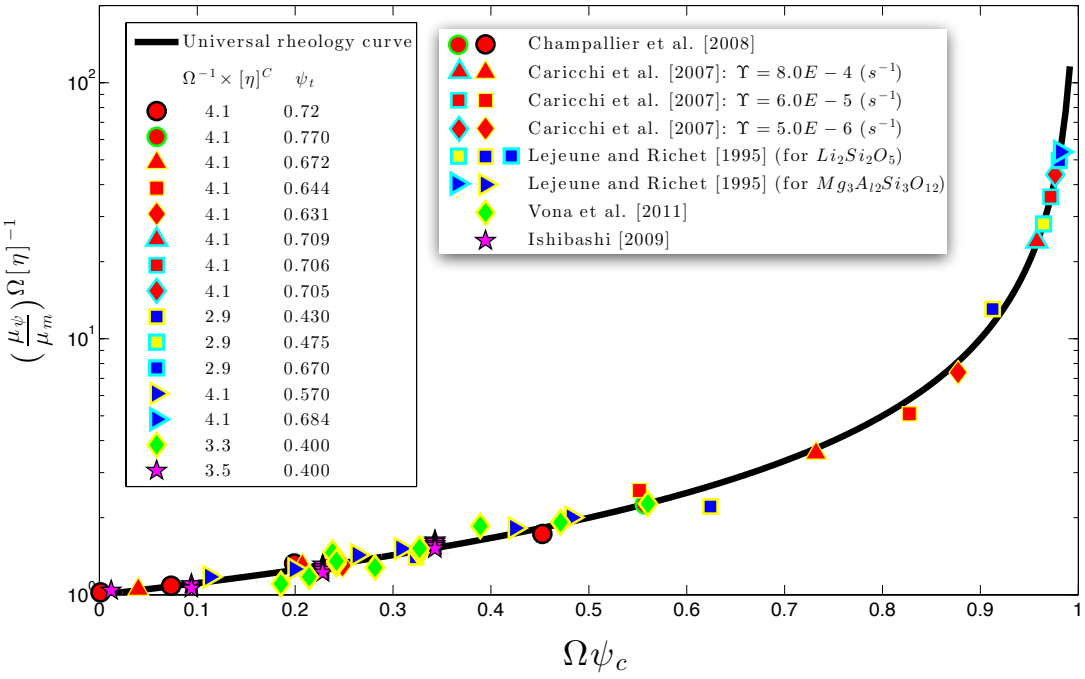

Figure 7.5: Same as in Fig. 7.4, but assuming different state variables for individual data beyond Region 1. Now each dataset with different ψ_t and $[\eta]^C$ can coincide with the unique rheological curve. This unification suggests that all experimental data are actually on a unified monotonic curve, but possess different state of dispersions. This also implies that, knowing $\Omega^{-1} \times [\eta]^C$ is constant in Region 1 and Region 2, an estimate of either the threshold packing limit or the intrinsic viscosity are the only requirements to develop a predictive rheology model.

maximum packing limit for a monomodal suspension with spheres, $\psi_{FC} = 0.7405$. Therefore, as no particle breakage is reported, it again indicates the presence of an anomaly. In this case, the anomaly was reported to be the presence of bubbles that facilitated the rate of deformation by localizing the shear.

CHAPTER VIII

APPLICATION II: HINDRANCE MODEL FOR SEDIMENTATION OF SPHERICAL PARTICLES

8.1 Introduction

The rate of particle settling and bubble rising in complex fluids has a wide range of applications in industry (e.g. pharmaceutical and fluidized bed reactors) and also in natural systems (e.g. sedimentation, emplacement and crystallization of magma, and bubble migration in vesiculating magmas). Understanding the force balance that governs the migration of particles (here bubbles, droplets and solid particles) suspended in a fluid and the effective viscosity are fundamental to quantify suspensions transport, sedimentation processes and the rate of phase segregation.

Although the relative velocity of a single crystal or bubble settling or rising in a quiescent fluid is well-characterized, the interplay of crystals/bubbles in multiparticle system, and the hindered velocity of a cloud of particles remains a challenging and important problem in many fields. In a complex fluid, particle motion undergoes fluctuations induced by hydrodynamic disturbances arising from neighboring particles. These hydrodynamic interactions eventually hinders the velocity of particles comparing to their individual motion in an infinite fluid. Based on the Smoluchowski's paradox (Sonshine *et al.* , 1966), two or more particles move faster than a single one in an unbounded fluid. However, the return flow induced by container walls and horizontal neighbors, satisfying the condition of no net overall flux of fluids across any horizontal plane, suppresses this paradox. Therefore, in a bounded system, an increase in drag force acting on particles is expected. The hindrance effects have been, to some extent, quantified and introduced through different models (Happel, 1958; Hasimoto, 1959; Oliver, 1961; Famularo & Happel, 1965; Wallis, 1969; Gal-Or, 1970; Barnea & Mizrahi, 1973; Schwarz, 1996; Koo, 2009; Blazejewski, 2012). In spite of a

large-body literature, a unified correlation on the relative hindered velocity applicable for both emulsions and suspensions of non-deformable particles over a wide range of particle concentration is still missing.

This chapter based on the rheology model developed in the previous chapters, aims at developing a theoretical model for the hindered velocity of particles in non-Brownian complex fluids with non-deformable fluid and solid particles in the creeping flow regime (low Reynolds numbers). To this end, we use the following assumptions"

- narrow size distribution of fluid particle inside the complex fluids (monomodal suspensions/emulsions),
- random initial distribution of particles,
- continuous and suspended phase are incompressible and immiscible,
- hydrodynamic interactions are the only reciprocal action accrued between particles and other interactions like kissing, tumbling and coalescence are neglected,
- fluid particles remains mostly spherical, i.e. $Ca < 1$.

Therefore, to predict the hindered velocity of a spherical particle inside a cloud of other particles, the model for a single particle velocity in an infinite complex fluids needs to be corrected for:

- the change in the effective viscosity (see previous chapters) and density of the bulk fluid,
- the effect of walls causing return flow,
- the short-range hydrodynamic interactions between particle mediated by the ambient fluid.

Note: the content of this chapter is published as:

Faroughi, S. A., & Huber, C. (2015). Unifying the relative hindered velocity in suspensions and emulsions of nondeformable particles. Geophysical Research Letters, 42(1), 53-59.

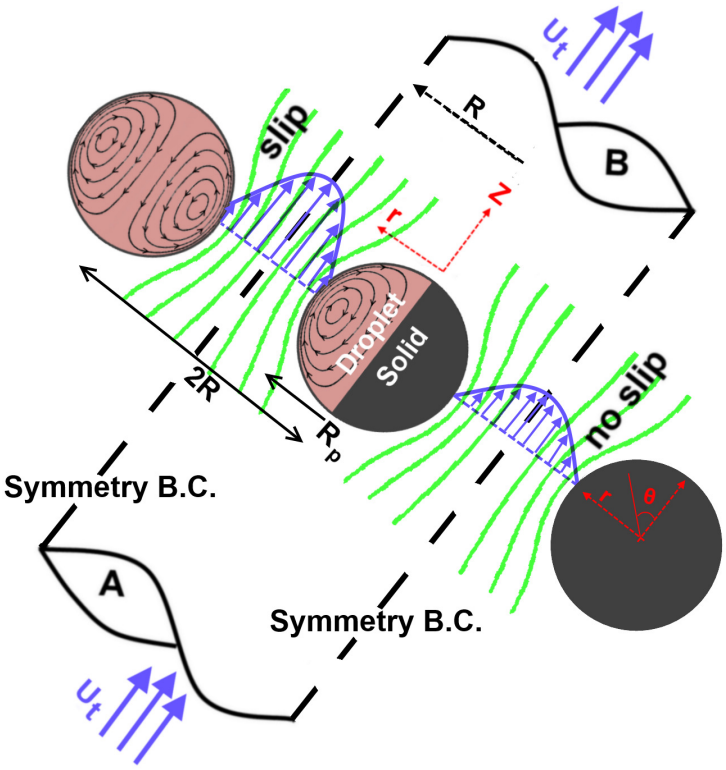

Figure 8.1: Conceptual model to predict the correction on drag coefficient caused by horizontal interactions; a streamtube containing a particle (can be either solid or fluid) with symmetry boundary condition.

8.2 Theory of suspensions settling

Stokes was the first to obtain a theoretical expression for the drag force, D, acting on a single spherical particle moving relative to a quiescent fluid at velocity U_t (Clift *et al.* , 2005),

$$D = 6\pi\mu_m U_t R_p. \tag{8.1}$$

This expression was later modified by Hadamard and Rybczynski (Clift *et al.* , 2005; Batchelor, 1967) independently to obtain the drag force acting on a single spherical fluid particle (droplet),

$$D = 2\pi\mu_m U_t R_p \left(\frac{2+3\lambda}{1+\lambda}\right). \tag{8.2}$$

Here, U_t is the relative terminal velocity for a single particle, R_p denotes the radius of the particle and λ is the viscosity ratio defined as a ratio of the viscosity of the dispersed

phase (μ_p) to that of the continuous fluid (μ_m) which for a solid particle $\lambda \to \infty$.

The effect of a cloud of particles on their buoyant migration through a viscous fluid is not only a function of ψ (particle volume fraction), but also of the ratio h/Γ (where h and Γ are characteristic lengths pertaining to the particle spacing and container size, respectively), especially in dilute systems where $\psi < 0.001$ (Sonshine *et al.* , 1966). In many industrial application, $h/\Gamma \ll 1$ and $\psi > 0.001$, thus we assume that the relative hindered velocity is only a function of ψ. This allows us to propose the following equation for the overall drag force acting on the surface of a particle inside a swarm of particles, so-called $D(\psi)$,

$$\frac{D(\psi)}{D} = f^{c_d}(\psi, \lambda) f^{\mu_m}(\psi, \lambda) \frac{U_\psi(\psi, \lambda)}{U_t}, \tag{8.3}$$

U_ψ represents the averaged relative velocity (hindered velocity) between particles and fluid, f^{c_d} and f^{μ_m} are respectively the local corrections on the drag coefficient and the viscosity of the continuous phase due to the presence of other particles in the complex fluids. The unknown correction function on the drag coefficient, f^{c_d}, is assumed to be composed of two parts. The first part, $f_N^{c_d}$, accounts for the change in drag coefficient due to the existence of neighboring particles and walls (return flow effect) in the plane normal to gravity (plane (r, ϕ) of the cylindrical coordinate system shown in Fig. 8.1) . The second part, $f_I^{c_d}$, accounts for shielding effects arising from the interaction of moving leading and trailing particles (Smoluchowski's effect) aligned with gravity (in the direction of z shown in Fig. 8.1). Other non-local interactions are conceptually modeled using the change in the effective viscosity because of the presence of other particles via f^{μ_m} that has been defined by Eq. (3.49) in chapter 3.

The ratio of the drag forces in Eq (8.3) can be calculated using the fact that in the steady state condition both drag forces are counterpoised with their correspond gravitational forces. Thus it becomes,

$$\frac{D(\psi)}{D} = \frac{G(\psi)}{G} = f^{\rho}(\psi). \tag{8.4}$$

As the volume fraction of the particles changes in the complex fluid, the effective hydrostatic pressure (the stress jump because of the difference in densities) changes. This effect

can by captured by the following definition for the complex fluid density, ρ_ψ, and using it as a replaced density for the ambient fluid density, ρ_m:

$$\begin{aligned} \rho_\psi &= \rho_p\psi + \rho_m(1-\psi) \\ \Delta\rho(\psi) &= \rho_\psi - \rho_p = (1-\psi)(\rho_m - \rho_p), \end{aligned} \tag{8.5}$$

$$\frac{G(\psi)}{G} = \frac{\Delta\rho(\psi)}{\Delta\rho} = 1-\psi, \tag{8.6}$$

where ρ_p is the density of particles. This argument is valid as long as buoyancy and drag are the dominant forces acting on particles. Substituting Eqs. (8.6) and (8.4) into Eq. (8.3), overall, one can find the following expression for the relative hindered velocity,

$$\frac{U_\psi}{U_t} = F(\psi,\lambda) = \frac{1-\psi}{f_N^{c_d} f_I^{c_d} f^{\mu_m}}, \tag{8.7}$$

where $F(\psi,\lambda)$ denotes the global hindrance function which is determined term by term in the following sections.

It should be noted that published theoretical and empirical relations and also experimental data documented in the literature, in order to determine the global correction function, mostly utilized different definitions and notations for the relative velocity between phases. These velocities are different to each other by a factor of ψ or $1-\psi$, in general. In Table 8.1 a list of these velocities and definitions is provided. For validation purposes, all published data and correlation are transformed into a consistent basis using Table 8.1.

8.3 Derivation of horizontal drag correction

The horizontal drag correction accounts for the hindrance associated with the return flow of ambient fluid in a bounded system. To quantify this correction, we consider a cluster of fluid particles that are positioned horizontally in the plane normal to gravity (particles are located in the plane (r,ϕ) as shown in Fig. 8.1). As the central distance between two particles in this cluster, $2R$ in Fig. 8.1, becomes smaller, the intensity of this correction is bigger and the velocity of particles is reduced.

Inspired by the model proposed in Oliver (1961), we shall consider a single incompressible fluid particle moving at velocity U_t through a clean (no surface tension gradients) and

Table 8.1: Different velocities used in the literature and their definitions

Velocity	Definition
U_t	Theoretical terminal velocity (relative velocity) for a single particle; Stokes solution for solid particle and Hadamard-Rybczynski solution for fluid particle.
U_∞	Experimental terminal velocity for a single particle in a infinite medium or in each individual setup.
$\overline{U}_p$	The averaged particle velocity in the suspension which is equal to the ratio of the superficial velocity of the particle (or volumetric flux q_p) over the particles volume fraction, ψ.
$\overline{U}_f$	The averaged continuous fluid velocity in the suspension which is equal to the ratio of the superficial velocity of the fluid (or volumetric flux q_f) over the fluid volume fraction, $(1-\psi)$.
U_ψ	The averaged relative velocity between particles and the continuous fluid determined by the vectorial difference of $\overline{U}_p$ and $\overline{U}_f$. For incompressible fluid and particle, it is equal to $\overline{U}_p(1-\psi)^{-1}$
U_s	The relative superficial velocity; vectorial difference between $\psi\overline{U}_p$ and $(1-\psi)\overline{U}_f$.

incompressible ambient fluid (or the particle is stationary and the ambient fluid is moving at $-U_t$). Based on the Hadamard-Rybczynski solution (see Clift *et al.* (2005)) obtained for a non-deformable spherical fluid particle in Stokes flow regime, we can write the following expression for the Stokes's stream function (and assuming an arbitrary streamtube bounding one particle to account for the change in drag) of the fluid flow in the ambient fluid, Ψ_m,

$$\Psi_m(r) = \frac{U_t r^2 sin^2\theta}{2}\left(1 - \left(\frac{R_p}{2r}\right)\frac{2+3\lambda}{1+\lambda} + \frac{1}{2}\left(\frac{R_p}{r}\right)^3\frac{\lambda}{1+\lambda}\right). \tag{8.8}$$

Here, R_p is the radius of the particle, and r is the radial coordinate system with the origin located at the center of the particle. To account for the presence of nearby particles in the plane normal to the gravity force (return flow effect), we consider a particle bounded by an arbitrary streamtube of radius $R > R_p$, as depicted in Fig. 8.1. The flow rate through this streamtube in the far field (far away from the particles causing perturbations in the flow) is $Q_f = \pi R^2 U_t$. We can also calculate the flow rate of the ambient fluid over a horizontal surface ($\theta = \pi/2$) crossing the center of the particle from streamlines ($\Psi_m(r)$) as $Q_s = 2\pi(\Psi_m(R) - \underbrace{\Psi_m(R_p)}_{zero})$,

$$Q_s = \pi U_t R^2\left(1 - \left(\frac{R_p}{2R}\right)\frac{2+3\lambda}{1+\lambda} + \frac{1}{2}\left(\frac{R_p}{R}\right)^3\frac{\lambda}{1+\lambda}\right). \tag{8.9}$$

Because both phases are incompressible, the flow rate through any cross section of the streamtube should be equal. Thus, the difference of flow rate ($Q_f - Q_s$) should be transported out of the streamtube. In the idealized geometry where other neighboring particles coexist in the same plane normal to gravity at a distance $2R$, streamlines cannot bend outward because of symmetry (see Fig. 8.1). Hence, the actual flow rate in the streamtube is modified by an increase in the drag force acting on the particle. The added drag force is similar to considering the following average countercurrent velocity against the particle motion,

$$U_c = U_t\left(\left(\frac{R_p}{2R}\right)\frac{2+3\lambda}{1+\lambda} + \frac{1}{2}\left(\frac{R_b}{R}\right)^3\frac{\lambda}{1+\lambda}\right). \tag{8.10}$$

Note, R is the radius of the streamtube which is equal to the halfway central distance between two particles on a horizontal surface as shown in Fig. 8.1. Using the volume

fraction definition for a homogeneous distribution of particles, we find the mean separation distance R proportional to $\psi^{\frac{1}{3}}$ Oliver (1961). This assertion is only valid for a homogeneous particle distribution in dilute complex fluids. Under dense packing conditions, a maximum random close packing fraction, i.e. the threshold packing ψ_t, should be introduced, therefore we assume that

$$\frac{R_p}{R} = \beta \left(\frac{\psi}{\psi_m} \right)^{\frac{1}{3}}, \tag{8.11}$$

where β is a geometrical proportionality constant, which is related to the shape of the streamtube in the real flow field. It will be shown later that $\beta = 0.45$ is the best value to fit the experimental data for random structure and that it does not depend on the viscosity ratio.

Finally, the horizontal local correction on drag caused by a cluster of particles located in the plane normal to gravity can be defined as the ratio of the terminal velocity of a single particle to that if the particle is hindered by being in the cluster, $f_N^{c_d}(\psi, \lambda) = U_t/(U_t - U_c)$, which yields

$$f_N^{c_d}(\psi, \lambda) = \left(1 - \frac{\beta}{2} \left(\frac{\psi}{\psi_m} \right)^{\frac{1}{3}} \frac{2 + 3\lambda}{1 + \lambda} + \frac{\beta^3}{2} \left(\frac{\psi}{\psi_t} \right) \frac{\lambda}{1 + \lambda} \right)^{-1}. \tag{8.12}$$

The magnitude of the correction provided by Eq. (8.12) is different when dealing with suspensions and emulsions because of the difference in boundary conditions on the surface of particles. For solid particles, no slip boundary condition results in less volumetric flux for return flow than for slip boundary condition on the surface of fluid particles as depicted in Fig. 8.1.

8.4 Derivation of vertical drag correction

In a complex fluids where horizontal clusters of particles are aligned along in the vertical direction, z, shown in Fig. 8.1, a reduction in drag even at low Reynolds number is expected owing to the fact that particles aligned with gravity experience significant acceleration due to viscous forces (Smoluchowski effect). Because the motion of particles is assumed to be in the creeping regime, this drag reduction, caused by short-range viscous effects, depends on the vertical distance between particles h (the central distance between the trailing and

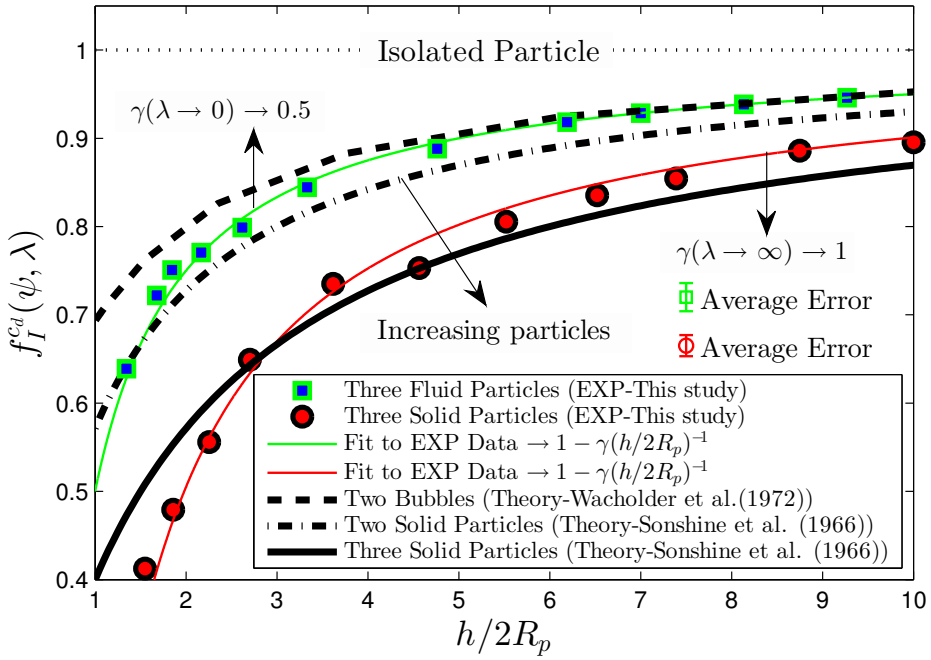

Figure 8.2: Theoretical and experimental data on drag coefficient reduction for two and three in-line descending particles which are aligned with gravity. See Table 8.3 for tabulated experimental data.

the leading particles). Sonshine *et al.* (1966) and Sonshine & Brenner (1966) showed that the intensity of these interactions increases when the number of particles in-line (number of horizontal clusters) increases or the vertical particle spacing h decreases.

In the creeping flow regime, based on Smoluchowski effect, leading and trailing particles aligned with gravity are interacting through a short-range viscous effects which depend on the vertical distance between particles h. This interaction decreases the drag coefficient on both leading and trailing particles. The results of Sonshine *et al.* (1966) highlight that the drag coefficient reduction follows approximately a function proportionally to $(h/2R_p)^{-1}$. Some of these analytical results are depicted in Fig. 8.2.

We performed a series of experiments ($Re \sim 10^{-2}$) with three equally-spaced particles moving parallel to their line-of-center, for both solid particles, using glass beads in 10000 CST (9.73 $Pa\ s$) silicone oil and fluid particles, using water in 10000 CST silicone oil, see Table 8.2 for more information about the properties of materials (and see Table8.3 for tabulated experimental data). These experiments are conducted in a large cylinder with radius

$\approx 40R_p$ and height $\approx 370R_p$. Results for the normalized drag force acting on the middle particle are depicted in Fig. 8.2. These empirical results confirm experimentally that the drag coefficient decreases proportional to $(h/2R_p)^{-1}$ for both solid and fluid particles. Assuming that the function $f_I^{cd}(\psi, \lambda)$ can be decomposed as $\Gamma(r, \theta, \psi)\Psi(z, \psi)$, where $\Gamma(r, \theta, \psi)$ is a measure of the areal density of particle perpendicular to the direction of gravity, we argue that $\Psi(z, \psi) \propto 2R_p/h \propto \psi/\psi_m$. Therefore, we can simply consider the following relationship based on the volume fraction to approximate the local viscous interactions,

$$f_I^{cd}(\psi, \lambda) = 1 - \beta^* \gamma(\lambda) \frac{\psi}{\psi_m}. \tag{8.13}$$

Here, β^* in a geometrical constant and we assume that the function γ is related to the boundary conditions at the surface of particles, thus we propose

$$\beta^* \gamma(\lambda) = \alpha \left(\frac{2 + 3\lambda}{1 + \lambda} \right) + \varepsilon. \tag{8.14}$$

α and ε are constants, however they can be function of the surface tension gradients if they exist. As the gradient of the surface tension increases, the rigidity of the surface increases, and consequently the shear force in the ambient fluid is balanced by the gradient in surface tension. In an extreme case, capillary forces suppress interface and internal circulations, and causes a fluid particle to behave like a solid particle. In the absence of surface tension gradients, we calculate the upper ($\lambda \to \infty$) and lower ($\lambda \to 0$) bounds of the function γ using the results of the in-line experiments shown in Fig. 8.2. These constraints allow us to obtain α and ε as 0.5 and -0.5, respectively.

8.5 Derivation for non-local interactions

As discussed in detail in Chapter 3, the existence of a cloud of particles inside a medium affects the mechanism by which momentum is diffused among particles through the ambient fluid or between a particle and the ambient fluid (considering the non-local interactions via the change in shear viscosity of the incompressible ambient fluid). This effect was studied in chapter 3 where we developed a generalized equation to determine the effective viscosity in concentrated emulsions subjected to a simple straining flow. When particles are not

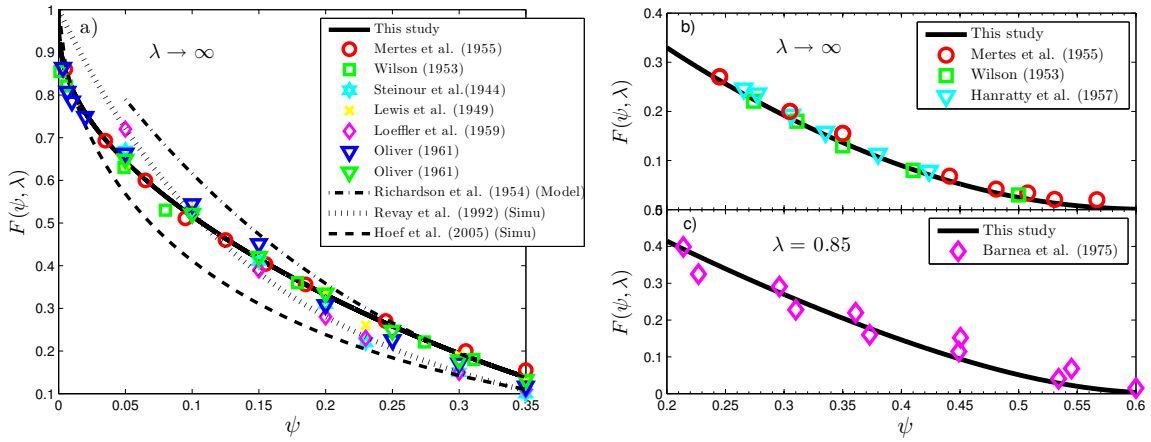

Figure 8.3: Comparison of the relative velocity predicted by the proposed model defined by Eq. (8.16) with a) published experimental data (Symbols) and three well-known models, for rigid solid particle suspensions ($\lambda \to \infty$); b) published experimental data in highly concentrated solid suspensions ($\lambda \to \infty$) and c) experiments on concentrated emulsions.

deformable, as assumed to be the case here, the generalized rheological equation reduces to to that of Eq. (3.48),

$$f^{\mu_m} = \frac{\mu_\psi}{\mu_m} = \left(\frac{\psi_t - \psi}{\psi_t(1-\psi)}\right)^{-\left(\frac{\psi_t}{1-\psi_t}\right)\left(\frac{1+2.5\lambda}{1+\lambda}\right)}. \tag{8.15}$$

To account for the change in viscosity ratio due to the presence of other particles, we correct the viscosity ratio to $\lambda_\psi = \lambda / f^{\mu_m}$.

8.6 Hindrance model

We obtain the final expression for the hindered velocity of a particle in complex fluids by substituting Eqs. (8.15), (8.13) and (8.12) into Eq. (8.7), which yields

$$\frac{U_\psi}{U_t} = F(\psi,\lambda) = \left(\frac{1-\psi}{1-\frac{1}{2}\left(\left(\frac{2+3\lambda}{1+\lambda}\right)-1\right)\frac{\psi}{\psi_t}}\right) \times \left(\frac{\psi_t - \psi}{\psi_t(1-\psi)}\right)^{\left(\frac{\psi_t}{1-\psi_t}\right)\left(\frac{1+2.5\lambda}{1+\lambda}\right)} \times \left(1 - \frac{\beta}{2}\left(\frac{\psi}{\psi_m}\right)^{\frac{1}{3}}\frac{2+3\lambda_\psi}{1+\lambda_\psi} + \frac{\beta^3}{2}\left(\frac{\psi}{\psi_t}\right)\frac{\lambda_\psi}{1+\lambda_\psi}\right). \tag{8.16}$$

Based on our assumptions, Eq. (8.16) is theoretically valid for systems of monomodal spherical particles. However, in nature, suspensions and emulsions generally involve polydisperse distributions of non-spherical particles. Therefore, the relative velocity of complex

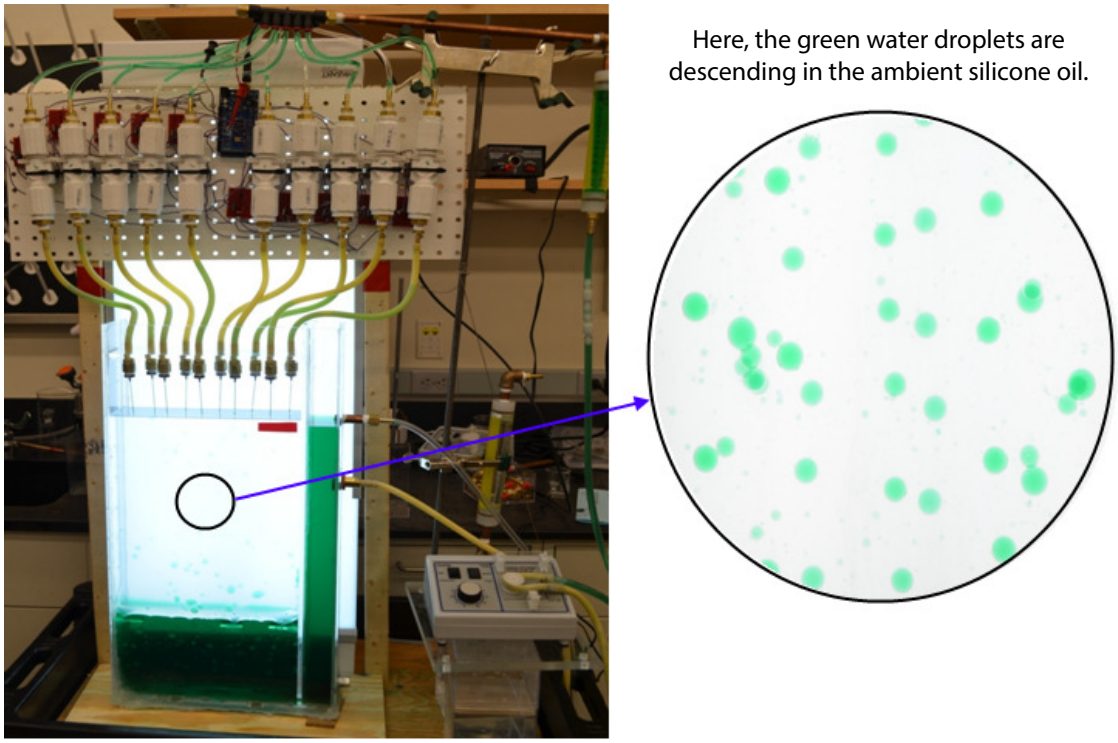

Figure 8.4: Experimental setup designed to measure the total hindrance function on the relative velocity for emulsions in the dilute regime. In experiments, the fluid flow is in the creeping regime and the method of continuous sedimentation is used to measure the relative velocity.

and more realistic systems depends not only on the volume fraction of the dispersed phase, but also on the particle shape, size ratio and size distribution. A first order correction on the hindered velocity model for polydisperse spheroids will be discussed in the next chapter.

To examine Eq. (8.16) a comprehensive experimental data for both suspensions and emulsions is required. In the literature, an extensive body of work has been devoted to solid particle sedimentation. However, only a few experiments have been reported for emulsions. Due to the lack of extensive data for emulsions in the creeping flow regime, we conducted a set of measurements for the relative hindered velocity in dilute emulsions (up to 10% particle volume fraction) that are presented in the next section.

8.7 Experiment setup

We used the method of continuous sedimentation Mertes & Rhodes (1955) by dropping the dispersed phase (dyed water in green) through a quiescent fluid (silicone oil) using

an injection system controlled by solenoid valves and adjusted in different arrangement to reduce local heterogeneities in dispersed phase concentration. The designed experimental setup is shown in Fig. 8.4 and the physical properties of the materials used are reported in Table 8.2. Photographs were taken during the experiment; one such photograph is shown in Fig. 8.4. During all experiments, the temperature was kept at $T = 20 \pm 1\,^{\circ}\mathrm{C}$ to avoid substantial changes in physical properties of materials. Note that in each set of experiments, we normalized the averaged relative velocity between interacting particles and the continuous fluid, U_ψ, using the terminal settling velocity, U_t, for a single fluid particles of the same averaged size measured separately. Please refer to Tables 8.4 and 8.5 for the tabulated experimental data.

8.8 Results

We use published experimental data in the creeping flow regime (see e.g.Barnea & Mizrahi (1973, 1975); Oliver (1961)) to test the ability of our model to predict the hindered velocity in different multiparticle systems. The comparison for dilute to intermediate particle concentration in suspensions ($\lambda \to \infty$) is depicted in Fig. 8.3(a), which shows a very good agreement between the model (using $\beta = 0.45$) and experimental data. In Figs. 8.3(b-c), we tested the model for two concentrated systems. Figure 8.3(b) shows a comparison between the values predicted by Eq. (8.16) and experimental data published in (Mertes & Rhodes, 1955; Wilson, 1953; Hanratty & Bandukwala, 1957) for a high range of solid particle concentration (up to 60%), and Fig. 8.3(c) shows the same comparison but with experiments involving dense emulsions. Note that the experimental data in Fig. 8.3(c) are provided in Barnea & Mizrahi (1975) for emulsions with $\lambda = 0.79$ and $\lambda = 0.92$, and we used an averaged value, $\lambda = 0.85$, in the model. In both comparisons, it is assumed that $\beta = 0.45$ which again highlights that β is a geometrical proportionality constant that does not depend on the boundary condition between the ambient and dispersed fluid phases. Based on these results, we see that the proposed model (Eq. (8.16)) predicts the relative velocity of particles in concentrated complex fluids very well.

The total hindrance function measured in our experiments for three different emulsions

Table 8.2: The physical properties of materials used in the experiments at $T = 20 \pm 1,^{\circ}$C

Dispersed	Continuous	μ_c $(Pa\ s)$	$\rho_d(Kg/m^3)$	$\rho_c(Kg/m^3)$	λ (—)	$\overline{R}_p(cm)$	$O(Re)$
Water	Silicone oil (10000CST)	9.73	998.2 ∓ 0.2	973.7 ∓ 0.1	1.0×10^{-4}	0.41	10^{-2}
Water	Silicone oil (5000CST)	4.86	998.2 ∓ 0.2	973.7 ∓ 0.1	2.0×10^{-4}	0.39	10^{-2}
Water	Silicone oil (1000CST)	0.97	998.2 ∓ 0.2	970.1 ∓ 0.2	1.0×10^{-3}	0.34	10^{-1}
Glass beads	Silicone oil (10000CST)	9.73	2450.5	973.7 ∓ 0.1	∞	0.25	10^{-2}

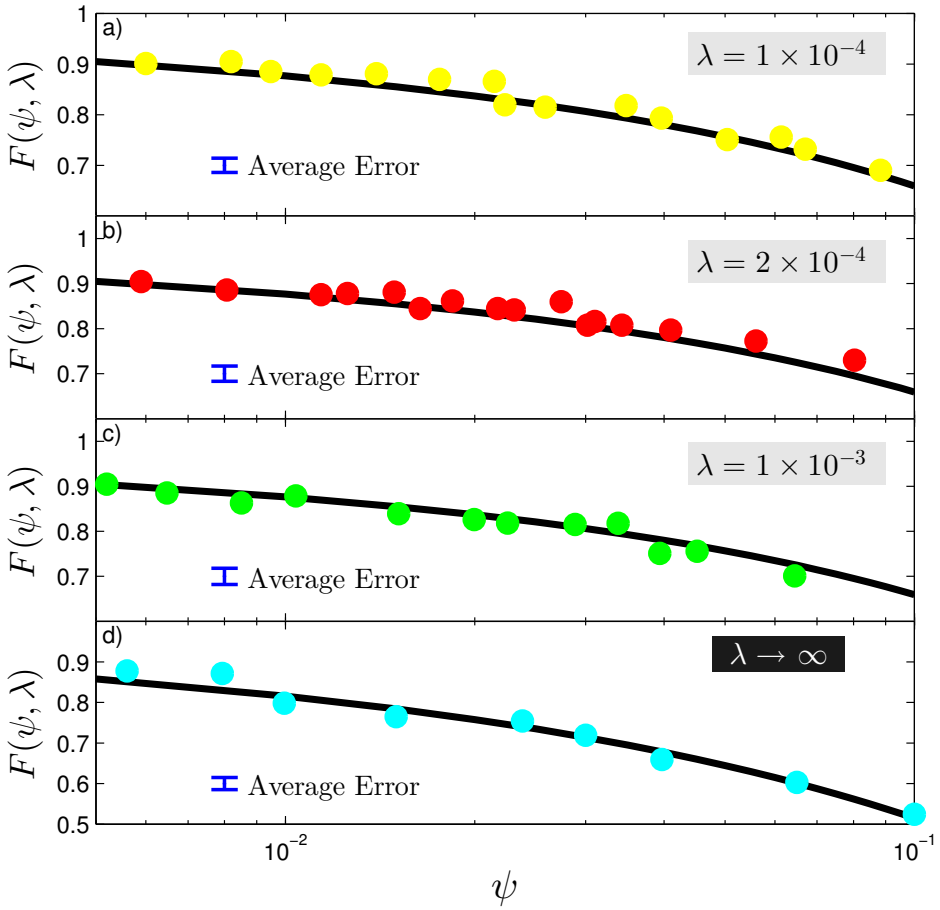

Figure 8.5: Comparison of values of the global hindrance factor predicted by Eq. (8.16) with new experimental data for dilute emulsions and suspension (see Tables 8.4 and 8.5 for tabulated experimental data).

and the prediction of Eq. (8.16) are compared in Figs. 8.5(a-c). We also performed an experiment for a dilute solid suspension shown in Fig. 8.5(d). The errorbars in Fig. 8.5 account for the dispersion around the average value of the measured experimental relative velocities. We observe that the model successfully reproduces the hindered velocity reduction of 35 to 50% depending on the viscosity ratio, over the dilute range of particle volume fraction ($\psi \leq 10\%$).

8.9 Application to crystal settling in magma chambers

We apply our theoretical model to study crystal settling in magma chambers following the model developed by Martin & Nokes (1988). We modified their model by replacing Stokes law with our hindered settling velocity to account for the particle volume fraction. Martin & Nokes (1989) proposed an exponential law to describe the decay of number of particles suspended in a convecting magma over time. The decay law was derived assuming that particles do not interact with each other and hinder settling. They found a good agreement between experiments, conducted at $\psi \leq 0.003$, and their exponential decay model, however it was found that the decay constant generally overestimated the settling efficiency even at these low volume fractions (their normalized decay constant is greater than predicted). Introducing our crystal settling law into the model of Martin & Nokes (1989), the decay law becomes,

$$\frac{\partial}{\partial t}\left(\frac{\psi}{1-\psi}\right) = -\frac{U_t}{L}\left(\frac{\psi}{1-\psi}\right) F(\psi, \lambda) \tag{8.17}$$

where L is the depth of the chamber and $F(\psi, \lambda)$ is calculated using Eq. (8.16). We solve Eq. (8.17) numerically with a Runge Kutta (4th order) solver for solid particle suspensions ($\lambda \to \infty$) starting with different initial volume fraction of particles. The volume fraction of particles that remain in suspension over time is plotted in Fig. 8.6(a). As expected, our results are in good agreement with those of Martin & Nokes (1989) at very low volume fraction of particles. However, as the initial concentration of crystals increases, the decay departs from exponential and becomes significantly slower than their predictions. Hindered settling increases the residence time of crystals in a convecting magma, the time for the

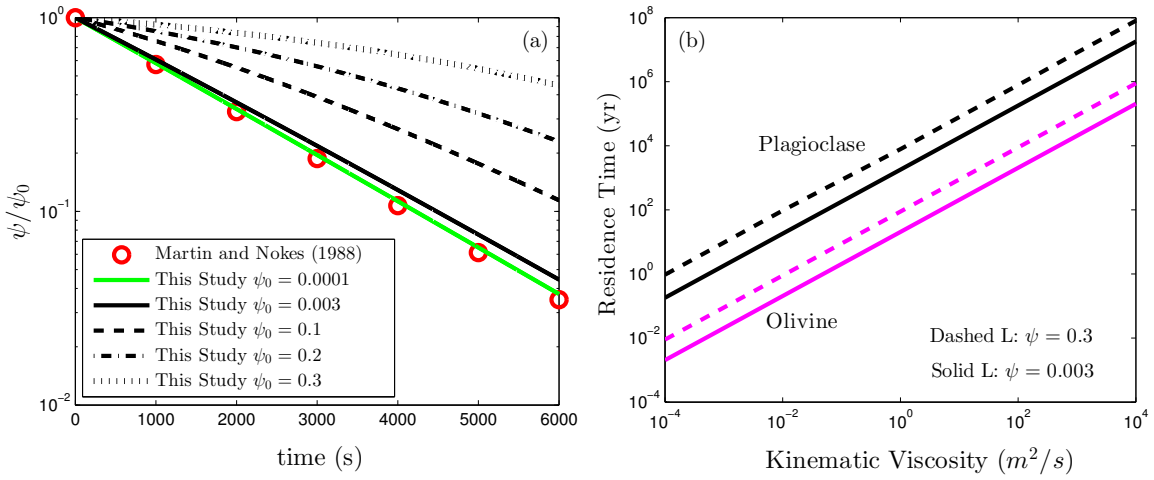

Figure 8.6: (a) Comparison of our model stated in Eq. (8.17) with the model of Martin & Nokes (1989) to predict the normalized volume fraction of crystals decaying with time in a system where we assume $U_t/L = 5.5 \times 10^{-4}$; (b) residence time of minerals in a kilometre thick magma chamber as function of melt kinematic viscosity Following Martin & Nokes (1988) we assumed $\Delta\rho = 50\ kg.m^{-3}$, $\rho_p = 2700\ kg.m^{-3}$ and $R_p = 0.05\ cm$ for plagioclase crystals and $\Delta\rho = 600\ kg.m^{-3}$, $\rho_p = 3300\ kg.m^{-3}$ and $R_p = 0.15\ cm$ for olivine crystals.

particle volume fraction to decrease by half, by up to a factor of 5 compared to Stokes settling law (see Fig. 8.6(a)).

Table 8.3: Experimental data presented in Fig 8.2. Each test was run three times to the best that was possible to adjust the initial distance between particles.

FIGURE 8.2 (three fluid particles)

Viscosity ratio (--)	suspended phase	continues phase	mean particle radius	Raynolds number (--)
0.0001	water	Silicon oil (10000CST)	0.3 cm	10^-2
	density (kg/m3)	density (kg/m3)		
	998.2 $^{+}_{-}$ 0.2	973.7 $^{+}_{-}$ 0.1		

$h/2R_p$ (--)	Drag Reduction (--)
1.68	0.722
1.35	0.6389
1.85	0.7507
2.17	0.7704
2.62	0.7988
3.33	0.8444
4.76	0.8881
6.19	0.9183
6.97	0.9286
8.14	0.9385
9.27	0.9461

Ave. dispersion around the mean drag reduction value (--)	0.016

FIGURE 8.2 (three solid particles)

Viscosity ratio (--)	suspended phase	continues phase	mean particle radius	Raynolds number (--)
infinity	Glass beads	Silicon oil (10000CST)	0.25 cm	10^-2
	density (kg/m3)	density (kg/m3)		
	2450.5	973.7 $^{+}_{-}$ 0.1		

$h/2R_p$ (--)	Drag Reduction (--)
1.55	0.4125
1.85	0.4791
2.25	0.5558
2.7	0.6492
3.62	0.735
4.56	0.753
5.52	0.8055
6.52	0.8353
7.39	0.8545
8.75	0.8859
9.98	0.8953

Ave. dispersion around the mean drag reduction value (--)	0.012

Table 8.4: Experimental data presented in Fig 8.5 (a) and (b). Each test was run three times, and, in each individual trial, the experiment was run for an hour to assure that the system reached to a dynamic equilibrium and that the results are reproducible.

FIGURE 8.5 (a)

Viscosity ratio (--)	suspended phase	continues phase	mean particle radius	Raynolds number (--)
0.0001	water	Silicon oil (10000CST)	0.41 cm	10^-2
	density (kg/m3)	density (kg/m3)		
	998.2 +- 0.2	973.7 +- 0.1		

Volume Fraction (--)	Relative Velocity (--)
0.0061	0.901
0.0081	0.9047
0.0094	0.8853
0.0113	0.8787
0.0139	0.8808
0.0175	0.8697
0.0214	0.8657
0.0223	0.8193
0.0258	0.815
0.0347	0.8179
0.0395	0.7931
0.0503	0.7509
0.0614	0.7556
0.0671	0.7318
0.0883	0.69

Ave. dispersion around the mean Relative velocity value (--)	0.014

FIGURE 8.5 (b)

Viscosity ratio (--)	suspended phase	continues phase	mean particle radius	Raynolds number (--)
2*0.0001	water	Silicon oil (5000CST)	0.39 cm	10^-2
	density (kg/m3)	density (kg/m3)		
	998.2 +- 0.2	973.7 +- 0.1		

Volume Fraction (--)	Relative Velocity (--)
0.0058	0.9044
0.008	0.8859
0.0114	0.8753
0.0125	0.8779
0.0148	0.881
0.0163	0.8443
0.0184	0.8615
0.0217	0.8446
0.0231	0.8414
0.0274	0.8596
0.0301	0.8076
0.031	0.8156
0.0342	0.8076
0.0409	0.7968
0.056	0.7726
0.0803	0.7301

Ave. dispersion around the mean Relative velocity value (--)	0.017

Table 8.5: Experimental data presented in Fig 8.5 (c) and (d). Each test was run three times, and, in each individual trial, the experiment was run for an hour to assure that the system reached to a dynamic equilibrium and that the results are reproducible.

FIGURE 8.5 (c)

Viscosity ratio (--)	suspended phase	continues phase	mean particle radius	Raynolds number (--)
0.001	water	Silicon oil (1000CST)	0.34 cm	10^-1
	density (kg/m3)	density (kg/m3)		
	998.2 +- 0.2	970.1 +- 0.2		

Volume Fraction (--)	Relative Velocity (--)
0.0051	0.9047
0.0064	0.8853
0.0085	0.8629
0.0103	0.8787
0.0151	0.839
0.0199	0.8259
0.0225	0.8183
0.0288	0.815
0.0337	0.8179
0.0393	0.7509
0.0451	0.7556
0.0645	0.7009

Ave. dispersion around the mean Relative velocity value (--)	0.017

FIGURE 8.5 (d)

Viscosity ratio (--)	suspended phase	continues phase	mean particle radius	Raynolds number (--)
infinity	Glass beads	Silicon oil (10000CST)	0.25 cm	10^-2
	density (kg/m3)	density (kg/m3)		
	2450.5	973.7 +- 0.1		

Volume Fraction (--)	Relative Velocity (--)
0.0056	0.878
0.0079	0.8715
0.0099	0.7981
0.015	0.7651
0.0238	0.7542
0.03	0.719
0.0396	0.6592
0.065	0.6031
0.1	0.5244

Ave. dispersion around the mean Relative velocity value (--)	0.015

CHAPTER IX

APPLICATION III: SEDIMENTATION OF NON-SPHERICAL PARTICLES - A HYDRODYNAMIC MODIFICATION ON HYDROMETER TEST

9.1 Introduction

Soils are commonly classified according to their particle size distribution. There is a direct relationship between the particle size distribution and other soil properties, such as the shear induced volume change, porosity, permeability and conductivity, consolidation and even nutrient retention. The most economical and reliable approaches to analyze the soil texture are sieving, for coarse-grained soils and the hydrometer and pipette tests for fine-grained soils. Sieving and hydrometer analyses are described in the standards of the American Society for Testing and Materials D6913-04 (2003) and D422-63 (2007) in details. Classical methods, aside from accuracy, are slow, operator- and instrument-dependent. However practically, sieve and hydrometer analyses (Bouyoucos, 1962; Day, 1965), are routinely applied to study the size distribution (nominal diameters) of coarse- and fine-grained soils, respectively.

The settling velocity for soil particles in the hydrometer test is based on Stokes law. As discussed in chapter 8, Stokes settling velocity results from the following assumptions; (i) the fluid flow around the particle is in the creeping flow regime (Reynolds number is much smaller than unity), (ii) particles are rigid and spherical, and finally (iii) the hydrodynamic interactions among particles in the suspension are neglected. The first assumption provides a constraint on the hydrometer test and its validity to particles with radius ranging from $0.1\ \mu m \leq r \leq 100\ \mu m$ (Lu *et al.* , 2000). However, this range of particle sizes can be increased by changing the shear dynamic viscosity of the suspending fluid. The lower bound, however, is a fixed limit because particles smaller than $0.1\mu m$ are colloids and

their behavior (Brownian motion) is not predictable with Stokes settling law. Therefore, practically speaking, this assumption does not invalidate the hydrometer test.

Soils particles are rarely spherical; they have irregular shapes ranging from platelet (e.g. kaolinite) to tubular (e.g. halloysite) and also display asperities and surface roughness. These particles experience complicated motions such as rotation and horizontal translation during sedimentation, unlike spherical particles. Therefore, the second assumption generally implies that Stokes' law does not lead to a true evaluation of the particle size distribution of soils. This problem has been addressed by many studies experimentally (Wen *et al.* , 2002; Konert & Vandenberghe, 1997; Nettleship *et al.* , 1997; Vitton & Sadler, 1997; Parslow & Jennings, 1986; Kunkel, 1948) and theoretically (Lu *et al.* , 2000), which has led to modifications to the treatment of the hydrometer test. In these modifications, the soil particles are approximated with randomly oriented spheroids with a specified aspect ratio $r_p = b/a$, where b is the polar radius and a is the equatorial radius, and the mean drag coefficient and settling velocity as function of the aspect ratio are calculated for a single particle (Lu *et al.* , 2000).

The effect of the third assumption, hydrodynamic interactions among the soil particles, is not accounted for in all previous studies. Therefore, the particle size distribution obtained through the conventional hydrometer test, for both spherical and non-spherical particles, has uncertainties that need to be addressed. This chapter investigates the hydrodynamic modification of the hydrometer test based on the hindrance model on the migration of particles when Brownian motion and inertial effects are neglected (high Péclet numbers and low Reynolds numbers). It is shown that hindrance resulting from hydrodynamic interactions greatly affects the residence time of particles in suspensions, and consequently the diameters of particles predicted by the hydrometer test.

Note: the content of this chapter is published as:

Faroughi, S. A., & Huber, C. (2016). A theoretical hydrodynamic modification on the soil texture analyses obtained from the hydrometer test. Gotechnique, 66(5), pp. 378-385.

9.2 Settling of non-spherical particles with in suspensions

In chapter 8, it is shown that the effect of hydrodynamic interactions on the terminal settling velocity of a particle within a suspension starts to be pronounced when $\psi > 0.001$, where ψ is the volume fraction of particles. The value of ψ in the hydrometer test is computed with

$$\psi = \frac{W_s}{W_s + G_s W_f}, \tag{9.1}$$

where W_s and W_f are the weight of the soil sample and the suspending fluid used in the hydrometer test, respectively, and G_s denotes the specific gravity of the soil particles. Based on ASTM D422-63 (2007), the value of ψ is roughly ranging from two to six percent. Therefore, hydrodynamic interactions among soil grains are important, and must be incorporated in the hydrometer test interpretation.

To characterize the hydrodynamic interactions in the soil sample inside the hydrometer, it is assumed that the suspension includes a homogeneous distribution of rigid particles that are settling through an incompressible fluid (e.g. water). Stokes' law provides the terminal velocity of a single particle in an infinite matrix, while in a bounded suspension, wall friction and return flow of the ambient fluid reduce the relative settling velocity. The hindrance velocity model for monomodal spherical droplet/particles settling in a complex fluids is derived in chapter 8 that for the solid particles reduces to,

$$\begin{aligned} H(\psi) = \left(\frac{1-\psi}{1-\frac{\psi}{\psi_t}}\right) \quad &\times \quad \left(1 - \frac{3\beta}{2}\left(\frac{\psi}{\psi_t}\right)^{\frac{1}{3}} + \frac{\beta^3}{2}\left(\frac{\psi}{\psi_t}\right)\right) \\ &\times \quad \left(1 - \Omega\frac{\psi}{1-\psi}\right)^{[\eta]\Omega^{-1}}, \end{aligned} \tag{9.2}$$

In Fig. 9.2, showing a very good agreement between Eq. (9.2) and experimental data on suspensions of spherical particles, one clearly observes that the velocity of particles might be hindered upto 40% in the range of particle volume fraction where the hydrometer test is operated (this range is shaded in Fig. 9.2). This reduction in velocity is even higher for non-spherical particles.

Suspensions of non-spherical particles may exhibit a non-Newtonian behavior even at small fraction of particles. We studied the effect of the particle shape on the rheology

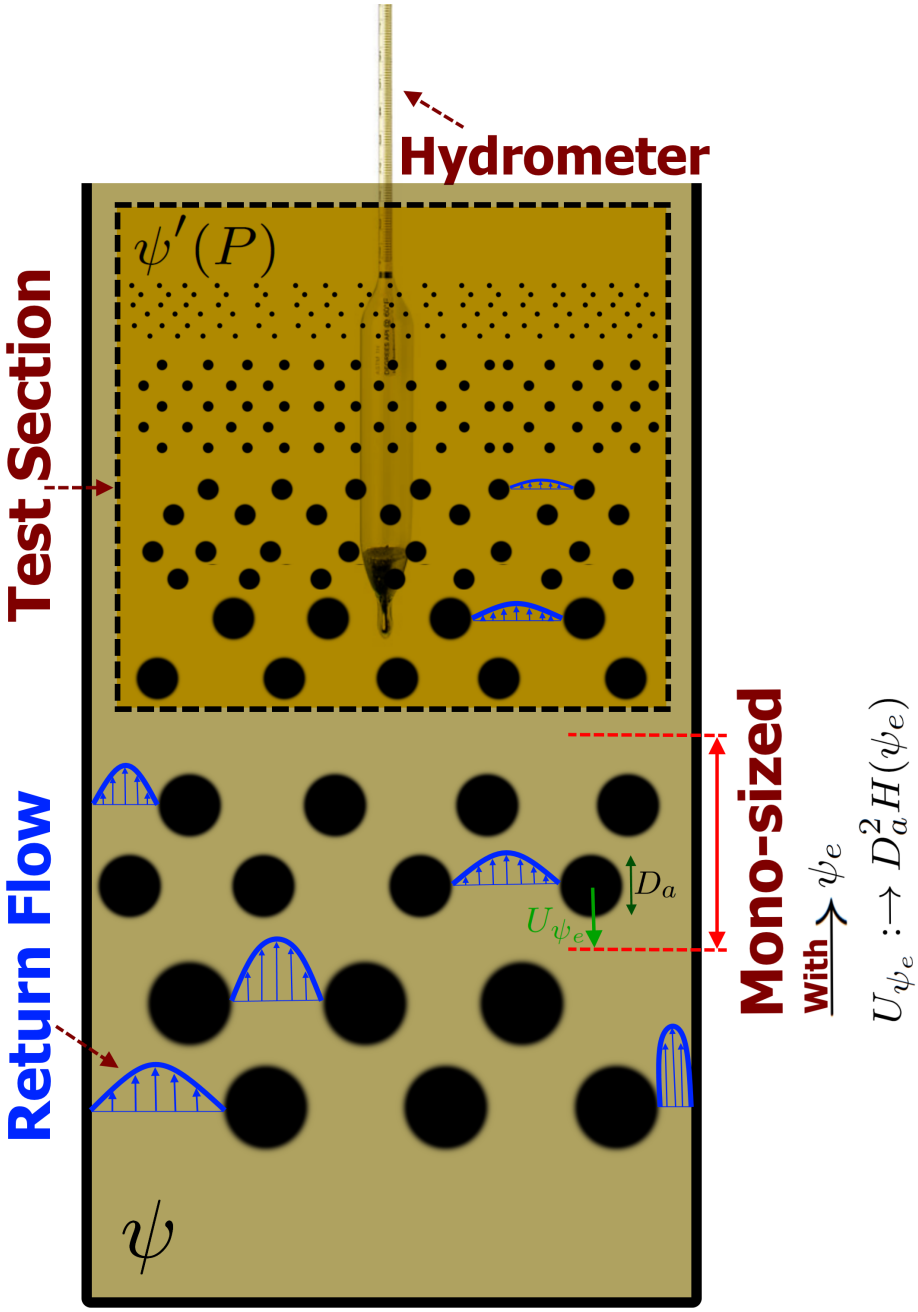

Figure 9.1: A schematic representation of the poly-disperse nature of soil sample in the hydrometer test and the hindrance effect due to return flow. For each quasi mono-disperse layer, the effective volume fraction ψ_e and hindered velocity U_{ψ_e} are calculated to obtain a correction on the particle diameter D_a.

of suspensions in chapter 6, and provided approximations for $[\eta]$ and ψ_t for non-spherical particle ranging from plate-like to rod-like shapes (see Eqs. (6.3), (6.6) and (6.7)). Here, oblate spheroids are used as a proxy for plate-like soil particles. For oblate spheroids with aspect ratio ranging $0.01 \leq R_p < 1$, the value of intrinsic viscosity and maximum close packing were approximated with (see chapter 6)

$$[\eta] = 2.5R_p + \frac{1012 + 2904R_p - 1855R_p^{1.5} - 2138.5R_p^2 + 77.94R_p^3}{1497R_p + R_p^2}, \tag{9.3}$$

$$\psi_t = 0.633 \left[\frac{166.74R_p + R_p^2}{5.08 + 193.38R_p - 124.94R_p^{1.5} + 57.77R_p^2 + 34.20R_p^3} \right]. \tag{9.4}$$

In Eq. (9.2), β is a proportionality constant

$$\beta = \frac{r}{\mathcal{L}} \left(\frac{\psi_t}{\psi} \right)^{1/3}, \tag{9.5}$$

that is related to the flow field around particles in the suspension (see chapter 8). This proportionality constant also requires a modification when dealing with non-spherical particles. In Eq. (9.5), $\mathcal{L}$ is a characteristic length of the medium, i.e. the mean diameter of a streamtube that encloses a particle in the suspension with particle volume fraction ψ. In chapter 8 we showed experimentally that β admits a value of 0.45 for spherical particles. The value of β changes as the particle shape departs from a sphere, i.e. we assume that $\beta = f(r_p, a, \psi_t)$ where a is the equatorial radius of the oblate spheroids. Based upon the proportionality between the packing configurations of spheres and oblate spheroids with equal volumes and using Eq. (9.5), we find

$$\beta(r_p) \approx \beta^{sphere} \times \left(\frac{1}{r_p} \right)^{1/3} \times \left(\frac{\psi_t^{oblate}}{\psi_t^{sphere}} \right)^{1/3}, \tag{9.6}$$

where $\beta^{sphere} = 0.45$. Equation (9.6) predicts that platy particles are characterized with higher β values, e.g. for oblate spheroids with aspect ratios $0.01 < R_p < 0.1$, the value of β varies between 0.895 and 1.3.

Note that the hindrance model, Eq. (9.2), is obtained for spherical particles where the attitude of falling does not affect the final velocity because of the symmetry. This

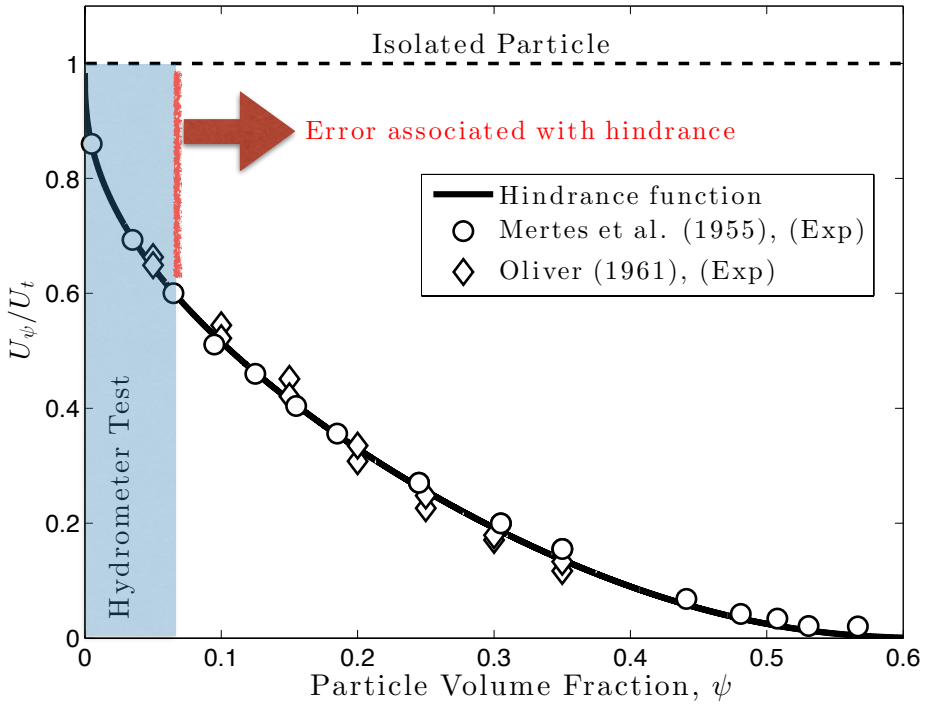

Figure 9.2: Comparison of the hindrance function with published experimental data conducted by Mertes et al. (1955) and Oliver (1961) on suspension of synthetic rigid spherical particles. For this calculation, we use $\psi_t = 0.633$, $[\eta] = 2.5$ and $\beta = 0.45$ to obtain the hindrance function proposed in Eq. (9.2). The shaded area highlights the typical volume fraction of solid particles at which the hydrometer test is performed.

model is then corrected for non-spherical particles (platelets) using the calculated values for the proportionality constant, the intrinsic viscosity and random close packing of randomly oriented spheroid particles, i.e. values are isotropically averaged over different attitudes. Therefore, the hindrance model, Eq. (9.2), can be applied to random configuration of spheroids, which may be a good approximation during the early stages of sedimentation of platelets.

9.3 Effect of Polydispersity on hydrodynamic correction

In the hydrometer test illustrated schematically in Fig. 9.1, the soil sample is poly-disperse. In many instances, the particle size may vary by up to three order of magnitudes (Lu *et al.* , 2000). However, the hindrance function, Eq. (9.2), is developed for suspensions of mono-disperse particles. In a poly-disperse suspension, the hindrance is not the same for

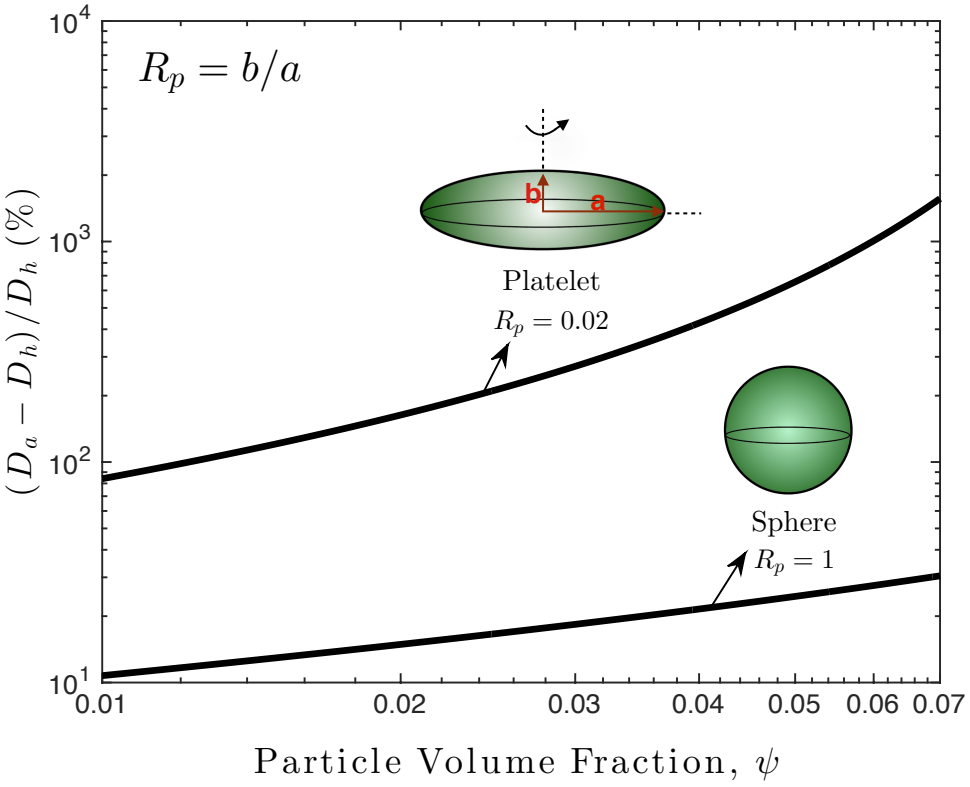

Figure 9.3: Comparison between the corrected and nominal diameters obtained by hydrometer test for monomodal spherical and plate-like particles. The percentage of error that affects the diameter estimation due to hindrance is plotted as function of the volume fraction of particles. To quantify the hindrance effect on the mono-disperse spherical particles with $R_p = 1$, we calculate $[\eta] = 2.5$ and $\psi_t = 0.633$ using Eqs. (9.3) and (9.4). The same set of equations retrieve $\psi_t = 0.243$ and $[\eta] = 35.58$ for mono-disperse plate-like particles possessing $R_p = 0.02$. β is calculated by Eq. (9.6).

all particles in the column. Practically, the smaller particles that settle slower are hindered more than larger particles. The reason for this phenomenon is that the larger particles cause more return flow (see Fig. 9.1), due to their size relative to the size of container, and also because larger particles travel ahead of the rest of the suspension. Thus, the small particle size classes encounter more resistance, and consequently, more hindrance. If one overlooks the effect of polydispersity, the hydrometer test results will underestimate the diameter of particles even when the hindrance processes described by Eq. (9.2) are accounted for.

The effect of polydispersity is here introduced by assuming that the sample consists of multiple mono-disperse size classes. The total hindrance that each size class experiences is composed of the hindrance associated with the volume fraction of particles ψ dispersed in

the column and an excess hindrance associated with the polydispersity accounting for the fact that larger particles settling at a faster rate increase the drag on smaller particles. The effective volume fraction of particles that causes the total hindrance is defined as,

$$\psi_e = \psi + \psi^*(P), \tag{9.7}$$

where

$$\psi^*(P) = \psi'|_{P=100} - \psi'(P), \tag{9.8}$$

represents the volume fraction of particles that leave the suspension at the level where the apparent density of the suspension is measured by the hydrometer. In Eq. (9.8), ψ' and P denote the volume fraction and the mass percentage of the soil grains that remain in the suspension at the measurement level. The definition of ψ' can be obtained from the expression of retained mass percentage, P. The mass percentage of the soil sample retained at the level of measurement is calculated using the first independent parameter (reading) of the test, called R in ASTM D422-63 (2007). Physically, R measures the specific gravity of the suspension at the measurement level, thus $R = \rho'_\psi/\rho_f$.

In the case where the method is applied to hydrometer 151H, the equation (1) of ASTM D422-63 (2007) can be written as

$$P = 100\frac{W_f}{W_s}\frac{G_s}{G_s - G_f}(R - G_f), \tag{9.9}$$

at the level where the hydrometer measures the density of the suspension. In Eq. (9.9), G_s and G_f are the specific gravity of the soil particles and the suspending fluid, $G_f = 1$ for water. The density of the suspension as function ψ' at the level of the measurement is determined using,

$$\rho'_\psi = \psi'\rho_s + (1 - \psi')\rho_f. \tag{9.10}$$

Alternatively, the last term of Eq. (9.9) can be written using the definition of the first reading, R, and Eq. (9.10)

$$R - G_f = \psi'(G_s - G_f). \tag{9.11}$$

Finally, the volume fraction of soil that remains in the suspension at the measurement level is

$$\psi' = \frac{P}{100}\frac{W_s}{G_s W_f}. \tag{9.12}$$

Substituting Eq. (9.12) into Eq. (9.8) leads to,

$$\psi^*(P) = \left(1 - \frac{P}{100}\right)\frac{W_s}{G_s W_f}. \tag{9.13}$$

where P is the mass percentage. If the soil sample is mono-disperse then $P \to 100\%$, and the effective volume fraction used in hindrance function reduces to the volume fraction of the soil sample, i.e. $\psi_e \to \psi$. ψ^* plays the role of an added volume fraction for each quasi mono-disperse layer to account for the extra hindrance caused by the larger size classes settling ahead.

In summary, the effective volume fraction that causes total hindrance on each separate mono-disperse layer of particles is determined

$$\psi_e = \frac{W_s}{W_s + G_s W_f} + \left(1 - \frac{P}{100}\right)\frac{W_s}{G_s W_f}, \tag{9.14}$$

and the total hindered velocity of a single particle within a poly-dispersed suspension is calculated using

$$U_{\psi_e} = U_t H(\psi_e) \tag{9.15}$$

where H, the total hindrance function is calculated from Eq. (9.2). Using this approach, one can see that the two independent parameters in the conventional hydrometer test, P and velocity are no longer decoupled.

It should be noted that the effect of hindrance varies with position and time for both mono and poly-disperse suspensions. Here, the effective volume fraction ψ_e is established as an averaged volume fraction to compute the hindrance on individual size classes, and correct the results obtained already by the standard hydrometer test.

9.4 Diameter modification in Hydrometer test

In the standard hydrometer test, the settling velocity of particles hindered due to the presence of other particles is experimentally measured. Stokes' law that totally neglects the

hindrance effect is then used to constrain the particles diameters based on the measured velocities, so-called nominal diameters (D422-63, 2007). Because of this disagreement between what is measured and what Stokes' theory implies, the standard hydrometer test always underestimates the (actual) particles diameters. To overcome this problem, a modification on the test results is required to include the effect of hindered particle settling on the predicted diameter of each mono-disperse layers. This modification amounts to

$$\text{Original test} \quad : \quad U_{\psi_e} \approx U_t :\rightarrow D_h^2, \tag{9.16}$$

$$\text{Modified test} \quad : \quad U_{\psi_e} = U_t H(\psi_e) :\rightarrow D_a^2 H(\psi_e), \tag{9.17}$$

where D_a represents the corrected diameter, D_h is the nominal diameter that is obtained from the original hydrometer test, and U_{ψ_e} is the total hindered velocity of a single particle sinking within a poly-dispersed suspension. Using Eqs. (9.16) and (9.17), the corrected particle diameters can be estimated with

$$D_a = D_h / \sqrt{H(\psi_e)}, \tag{9.18}$$

where ψ_e and H are computed with Eqs. (9.14) and (9.2), respectively.

For mono-disperse spheres and plate-like particles, the normalized difference between the corrected and original diameters, $(D_a - D_h)/D_h$, as function of the particle volume fraction in the suspension is illustrated in Fig 9.3. One observes that the error associated with mono-disperse hindrance increases as ψ increases, and as the particle shape departs from spherical. For instance, at a typical particle volume fraction of soil grains used for the hydrometer test, $\psi \approx 0.018$, the error associated with the estimation of the particle diameter ranges between 14 and 146 percent, if particles are spherical and platy upto aspect ration of $R_p = 0.02$, respectively. Additionally, it should be noted that neglecting the effect of polydispersity, introduced through the effective volume fraction, ψ_e, further increases the error on diameter predictions, especially for smaller size classes.

9.5 Results

The proposed model is tested against laboratory data obtained with the standard hydrometer and laser diffraction methods on the same soil samples. Several studies (Konert &

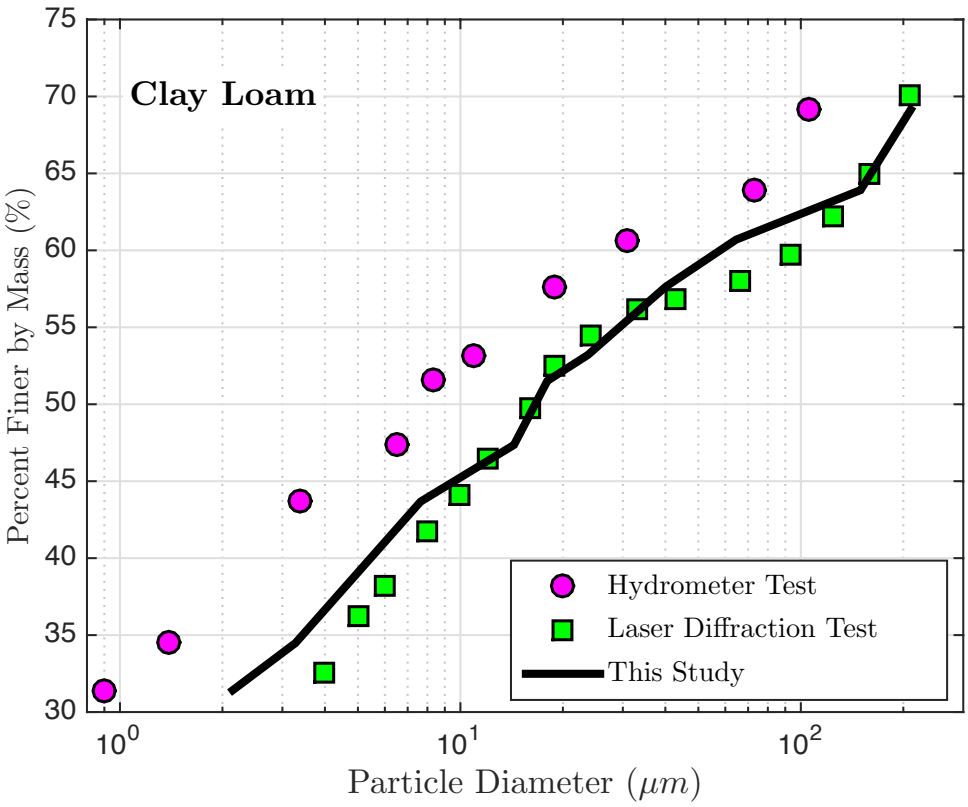

Figure 9.4: Comparison of the proposed model, Eq. (9.18), with the experimental data reported by Di Stefano *et al.* (2010) on Clay loam soil. Considering a plate-like shape for clay particles, we assume $R_p = 0.03$ and calculate $[\eta] = 24.29$, $\psi_t = 0.306$ and $\beta = 1.137$ using the approximations stated in Eqs. (9.3), (9.4) and (9.6) respectively to quantify the hindrance effect on the clay particles. Additionally, we use $\psi = 0.0182$ calculated from Eq. (9.1) with 50 grams of dried soil particles with $G_s \approx 2.7$ released in 1000 grams of water.

Vandenberghe, 1997; Ferro & Mirabile, 2009; Di Stefano *et al.* , 2010) have shown that results of particle size analysis for sedimentation (e.g. hydrometer and pipette) and laser diffraction techniques are comparable for coarse-grained particles, while there is considerable differences for fine-grained particles. As discussed earlier, the hydrometer technique considers a finite number of mono-disperse layers of particles, and provides the particle size distribution based on these divisions. While, the laser diffractometry method supplies a continuous curve for particle size distribution based on the fact that the light is diffracted at specific angles as function of the size of particles. In the analysis of laser diffraction data, it is commonly assumed that particle have a spherical shape, and the optical diameter of the particles is obtained from the measurement of their cross-sectional areas (Beuselinck

et al. , 1998; Di Stefano *et al.* , 2010). The studies of Beuselinck *et al.* (1998); Eshel *et al.* (2004) provide additional information about the laser diffraction method. Di Stefano *et al.* (2010) have shown that the clay content is overestimated and by extension the diameters of fine-grained (clay) particles is underestimated when comparing the results of the hydrometer test to laser diffraction data. This problem can be solved to some extent if one accounts for hindrance and polydispersity effects.

Equation (9.18) is tested against two sets of published experiments (Di Stefano *et al.* , 2010; Lu *et al.* , 2000). In these experiments, the aspect ratio of particles and the specific gravity for the considered soil sample have not been reported specifically. For soil particles, aspect ratio generally expresses the ratio of the major dimension (diameter) to that of the minor dimension, or vice versa that is applied in this study. For a platy clay particle the aspect ratio then reduces to the ratio of its thickness to its major planar diameter, and thus most likely the aspect ratio of particles varies for coarse and fine particles (Gantenbein *et al.* , 2011). For instance, Cornish kaolins possesses $R_p \approx 0.1$ for coarse particles and $R_p \approx 0.02$ for the fine grains (Slepetys & Cleland, 1993), see Weber *et al.* (2014); Slepetys & Cleland (1993); Gantenbein *et al.* (2011) for more details. In this study a representative (constant) aspect ratio is considered for all mono-disperse layers, and the specific gravity $G_s = 2.7$ is assumed for soil particles.

The first set of measurements was presented by Di Stefano *et al.* (2010) using Clay loam soil collected from the Sicilian basin, Imera Meridionale. The size distribution of the soil sample was analyzed with both standard hydrometer and laser diffraction methods leading to $D_{50}^H = 7\ \mu m$ and $D_{50}^L = 16\ \mu m$, respectively, as shown in Fig. 9.4. The proposed diameter modification, Eq. (9.18), is applied to account for the poly-dispersed hindrance effect on the standard hydrometer test results. For this example, we find $\psi = 0.0182$ using Eq. (9.1) based on the addition of 50 grams of dried soil particles with $G_s \approx 2.7$ into 1000 grams of water (see ASTM D422-63 (2007)). The effective volume fraction for each mono-sized layers of particles is computed using Eq. (9.14). Results for the modified particle size distribution are illustrated in Fig 9.4 as a solid line. A fixed aspect ratio for all mono-disperse layers is assumed, $R_p = 0.03$, which is an acceptable averaged aspect ratio for particle size ranging

from 1 μm to 100 μm (Lu *et al.* , 2000; Lambe & Whitman, 1969). The modified hydrometer test retrieves $D_{50} = 16\ \mu m$ which agrees well with the laser diffraction data. We also note an excellent agreement between the proposed model and laser diffraction data for the texture analysis of this soil sample over the whole range of particle sizes.

The second set of experiments was conducted by Lu *et al.* (2000) on Georgia kaolinite using the standard hydrometer method and laser diffraction analysis. It was shown that the actual average major dimension for the platy kaolinite particles obtained using the laser diffraction is comparable to the scanning electron microscope analysis, while the data from the standard hydrometer test underestimates it by a factor of about 4.5 (Lu *et al.* , 2000). The results of the soil particle size distribution form the laboratory measurements and Eq. (9.18) are shown in Fig. 9.5. Here, again, a fixed aspect ratio for all mono-disperse layers is assumed, $R_p = 0.02$. According to Fig. 9.5, the standard hydrometer test and laser diffraction retrieve $D_{50}^H = 0.55\ \mu m$ and $D_{50}^L = 2.5\ \mu m$, and the analysis using the modified method obtain $D_{50} = 2.1\ \mu m$. A very good agreement between the modified hydrometer test and the laser diffraction method is observed over the entire particle size distribution of Georgia kaolinite. It should be also noted that varying the value of aspect ratio results in a different particle size distribution based on Eq. (9.18), and if one considers different aspect ratios for different mono-disperse layers in the system a better agreement would be expected.

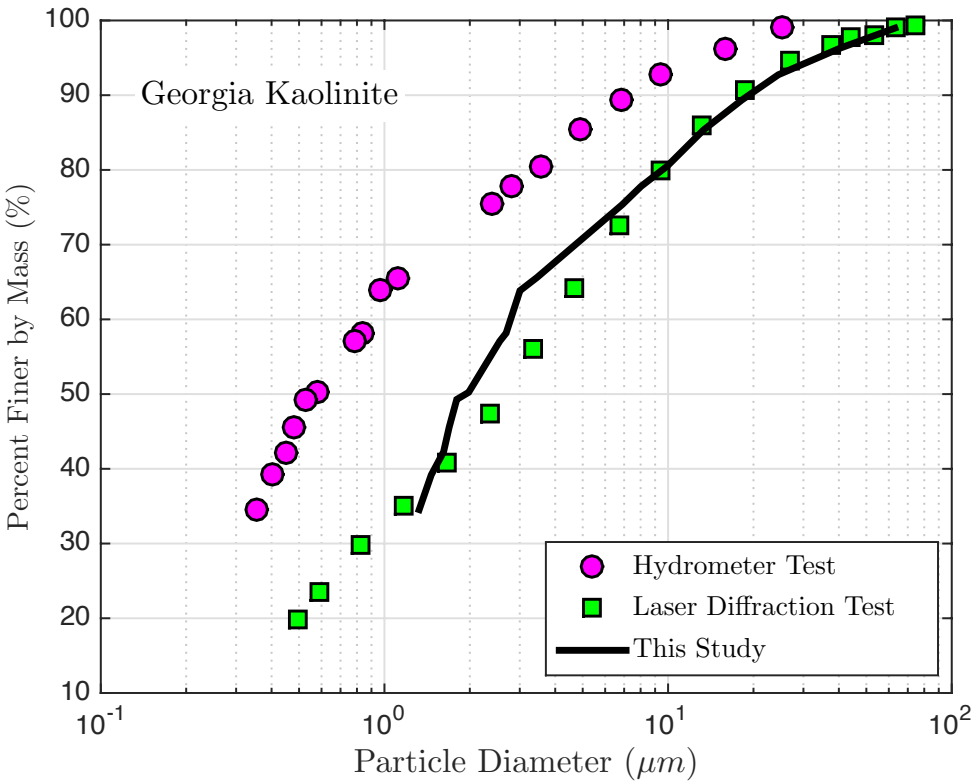

Figure 9.5: Comparison of the proposed model, Eq. (9.18), with the experimental data reported by Lu *et al.* (2000) on Georgia kaolinite soil. Considering a plate-like shape for kaolinite particles, we assume $R_p = 0.02$ and calculate $[\eta] = 35.58$, $\psi_t = 0.243$ and $\beta = 1.205$ using the approximations stated in Eqs. (9.3), (9.4) and (9.6) respectively to quantify the hindrance effect on the clay particles. Additionally, we use $\psi = 0.0182$ calculated from Eq. (9.1) with 50 grams of dried soil particles with $G_s \approx 2.7$ released in 1000 grams of water.

CHAPTER X

OTHER CONTRIBUTIONS AND FUTURE WORK

In this chapter, two other applications carried out during the course of the PhD are shortly discussed and followed by a discussion where several future directions are suggested.

10.1 Other studies carried out during this thesis

- Related to the Differential Effective Medium theory developed in chapter 3:

  We proposed a theoretical model to compute the effective thermal conductivity of metal and dielectric spherical particle reinforced composites with interfacial thermal resistance. We consider a wide range of filler volume fraction with sizes ranging from nano- to macro-scale. The model, based on the differential effective medium theory, accounts for particle interactions through two sets of volume fraction corrections discussed in chapter 3. The model is compared to other published models, experiments and numerical simulations for different types of composites. We observed an excellent agreement between the model and published datasets over a wide range of particle volume fractions and material properties of the composite constituents.

  This additional study is published under:

  Faroughi, S. A., & Huber, C. (2015). Effective thermal conductivity of metal and non-metal particulate composites with interfacial thermal resistance at high volume fraction of nano to macro-sized spheres. Journal of Applied Physics, 117(5), 055104.

- Related to the rheological and hindrance models developed in chapter 3 and 8, respectively:

  The analysis on the gravitational settling in suspensions led to study the buoyant migration of magmatic vapor phase in zoned magma reservoirs. By investigating the

fluid dynamics that controls the transport of the vapor bubbles in crystal-rich and crystal-poor magmas, we show how the interplay between capillary stresses and the viscosity contrast between the bubbles and the host melt results in a counterintuitive dynamics, whereby the vapor bubbles tends to migrate efficiently in crystal-rich parts of a magma reservoir and accumulate in crystal-poor regions. The accumulation of low-density bubbles in crystal-poor magmas has implications for the eruptive potential of magmas, and is the likely source of the excess sulfur released during explosive eruptions.

This study is also published under:
Parmigiani, A., Faroughi, S., Huber, C., Bachmann, O., & Su, Y. (2016). Bubble accumulation and its role in the evolution of magma reservoirs in the upper crust. Nature, 532(7600), 492-495.

10.2 Future work

Based on the theoretical developments discussed in this dissertation, several extensions and new direction can be outlined as follows.

- Developing a fully predictive rheology model for suspensions:

  The development of a predictive rheological model for suspensions requires additional experimental studies to better constrain the dependence of the state variables on the particle shape and particle size distribution under a wide range of shear conditions. Equation (3.49) along with Eqs. (6.6), (6.7), (6.12) and (6.13) suggest a framework for a predictive rheology model to parameterize the evolution of the microstructures and its effect on the effective viscosity of suspensions subjected to very low (near zero) shear rates. When suspensions are subjected to a broader range of shear conditions, the closure of the model depends on an additional degree of freedom. Under conditions where $\Omega^{-1}(\tau, r_p) \times [\eta(\tau, r_p)]^C$ again depends solely on the particle shape and not on the imposed shear condition, a predictive model can be constructed from either the knowledge of the threshold packing limit or the intrinsic viscosity of the suspension under different flow or stress conditions. Experimentally, the threshold packing limit

is easier to constrain as function of shear conditions. But, more experiments designed to test the dependence of $\Omega^{-1}(\tau, r_p) \times [\eta(\tau, r_p)]^C$ and hence the threshold packing limit with respect to the particle shape under various shear conditions are required to develop a fully predictive rheology model.

- Constrain $\Omega^{-1}(\tau, r_p) \times [\eta(\tau, r_p)]^C$ for wider ranges of particle aspect ratio and shear conditions:

  It would be significant to constrain $\Omega^{-1}(\tau, r_p) \times [\eta(\tau, r_p)]^C$ for a wider range of particle aspect ratio using particle-based numerical model, including Lattice Boltzmann, Immersed boundary and Discrete Element methods. In fact, using these models, one may study how microstructures evolve in complex fluids under different stress conditions, and how microstructure rearrangement impacts the mechanics and the rheophysics of complex fluids.

- A physical interpretation for $[\eta]^C$:

  It was shown that $[\eta]^C$ differs from $[\eta]^D$, and varies with microstructural changes. At this point, no clear physical definition is found for $[\eta]^C$. One may study the physical meaning of $[\eta]^C$ using particle-based simulations to understand its relation with the crowding factor, Ω (which physically accounts for the ratio of dead fluid between particles and fraction of particles at jamming condition). It would be also beneficial to constrain how polydispersity and possible shear-induced heterogeneities developed during deformation affect $[\eta]^C$.

- Mechanic of composites using Differential Effective Medium theory:

  The Differential Effective Medium theory developed in chapter 3 can be simply employed to study other mechanical properties of complex fluids and composites with different particle size (as have been performed for the effective thermal conductivity). Such properties for composites may include Poisson's ratio, shear modulus, elastic modulus and other thermophysical proprieties.

CHAPTER XI

CONCLUSIONS

This dissertation aims at studying of the effective shear viscosity of complex fluids from a process-based point of view. A generalized rheology model is first developed to determine the relative viscosity of concentrated complex fluids made of two Newtonian incompressible and immiscible fluids under a simple straining flow. In the derivation, two volume corrections are introduced. The first correction accounts for a finite spatial domain where the addition of a particle requires the removal of the same volume of the ambient fluid. The second volume correction accounts for the amount of the matrix inaccessible to other particles and trapped in the interstices formed by particles through a self-crowding factor. The resulting general model is a function of the viscosity ratio, capillary number (or particle deformation), particle volume fraction and the threshold volume fraction for random close packing of particles. The theoretical model is then extended to account for the effect of bimodal particle size distributions on the rheology of suspensions of solid spherical particles. Various processes that lead to non-Newtonian behaviors in concentrated suspensions are reviewed and discussed, and ways to include them in the rheology model are proposed. The model is then extended to the suspensions of rigid, bi-axially symmetric ellipsoids that allows to characterize the effect of the particles aspect ratio and applied shear conditions on the viscosity of suspensions.

The introduction of two state variables, the intrinsic viscosity $[\eta]^C$ and the self-crowding factor Ω, is used to study microstructural rearrangement and evolution in suspensions. The state variables approach defines the state of dispersion of particles in a suspension. It is found that the experimental data conducted on suspension with rigid solid particles of arbitrary shapes can be collapsed on a unique rheological curve, which requires only the knowledge of the state of dispersion by measuring either $[\eta]^C$ or Ω. The intrinsic viscosity $[\eta]^C$ and the self-crowding factor Ω are strongly interrelated and isolating their

individual dependency on the shearing conditions and particle shape is difficult. Using published experimental data conducted with spherical particles, it is shown that the product $\Omega^{-1} \times [\eta]^C$ is invariant with respect to the induced shear stresses, and $\Omega^{-1} \times [\eta]^C \approx 4.1$. A similar invariant for suspensions involving non-spherical particles is then postulated. Using available published experimental and numerical data, it is confirmed that $\Omega^{-1}(\tau, r_p) \times [\eta(\tau, r_p)]^C$ depends only on the particle shape and that this dependency can be constrained for suspensions including particles with aspect ratios ranging from plate-like to rod-like particles.

The self-similar behavior of the rheology model proposed here suggests the existence of a predictive rheology model for the effective viscosity of suspensions of rigid particles at low shear stresses (or shear rates), where the threshold packing limit as well as $\Omega^{-1}(\tau, r_p) \times [\eta(\tau, r_p)]^C = \mathfrak{f}(r_p)$ are fully constrained. Alternatively, the same approach can be used to retrieve the state variables (self-crowding factor and intrinsic viscosity) characterizing the state of dispersion of suspensions with particles of different shapes deformed under different flow conditions. This approach, however, still needs to be further tested for a wider range of particle shape and shearing condition. To this end, a set of experiments designed to test the relation of $\Omega^{-1} \times [\eta]^C$ with the particle shape and applied shear conditions is required.

REFERENCES

Abedian, B, & Kachanov, M. 2010. On the effective viscosity of suspensions. *International Journal of Engineering Science*, **48**(11), 962–965.

Arbaret, L., Bystricky, M., & Champallier, R. 2007. Microstructures and rheology of hydrous synthetic magmatic suspensions deformed in torsion at high pressure. *Journal of Geophysical Research*, **112**(B10208).

Arp, P. A., & Mason, S. G. 1977. The kinetics of flowing dispersions: VIII. Doublets of rigid spheres (theoretical). *Journal of Colloid and Interface Science*, **61**(1), 21–43.

Arzi, A. 1978. Critical phenomena in the rheology of partially melted rocks. *Tectonophysics*, **44**, 173–184.

Avazmohammadi, Reza, & Ponte Castañeda, Pedro. 2015. The rheology of non-dilute dispersions of highly deformable viscoelastic particles in Newtonian fluids. *Journal of Fluid Mechanics*, **763**, 386–432.

Bagdassarov, N, & Dorfman, A. 1998. Granite rheology: magma flow and melt migration. *Journal of the Geological Society*, **155**(5), 863–872.

Bagdassarov, N Sh, & Dingwell, Donald B. 1992. A rheological investigation of vesicular rhyolite. *Journal of volcanology and geothermal research*, **50**(3), 307–322.

Barnea, E, & Mizrahi, J. 1973. A generalized approach to the fluid dynamics of particulate systems: Part 1. General correlation for fluidization and sedimentation in solid multiparticle systems. *The Chemical Engineering Journal*, **5**(2), 171–189.

Barnea, E, & Mizrahi, J. 1975. A generalised approach to the fluid dynamics of particulate systems part 2: sedimentation and fluidisation of clouds of spherical liquid drops. *The Canadian Journal of Chemical Engineering*, **53**(5), 461–468.

Barnes, H. A. 1995. A review of the slip (wall depletion) of polymer solutions, emulsions and particle suspensions in viscometers: its cause, character, and cure. *Journal of Non-Newtonian Fluid Mechanics*, **56**(3), 221–251.

Barnes, H. A., & Carnali, J. O. 1990. The vane-in-cup as a novel rheometer geometry for shear thinning and thixotropic materials. *Journal of Rheology*, **34**(6), 841–866.

Barthelmes, G, Pratsinis, SE, & Buggisch, H. 2003. Particle size distributions and viscosity of suspensions undergoing shear-induced coagulation and fragmentation. *Chemical Engineering Science*, **58**(13), 2893–2902.

Batchelor, G. K. 1967. *An introduction to fluid dynamics*. Cambridge University Press.

Batchelor, G. K., & Green, J. T. 1972. The determination of the bulk stress in a suspension of spherical particles to order c2. *Journal of Fluid Mechanics*, **56**(3), 401–427.

Bénito, Sylvain, Bruneau, C-H, Colin, Thierry, Gay, Cyprien, & Molino, François. 2008. An elasto-visco-plastic model for immortal foams or emulsions. *The European Physical Journal E*, **25**(3), 225–251.

Bertevas, Erwan, Fan, Xijun, & Tanner, Roger I. 2010. Simulation of the rheological properties of suspensions of oblate spheroidal particles in a Newtonian fluid. *Rheologica acta*, **49**(1), 53–73.

Beuselinck, Laurent, Govers, Gerard, Poesen, Jean, Degraer, G, & Froyen, Ludo. 1998. Grain-size analysis by laser diffractometry: comparison with the sieve-pipette method. *Catena*, **32**(3), 193–208.

Biazzo, Indaco, Caltagirone, Francesco, Parisi, Giorgio, & Zamponi, Francesco. 2009. Theory of amorphous packings of binary mixtures of hard spheres. *Physical review letters*, **102**(19), 195701.

Bicerano, J., Douglas, J. F., & Brune, D. A. 1999. Model for the viscosity of particle dispersions. *Journal of Macromolecular Science, Part C: Polymer Reviews*, **39**(4), 561–642.

Blazejewski, Ryszard. 2012. Apparent viscosity and settling velocity of suspensions of rigid monosized spheres in Stokes flow. *International Journal of Multiphase Flow*, **39**, 179–185.

Boek, ES, Coveney, PV, Lekkerkerker, HNW, & van der Schoot, PPAM. 1997. Simulating the rheology of dense colloidal suspensions using dissipative particle dynamics. *Physical Review E*, **55**(3), 3124.

Bossis, Georges, & Brady, John F. 1984. Dynamic simulation of sheared suspensions. I. General method. *The Journal of chemical physics*, **80**(10), 5141–5154.

Bournonville, B, Coussot, P, & Chateau, X. 2004. Modification du modèle de Farris pour la prise en compte des interactions géométriques d?un mélange polydisperse de particules. *Rhéologie*, **7**, 1–8.

Bouyoucos, George John. 1962. Hydrometer method improved for making particle size analyses of soils. *Agronomy Journal*, **54**(5), 464–465.

Boyer, F., Guazzelli, E., & Pouliquen, O. 2011. Unifying suspension and granular rheology. *Physical Review Letters*, **107**(188301).

Brady, J. F., & Bossis, G. 1988. Stokesian dynamics. *Annual review of fluid mechanics*, **20**, 111–157.

Brenner, Howard. 1974. Rheology of a dilute suspension of axisymmetric Brownian particles. *International journal of multiphase flow*, **1**(2), 195–341.

Brinkman, H. C. 1952. The viscosity of concentrated suspensions and solutions. *The Journal of Chemical Physics*, **20**(4), 571–571.

Brouwers, H. J. H. 2010. Viscosity of a concentrated suspension of rigid monosized particles. *Physical Review E*, **81**(5), 051402.

Brouwers, H. J. H. 2013. Random packing fraction of bimodal spheres: An analytical expression. *Physical Review E*, **87**(032202).

Brown, Eric, & Jaeger, Heinrich M. 2014. Shear thickening in concentrated suspensions: phenomenology, mechanisms and relations to jamming. *Reports on Progress in Physics*, **77**(4), 046602.

Brown, Eric, Forman, Nicole A, Orellana, Carlos S, Zhang, Hanjun, Maynor, Benjamin W, Betts, Douglas E, DeSimone, Joseph M, & Jaeger, Heinrich M. 2010. Generality of shear thickening in dense suspensions. *Nature materials*, **9**(3), 220–224.

Brumby, Paul E, Sato, Toru, Nagao, Jiro, Tenma, Norio, & Narita, Hideo. 2015. Coupled LBM–DEM Micro-scale Simulations of Cohesive Particle Erosion Due to Shear Flows. *Transport in Porous Media*, 1–18.

Buscall, R. 2010. Letter to the Editor: Wall slip in dispersion rheometry. *Journal of Rheology*, **54**(6), 1177–1183.

Buscall, R., McGowan, J. I., & MortonJones, A. J. 1993. The rheology of concentrated dispersions of weakly attracting colloidal particles with and without wall slip. *Journal of Rheology*, **37**(4), 621–641.

Caricchi, L., Burlini, L., Ulmer, P., Gerya, T., Vassalli, M., & Papale, P. 2007. Non-Newtonian rheology of crystal-bearing magmas and implications for magma ascent dynamics. *Earth and Planetary Science Letters*, **264**, 402–419.

Carotenuto, Claudia, Vananroye, Anja, Vermant, Jan, & Minale, Mario. 2015. Predicting the apparent wall slip when using roughened geometries: A porous medium approach. *Journal of Rheology (1978-present)*, **59**(5), 1131–1149.

Chaffey, C. E., & Brenner, H. 1967. A second-order theory for shear deformation of drops. *Journal of Colloid and Interface Science*, **24**(2), 258–269.

Champallier, R., Bystricky, M., & Arbaret, L. 2008. Experimental investigation of magma rheology at 300 MPa: From pure hydrous melt to 76 vol.% of crystals. *Earth and Planetary Science Letters*, **267**, 571–583.

Chang, C., & Powell, R. L. 1994. Effect of particle size distributions on the rheology of concentrated bimodal suspensions. *Journal of Rheology*, **38**(1), 85–98.

Chang, C., & Powell, R. L. 2002. Hydrodynamic transport properties of concentrated suspensions. *AIChE journal*, **48**(11), 2475–2480.

Cheng, Z., Zhu, J., Chaikin, M., P., Phan, S. E., & Russel, W. B. 2002. Nature of the divergence in low shear viscosity of colloidal hard-sphere dispersions. *Physical Review E*, **65**(041405).

Choi, Seung Jung, & Schowalter, WR. 1975. Rheological properties of nondilute suspensions of deformable particles. *Physics of Fluids (1958-1988)*, **18**(4), 420–427.

Chong, J. S., Christiansen, E. B., & Baer, A. D. 1971. Rheology of concentrated suspensions. *Journal of Applied Polymer Science*, **15**(8), 2007–2021.

Cichocki, B., & Felderhof, B. U. 1991. Linear viscoelasticity of semidilute hard-sphere suspensions. *Physical Review A*, **43**(10), 5405.

Cimarelli, C., Costa, A., Mueller, S., & Mader, H. M. 2011. Rheology of magmas with bimodal crystal size and shape distributions: Insights from analog experiments. *Geochemesty Geophysics Geosystems*, **12**(Q07024).

Claeys, Ivan L, & Brady, John F. 1993a. Suspensions of prolate spheroids in Stokes flow. Part 1. Dynamics of a finite number of particles in an unbounded fluid. *Journal of Fluid Mechanics*, **251**, 411–411.

Claeys, Ivan L, & Brady, John F. 1993b. Suspensions of prolate spheroids in Stokes flow. Part 2. Statistically homogeneous dispersions. *Journal of Fluid Mechanics*, **251**, 443–477.

Claeys, Ivan L, & Brady, John F. 1993c. Suspensions of prolate spheroids in Stokes flow. Part 3. Hydrodynamic transport properties of crystalline dispersions. *Journal of Fluid Mechanics*, **251**, 479–500.

Clarke, AS, & Wiley, JD. 1987. Numerical simulation of the dense random packing of a binary mixture of hard spheres: Amorphous metals. *Physical Review B*, **35**(14), 7350.

Clift, Roland, Grace, John R, & Weber, Martin E. 2005. *Bubbles, drops, and particles.* Courier Corporation.

Clusel, Maxime, Corwin, Eric I, Siemens, Alexander ON, & Brujić, Jasna. 2009. A granocentricmodel for random packing of jammed emulsions. *Nature*, **460**(7255), 611–615.

Cordonnier, B., Hess, K. U., Lavallée, Y., & Dingwell, D. B. 2009. Rheological properties of dome lavas: Case study of Unzen volcano. *Earth and Planetary Science Letters*, **279**, 263–272.

Cordonnier, B., Caricchi, L., Pistone, M., Castro, J., Hess, K. U., Manga, M., Dingwell, D.B., & Burlini, L. 2012a. The viscous-brittle transition of crystal-bearing silicic melt: Direct observation of magma rupture and healing. *Geology*, **40**(7), 611–614.

Cordonnier, B., Schmalholz, S. M., Hess, K. U., & Dingwell, D. B. 2012b. Viscous heating in silicate melts: An experimental and numerical comparison. *Journal of Geophysical Research*, **117**(B02203).

Costa, A. 2005. Viscosity of high crystal content melts: Dependence on solid fraction. *Geophysical Research Letters*, **32**(L22308).

Costa, A., Caricchi, L., & Bagdassarov, N. 2009. A model for the rheology of particle-bearing suspensions and partially molten rocks. *Geochemesty Geophysics Geosystems*, **10**(Q03010).

Coussot, P. 2005. *Rheometry of pastes, suspensions and granular materials.* Wiley.

Coussot, Philippe. 2014. Suspensions. *Pages 81–119 of: Rheophysics.* Springer.

Cox, RG. 1970. The motion of long slender bodies in a viscous fluid part 1. general theory. *Journal of Fluid mechanics*, **44**(04), 791–810.

Cox, RG. 1971. The motion of long slender bodies in a viscous fluid. Part 2. Shear flow. *Journal of Fluid Mechanics*, **45**(04), 625–657.

Cross, Malcolm M. 1965. Rheology of non-Newtonian fluids: a new flow equation for pseudoplastic systems. *Journal of colloid science*, **20**(5), 417–437.

Cwalina, Colin D, & Wagner, Norman J. 2014. Material properties of the shear-thickened state in concentrated near hard-sphere colloidal dispersions. *Journal of Rheology (1978-present)*, **58**(4), 949–967.

D422-63. 2007. Standard test method for particle-size analysis of soils.

D6913-04. 2003. Standard Test Methods for Particle-Size Distribution (Gradation) of Soils Using Sieve Analysis.

Dai, Shao-Cong, Bertevas, Erwan, Qi, FZ, & Tanner, Roger I. 2013. Viscometric functions for noncolloidal sphere suspensions with Newtonian matrices. *Journal of Rheology*, **57**(2), 493–510.

Day, Paul R. 1965. Particle fractionation and particle-size analysis. *Methods of Soil Analysis. Part 1. Physical and mineralogical properties, including statistics of measurement and sampling*, 545–567.

de Cagny, Henri, Fall, Abdoulaye, Denn, Morton M, & Bonn, Daniel. 2015. Local rheology of suspensions and dry granular materials. *Journal of Rheology (1978-present)*, **59**(4), 957–969.

Del Gaudio, P. 2014. Rheology of bimodal crystals suspensions: Results from analogue experiments and implications for magma ascent. *Geochemesty Geophysics Geosystems*, **15**, 284–291.

Denn, M. M., & Morris, J. F. 2014. Rheology of Non-Brownian Suspensions. *Annual Review of Chemical and Biomolecular Engineering*, **5**, 203–228.

Deubelbeiss, Y., Kaus, B. J. P., Connolly, J. A. D., & Caricchi, L. 2011. Potential causes for the non-Newtonian rheology of crystal-bearing magmas. *Geochemesty Geophysics Geosystems*, **12**(Q05007).

Di Stefano, C, Ferro, V, & Mirabile, S. 2010. Comparison between grain-size analyses using laser diffraction and sedimentation methods. *biosystems engineering*, **106**(2), 205–215.

Dingwell, D. B. 1996. Volcanic dilemma: flow or blow? *Science*, **273**(5278), 1054–1055.

Divoux, Thibaut, Fardin, Marc A, Manneville, Sébastien, & Lerouge, Sandra. 2015. Shear Banding of Complex Fluids. *arXiv preprint arXiv:1503.04130*.

Doi, Masao. 1980. Rheological properties of rodlike polymers in isotropic and liquid crystalline phases. *Ferroelectrics*, **30**(1), 247–254.

Donev, A., Cisse, I., Sachs, D., Variano, E. A., Stillinger, F. H., Connelly, R., Torquato, S., & Chaikin, P. M. 2004. Improving the density of jammed disordered packings using ellipsoids. *Science*, **303**(5660), 990–993.

Dörr, Aaron, Sadiki, Amsini, & Mehdizadeh, Amirfarhang. 2013. A discrete model for the apparent viscosity of polydisperse suspensions including maximum packing fraction. *Journal of Rheology (1978-present)*, **57**(3), 743–765.

Douglas, J. F., & Garboczi, E. J. 1995. Intrinsic viscosity and the polarizability of particles having a wide range of shapes. *Advances in chemical physics*, **91**, 85–154.

Ducamp, V. C., & Raj, R. 1989. Shear and densification of glass powder compacts. *Journal of the American Ceramic Society*, **72**(5), 798–804.

Dufek, J., Huber, C., & Karlstrom, L. 2013. Magma chamber dynamics and thermodynamics. *Pages 5–31 of:* Fagents, S. A., Gregg, T. K. P., & Lopez, R. C. (eds), *Modeling volcanic processes: The physics and mathematics of volcanism.* Cambridge University Press.

Eilers, V. H. 1943. Die Viskositäts-Konzentrationsabhängigkeit kolloider Systeme in organischen Lösungsmitteln. *Kolloid-Zeitschrift*, **102**(2), 154–169.

Einstein, A. 1906. Eine neue Bestimmung der Moleküldimensionen. *Annalen Der Physik*, **324**(2), 289–306.

Einstein, A. 1911. Berichtigung zu meiner Arbeit: Eine neue Bestimmung der Moleküldimensionen. *Annalen Der Physik*, **339**(3), 591–592.

Eshel, G, Levy, GJ, Mingelgrin, U, & Singer, MJ. 2004. Critical evaluation of the use of laser diffraction for particle-size distribution analysis. *Soil Science Society of America Journal*, **68**(3), 736–743.

Famularo, Jack, & Happel, John. 1965. Sedimentation of dilute suspensions in creeping motion. *AIChE Journal*, **11**(6), 981–988.

Farr, Robert S. 2014. Simple heuristic for the viscosity of polydisperse hard spheres. *The Journal of chemical physics*, **141**(21), 214503.

Farris, R. J. 1968. Prediction of the viscosity of multimodal suspensions from unimodal viscosity data. *Transactions of The Society of Rheology*, **12**(2), 281–301.

Favier, Julien, Revell, Alistair, & Pinelli, Alfredo. 2014. A Lattice Boltzmann–Immersed Boundary method to simulate the fluid interaction with moving and slender flexible objects. *Journal of Computational Physics*, **261**, 145–161.

Feng, YT, Han, K, & Owen, DRJ. 2010. Combined three-dimensional lattice Boltzmann method and discrete element method for modelling fluid–particle interactions with experimental assessment. *International journal for numerical methods in engineering*, **81**(2), 229–245.

Ferro, Vito, & Mirabile, Stefano. 2009. Comparing particle size distribution analysis by sedimentation and laser diffraction method. *Journal of Agricultural Engineering*, **40**(2), 35–43.

Forien, M., Arbaret, L., Burgisser, A., & Champallier, R. 2011. Experimental constrains on shear–induced crystal breakage in magmas. *Journal of Geophysical Research*, **116**(B08217).

Frankel, N. A., & Acrivos, A. 1967. On the viscosity of a concentrated suspension of solid spheres. *Chemical Engineering Science*, **22**(6), 847–853.

Frankel, N. A., & Acrivos, A. 1970. The constitutive equation for a dilute emulsion. *Journal of Fluid Mechanics*, **44**(1), 65–78.

Gadala-Maria, F., & Acrivos, A. 1980. Shear-Induced Structure in a Concentrated Suspension of Solid Spheres. *Journal of Rheology*, **24**(6), 799–814.

Gal-Or, Benjamin. 1970. On motion of bubbles and drops. *The Canadian Journal of Chemical Engineering*, **48**(5), 526–531.

Ganani, E, & Powell, RL. 1985. Suspensions of rodlike particles: literature review and data correlations. *Journal of composite materials*, **19**(3), 194–215.

Gantenbein, Daniel, Schoelkopf, Joachim, Matthews, G Peter, & Gane, Patrick AC. 2011. Determining the size distribution-defined aspect ratio of platy particles. *Applied Clay Science*, **53**(4), 544–552.

Gao, Tong, Hu, Howard H, & Castañeda, Pedro Ponte. 2011. Rheology of a suspension of elastic particles in a viscous shear flow. *Journal of Fluid Mechanics*, **687**, 209–237.

Gay, E. C., Nelson, P. A., & Armstrong, W. P. 1969. Flow properties of suspensions with high solids concentration. *AIChE journal*, **15**(6), 815–822.

Giordano, D., Mangiacaprac, A., Potuzak, M., Russell, J. K., Romano, C., Dingwell, D. B., & Di Muro, A. 2006. An expanded non-Arrhenian model for silicate melt visocsity: a treament for metaluminous, peraluminous and peralkaline liquids. *Chemical Geology*, **229**, 42–56.

Giordano, D., Russell, J. K., & Dingwell, D. B. 2008. Viscosity of magmatic liquids: a model. *Earth and Planetary Science Letters*, **271**, 123–134.

Glowinski, Roland, Pan, T-W, Hesla, Todd I, & Joseph, Daniel D. 1999. A distributed Lagrange multiplier/fictitious domain method for particulate flows. *International Journal of Multiphase Flow*, **25**(5), 755–794.

Goddard, J. D., & Miller, C. 1967. Nonlinear effects in the rheology of dilute suspensions. *Journal of Fluid Mechanics*, **28**(4), 657–673.

Goldsmith, Harry Leonard. 1967. The microrheology of dispersions. *Rheology*, **4**.

Goldsmith, HL, & Mason, SG. 1962. The flow of suspensions through tubes. I. Single spheres, rods, and discs. *Journal of Colloid Science*, **17**(5), 448–476.

Gonnermann, H. M., & Manga, M. 2007. The fluid mechanics inside a volcano. *Annu. Rev. Fluid Mech.*, **39**, 321–356.

Gonnermann, H. M., & Manga, M. 2013. Magma ascent in the volcanic conduit. *Pages 55–84 of:* Fagents, S. A., Gregg, T. K. P., & Lopez, R. C. (eds), *Modeling volcanic processes: The physics and mathematics of volcanism.* Cambridge University Press.

Graham, A. L., Altobelli, S. A., Fukushima, E., Mondy, L. A., & Stephens, T. S. 1991. Note: NMR imaging of shear-induced diffusion and structure in concentrated suspensions undergoing Couette flow. *Journal of Rheology*, **35**(1), 191–201.

Greco, Francesco. 2002. Second-order theory for the deformation of a Newtonian drop in a stationary flow field. *Physics of Fluids (1994-present)*, **14**(3), 946–954.

Haber, Shimon, & Brenner, Howard. 1984. Rheological properties of dilute suspensions of centrally symmetric Brownian particles at small shear rates. *Journal of colloid and interface science*, **97**(2), 496–514.

Hackley, Vincent A, & Ferraris, Chiara F. 2001. *Guide to rheological nomenclature: Measurements in ceramic particulate systems*. National Institute of Standards and Technology Gaithersburg, MD, USA.

Hanratty, Thomas J, & Bandukwala, Abdemannan. 1957. Fluidization and sedimentation of spherical particles. *AIChE Journal*, **3**(2), 293–296.

Happel, John. 1958. Viscous flow in multiparticle systems: slow motion of fluids relative to beds of spherical particles. *AIChE Journal*, **4**(2), 197–201.

Happel, John, & Brenner, Howard. 2012. *Low Reynolds number hydrodynamics: with special applications to particulate media*. Vol. 1. Springer Science & Business Media.

Harris, A. J. L. 2013. Lava flows. *Pages 85–106 of:* Fagents, S. A., Gregg, T. K. P., & Lopez, R. C. (eds), *Modeling volcanic processes: The physics and mathematics of volcanism*. Cambridge University Press.

Hasimoto, H. 1959. On the periodic fundamental solutions of the Stokes equations and their application to viscous flow past a cubic array of spheres. *Journal of Fluid Mechanics*, **5**(02), 317–328.

Hatschek, Emil. 1913. The general theory of viscosity of two-phase systems. *Transactions of the Faraday Society*, **9**, 80–92.

Hayat, Tasawar, Abbasi, Fahad Munir, Ahmad, Bashir, & Alsaedi, Ahmed. 2014. Peristaltic transport of Carreau-Yasuda fluid in a curved channel with slip effects. *PloS one*, **9**(4), e95070.

He, D, Ekere, NN, & Cai, L. 1999. Computer simulation of random packing of unequal particles. *Physical Review E*, **60**(6), 7098.

Herschel, Winslow H, & Bulkley, Ronald. 1926. Konsistenzmessungen von gummi-benzollösungen. *Kolloid-Zeitschrift*, **39**(4), 291–300.

Hess, K. U., & Dingwell, D. B. 1996. Viscosities of hydrous leucogranitic melts: A non-Arrhenian model. *American Mineralogist*, **81**, 1297–1300.

Hess, K. U., Cordonnier, B., Lavallee, Y., & Dingwell, D. B. 2008. Viscous heating in rhyolite: An in situ experimental determination. *Earth and Planetary Science Letters*, **275**(1-2), 121–126.

Hoffman, RL. 1972. Discontinuous and dilatant viscosity behavior in concentrated suspensions. I. Observation of a flow instability. *Transactions of The Society of Rheology (1957-1977)*, **16**(1), 155–173.

Hoogerbrugge, PJ, & Koelman, JMVA. 1992. Simulating microscopic hydrodynamic phenomena with dissipative particle dynamics. *EPL (Europhysics Letters)*, **19**(3), 155.

Hookham, P. A. 1986. *Concentration and velocity measurements in suspensions flowing through a rectangular channel*. Ph.D Thesis, California Institute of Technology.

Housiadas, kostas D. 2015. An effective medium approach for the elongational viscosity of non-colloidal and non-Brownian hard-sphere suspensions. *Physics of Fluids*, **27**(8).

Housiadas, Kostas D., & Tanner, Roger I. 2014. A model for the shear viscosity of non-colloidal suspensions with Newtonian matrix fluids. *Rheologica Acta*, **53**(10-11), 831–841.

Huang, Nicolas, & Bonn, Daniel. 2007. Viscosity of a dense suspension in Couette flow. *Journal of fluid mechanics*, **590**, 497–507.

Hwang, Wook Ryol, & Hulsen, Martien A. 2006. Direct numerical simulations of hard particle suspensions in planar elongational flow. *Journal of non-newtonian fluid mechanics*, **136**(2), 167–178.

Ishibashi, H. 2009. Non-Newtonian behaviour of plagioclase-bearing basaltic magma: subliquidus viscosity measurement of the 1707 basalt of Fuji volcano, Japan. *Journal of Volcanology and Geothermal Research*, **181**, 78–88.

Jabbarzadeh, Ahmad, & Tanner, Roger I. 2006. Molecular dynamics simulation and its application to nano-rheology. *Rheology Reviews*, **2006**, 165.

Javaran, Ebrahim Jahanshahi, Rahnama, Mohammad, & Jafari, Saeed. 2014. Particulate flow simulation using Lattice Boltzmann Method: A rheological study. *Advanced Powder Technology*, **25**(4), 1325–1333.

Jeffery, George B. 1922. The motion of ellipsoidal particles immersed in a viscous fluid. *Pages 161–179 of: Proceedings of the Royal Society of London A: Mathematical, Physical and Engineering Sciences*, vol. 102. The Royal Society.

Kachanov, Mark, & Abedian, Behrouz. 2015. On the isotropic and anisotropic viscosity of suspensions containing particles of diverse shapes and orientations. *International Journal of Engineering Science*, **94**, 71–85.

Kalyon, Dilhan M, & Aktas, Seda. 2014. Factors affecting the rheology and processability of highly filled suspensions. *Annual review of chemical and biomolecular engineering*, **5**, 229–254.

Kansal, Anuraag R, Torquato, Salvatore, & Stillinger, Frank H. 2002. Computer generation of dense polydisperse sphere packings. *The Journal of chemical physics*, **117**(18), 8212–8218.

Karnis, A., Goldsmith, H. L., & Mason, S. G. 1966. The kinetics of flowing dispersions: I. Concentrated suspensions of rigid particles. *Journal of Colloid and Interface Science*, **22**(6), 531–553.

Kerr, R. C., & Lister, J. R. 1991. The effects of shape on crystal settling and on the rheology of magmas. *The Journal of Geology*, **99**(3), 457–467.

Konert, Martin, & Vandenberghe, JEF. 1997. Comparison of laser grain size analysis with pipette and sieve analysis: a solution for the underestimation of the clay fraction. *Sedimentology*, **44**(3), 523–535.

Koo, Sangkyun. 2009. Estimation of hindered settling velocity of suspensions. *Journal of Industrial and Engineering Chemistry*, **15**(1), 45–49.

Krieger, I. M., & Dougherty, T. J. 1959. A mechanism for non-Newtonian flow in suspensions of rigid spheres. *Transactions of The Society of Rheology*, **3**, 137–152.

Krieger, Irvin M. 1972. Rheology of monodisperse latices. *Advances in Colloid and Interface Science*, **3**(2), 111–136.

Kunkel, Wulf B. 1948. Magnitude and character of errors produced by shape factors in Stokes' law estimates of particle radius. *Journal of Applied Physics*, **19**(11), 1056–1058.

Kyrylyuk, Andriy V, Wouterse, Alan, & Philipse, Albert P. 2010. Percolation and jamming in random heterogeneous materials with competing length scales. *Pages 29–33 of: Trends in Colloid and Interface Science XXIII*. Springer.

Ladd, AJC, & Verberg, R. 2001. Lattice-Boltzmann simulations of particle-fluid suspensions. *Journal of Statistical Physics*, **104**(5-6), 1191–1251.

Ladd, Anthony JC. 1994. Numerical simulations of particulate suspensions via a discretized Boltzmann equation. Part 2. Numerical results. *Journal of Fluid Mechanics*, **271**, 311–339.

Lambe, T William, & Whitman, Robert V. 1969. *Soil mechanics SI version*. John Wiley & Sons.

Landau, L. D., & Lifshitz, E. M. 1987. *Course Of Theoretical Physics, Volume 6, Fluid Mechanics*. Pergamon Press.

Lavallée, Y., Hess, K. U., Cordonnier, B., & Dingwell, D. B. 2007. Non-Newtonian rheological law for highly crystalline dome lavas. *Geology*, **35**(9), 843–846.

Lavallée, Y., Meredith, P. G., Dingwell, D. B., Hess, K. U., Wassermann, J., Cordonnier, B., Gerik, A., & Kruhl, J. H. 2008. Seismogenic lavas and explosive eruption forecasting. *Nature*, **453**, 507–510.

Lee, Cheng-Hsien, Huang, Zhenhua, & Chiew, Yee-Meng. 2015. An extrapolation-based boundary treatment for using the lattice Boltzmann method to simulate fluid-particle interaction near a wall. *Engineering Applications of Computational Fluid Mechanics*, **9**(1), 370–381.

Leighton, D., & Acrivos, A. 1987. The shear-induced migration of particles in concentrated suspensions. *Journal of Fluid Mechanics*, **181**, 415–439.

Leighton, David, & Acrivos, Andreas. 1986. Viscous resuspension. *Chemical engineering science*, **41**(6), 1377–1384.

Lejeune, A., & Richet, P. 1995. Rheology of crystal-bearing silicate melts: An experimental study at high viscosity. *Journal of Geophysical Research*, **100**, 4215–4229.

Leonardi, Alessandro, Wittel, Falk K, Mendoza, Miller, & Herrmann, Hans J. 2014. Coupled DEM-LBM method for the free-surface simulation of heterogeneous suspensions. *Computational Particle Mechanics*, **1**(1), 3–13.

Lewis, Wo K, Gilliland, ER, & Bauer, WC. 1949. Characteristics of fluidized particles. *Industrial & Engineering Chemistry*, **41**(6), 1104–1117.

Li, Xiaoyi, & Sarkar, Kausik. 2005. Effects of inertia on the rheology of a dilute emulsion of drops in shear. *Journal of Rheology (1978-present)*, **49**(6), 1377–1394.

Lim, Yun Mee, Seo, Dongjin, & Youn, Jae Ryoun. 2004. Rheological behavior of dilute bubble suspensions in polyol. *Korea-Australia Rheology Journal*, **16**(1), 47–54.

Lin, Yuan, Phan-Thien, Nhan, & Khoo, Boo Cheong. 2015. Shear induced organization of particles in non-colloidal suspensions in steady shear flow. *Journal of Non-Newtonian Fluid Mechanics*.

Llewellin, EW, & Manga, M. 2005. Bubble suspension rheology and implications for conduit flow. *Journal of Volcanology and Geothermal Research*, **143**(1), 205–217.

Lourakis, Manolis IA. 2005. A brief description of the Levenberg-Marquardt algorithm implemented by levmar. *Foundation of Research and Technology*, **4**, 1–6.

Lu, Ning, Ristow, Gerald H, & Likos, William J. 2000. The accuracy of hydrometer analysis for fine-grained clay particles. *ASTM geotechnical testing journal*, **23**(4), 487–495.

Luciani, André, Leterrier, Yves, & Månson, Jan-Anders E. 1999. Rheological behaviour of dilute suspensions of platelet particles. *Rheologica acta*, **38**(5), 437–442.

Mackaplow, Michael B, & Shaqfeh, Eric SG. 1996. A numerical study of the rheological properties of suspensions of rigid, non-Brownian fibres. *Journal of Fluid Mechanics*, **329**, 155–186.

Mackenzie, JK. 1950. The elastic constants of a solid containing spherical holes. *Proceedings of the Physical Society. Section B*, **63**(1), 2.

Mader, H. M., Llewellin, E. W., & Mueller, S. P. 2013. The rheology of two-phase magmas: A review and analysis. *Journal of Volcanology and Geothermal Research*, **257**, 135–158.

Manga, M, & Loewenberg, M. 2001. Viscosity of magmas containing highly deformable bubbles. *Journal of Volcanology and Geothermal Research*, **105**(1), 19–24.

Mari, Romain, Seto, Ryohei, Morris, Jeffrey F, & Denn, Morton M. 2014. Shear thickening, frictionless and frictional rheologies in non-Brownian suspensions. *Journal of Rheology (1978-present)*, **58**(6), 1693–1724.

Maron, S. H., & Levy-Pascal, A. E. 1955. Rheology of synthetic latex: VI. The flow behavior of neoprene latex. *Journal of Colloid Science*, **10**(5), 494–503.

Maron, S. H., & Pierce, P. E. 1956. Application of Ree-Eyring generalized flow theory to suspensions of spherical particles. *Journal of Colloid Science*, **11**(1), 80–95.

Maron, S. H., & Shiu Ming, F. 1955. Rheology of synthetic latex: V. Flow behavior of low-temperature GR-S latex. *Journal of Colloid Science*, **10**(5), 482–493.

Marti, I., Höfler, O., Fischer, P., & Windhab, E. J. 2005. Rheology of concentrated suspensions containing mixtures of spheres and fibres. *Rheologica acta*, **44**(5), 502–512.

Martin, D., & Nokes, R. 1988. Crystal settling in a vigorously convecting magma chamber. *Nature*, **332**, 534–536.

Martin, D., & Nokes, R. 1989. A fluid-dynamical study of crystal settling in convecting magmas. *Journal of Petrology*, **30**(6), 1471–1500.

Martys, Nicos S. 2005. Study of a dissipative particle dynamics based approach for modeling suspensions. *Journal of Rheology (1978-present)*, **49**(2), 401–424.

Mendoza, C. I. 2011. Effective static and high-frequency viscosities of concentrated suspensions of soft particles. *Journal of Chemical Physics*, **135**(5), 054904.

Mertes, TS, & Rhodes, HB. 1955. Liquid-particle behavior. *Chem. Eng. Progr*, **51**(429-432), 517–522.

Mewis, Jan, & Wagner, Norman J. 2009a. Current trends in suspension rheology. *Journal of Non-Newtonian Fluid Mechanics*, **157**(3), 147–150.

Mewis, Jan, & Wagner, Norman J. 2009b. Thixotropy. *Advances in Colloid and Interface Science*, **147**, 214–227.

Mewis, Jan, & Wagner, Norman J. 2012. *Colloidal suspension rheology*. Cambridge University Press.

Mikulencak, Duane R, & Morris, Jeffrey F. 2004. Stationary shear flow around fixed and free bodies at finite Reynolds number. *Journal of Fluid Mechanics*, **520**, 215–242.

Moitra, P, & Gonnermann, HM. 2015. Effects of crystal shape-and size-modality on magma rheology. *Geochemistry, Geophysics, Geosystems*, **16**(1), 1–26.

Mooney, M. E. 1951. The viscosity of a concentrated suspension of spherical particles. *Journal of Colloid Science*, **6**(2), 162–170.

Morris, Jeffrey F. 2009. A review of microstructure in concentrated suspensions and its implications for rheology and bulk flow. *Rheologica acta*, **48**(8), 909–923.

Morris, Jeffrey F, & Boulay, Fabienne. 1999. Curvilinear flows of noncolloidal suspensions: The role of normal stresses. *Journal of Rheology (1978-present)*, **43**(5), 1213–1237.

Mueller, S., Llewellin, E. W., & Mader, H. M. 2010. The rheology of suspensions of solid particles. *Proceedings of the Royal Society A*, **466**, 1201–1228.

Mueller, S., Llewellin, E. W., & Mader, H. M. 2011. The effect of particle shape on suspension viscosity and implications for magmatic flows. *Geophysical Research Letters*, **38**(L13316).

Nakayama, Yasuya, & Yamamoto, Ryoichi. 2005. Simulation method to resolve hydrodynamic interactions in colloidal dispersions. *Physical Review E*, **71**(3), 036707.

Nasseri, S, Phan-Thien, N, & Fan, X-J. 2000. Lubrication approximation in completed double layer boundary element method. *Computational mechanics*, **26**(4), 388–397.

Ness, Christopher, & Sun, Jin. 2015. Flow regime transitions in dense non-Brownian suspensions: Rheology, microstructural characterization, and constitutive modeling. *Physical Review E*, **91**(1), 012201.

Nettleship, I, Cisko, L, & Vallejo, L. 1997. Aggregation of clay in the hydrometer test. *Canadian geotechnical journal*, **34**(4), 621–626.

Neuville, D. R. 2006. Viscosity, structure and mixing in (Ca, Na) silicate melts. *Chemical Geology*, **229**, 28–41.

Niu, XD, Shu, C, Chew, YT, & Peng, Y. 2006. A momentum exchange-based immersed boundary-lattice Boltzmann method for simulating incompressible viscous flows. *Physics Letters A*, **354**(3), 173–182.

Norris, A. N., Callegari, A. J., & Sheng, P. 1985. A generalized differential effective medium theory. *Journal of the Mechanics and Physics of Solids*, **33**(6), 525–543.

Oldroyd, JG. 1959. *Complicated Rheological Properties in Rheology of Disperse Systems.*

Oliver, DR. 1961. The sedimentation of suspensions of closely-sized spherical particles. *Chemical Engineering Science*, **15**(3), 230–242.

Oliver, DR, & Ward, Stacey G. 1953. Relationship between relative viscosity and volume concentration of stable suspensions of spherical particles. *Nature*, **171**, 396–397.

Owens, Robert G, & Phillips, Timothy N. 2002. *Computational rheology.* Vol. 2. World Scientific.

Pal, Rajinder. 1992. Rheology of polymer-thickened emulsions. *Journal of Rheology (1978-present)*, **36**(7), 1245–1259.

Pal, Rajinder. 1996. Viscoelastic properties of polymer-thickened oil-in-water emulsions. *Chemical engineering science*, **51**(12), 3299–3305.

Pal, Rajinder. 2000. Relative viscosity of non-Newtonian concentrated emulsions of noncolloidal droplets. *Industrial & engineering chemistry research*, **39**(12), 4933–4943.

Pal, Rajinder. 2001. Evaluation of theoretical viscosity models for concentrated emulsions at low capillary numbers. *Chemical Engineering Journal*, **81**(1), 15–21.

Pal, Rajinder. 2003a. Rheological behavior of bubble-bearing magmas. *Earth and Planetary Science Letters*, **207**(1), 165–179.

Pal, Rajinder. 2003b. Rheology of concentrated suspensions of deformable elastic particles such as human erythrocytes. *Journal of biomechanics*, **36**(7), 981–989.

Pal, Rajinder. 2003c. Viscous behavior of concentrated emulsions of two immiscible Newtonian fluids with interfacial tension. *Journal of colloid and interface science*, **263**(1), 296–305.

Pal, Rajinder. 2004. Rheological constitutive equation for bubbly suspensions. *Industrial & engineering chemistry research*, **43**(17), 5372–5379.

Pal, Rajinder, & Rhodes, Edward. 1989. Viscosity/concentration relationships for emulsions. *Journal of Rheology (1978-present)*, **33**(7), 1021–1045.

Pan, Zhongcheng, de Cagny, Henri, Weber, Bart, & Bonn, Daniel. 2014. S-Shaped Discontinuous Shear Thickening Flow Curve in Granular Suspensions. *arXiv preprint arXiv:1412.5333.*

Parslow, K, & Jennings, BR. 1986. Simultaneous size and thickness measurements for heterogeneous micrometre-sized particles. *Journal of Physics D: Applied Physics*, **19**(7), 1233.

Pasquino, Rossana, Grizzuti, Nino, Maffettone, Pier Luca, & Greco, Francesco. 2008. Rheology of dilute and semidilute noncolloidal hard sphere suspensions. *Journal of Rheology (1978-present)*, **52**(6), 1369–1384.

Passchier, CW, & Trouw, RAJ. 2005. *Microtectonics, 366 pp.*

Patankar, Neelesh A, & Hu, Howard H. 2002. Finite Reynolds number effect on the rheology of a dilute suspension of neutrally buoyant circular particles in a Newtonian fluid. *International journal of multiphase flow*, **28**(3), 409–425.

Petford, N. 2003. Rheology of granitic magmas during ascent and emplacement. *Annu. Rev. Earth Planet. Sci*, **31**, 399–427.

Phan-Thien, N, & Pham, DC. 2000. Differential multiphase models for polydispersed spheroidal inclusions: thermal conductivity and effective viscosity. *International Journal of Engineering Science*, **38**(1), 73–88.

Philippe, AM, Baravian, C, Bezuglyy, V, Angilella, JR, Meneau, F, Bihannic, I, & Michot, LJ. 2013. Rheological study of two-dimensional very anisometric colloidal particle suspensions: from shear-induced orientation to viscous dissipation. *Langmuir*, **29**(17), 5315–5324.

Phillips, R. J., Armstrong, R. C., Brown, R. A., Graham, A. L., & Abbott, J. R. 1992. A constitutive equation for concentrated suspensions that accounts for shearinduced particle migration. *Physics of Fluids A: Fluid Dynamics*, **4**(1), 30–40.

Picard, D., Arbaret, L., Pichavant, M., Champallier, R., & Launeau, P. 2011. Rheology and microstructure of experimentally deformed plagioclase suspensions. *Geology*, **39**, 747–750.

Picard, D., Arbaret, L., Pichavant, M., Champallier, R., & Launeau, P. 2013. The rheological transition in plagioclase-bearing magmas. *Journal of Geophiscal Research*, **118**, 1363–1377.

Pishvaei, M, Graillat, C, Cassagnau, P, & McKenna, TF. 2006. Modelling the zero shear viscosity of bimodal high solid content latex: Calculation of the maximum packing fraction. *Chemical engineering science*, **61**(17), 5768–5780.

Pistone, Mattia, Caricchi, Luca, Ulmer, Peter, Burlini, Luigi, Ardia, Paola, Reusser, Eric, Marone, Federica, & Arbaret, Laurent. 2012. Deformation experiments of bubble-and crystal-bearing magmas: Rheological and microstructural analysis. *Journal of Geophysical Research: Solid Earth (1978–2012)*, **117**(B5).

Pistone, Mattia, Caricchi, Luca, Ulmer, Peter, Reusser, Eric, & Ardia, Paola. 2013. Rheology of volatile-bearing crystal mushes: mobilization vs. viscous death. *Chemical Geology*, **345**, 16–39.

Pivkin, Igor V, & Karniadakis, George Em. 2005. A new method to impose no-slip boundary conditions in dissipative particle dynamics. *Journal of Computational Physics*, **207**(1), 114–128.

Poslinski, A. J., Ryan, M. E., Gupta, R. K., Seshadri, S. G., & Frechette, F. J. 1988. Rheological Behavior of Filled Polymeric Systems I. Yield Stress and ShearThinning Effects. *Journal of Rheology*, **32**(7), 703–735.

Probstein, R Fi, Sengun, MZ, & Tseng, T-C. 1994. Bimodal model of concentrated suspension viscosity for distributed particle sizes. *Journal of Rheology (1978-present)*, **38**(4), 811–829.

Qi, Fuzhong, & Tanner, Roger I. 2012. Random close packing and relative viscosity of multimodal suspensions. *Rheologica acta*, **51**(4), 289–302.

Quemada, D. 1977. Rheology of concentrated disperse systems and minimum energy dissipation principle. *Rheologica Acta*, **16**(1), 82–94.

Robinson, James V. 1949. The Viscosity of Suspensions of Spheres. *The Journal of Physical Chemistry*, **53**(7), 1042–1056.

Rodriguez, B. E., Kaler, E. W., & Wolfe, M. S. 1992. Binary mixtures of mono-disperse latex dispersions. 2. Viscosity. *Langmuir*, **8**(10), 2382–2389.

Roozbahani, Mohammad Mahdi, Huat, Bujang BK, & Asadi, Afshin. 2013. The effect of different random number distributions on the porosity of spherical particles. *Advanced Powder Technology*, **24**(1), 26–35.

Roscoe, R. 1952. The viscosity of suspensions of rigid spheres. *British Journal of Applied Physics*, **3**(8), 267–269.

Roscoe, R. 1967. On the rheology of a suspension of viscoelastic spheres in a viscous liquid. *Journal of Fluid Mechanics*, **28**(2), 273–293.

Rosén, Tomas, Do-Quang, M, Aidun, CK, & Lundell, F. 2015. The dynamical states of a prolate spheroidal particle suspended in shear flow as a consequence of particle and fluid inertia. *Journal of Fluid Mechanics*, **771**, 115–158.

Rushmer, T. 1995. An experimental deformation study of partially molten amphibolite: Application to low-melt fraction segregation. *Journal of Geophysical Research*, **100**(B8), 15681–15695.

Rust, AC, & Manga, Michael. 2002. Effects of bubble deformation on the viscosity of dilute suspensions. *Journal of Non-Newtonian Fluid Mechanics*, **104**(1), 53–63.

Rutgers, Ir R. 1962. Relative viscosity and concentration. *Rheologica Acta*, **2**(4), 305–348.

Rutter, E., & Neumann, D. 1995. Experimental deformation of partially molten Westerly granite under fluid-absent conditions, with implications for the extraction of granitic magmas. *Journal of Geophysical Research*, **100**(B8), 15697–15715.

Saitô, Nobuhiko. 1950. Concentration dependence of the viscosity of high polymer solutions. I. *Journal of the Physical Society of Japan*, **5**(1), 4–8.

Santiso, Erik, & Müller, Erich A. 2002. Dense packing of binary and polydisperse hard spheres. *Molecular Physics*, **100**(15), 2461–2469.

Schall, Peter, & van Hecke, Martin. 2009. Shear bands in matter with granularity. *Annual Review of Fluid Mechanics*, **42**(1), 67.

Scherer, George W. 1979. Sintering inhomogeneous glasses: application to optical waveguides. *Journal of non-crystalline solids*, **34**(2), 239–256.

Schowalter, WR, Chaffey, CiE, & Brenner, Howard. 1968. Rheological behavior of a dilute emulsion. *Journal of colloid and interface science*, **26**(2), 152–160.

Schwarz, MP. 1996. Simulation of gas injection into liquid melts. *Applied Mathematical Modelling*, **20**(1), 41–51.

Scott, G. D., & Kilgour, D. M. 1969. The density of random close packing of spheres. *Journal of Physics D: Applied Physics*, **2**(6), 863.

Scott, T., & Kohlstedt, D. L. 2006. The effect of large melt fraction on the deformation behavior of peridotite. *Earth and Planetary Science Letters*, **246**(3-4), 177–187.

Seta, Takeshi, Rojas, Roberto, Hayashi, Kosuke, & Tomiyama, Akio. 2014. Implicit-correction-based immersed boundary–lattice Boltzmann method with two relaxation times. *Physical Review E*, **89**(2), 023307.

Sevostianov, Igor, & Kachanov, Mark. 2012. Effective properties of heterogeneous materials: Proper application of the non-interaction and the dilute limit approximations. *International Journal of Engineering Science*, **58**, 124–128.

Shakib-Manesh, A, Raiskinmäki, P, Koponen, A, Kataja, M, & Timonen, J. 2002. Shear stress in a Couette flow of liquid-particle suspensions. *Journal of statistical physics*, **107**(1-2), 67–84.

Shapiro, A. P., & Probstein, R. F. 1992. Random packings of spheres and fluidity limits of monodisperse and bidisperse suspensions. *Physical Review Letters*, **68**(9), 1422.

Shewan, Heather M, & Stokes, Jason R. 2014. Analytically predicting the viscosity of hard sphere suspensions from the particle size distribution. *Journal of Non-Newtonian Fluid Mechanics*.

Sierou, A, & Brady, JF. 2002. Rheology and microstructure in concentrated noncolloidal suspensions. *Journal of Rheology (1978-present)*, **46**(5), 1031–1056.

Simha, Robert. 1952. A treatment of the viscosity of concentrated suspensions. *Journal of Applied physics*, **23**(9), 1020–1024.

Singh, Anugrah, & Nott, Prabhu R. 2000. Normal stresses and microstructure in bounded sheared suspensions via Stokesian dynamics simulations. *Journal of Fluid Mechanics*, **412**, 279–301.

Slepetys, RA, & Cleland, AJ. 1993. Determination of shape of kaolin pigment particles. *Clay Minerals*, **28**(4), 495–508.

Snabre, P., & Mills, P. 1999. Rheology of concentrated suspensions of viscoelastic particles. *Colloids and Surfaces A: Physicochemical and Engineering Aspects*, **152**(1), 79–88.

Song, C., Wang, P., & Makse, H. A. 2008. A phase diagram for jammed matter. *Nature*, **453**(7195), 629–632.

Song, Dongxing, Jing, Dengwei, Geng, Jiafeng, & Ren, Yuxun. 2015. A modified aggregation based model for the accurate prediction of particle distribution and viscosity in magnetic nanofluids. *Powder Technology*, **283**, 561–569.

Sonshine, Richard M, & Brenner, Howard. 1966. The Stokes translation of two or more particles along the axis of an infinitely long circular cylinder. *Applied Scientific Research*, **16**(1), 425–454.

Sonshine, Richard M, Cox, Raymond G, & Brenner, Howard. 1966. The Stokes translation of a particle of arbitrary shape along the axis of a circular cylinder. *Applied Scientific Research*, **16**(1), 273–300.

Spangenberg, Jon, Roussel, N, Hattel, JH, Stang, H, Skocek, J, & Geiker, MR. 2012. Flow induced particle migration in fresh concrete: Theoretical frame, numerical simulations and experimental results on model fluids. *Cement and Concrete Research*, **42**(4), 633–641.

Spangenberg, Jon, Scherer, George W, Hopkins, Adam B, & Torquato, Salvatore. 2014. Viscosity of bimodal suspensions with hard spherical particles. *Journal of Applied Physics*, **116**(18), 184902.

Srivastava, Priyesh. 2013. *Shear rheology of concentrated emulsions at finite inertia: a numerical study*. Ph.D. thesis, University of Delaware.

Stein, Daniel J, & Spera, Frank J. 1992. Rheology and microstructure of magmatic emulsions: theory and experiments. *Journal of Volcanology and Geothermal Research*, **49**(1), 157–174.

Stein, Daniel J, & Spera, Frank J. 2002. Shear viscosity of rhyolite-vapor emulsions at magmatic temperatures by concentric cylinder rheometry. *Journal of Volcanology and Geothermal Research*, **113**(1), 243–258.

Steller, Ryszard T. 2001. Generalized slit flow of an Ellis fluid. *Polymer Engineering & Science*, **41**(11), 1859–1870.

Stickel, J. J., & Powell, R. L. 2005. Fluid mechanics and rheology of dense suspensions. *Annual Review of Fluid Mechanics*, **37**, 129–149.

Storms, R. F., Ramarao, B. V., & Weiland, R. H. 1990. Low shear rate viscosity of bimodally dispersed suspensions. *Powder Technology*, **63**(3), 247–259.

Sutherland, W. 1905. A dynamical theory of diffusion for non-electrolytes and the molecular mass of albumin. *Philosophical Magazine*, **9**(54), 781–785.

Taylor, G. I. 1932. The viscosity of a fluid containing small drops of another fluid. *Proceedsings of the Royal Society of London Series A*, **138**(834), 41–48.

Thomas, Cristina Urdaneta, & Muthukumar, M. 1991. Three-body hydrodynamic effects on viscosity of suspensions of spheres. *The Journal of chemical physics*, **94**(7), 5180–5189.

Thomas, D. G. 1965. Transport characteristics of suspension: VIII. A note on the viscosity of Newtonian suspensions of uniform spherical particles. *Journal of Colloid Science*, **20**(3), 267–277.

Tolpekin, VA, Duits, MHG, Van den Ende, D, & Mellema, J. 2004. Aggregation and breakup of colloidal particle aggregates in shear flow, studied with video microscopy. *Langmuir*, **20**(7), 2614–2627.

van der Kooij, Felix M, Boek, Edo S, & Philipse, Albert P. 2001. Rheology of dilute suspensions of hard platelike colloids. *Journal of colloid and interface science*, **235**(2), 344–349.

van der Molen, I., & Paterson, M. 1979. Experimental deformation of partially melted granite. *Contributions to Mineralogy and Petrology*, **70**(3), 299–318.

Van Loon, Sylvie, Fransaer, Jan, Clasen, Christian, & Vermant, Jan. 2014. String formation in sheared suspensions in rheologically complex media: The essential role of shear thinning. *Journal of Rheology (1978-present)*, **58**(1), 237–254.

Vand, Vladimir. 1948. Viscosity of solutions and suspensions. I. Theory. *The Journal of Physical Chemistry*, **52**(2), 277–299.

Verberg, R, De Schepper, IM, & Cohen, EGD. 1997. Viscosity of colloidal suspensions. *Physical Review E*, **55**(3), 3143.

Vetere, F., Behrens, H., Holtz, F., & Neuville, D. R. 2006. Viscosity of andesitic melts - new experimental data and a revised calculation model. *Chemical Geology*, **228**, 233–245.

Vigneresse, JEAN LOUIS, BARBEY, PIERRE, & CUNEY, MICHEL. 1996. Rheological transitions during partial melting and crystallization with application to felsic magma segregation and transfer. *Journal of Petrology*, **37**(6), 1579–1600.

Vitton, SJ, & Sadler, LY. 1997. Particle-size analysis of soils using laser light scattering and X-ray absorption technology. *ASTM geotechnical testing journal*, **20**(1), 63–73.

Vona, A., Romano, C., Dingwell, D. B., & Giordano, D. 2011. The rheology of crystal-bearing basaltic magmas from Stromboli and Etna. *Geochimica et Cosmochimica Acta*, **75**(11), 3214–3236.

Vu, Thai-Son, Ovarlez, Guillaume, & Chateau, Xavier. 2010. Macroscopic behavior of bidisperse suspensions of noncolloidal particles in yield stress fluids. *Journal of Rheology (1978-present)*, **54**(4), 815–833.

Wagner, NJ, & Woutersen, ATJ. 1994. The viscosity of bimodal and polydisperse suspensions of hard spheres in the dilute limit. *Journal of Fluid Mechanics*, **278**, 267–287.

Wallis, Graham B. 1969. *One-dimensional two-phase flow*. Vol. 1. McGraw-Hill New York.

Webb, S. L., & Dingwell, D. B. 1990. Non-Newtonian rheology of igneous melts at high stresses and strain rates: Experimental results for rhyolite, andesite, basalt, and nephelinite. *Journal of Geophysical Research*, **95**(B10), 15695–15701.

Weber, C, Heuser, M, Mertens, G, & Stanjek, H. 2014. Determination of clay mineral aspect ratios from conductometric titrations. *Clay Minerals*, **49**(1), 17–26.

Wen, Baoping, Aydin, Adnan, & Duzgoren-Aydin, Nurdan S. 2002. A comparative study of particle size analyses by sieve-hydrometer and laser diffraction methods. *ASTM geotechnical testing journal*, **25**(4), 434–442.

Whittington, A.G., Hellwig, B.M., Behrens, H., Joachim, B., Stechern, A., & Vetere, F. 2009. The viscosity of hydrous dacitic liquids: implications for the rheology of evolving silicic magmas. *Bulletin of Volcanology*, **71**, 185–199.

Wildemuth, C. R., & Williams, M. C. 1984. Viscosity of suspensions modeled with a shear-dependent maximum packing fraction. *Rheologica Acta*, **23**(6), 627–635.

Williams, S. R., & Philipse, A. P. 2003. Random packings of spheres and spherocylinders simulated by mechanical contraction. *Physical Review E*, **67**(5), 051301.

Wilson, BW. 1953. The sedimentation of dense suspensions of microscopic spheres. *Aust. J. Appl. Sci*, **4**, 274–299.

Wouterse, Alan, Williams, Stephen R, & Philipse, Albert P. 2007. Effect of particle shape on the density and microstructure of random packings. *Journal of Physics: Condensed Matter*, **19**(40), 406215.

Wylie, J. J., Voight, B., & Whitehead, J. A. 1999. Instability of magma flow from volatile-dependent viscosity. *Science*, **285**, 1883–1885.

Yadav, S, Reddy, M Mallikarjuna, & Singh, Anugrah. 2015. Shear-induced particle migration in three-dimensional bifurcation channel. *International Journal of Multiphase Flow*, **76**, 1–12.

Yuan, Hai-Zhuan, Niu, Xiao-Dong, Shu, Shi, Li, Mingjun, & Yamaguchi, Hiroshi. 2014. A momentum exchange-based immersed boundary-lattice Boltzmann method for simulating a flexible filament in an incompressible flow. *Computers & Mathematics with Applications*, **67**(5), 1039–1056.

Zarraga, Isidro E, Hill, Davide A, & Leighton Jr, David T. 2000. The characterization of the total stress of concentrated suspensions of noncolloidal spheres in Newtonian fluids. *Journal of Rheology (1978-present)*, **44**(2), 185–220.

Zhang, Chi, O'Donovan, Cathal B, Corwin, Eric I, Cardinaux, Frédéric, Mason, Thomas G, Möbius, Matthias E, & Scheffold, Frank. 2015a. Structure of marginally jammed polydisperse packings of frictionless spheres. *Physical Review E*, **91**(3), 032302.

Zhang, Hao, Tan, Yuanqiang, Shu, Shi, Niu, Xiaodong, Trias, Francesc Xavier, Yang, Dongmin, Li, Hao, & Sheng, Yong. 2014. Numerical investigation on the role of discrete element method in combined LBM–IBM–DEM modeling. *Computers & Fluids*, **94**, 37–48.

Zhang, Hao, Trias, F Xavier, Oliva, Assensi, Yang, Dongmin, Tan, Yuanqiang, Shu, Shi, & Sheng, Yong. 2015b. PIBM: Particulate immersed boundary method for fluid–particle interaction problems. *Powder Technology*, **272**, 1–13.

Zia, Roseanna N, & Brady, John F. 2015. Theoretical microrheology. *Pages 113–157 of: Complex Fluids in Biological Systems*. Springer.

Zinchenko, Alexander Z, *et al.* . 2003. Large–scale simulations of concentrated emulsion flows. *Philosophical Transactions of the Royal Society of London A: Mathematical, Physical and Engineering Sciences*, **361**(1806), 813–845.

VITA

Salah Aldin Faroughi was born in Boukan, West Azarbaijan, Iran in 1987. He finished his bachelor's degree in Mechanical Engineering-Fluid Mechanics at Urmia University. He received a Master of Engineering in Mechanical Engineering-Fluid Mechanics from Sharif University of Technology, where he was working on multi-phase flow in porous media. He also holds a Master of Science in Earth and Atmospheric Sciences focusing on Geofluids from Georgia Institute of Technology. He has been studying fluid mechanics since 2004, and currently, his research interests focus on the rheophysics of soft condensed matters, particle-laden flow, bubbly flows, and in general, the thermal and mechanical properties of particulate matters. During his PhD study at Georgia Institute of Technology, he published several papers in prestigious leading journals. He also participated in a research, as a intern and technical consultant, with American Air Liquide working on the rheology of particle-laden foams.